Challenge Journal of
CONCRETE RESEARCH LETTERS

Vol.17 No.2 (2026)

acoustic emission aerated concrete artificial neural network compressive strength corrosion cracking ductility durability energy absorption ferrocement flexural strength fly ash fracture mechanics mechanical properties mortar optimization nanoparticle palm oil fuel ash polymer concrete reinforced concrete self-compacting concrete steam curing strengthening superplasticizer tensile strength workability waste disposal water absorption

ISSN 2548-0928

TULPAR ACADEMIC PUBLISHING

Challenge Journal of
CONCRETE RESEARCH LETTERS

E-mail: *cjcrl@challengejournal.com*

Web page: *cjcrl.challengejournal.com*

Tulpar Academic Publishing
www.tulparpublishing.com

Challenge Journal of
CONCRETE RESEARCH LETTERS

CONTENTS

Research Articles

Challenge Journal of CONCRETE RESEARCH LETTERS

Research Article

Influence of casting delay on concrete compressive strength

Md. Aminul Islam [a,b], Md. Mahabub Rahman [c,*], Md. Jakiul Alam Chy [d]

[a] *BUET-Japan Institute of Disaster Prevention and Urban Safety, Bangladesh University of Engineering and Technology, Dhaka-1000, Bangladesh*
[b] *Department of Civil Engineering, Auburn University, Auburn-36830, AL, USA*
[c] *Department of Civil Engineering, Hajee Mohammad Danesh Science and Technology University, Dinajpur-5200, Bangladesh*
[d] *Square Toiletries Ltd., Dhaka-1212, Bangladesh*

ABSTRACT

This research aims to evaluate the effect of evaporation and casting delay (delaying in pouring concrete after mixing, up to 120 minutes) on the concrete compressive strength (CCS) after 7, 14, and 28 days. To examine this, Portland Composite Cement (PCC) and Ordinary Portland Cement (OPC) were utilized with water-cement (w/c) ratios of 0.5 and 0.6. The CCS was assessed for four distinct casting delay durations (0, 30, 60, and 120 minutes) and for two conditions: with and without evaporation. A total of 288 cylinders (4"×8") were made, and a CCS test was conducted. The test findings showed that, for a w/c of 0.6, using a casting delay of 120 minutes increased the CCS of specimens made with OPC cement by about 23%, 22.5%, and 2% at 28, 14, and 7 days, respectively, when evaporation was allowed. However, with a w/c of 0.5, it increased 28%, 42%, and 21% at 28, 14, and 7 days, respectively. The strength test results revealed increases of 18.9%, 36%, and 17.8% for 0.5 w/c when evaporation was prohibited. Specimens made with PCC (w/c of 0.5 and 0.6) showed opposite results, with strength decreasing with casting delay for both evaporation and non-evaporation conditions. At 0.6 w/c, the strength decreased by 6.4%, 6.2%, and 28.3% at 28, 14, and 7 days when evaporation was allowed, and the strength decreased by 5%, 2%, and 11.3% at 28, 14, and 7 days when evaporation was not allowed. Compared to OPC, the PCC exhibits a very slight increase in strength.

ARTICLE INFO

Article history:
Received – November 14, 2025
Revision requested – January 9, 2026
Revision received – February 6, 2026
Accepted – February 20, 2026

Keywords:
Concrete
Compressive strength
Evaporation
Casting delay
Durability

Citation: Islam MA, Rahman MM, Chy MJA (2026). Influence of casting delay on concrete compressive strength. *Challenge Journal of Concrete Research Letters*, 17(2), 82–93.

1. Introduction

Concrete is a basic composite material that includes aggregates (sand, gravel, or crushed stone) and cement paste (Gagg 2014). Concrete is one of the most widely used construction materials because it is readily available, inexpensive, easily cast into any shape, and has favorable handling characteristics (Hasan and Kabir 2011; Roknuzzaman et al. 2024, 2025). The behavior of a structure made with reinforced concrete is affected by numerous parameters, such as the quality of the concrete, reinforcements, and workmanship. The concrete compressive strength (CCS) is an important parameter to measure its performance. The non-homogeneous characteristic of the concrete renders it vulnerable to performance problems that may be a result of inappropriate design or defective mix proportioning of its materials (Nasir et al. 2020; Roknuzzaman and Rahman 2024). Besides, the CCS depends on various factors such as concrete age, period of curing, curing temperature, and the amount of superplasticizer applied; incubation time before curing and water rate in the mix are also among these factors (Hardjito et al. 2004; Esparham and Moradikhou 2021). The casting delay time can be another such factor affecting the CCS (Sapkota and Mishra 2024), which is thereafter called the time lag between the finishing of concrete mixing and pouring for the making of cylinders.

* *Corresponding author*. E-mail address: mmr.civil@hstu.ac.bd (M. M. Rahman)
ISSN: 2548-0928 / DOI: https://doi.org/10.20528/cjcrl.2026.02.001

In the computation of the CCS by compression test on a concrete cube or cylinder, the water-cement (w/c) ratio is believed to be the most important parameter that influences concrete strength (Ayanlere et al. 2023). For instance, Shamsai et al. (2012) obtained an enhancement in CCS by 34.4–35.2% with the decrease of w/c from 0.5 to 0.33. In the same way, through an aggregate replacement of burnt brick in concrete production and by decreasing the value of the w/c ratio from 0.5 to 0.4, it was found that CCS increased more than 30% (Kumar et al. 2023). On the other hand, for quarry dust concrete, compressive strength and split tensile strength were reduced as the w/c ratio increased from 0.5 to 0.65 (Rao and Sen 2017). Gavela et al. (2018) also reported that the use of limestone as a coarse aggregate with superplasticizer and reduction of the w/c ratio from 0.54 to 0.46 enhanced CCS from 69 to 80 MPa. In addition to the w/c ratio, other factors significantly affect concrete performance. Contaminated mix water, which is often contributed by sewage or swamps and contains sulfate ions, could potentially reduce CCS of concrete as well as retard initial and final setting times for OPC and PPC (N'Simba et al. 2023). Moreover, the longer curing time will result in a higher degree of hydration and thus better performance of concrete at compressive strength (Roknuzzaman et al. 2025). Additives such as superplasticizers and retarders possessing excellent compatibilities can help improve the workability of concrete and avoid segregation, but if in greater quantities, they will have an adverse effect (Barbhuiya et al. 2025). In fact, it can be seen that the cement composites with superplasticizers, retarders, and fly ash also significantly contributed to enhancing both the CCS and flexural strength of the concrete (Singh et al. 2015). The process of re-tempering has also been studied for its effects. Abdel-Aziz et al. (2019) investigated the effect of water as a re-tempering agent on the compressive and tensile strength of concrete. They found that 10% water added after a delay of 45 min restored the original slump value, however. They found that re-tempering for 1 hour or longer made the steel harder, but that re-tempering for 0 to 120 minutes weakened it in both compressive and tensile strength. Similarly, the effect of superplasticizer dosage and time delay (up to 90 minutes) on the slump value and CCS of self-compacting concrete was studied by Zeyad and Almalki (2020). They also found that the maximum value of CCS was obtained with a 15 min delay and then started to decrease. Furthermore, the slump flow decreased by 6%, 19%, and 27% with increasing mixing times of 30, 60, and 90 minutes, compared to the slump flow observed at a mixing time of only 15 minutes.

Unlike some results, Chy. et al. (2016) showed that the cast delay did not reduce but enhanced the CCS for different OPC w/c ratios. But in the case of ready-mixed concrete firms, Sobhani et al. (2012) identified that delays in casting lead to a high reduction of workability and effectively may make the concrete unworkable. Too long of a pour delay will result in unfit concrete being placed. Other studies have reported inconsistent findings on this issue. Rathi and Kolase (2013) stated that in the absence of a retarder, the late placing of the second part caused an increase in the strength of a concrete sample. More precisely, the CCS was higher for delay times up to initial setting time and lower for delay times beyond initial setting time. Likewise, Mohamadien (2013) investigated the influence of the cold joints for a second layer of concrete with delay times of 4, 9, and 16 h. It was concluded that the CCS reduced with an increase in the casting times at which the second layer was cast. Contradictorily, the CCS was reduced by 3%, 4%, and 7% at ages of 4, 9, and 16 h as a result of the grouting between two layers. Mahzuz et al. (2020) analyzed the effects of casting delay on the 28-day compressive strength for PLC and OPC. Their results showed that replacing the water lost every hour to maintain workability led to a decrease in CCS of cylinders over time, whereas adding no water after a resting period resulted in rapid loss of workability and strength.

On the worksite, concrete cannot be placed just-in-time because of the transit time to the site, site logistics, workforce availability, etc. This may delay the pouring of concrete, meaning that the mixture loses workability. This situation may injure the concrete's mechanical characteristics. For example, Mahzuz et al. (2020) indicated that adding water to recover the workability decreased the CCS. Despite the above-mentioned studies, the combined influence of evaporation and delayed casting time on CCS has received limited attention in the research area. Therefore, the purpose of this study was to examine the effect of placement delay and moisture loss on compressive strength of freshly mixed concrete made with OPC and PCC using two different w/c ratios of 0.5 and 0.6.

2. Materials and Methods

The materials characteristic's (binder, sand, and coarse aggregate), the sample preparation, and the testing procedure are discussed in this section.

2.1. Material properties

Two types of cement were utilized as binding agents in this investigation. OPC is made of 95-100% clinker, 0% limestone, and 0-5% gypsum (ASTM C150/C150M 2024), while PCC is composed of 72-79% clinker, 21-28% blast furnace slag and limestone, and 0-5% gypsum (BDS EN 197-1 2010; ASTM C595/C595M 2012). According to ASTM C191 (2021), the VICAT Apparatus is used to estimate the setting time of cements. Following ASTM C187 (2023), the typical consistency of OPC and PCC was evaluated. As a fine aggregate, Sylhet sand was used, which was locally available and widely used fine aggregate in the construction field of Bangladesh. Sieve analysis was conducted for the sand in compliance with ASTM C136 (2019) to determine the fineness modulus. Bulk density, specific gravity, and water absorption of sand were determined in accordance with ASTM C29/C29M (2023) and ASTM C128 (2025). In this study, crushed stone up to ¾ inch in dimension was used as a coarse aggregate. Table 1 depicts the properties of coarse and fine aggregate.

Bulk specific gravity and absorption were assessed following ASTM C127 (1992). The standard consistency, and setting time of both OPC and PCC are listed in Table 2 (throughout the paper, hr. refers to hour and min. refers to minutes).

Table 1. Characteristics of course and fine aggregate.

Properties	Sand	Stone-chips
Bulk specific gravity	2.52	2.61
Absorption	1.94 %	1.2%
Unit weight	1525 kg/m^3	1518 kg/m^3
Fineness modulus	2.6	–

Table 2. Setting times and consistency of cement.

Type of cement	Consistency	Initial setting time	Final setting time
OPC	25%	1 hr. 55 min.	4 hr. 40 min.
PCC	27%	2 hr. 20 min.	5 hr. 25 min.

2.2. Sample preparation

This study aims to determine how the casting delay time (delaying in casting after mixing concrete) affects the concrete compressive strength built using locally available PCC and OPC. For the study purpose, the placement time has been altered for two circumstances, leaving the other attributes of the concrete component (coarse aggregate, fine aggregate) unchanged. One condition permits evaporation exposing concrete mixture in air before pouring into molds, whereas the other does not allow evaporation and this was ensured by covering concrete mixture by a plastic sheet before pouring into molds. For two distinct w/c ratios (0.5 and 0.6), PCC and OPC are used in various ways when producing concrete. For both w/c ratios, the amounts of cement and concrete constituents had been computed. Table 3 lists the necessary quantity of concrete materials for casting concrete based on the ACI mix design procedure (ACI 211.1 1991).

Table 3. Quantity of concrete ingredients.

w/c ratio	Cement (ft^3)	Water (lb)	Sand (ft^3)	Stone-chips (ft^3)
0.5	1.4	44	2.1	4.2
0.6	1.4	53	2.1	4.2

ASTM C470/C470M (2023) standard was followed to create the standard concrete specimen molds. The mold utilized in this study is cylindrical in form, measuring 4" in diameter by 8" in height. Before any concrete was poured, each mold was carefully cleaned, dried, and an oil layer was applied to prevent the concrete from sticking to the mold. The mixing proportion of cement, sand and stone-chips was 1: 1.5: 3 for both w/c ratios (0.5 and 0.6). The mixing of the concrete elements was completed using a concrete mixer. The goal of the mixing process, which basically consists of rotating or stirring, was to integrate all the concrete elements into a homogenous mass and apply cement paste to the surface of every aggregate particle. The concrete was filled into the cylinder and was compacted using a standard vibrator. The process of compaction and specimen preparation is shown in Fig. 1. We generated four distinct concrete specimens by exposing the concrete to air for evaporation (evaporation allowed), corresponding to delay durations of 0, 30, 60, and 120 minutes. The concrete mix was kept in rest during these casting delay time. There was a little slump loss but it was within the standard limit as prescribed by ACI. The casting was conducted during winter, and the atmospheric temperature was almost unchangeable during the casting delay period.

Fig. 1. Specimen preparation and vibration.

A total of 288 concrete specimens were made under this situation, accounting for two distinct water-to-cement ratios. Concrete was encased in thick plastic to inhibit evaporation (evaporation not allowed), and four more types of concrete specimens were created, considering four specific delay intervals: 0, 30, 60, and 120 minutes.

Before the molds were taken out, the concrete samples were kept in air for about a day, and then the specimens were soaked in water for curing of prepared cylinders. For four distinct casting delay times (shown in Table 4), the cylinders were prepared with and without permitting evaporation. Table 4 displays general information about specimen preparation and testing.

Table 4. Details of specimen preparation and testing.

General information on specimen preparation and testing	
Cement type	OPC and PCC
w/c ratios	0.5 and 0.6
Curing type	Continuous curing up to the breaking of specimens
Casting delays considered	0, 30, 60, 120 min.
Test repeated for a particular group	3
Period of concrete testing	7, 14, 28-days

2.3. Testing

After being removed from soaking storage, a compressive strength test of the moist-cured specimens was conducted. Before testing, the ends of the specimens were smoothed with a grinder so that the load became uniform over the surface. The concrete specimens were tested after 7, 14, and 28-days in a CCS test machine to evaluate concrete strength. The tests were conducted following ASTM C39/C39M (2014). Fig. 2 displays the testing of a concrete specimen.

The CCS of a specimen is determined by dividing the highest load by its average x-sectional area. The concrete specimens were subjected to a load till it failed. Eq. (1) was used to assess the CCS of the specimens.

$$F_m = \frac{P}{A} \tag{1}$$

where, F_m = CCS of specimen (psi); P = highest load recorded from the test (lb); A = average x-sectional area of specimen (in^2).

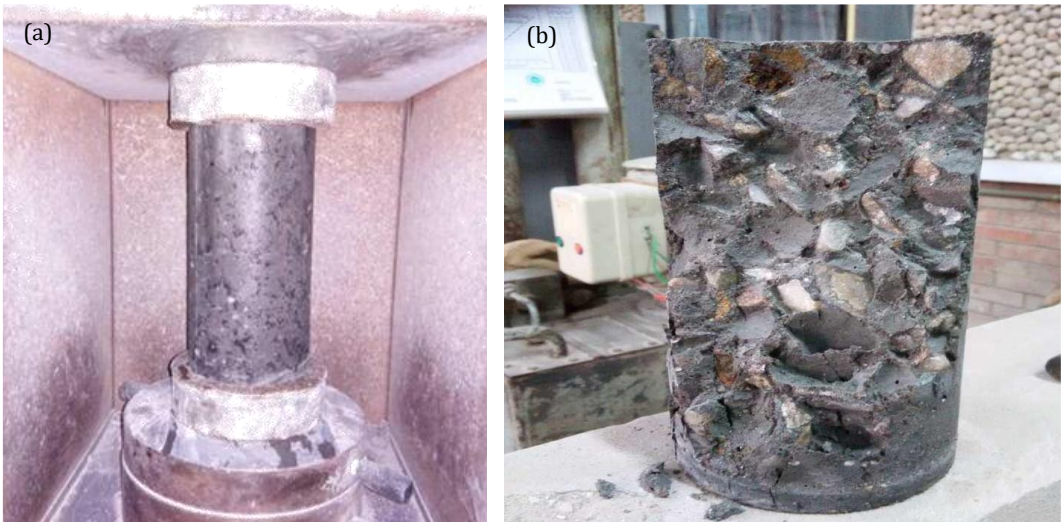

Fig. 2. Concrete specimen testing: (a) During test; (b) After failure.

3. Results and Discussion

The summary of the test results is provided in the following subsections.

3.1. Effect of casting delay allowing evaporation

Figs. 3 to 6 present the outcomes of CCS tests conducted using two distinct cement types: OPC and PCC, with water-to-cement ratios of 0.5 and 0.6. Four different casting delay times were considered, and evaporation was permitted. Overall, it is clear that OPC with a water-to-cement ratio of 0.5 obtained the highest CCS (Fig. 3), while PCC with a water-to-cement ratio of 0.6 achieved the lowest compressive strength (Fig. 6). The concrete compressive strength increased by around 28%, 42%, and 21% at 28, 14, and 7-days, respectively, for OPC with a w/c ratio of 0.5 (Fig. 3) when the casting delay time was 120 minutes, as opposed to zero minutes of casting delay. However, for the same cement with a w/c ratio of 0.6 (Fig. 4), this increase in CCS is around 23%, 22.5%, and 2% at 28, 14, and 7-days, respectively. For OPC, the CCS generally increases as the casting delay time increases for both water-to-cement ratios.

PCC has an adverse effect on strength gain with casting delay time. Compressive strength in PCC decreases as casting delay time increases for a w/c ratio of 0.6 (Fig. 6) and this happened at 120 minutes casting delay. The decrease in CCS is around 28.3%, 6.2%, and 6.4% at 7, 14, and 28-days, respectively, with 120 minutes casting delay compared to zero minutes casting delay. The possible reason is that the delay time is close to the initial setting time which cause loss of plasticity (loss of monolithic behavior) and microcrack formation (Ne-

ville 2011). At a 0.5 w/c, the compressive strength of concrete gradually increases with the increase of casting delay (Fig. 5). The reason behind this strength increase with casting delay was pre-hydration densification (Neville 2011). Due to the moderate delay in casting, the concrete paste became more cohesive (formation of Calcium Silicate Hydrate, C-S-H), the bleeding was reduced, refined the interfacial transition zone (ITZ), resulting in lower capillary porosity and higher compressive strength (Neville 2011). In conclusion, the CCS composed of PCC with a w/c equal to 0.6 negatively impacted by casting delay time; however, for OPC, the concrete compressive strength rose noticeably with casting delay.

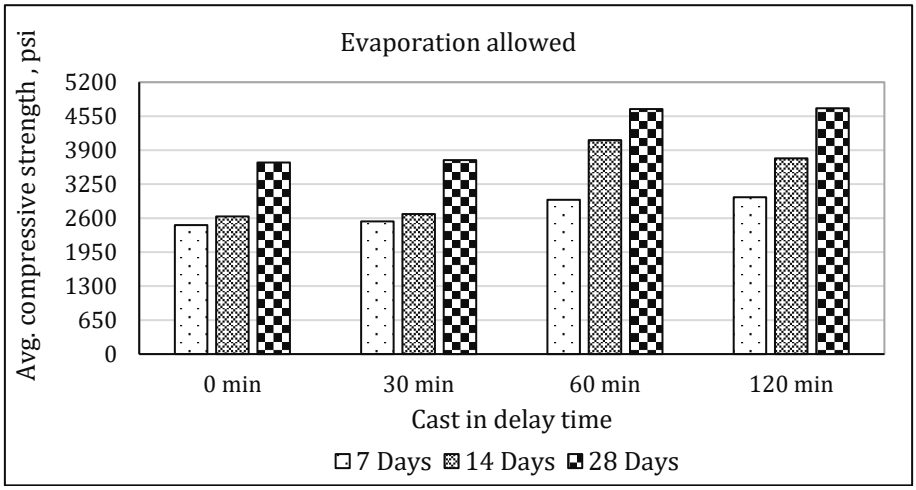

Fig. 3. Variation of CCS with casting delay (OPC, w/c =0.5).

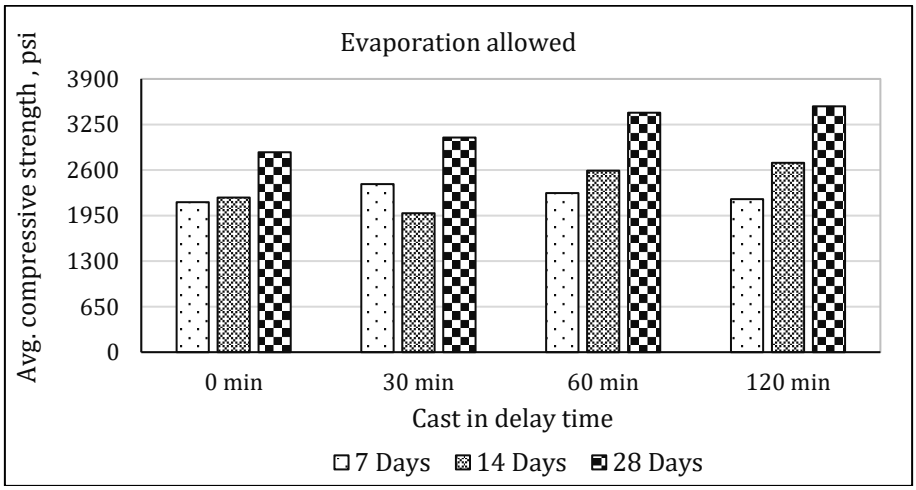

Fig. 4. Variation of CCS with casting delay (OPC, w/c =0.6).

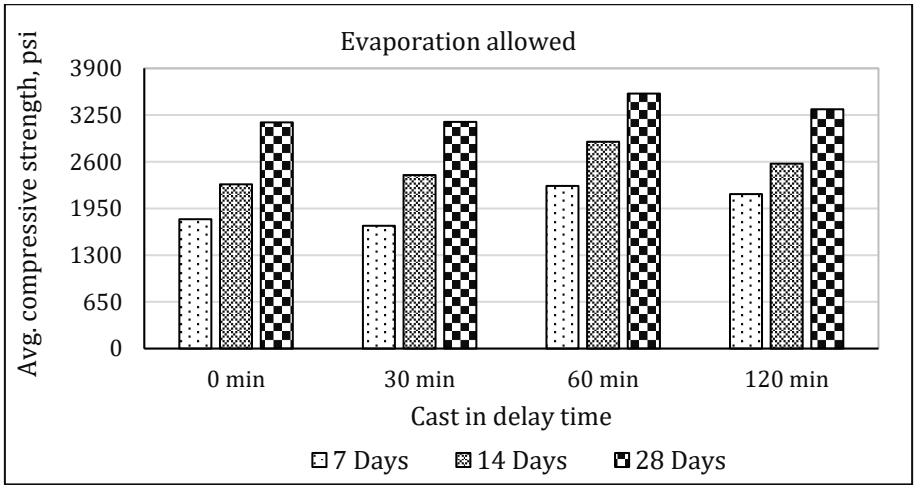

Fig. 5. Variation of CCS with casting delay (PCC, w/c =0.5).

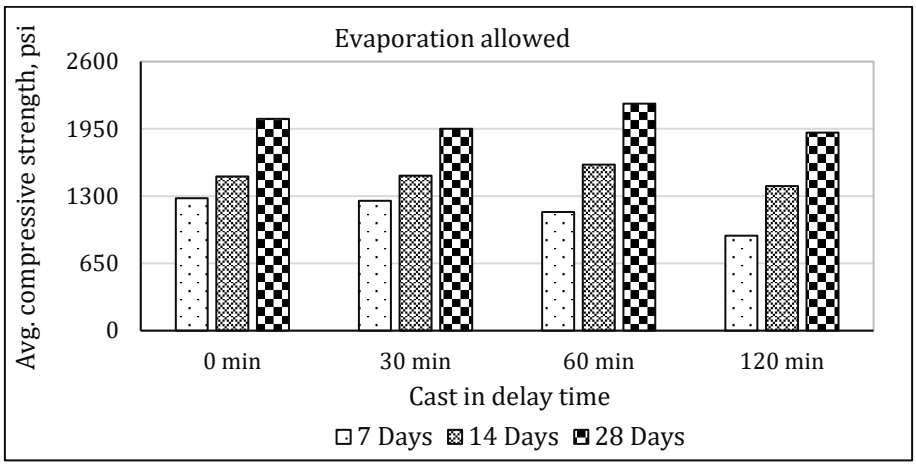

Fig. 6. Variation of CCS with casting delay (PCC, w/c =0.6).

3.2. Effect of casting delay not allowing evaporation

The CCS of the specimens using OPC and PCC with varying casting delays was evaluated, ensuring no evaporation occurred. Figs. 7–10 indicate the change in the compressive strength of concrete specimens made with varying casting delays, without permitting evaporation.

It is evident from Figs. 7–10 that the highest CCS was achieved when OPC had a w/c ratio of 0.5 and the lowest compressive strength was when PCC had a w/c of 0.6.

The maximal strength increases for OPC with a w/c of 0.5 are about 31.3% for seven days at a casting delay of 60 minutes and 36% for fourteen days with a casting delay of 120 minutes. Strength increased by 23% after 28 days with a 60-minute casting delay period. The concrete compressive strength increased by only 11% after seven days with a 30-minute casting delay for a w/c of 0.6. Conversely, with a 120-minute casting delay, the compressive strength increases by 14.9% and 15.7% after 28 and 14 days, respectively.

It is important to note that for OPC, the maximum CCS was obtained at 28 days with 60-minute casting delays. The ideal casting delay period without evaporation in this situation is sixty minutes.

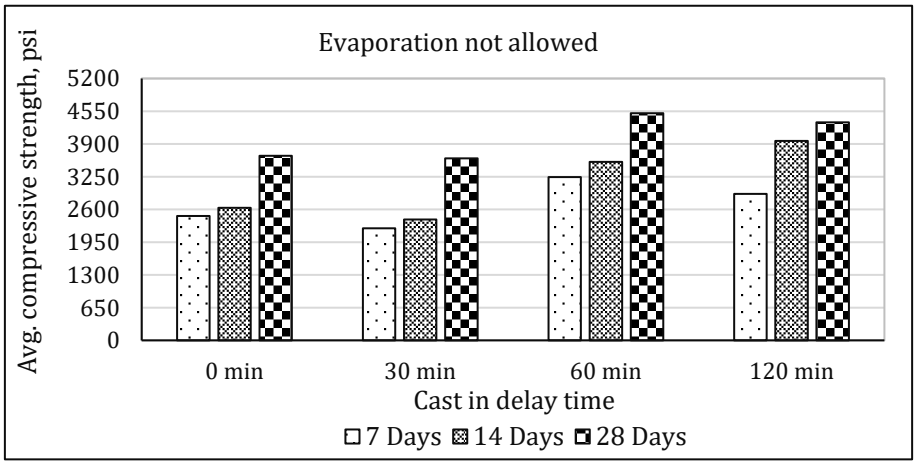

Fig. 7. Variation of CCS with casting delay (OPC, w/c =0.5).

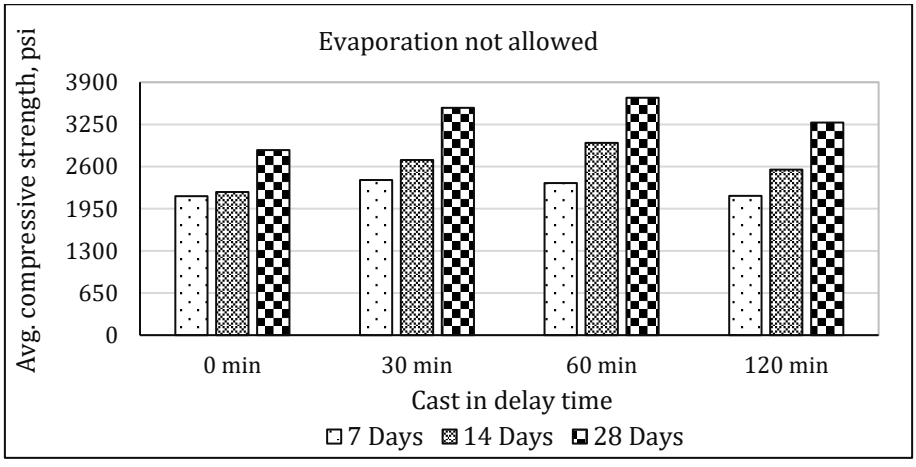

Fig. 8. Variation of CCS with casting delay (OPC, w/c =0.6).

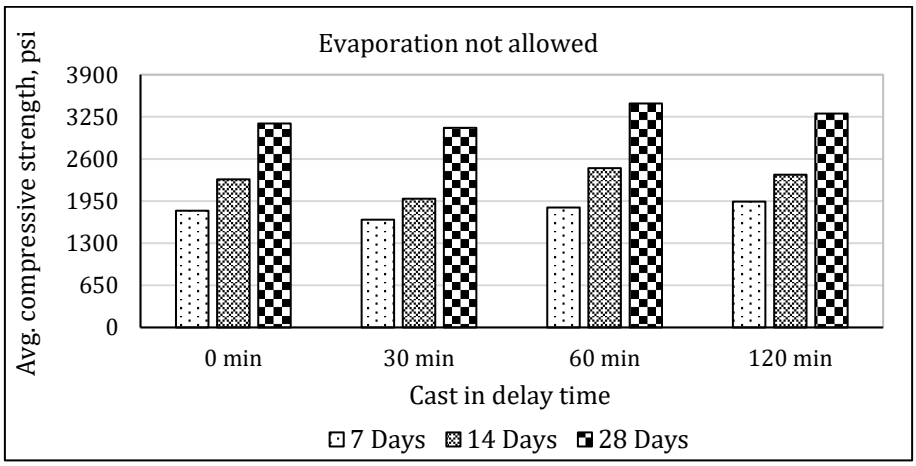

Fig. 9. Variation of CCS with casting delay (PCC, w/c =0.5).

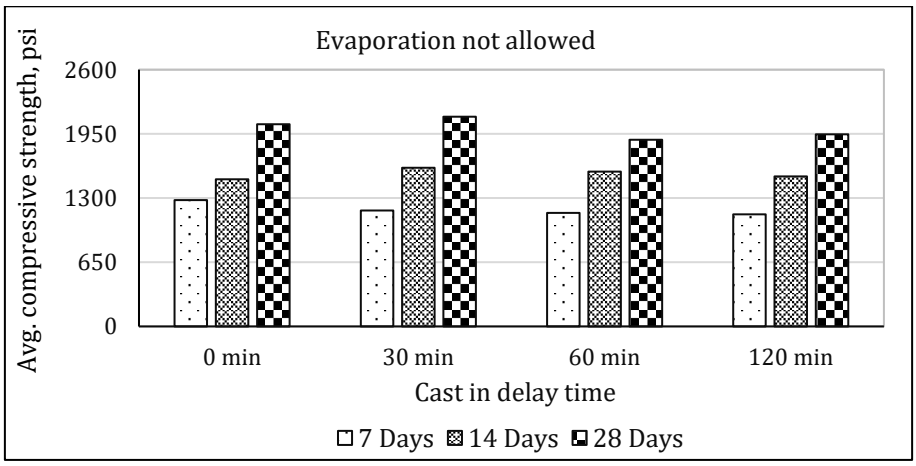

Fig. 10. Variation of CCS with casting delay (PCC, w/c =0.6).

Fig. 9 illustrates that the PCC with a w/c of 0.5 exhibits the highest CCS after 28 days following a casting delay of 60 minutes. In case of 7- and 14-days strength, the effect of casting delay is insignificant. With a w/c of 0.6, casting delay time without evaporation greatly influences the compressive strength of PCC and a decrease in the CCS occurs. Strength was greatly reduced for 7 days concrete, and it was 11.3%; however, for 14- and 28-day concrete, strength was reduced by 2% and 5%, respectively when compared between 120 minutes and zero minutes casting delay (without evaporations).

3.3. Comparison of compressive strength

The comparison of the CCS of OPC and PCC cylinders after 7, 14, and 28 days when evaporation was permitted is shown in Figs.11–13. Among the specimens, OPC with w/c of 0.5 exhibits the maximum strength, whereas PCC with w/c of 0.6 exhibits the lowest strength after 7, 14, and 28 days of curing. At 60- and 120-minute casting delay conditions, the strength of OPC with w/c of 0.6 and PCC with w/c of 0.5 is comparable. Concrete strength decreases as casting delay time increases for PCC with a w/c of 0.6 after seven days, and the lowest strength was found for casting that was delayed by 120 minutes. The greatest strength was found for a 60-minute casting delay for OPC with a w/c of 0.5 at 28 days.

The comparison of the 7-, 14-, and 28-day strengths of OPC and PCC cylinders when evaporation was prohibited is shown in Figs. 14-16. The maximum compressive strength was found for OPC with a w/c of 0.5 and a 60-minute casting delay at 28 days. The PCC with a w/c of 0.6 showed less strength for all casting delay times. Overall, OPC showed highest strength than PCC for all casting delay time and water-cement ratios.

The relative change of the CCS for 120 minutes casting delay time, which is close to the initial setting time, is shown in Figs. 17-18. This percentage strength change was calculated with zero minutes of casting delay. The CCS of cylinder specimens made with OPC shows an increase in compressive strength for both w/c. However, for w/c of 0.6, the concrete specimen made with PCC exhibits the opposite pattern. In this case (PCC, w/c 0.6), the CCS decreased. For PCC with w/c 0.5, the strength change was very similar for 28 days, irrespective of whether evaporation was allowed or not allowed. Overall, the highest percentage change in concrete compressive strength was 14 days in the case of OPC (w/c 0.5). After 120 minutes of delay casting, the strength of OPC with w/c 0.5 decreased a bit. The 28-day concrete strength for PCC with a w/c of 0.6 remained almost constant, irrespective of whether evaporation was allowed or not allowed. PCC showed very little increase in strength with a w/c of 0.5- and 120-minutes casting delay.

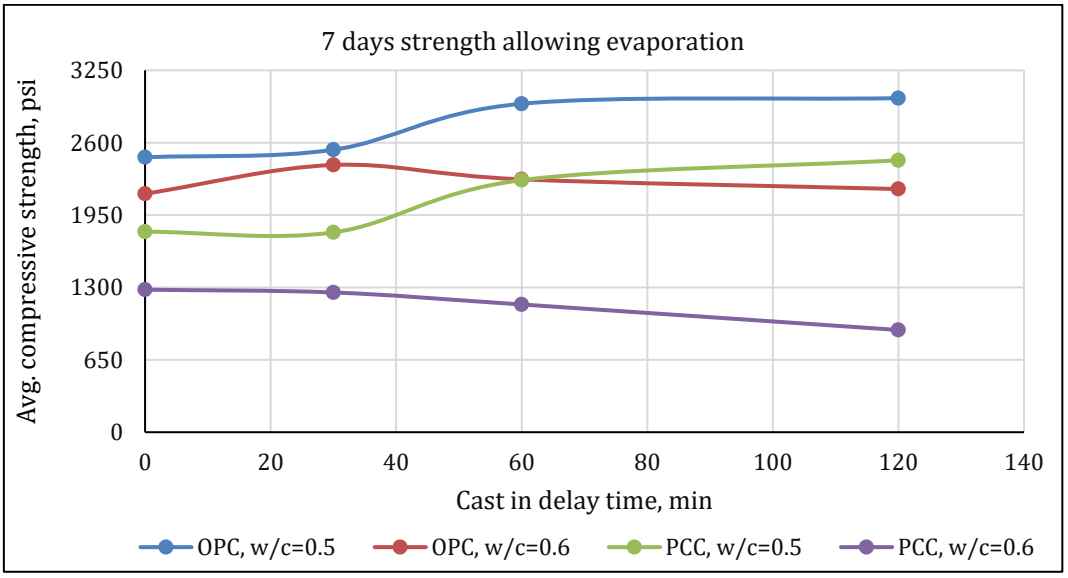

Fig. 11. Variation of 7 days CCS with casting delay.

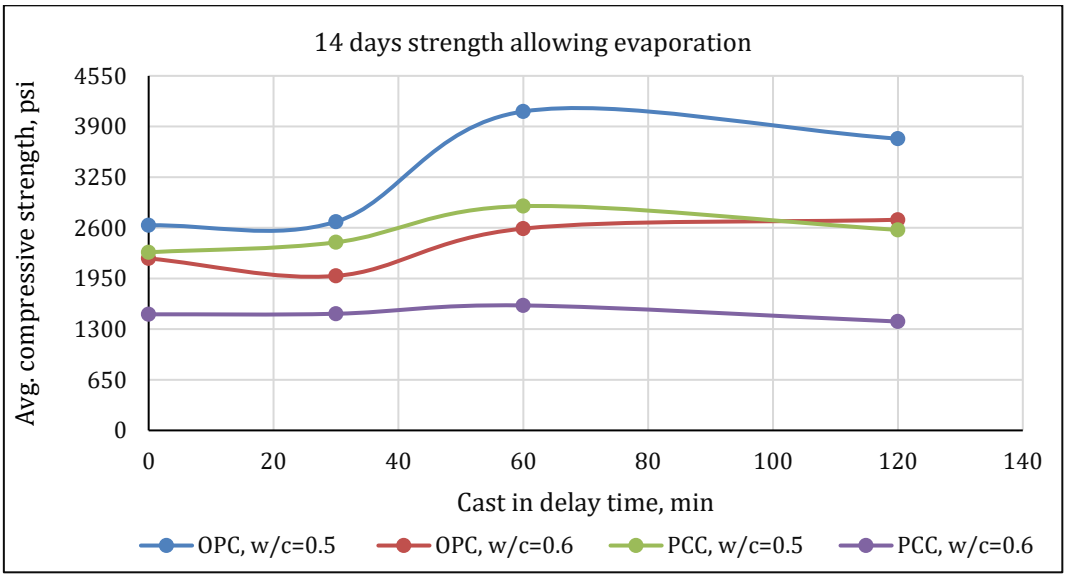

Fig. 12. Variation of 14 days CCS with casting delay.

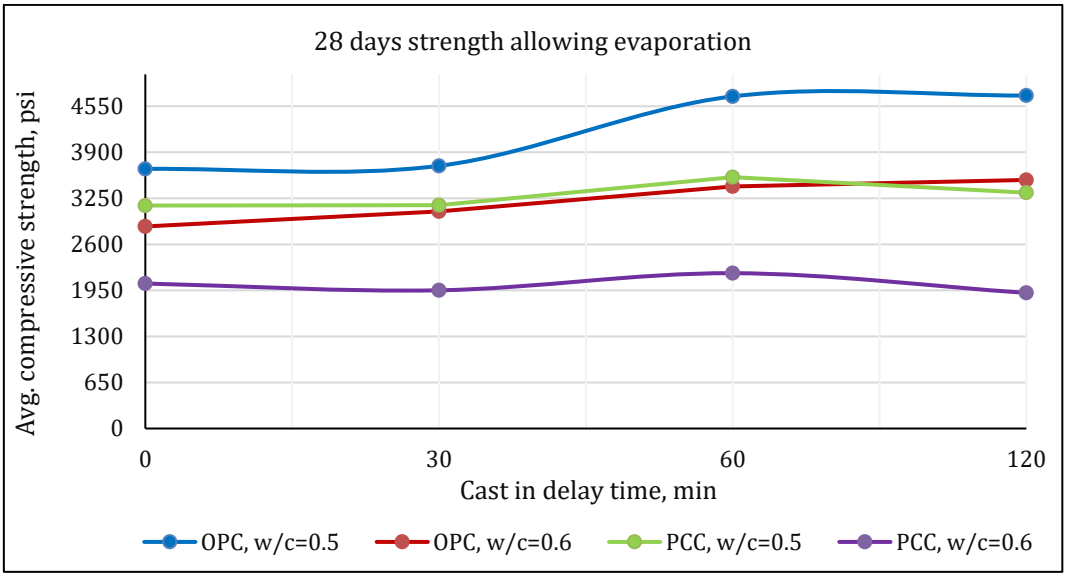

Fig. 13. Variation of 28 days CCS with casting delay.

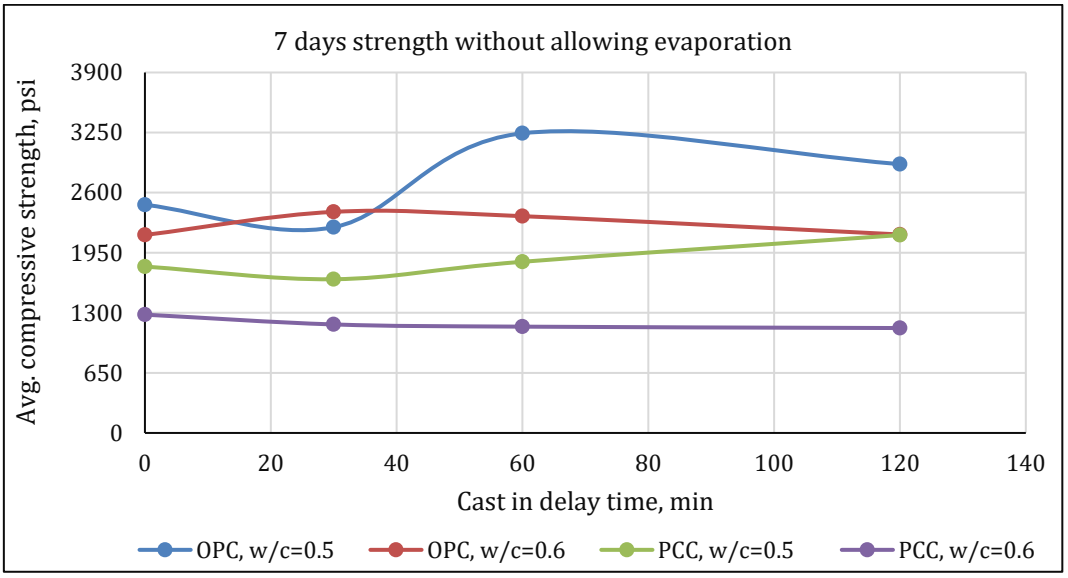

Fig. 14. Variation of 7 days CCS with casting delay.

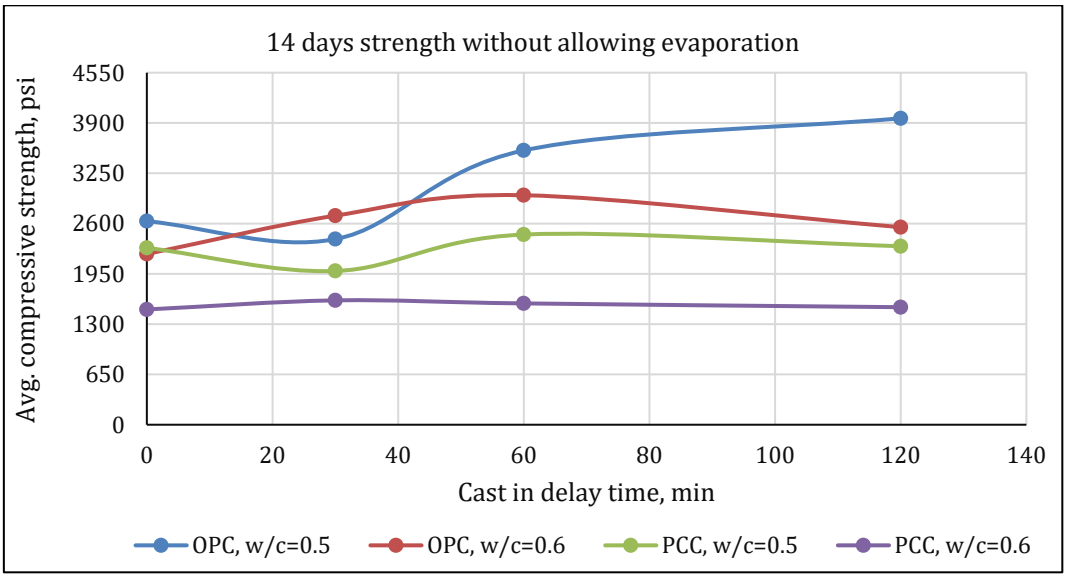

Fig. 15. Variation of 14 days CCS with casting delay.

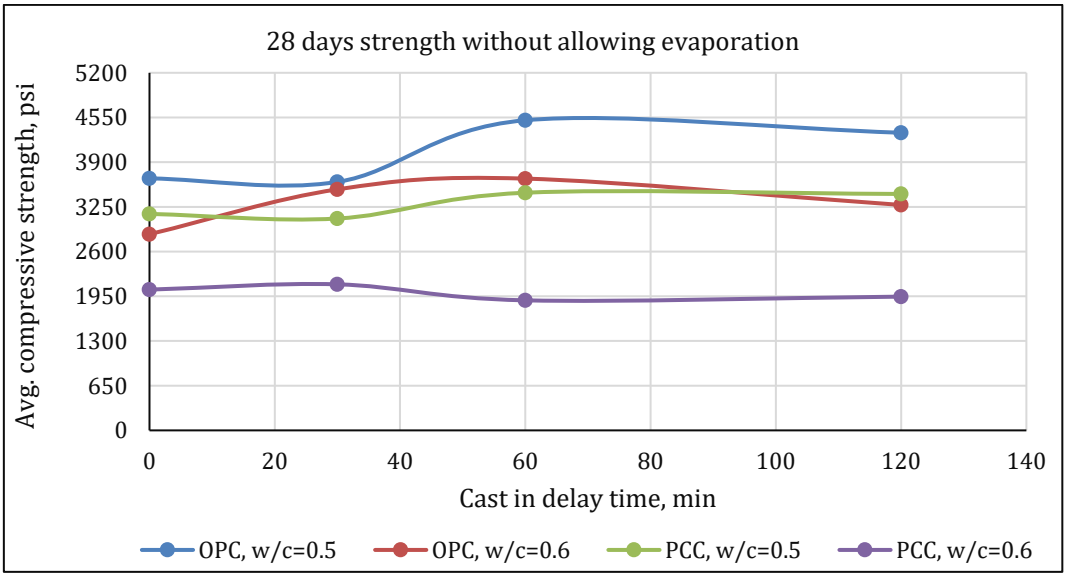

Fig. 16. Variation of 28 days CCS with casting delay.

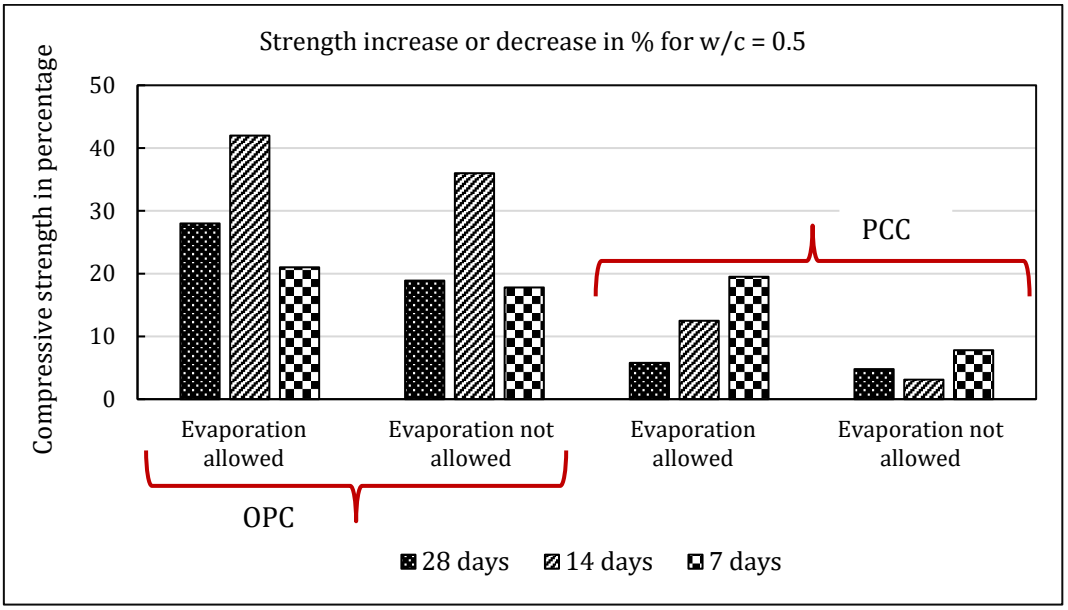

Fig. 17. Compressive strength increase or decrease for 120 min delayed casting for 0.5 w/c.

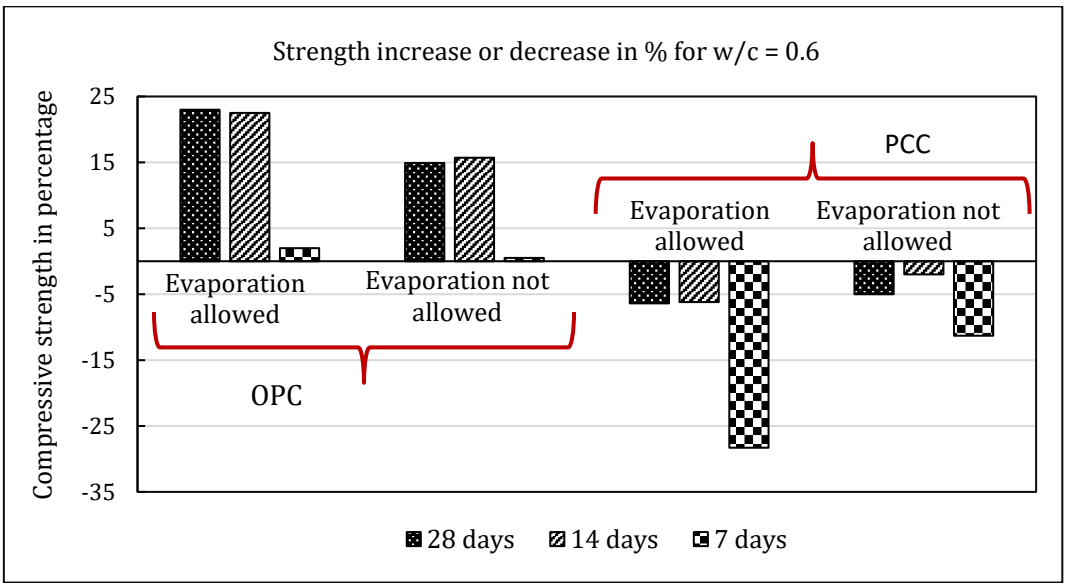

Fig. 18. Compressive strength increase or decrease for 120 min delayed casting for 0.6 w/c.

4. Conclusions

The effect of casting delay on the CCS, with and without allowing evaporation, was investigated in this research. Concrete cylinders were prepared using two types of cement: OPC and PCC, at two w/c, e.g., 0.5 and 0.6. Four casting delay times were considered: 0, 30, 60, and 120 min., to evaluate the influence of delayed casting on strength development. The CCS tests were conducted after 7, 14, and 28 days of continuous cure. The following conclusion can be drawn based on the experimental results:

- The CCS decreased with increasing water-cement ratio. Strength reduction became prominent for a w/c of 0.6, indicating that a w/c of 0.5 provided the optimum strength for both cement types.
- Casting delay influenced strength development differently depending on cement type. For mixtures prepared with OPC, compressive strength generally increased with increasing casting delay time, whereas mixtures prepared with PCC exhibited a reduction in strength with prolonged delay.
- Concrete made with OPC obtained the highest compressive strength, while the concrete made with PCC showed the lowest compressive strength.
- For OPC concrete, both evaporation-allowed and evaporation-restricted conditions produced maximum compressive strength at a casting delay of approximately 60 minutes. A slight reduction in 28-day strength relative to 14-day strength was observed; however, OPC mixtures demonstrated an overall increase in long-term strength sufficient to meet typical 28-day design requirements
- In the case of concrete made with PCC, the optimum w/c is 0.5. Increasing the w/c beyond this value resulted in strength loss. Strength gain was more pro-

nounced at early ages (7 days) compared with later ages (14 and 28 days), suggesting comparatively slower long-term strength development. It can be anticipated that the design strength (28-day strength) might be less than expected.

- Evaporation significantly influenced the compressive strength of concrete. In general, limited evaporation produced a slight increase in compressive strength compared with specimens where evaporation was prevented, likely due to a reduction in concrete pores and an increase of cohesiveness.

Subsequent investigations are advised for future research by examining the data and discussion of the test outcomes from this progressive research. They are: a) Further analysis may be conducted by retempering the mixture with water after the completion of its initial setting period. b) The research may proceed using brick chips. c) Additional study may be conducted by examining various w/c. d) The impact of admixture on casting delay may be examined.

Acknowledgements

The authors are very grateful to the Department of Civil Engineering, Bangladesh University of Engineering and Technology, Bangladesh, for providing the testing facilities.

Funding

The authors received no financial support for the research, authorship, and/or publication of this manuscript.

Conflict of Interest

The authors declare no potential conflicts of interest with respect to the research, authorship, and/or publication of this manuscript.

Data Availability

The datasets generated and/or analyzed during the current study are not publicly available but are available from the corresponding author upon reasonable request.

AI Assistance

No AI-based tools were used in the preparation of this manuscript.

Author Contributions

All authors made substantial contributions to the conception and design of the study, acquisition of data, analysis and interpretation of data; drafted or critically revised the manuscript for important intellectual content; and approved the final version to be published.

REFERENCES

Abdel-Aziz MA, Arab MA, Hossien RM (2019). Effect of concrete retempering methods on fresh and hardened concrete properties for normal and high strength concrete. *Journal of Engineering and Applied Science*, 14(23), 8903-8911.

ACI 211.1-91 (1991). Standard practice for selecting proportions for normal, heavyweight, and mass concrete. American Concrete Institute, Farmington Hills, MI, USA.

ASTM C127 (1992). Test method for specific gravity and adsorption of coarse aggregate. ASTM International, West Conshohocken, PA, USA.

ASTM C128 (2025). Standard test method for relative density (specific gravity) and absorption of fine aggregate. ASTM International, West Conshohocken, PA, USA.

ASTM C136/C136M (2019). Standard test method for sieve analysis of fine and coarse aggregates. ASTM International, West Conshohocken, PA, USA.

ASTM C150/C150M (2024). Standard specification for portland cement. ASTM International, West Conshohocken, PA, USA.

ASTM C187 (2023). Standard test method for amount of water required for normal consistency of hydraulic cement paste. ASTM International, West Conshohocken, PA, USA.

ASTM C191 (2021). Standard test methods for time of setting of hydraulic cement by vicat needle. ASTM International, West Conshohocken, PA, USA.

ASTM C29/C29M (2023). Standard test method for bulk density ("unit weight") and voids in aggregate. ASTM International, West Conshohocken, PA, USA.

ASTM C39/C39M (2014). Standard test method for compressive strength of cylindrical concrete specimens. ASTM International, West Conshohocken, PA, USA.

ASTM C470/C470M (2023). Standard specification for molds for forming concrete test cylinders vertically. ASTM International, West Conshohocken, PA, USA.

ASTM C595/C595M (2012). Standard specification for blended hydraulic cements. ASTM International, West Conshohocken, PA, USA.

Ayanlere SA, Ajamu SO, Odeyemi SO, Ajayi OE, Kareem MA (2023). Effects of water-cement ratio on bond strength of concrete. *Materials Today: Proceedings*, 86, 134-139.

Barbhuiya S, Das BB, Adak D (2025). Effects of chemical admixtures on the properties of concrete. In: Singh NB, Goyal R, Middendorf B, editors. *Binding Materials for Sustainable Construction*. Woodhead Publishing, Sawston, UK, 329–362.

BDS EN 197-1:2003 (2010). Cement – Part 1: Composition, specifications and conformity criteria for common cements. Bangladesh Standards and Testing Institution, Dhaka, Bangladesh.

Chy MJA, Kayes MI, Ali SKS (2016). Effect of delay in casting on compressive strength of concrete. *Proceedings of the 3rd International Conference on Advances in Civil Engineering*, 21-33.

Esparham A, Moradikhou AB (2021). Factors influencing compressive strength of fly ash-based geopolymer concrete. *Amirkabir Journal of Civil Engineering*, 53(3), 21-31.

Gagg CR (2014). Cement and concrete as an engineering material: An historic appraisal and case study analysis. *Engineering Failure Analysis*, 40, 114-140.

Gavela S, Nikoloutsopoulos N, Papadakos G, Passa D, Sotiropoulo A (2018). Multifactorial experimental analysis of concrete compressive strength as a function of time and water-to-cement ratio. *Procedia Structural Integrity*, 10, 135-140.

Hardjito D, Wallah SE, Sumajouw DMJ, Rangan BV (2004). Factors influencing the compressive strength of fly ash-based geopolymer concrete. *Civil Engineering Dimension*, 6(2), 88-93.

Hasan MM, Kabir A (2011). Prediction of compressive strength of concrete from early age test result. *Proceedings of the 4th Annual Paper Meet and 1st Civil Engineering Congress*, 978-984.

Kumar R, Lakhani R, Abhilasha, Rawat N, Khan S (2023). Microstructural and thermo-mechanical properties of energy-efficient structural lightweight concrete with LECA, fly ash and marble slurry. *Proceedings of Innovative and Sustainable Materials & Technologies (ISCMT-2023)*, New Delhi, India.

Mahzuz HMA, Bhuiyan MMH, Oshin NJ (2020). Influence of delayed casting on compressive strength of concrete: An experimental study. *SN Applied Sciences*, 2(3), 316.

Mohamadien HA (2013). The impact of the time when casting the second layer of concrete on its mechanical properties. *Journal of Engineering Sciences*, 41(3), 919-929.

N'Simba KYW, Kaluli JW, Mwangi BM, Mwangi HM (2023). Effect of thermal treatment on the pozzolanic activity of natural clay from selected Kenyan wetlands. *Journal of Sustainable Research in Engineering*, 7(4), 137-154.

Nasir M, Gazder U, Maslehuddin M, Baghabra Al-Amoudi OS, Syed IA (2020). Prediction of properties of concrete cured under hot weather using multivariate regression and ANN models. *Arabian Journal for Science and Engineering*, 45(5), 4111-4123.

Rao B, Sen S (2017). Effect of water cement ratio on the workability and strength of low strength quarry dust concrete. *International Journal of Civil Engineering and Technology*, 8(10), 1448-1455.

Rathi V, Kolase P (2013). Effect of cold joint on strength of concrete. *International Journal of Innovative Research in Science, Engineering and Technology*, 2(9), 4671-4679.

Roknuzzaman M, Raman MM (2024). Compressive strength of recycled green concrete affected by chloride and sulfate exposures. *Journal of Rehabilitation in Civil Engineering*, 12(4), 55-65.

Roknuzzaman M, Serker NHMK, Rahman MM (2024). Old residual mortar as a quality indicator of recycled brick aggregate. *Sustainable Structures*, 4(3), 000061.

Roknuzzaman M, Rahman MM, Islam MM (2025). Performance and usability assessment of recycled aggregate extracted from demolished concrete subjected to multiple recycling. *Journal of Rehabilitation in Civil Engineering*, 13(4), 161-176.

Sapkota LP, Mishra K (2024). Impact analysis of the time elapsed between mixing and placing on compressive strength of concrete for commercial production. *The International Journal of Science, Mathematics and Technology Learning*, 31(1), 128-146.

Shamsai A, Rahmani K, Peroti S, Rahemi L (2012). The effect of water-cement ratio in compressive and abrasion strength of the nano silica concretes. *World Applied Sciences Journal*, 17(4), 540-545.

Singh B, Ishwarya G, Gupta M, Bhattacharyya SK (2015). Geopolymer concrete: A review of some recent developments. *Construction and Building Materials*, 85, 78-90.

Sobhani J, Najimi M, Pourkhorshidi AR (2012). Effects of retempering methods on the compressive strength and water permeability of concrete. *Scientia Iranica*, 19(2), 211-217.

Zeyad AM, Almalki A (2020). Influence of mixing time and superplasticizer dosage on self-consolidating concrete properties. *Journal of Materials Research and Technology*, 9(3), 6101-6115.

Challenge Journal of CONCRETE RESEARCH LETTERS

Research Article

Influence of calcium leaching on high-volume fly ash roller compacted concrete

Worachai Ponloa [a,*], Suvimol Sujjavanich [b], Prasert Suwanvitaya [b]

[a] *Department of Civil Engineering, Bangkokthonburi University, 10710 Bangkok, Thailand*
[b] *Department of Civil Engineering, Kasetsart University, 10900 Bangkok, Thailand*

ABSTRACT

Calcium leaching is a chemical deterioration process that adversely affects the performance and service life of concrete structures exposed to water. This study aims to examine calcium leaching in high-volume fly ash roller-compacted concrete (HVFA–RCC) under varying permeation pressures and to clarify the influence of pressure-driven transport on calcium loss, microstructural degradation, porosity development, and compressive strength reduction. Concrete specimens prepared with a mix design representative of RCC dams were used in the experimental program, employing a high-volume fly ash mixture with a fly ash-to-cement ratio of 1.11 by weight. To accelerate calcium leaching, the specimens were subjected to permeation pressures of 4, 6, and 9 bar in an ammonium chloride (NH_4Cl) solution for 28 days. After the leaching procedure, the specimens were evaluated through compressive strength testing and microstructural characterization using X-ray diffraction (XRD), scanning electron microscopy (SEM), and energy-dispersive X-ray spectroscopy (EDS). The results indicate that calcium leaching tends to reduce compressive strength and is accompanied by progressive microstructural degradation, with the severity of deterioration increasing as permeation pressure increases. The incorporation of HVFA helps to reduce calcium loss and limits the associated degradation in both microstructure and mechanical performance. These findings suggest that pressure-driven transport contributes to the acceleration of calcium leaching in RCC, while the use of HVFA enhances resistance to leaching-induced damage, thereby supporting improved durability of RCC dams exposed to sustained hydraulic pressure through the mitigation of long-term degradation processes.

ARTICLE INFO

Article history:
Received – December 2, 2025
Revision requested – December 23, 2025
Revision received – February 7, 2026
Accepted – February 20, 2026

Keywords:
Calcium leaching
High-volume fly ash
Durability
Roller compacted concrete
Permeation pressure

Citation: Ponloa W, Sujjavanich S, Suwanvitaya P (2026). Influence of calcium leaching on high-volume fly ash roller compacted concrete. *Challenge Journal of Concrete Research Letters*, 17(2), 94–108.

1. Introduction

Calcium leaching is a chemical deterioration process that affects the durability and service life of concrete structures exposed to water. Hydraulic structures such as dams remain in long-term contact with water during service. This exposure promotes the dissolution of calcium-bearing hydration products from the cement matrix. The process modifies pore structure and gradually weakens the solid skeleton of concrete. As a result, permeability increases and mechanical properties tend to decrease over time, which raises concerns for the long-term performance of concrete dams (Carde and François 1997; Marchand et al. 2001).

Among cement hydration products, calcium hydroxide plays an important role in strength and durability. It exhibits higher solubility than other hydration phases and shows greater sensitivity to water exposure. Calcium leaching commonly initiates with portlandite dissolution and then progresses to gradual decalcification

* *Corresponding author*. E-mail address: worachai.p@ku.th (W. Ponloa)
ISSN: 2548-0928 / DOI: https://doi.org/10.20528/cjcrl.2026.02.002

of C–S–H. This chemical degradation increases porosity and enhances transport-related properties such as diffusivity and permeability. Previous studies reported that leaching-induced pore structure changes strongly influence calcium transport and damage evolution in cementitious materials (Choi and Yang 2013; Cheng et al. 2013; Zhang et al. 2020).

High-volume fly ash (HVFA) concrete has been widely applied in mass concrete and roller-compacted concrete (RCC) dams. Fly ash reduces portlandite content through pozzolanic reactions and contributes to pore structure refinement, a mechanism also observed in silica-fume-modified cementitious materials, where calcium hydroxide consumption and additional C–S–H formation produce a denser matrix and restrict the ingress of aggressive agents (Al-Safi et al. 2025). These effects may enhance resistance to calcium leaching and associated durability loss. Several studies observed that fly ash can slow calcium depletion and mitigate strength degradation under aggressive exposure conditions. However, the effectiveness of fly ash depends on mixture composition, environmental conditions, and binder chemistry, because its pozzolanic contribution may be limited when portlandite availability in the hydrated matrix is insufficient (Kadhim and Keskin 2024). At suitable replacement levels, fly ash can promote particle packing and additional C–S–H formation, whereas excessive substitution of mineral by-products may increase porosity and reduce mechanical and durability performance despite the beneficial filler and pozzolanic effects observed at suitable proportions (Rozière et al. 2009; Fanghui et al. 2014; Shi et al. 2019; Wang et al. 2021; Turan et al. 2025; Shaheen et al. 2025). Comparable improvements have been reported in concretes containing silica- and calcium-rich waste powders, where suitable replacement levels promoted additional C–S–H formation and reduced water penetration through pore refinement (Mahmud et al. 2025).

In actual RCC dams, water seepage develops under hydraulic pressure gradients along the dam height, while fluctuating reservoir and uplift pressures alter the internal stress and displacement states of gravity dams (Pandimani 2025). Seepage rate and flow velocity vary with elevation and internal pressure. Field observations indicated that calcium concentration in seepage water differs between locations within the dam body. These observations suggest that calcium leaching is not governed by diffusion alone. Pressure-driven percolation and advective transport contribute to leaching progression under in-service conditions (Inmala and Soralump 2010; Liu et al. 2022; Chen et al. 2023). Moreover, cracks exposed to reservoir water may facilitate seepage and create additional transport pathways, thereby increasing the potential for pressure-driven calcium leaching and associated durability degradation in RCC dams (Soysal 2025). This concern is further supported by numerical analyses showing that reservoir-induced hydrodynamic pressure can increase principal tensile stresses and seismic damage demand in RCC dams, thereby increasing the likelihood of crack formation under service-related loading combinations (Şermet et al. 2024).

Most previous studies on calcium leaching focused on diffusion-controlled or immersion-based exposure conditions. Limited attention has been given to calcium leaching under pressure-driven percolation, particularly in HVFA roller-compacted concrete. Although machine-learning models have been successfully used to estimate the compressive strength of cementitious materials from mixture proportions, such models do not directly characterize the residual strength loss caused by pressure-driven chemical degradation (Harirchian 2024). The influence of hydraulic pressure on the coupled evolution of transport behavior, chemical degradation, and mechanical performance remains insufficiently documented. This study examines calcium leaching in HVFA–RCC under different permeation pressures. The objective is to clarify how pressure-driven transport affects calcium loss, microstructural degradation, and strength reduction. The findings aim to provide mechanistic insight that is relevant to durability assessment of RCC dams under long-term service conditions.

2. Experimental Procedure

2.1. Materials

The study used materials similar to the RCC mix design of a large local RCC dam. The mixture compositions consisted of Type I Portland cement in accordance with ASTM C150-90, moderate local calcium fly ash derived from lignite, and fine and coarse basalt aggregates obtained from the nearby borrow pit of the studied RCC dam.

2.1.1. Chemical composition of materials

The chemical compositions of cement, fly ash, and basalt aggregates were determined using an X-ray fluorescence (XRF) spectrometer. The results are presented in Table 1.

Table 1. Chemical compositions of the materials.

Oxides	Composition, %									
	CaO	SiO_2	Al_2O_3	Fe_2O_3	K_2O	Na_2O	MgO	SO_3	NiO	Ignition
Cement	62.67	20.70	4.42	3.07	0.27	0.37	0.91	4.64	2.39	0.56
Fly ash	19.52	31.20	15.59	16.00	1.69	0.03	2.38	9.47	0.01	–
Basalt	6.44	51.28	15.37	9.26	1.63	6.99	2.35	–	–	–

2.1.2. Mix proportions

Three groups of specimens were prepared: paste, mortar, and concrete. Each group was divided into two subgroups: plain cement and cement partially replaced with fly ash at a cement-to-fly ash ratio of 0.9, corresponding to 90 kg/m^3 of cement and 100 kg/m^3 of fly ash. The specimen nomenclature was delineated below: plain cement paste (PC), cement–fly ash paste (PCF), plain cement mortar (MC), cement–fly ash mortar (MCF), plain cement concrete (RC), and fly ash–cement concrete (RCF). Three water-to-binder (w/b) ratios of 0.5, 0.6, and 0.8 were employed, as denoted by the numeral at the commencement of the specimen designation; for instance, 5RCF signifies a concrete mixture incorporating fly ash with a w/b ratio of 0.5. Crushed basalt served as the fine aggregate, exhibiting a fineness modulus (FM) of 3.19, whereas the coarse aggregates were categorized into three groups: G1, G2, and G3, with maximum sizes of 47.25 mm, 31.50 mm, and 16 mm, respectively. Table 2 shows the mix proportion compositions of each specimen type used in this study.

2.1.3. Specimen preparation

Concrete mixes with Vebe times of 75, 60, 55, 50, 45, and 40 seconds, in accordance with ASTM C1170/C1170M, corresponding to specimens 5RC, 5RCF, 6RC, 6RCF, 8RC, and 8RCF, respectively, were cast in cylindrical molds with dimensions of 15 × 30 cm. The specimens were demolded after 24 hours and cured in a water bath at 21 ± 1 °C for 90 days before being subjected to leaching. Cement paste and mortar specimens were cast in short cylindrical molds with dimensions of 15 × 6.40 cm using the same mix compositions as those for the concrete specimens, as shown in Fig. 1.

Table 2. Mix proportions of the specimens.

Specimen	Water/Binder	Cement (kg/m^3)	Fly ash (kg/m^3)	Crushed sand[1] (kg/m^3)	Coarse aggregate[2] (kg/m^3)		
					G1	G2	G3
5PC/5MC[1]/5RC[2]	0.50	190	–	673	568	355	497
6PC/6MC[1]/6RC[2]	0.60	190	–	673	568	355	497
8PC/8MC[1]/8RC[2]	0.80	190	–	673	568	355	497
5PCF/5MCF[1]/5RCF[2]	0.50	90	100	673	568	355	497
5PCF/5MCF[1]/5RCF[2]	0.60	90	100	673	568	355	497
5PCF/5MCF[1]/5RCF[2]	0.80	90	100	673	568	355	497

Note: [1]mortar, [2]concrete

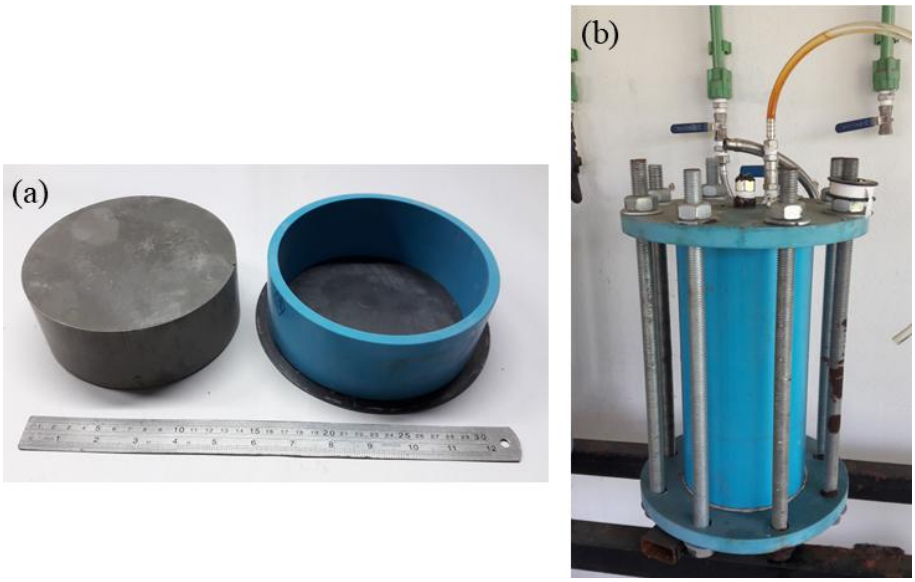

Fig. 1. The shape and size of test specimens: (a) Paste and mortar; (b) RCC.

2.2. Test methods

2.2.1. Accelerated calcium leaching

A 6 M ammonium chloride (NH_4Cl) solution, corresponding to a concentration of 480 g/L, was used to accelerate calcium leaching in this study (Hu et al., 2012). The chemical reactions between ammonium chloride and calcium hydroxide (portlandite, $Ca(OH)_2$) are described in Eqs. (1) and (2).

$$Ca(OH)_2 + 2NH_4Cl \rightarrow CaCl_2 + 2NH_3 + 2H_2O \quad (1)$$

$$CaOSiOH_2O + 2NH_4Cl \rightarrow CaCl_2 + 2NH_3 + SiO_2\,(gel) + H_2O \quad (2)$$

The calcium leaching rate was indirectly assessed by monitoring the pH value of the leaching solution. A decrease in pH reflects the progressive dissolution of calcium-bearing hydration products, particularly calcium hydroxide (CH), which is the most soluble phase during the early stage of leaching. As Ca^{2+} ions are released into the solution, the buffering capacity of the cement matrix is reduced, leading to a measurable decrease in pH. This approach has been widely adopted as an indirect indicator of calcium leaching development in accelerated leaching studies using ammonium chloride solutions (Hu et al. 2012).

2.2.2. Leaching process

A modified percolation leaching apparatus was used to simulate saturated Darcian flow, representing conditions in an RCC dam (Ekström 2003). The specimens were assumed to be isotropic and homogeneous, with randomly distributed pore structures. The test system consisted of a water tank, a high-pressure water pump equipped with a pressure regulator, a piping system, and leaching test cells. Water pressure was applied at 4, 6, and 9 bars to simulate hydraulic heads corresponding to heights of 40, 60, and 90 m, respectively. The leaching tests were conducted for a duration of 28 days. Fig. 2 illustrates the equipment arrangement and leaching setup. Three specimens were tested for each mixture and exposure condition, and the reported values represent average results.

After completion of the leaching procedure, paste and mortar specimens were mechanically cored to obtain cylindrical samples with a diameter of 32 mm and a height of 64 mm for compressive strength testing. Additional sections of each specimen were sectioned into blocks measuring 5 × 5 × 0.5 cm for pore volume determination and microstructural characterization.

Fig. 2. Experimental setup and representative specimens after calcium leaching: (a) Test cell; (b) Percolation apparatus; (c) Leaching process; (d) RCC specimen; (e) Mortar specimen; (f) Sliced paste samples.

2.2.3. Porosity

Three types of specimens—paste, mortar, and concrete—were used for porosity investigation. The pore volume test was conducted in accordance with ASTM C642. After leaching, paste and mortar specimens were cut into pieces measuring 5 × 5 × 0.5 cm. Concrete specimens were cut into disks with a diameter of 150 mm and a thickness of 60 mm for porosity testing.

2.2.4. Microstructure analysis

Microstructural analysis was conducted before and after leaching using scanning electron microscopy (SEM) coupled with energy-dispersive X-ray spectroscopy (EDS). Mineralogical changes induced by leaching were analyzed using X-ray diffraction (XRD). The XRD analysis focused on phase evolution after leaching.

2.2.5. Compressive strength testing

Compressive strength testing was conducted in accordance with ASTM C39 on two types of specimens. The first type consisted of small cylindrical specimens of paste and mortar, with a diameter of 32 mm and a height of 64 mm. The second type consisted of standard concrete specimens, with a diameter of 150 mm and a height of 300 mm.

3. Results and Discussion

Three specimen types—paste, mortar, and concrete—were subjected to leaching for 28 days under applied pressures of 4, 6, and 9 bars. The results are presented below.

3.1. Leaching chemical test

Fig. 3 presents the permeability results of paste and mortar specimens under leaching pressures of 4, 6, and 9 bars. In this study, permeability was used as an indirect indicator of calcium leaching development. Specimens with a water-to-binder ratio (w/b) of 0.8 exhibited the highest permeability for both paste and mortar at all pressure levels. Plain cement paste showed higher permeability than fly ash–cement paste. Plain cement mortar also exhibited higher permeability than fly ash–cement mortar.

At a leaching pressure of 9 bars, permeability reached the highest level. The permeability values at 4 and 6 bars were comparable. Specimens with a w/b ratio of 0.6 showed the lowest permeability at all pressure levels. Mortar specimens exhibited lower permeability than paste specimens, particularly under a leaching pressure of 9 bars. This result indicates a more resistant pore structure in mortar mixtures.

The incorporation of fly ash reduced permeability at all pressure levels. The reduction was more evident at higher water-to-binder ratios and under high pressure. This reduction is attributed to pore-filling effects and pozzolanic reactions. These mechanisms produced a denser cement matrix and improved the interfacial transition zone (ITZ).

The permeability trends are consistent with the porosity results and microstructural observations presented in subsequent sections. This consistency supports the indirect assessment of calcium leaching severity.

The permeability results of concrete specimens under leaching pressures of 6 and 9 bars are shown in Fig. 4. For both fly ash–cement and plain cement concrete, permeability followed a descending order of water-to-binder ratios of 0.8, 0.5, and 0.6.

At a leaching pressure of 9 bars, concrete specimens with w/b ratios of 0.5 and 0.6 exhibited similar permeability values, ranging from approximately 5.2×10^{-9} to 5.6×10^{-9} m/s. These values were lower than those measured for specimens with a higher w/b ratio of 0.8.

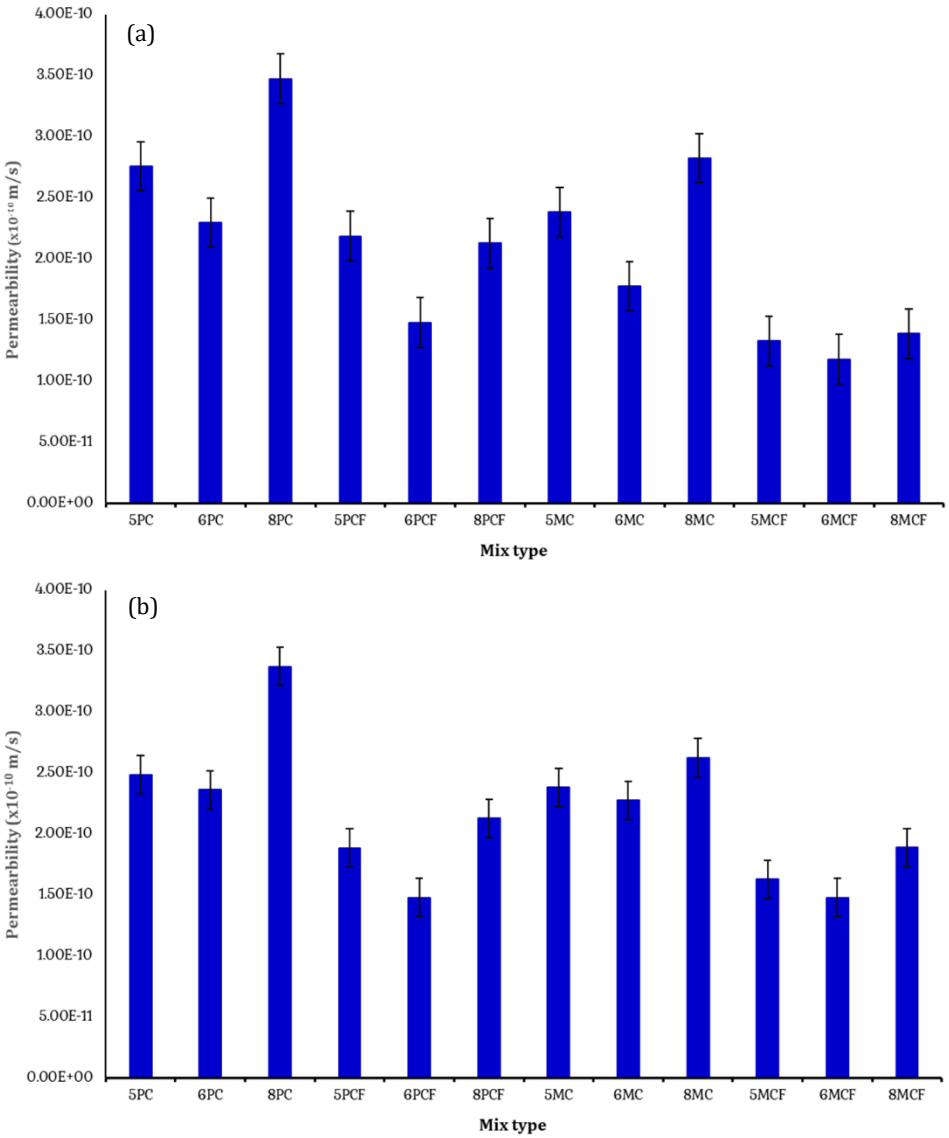

Fig. 3. (continued)

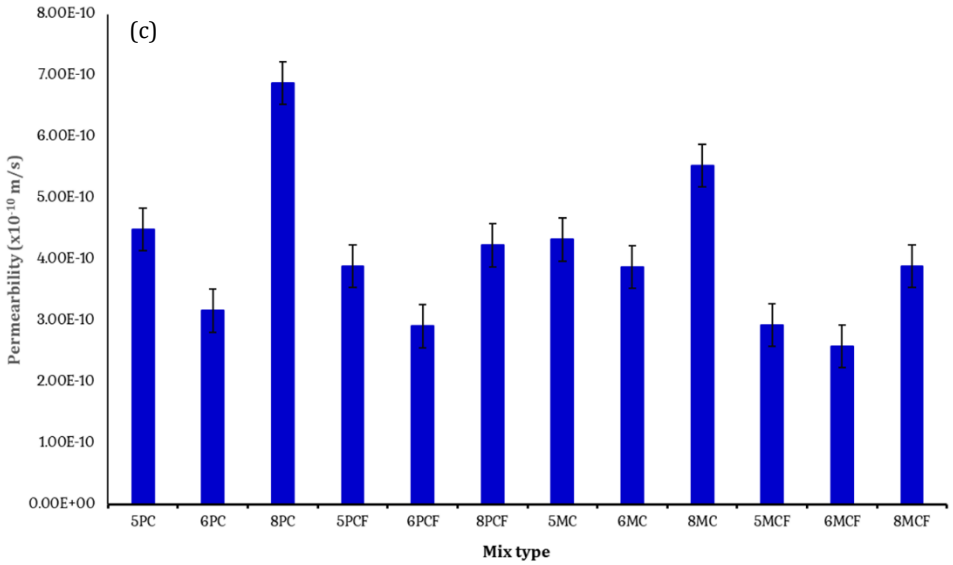

Fig. 3. Average permeability of paste and mortar under different pressure: (a) 4 bars; (b) 6 bars; (c) 9 bars.

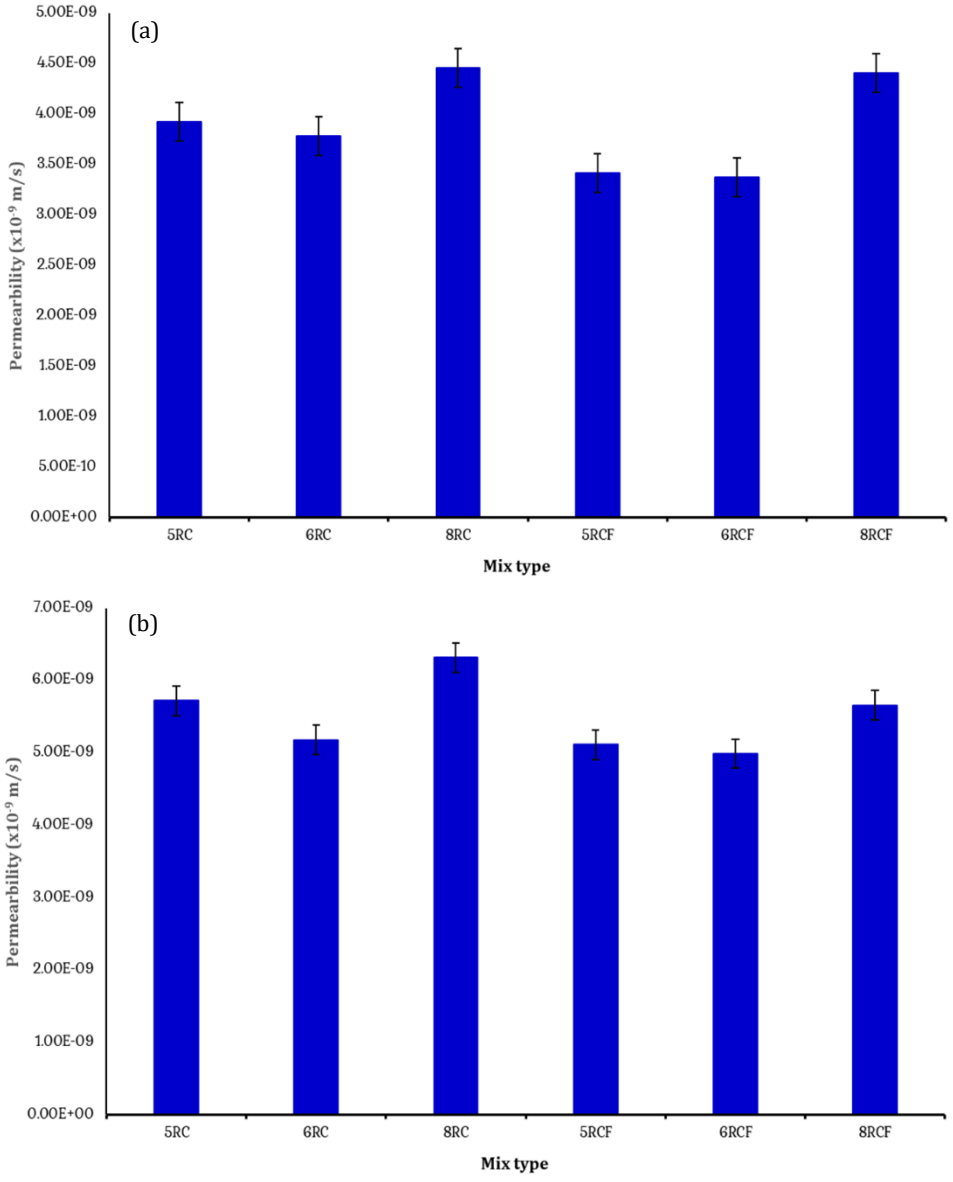

Fig. 4. Permeability of concrete specimens under high pressure: (a) 6 bars; (b) 9 bars.

3.2. Porosity

The porosity characteristics of paste specimens after calcium leaching are shown in Fig. 5. Calcium leaching increased the volume of voids (%) in all specimens. The extent of the increase depended on leaching pressure and water-to-binder ratio.

At a leaching pressure of 4 bars, the volume of voids (%) increased slightly. Specimens with low water-to-binder ratios (w/b = 0.5 and 0.6) showed an increase in void volume of approximately 14–16%. Specimens with a higher water-to-binder ratio (w/b = 0.8) showed a larger increase in void volume.

At a leaching pressure of 6 bars, the volume of voids (%) increased further in all mixtures. The increase ranged from 14–18% for specimens with lower w/b ratios. Specimens with a w/b ratio of 0.8 showed an increase in void volume of up to approximately 20%.

At a leaching pressure of 9 bars, the void volume (%) reached the highest level. All specimens showed a substantial increase in void volume. The increase was more pronounced in specimens with higher water-to-binder ratios. This reflects severe degradation of the cement matrix under high permeation pressure.

The porosity results confirm that both leaching pressure and water-to-binder ratio govern pore structure development. Higher leaching pressure increased calcium dissolution. A higher w/b ratio increased void volume and pore connectivity.

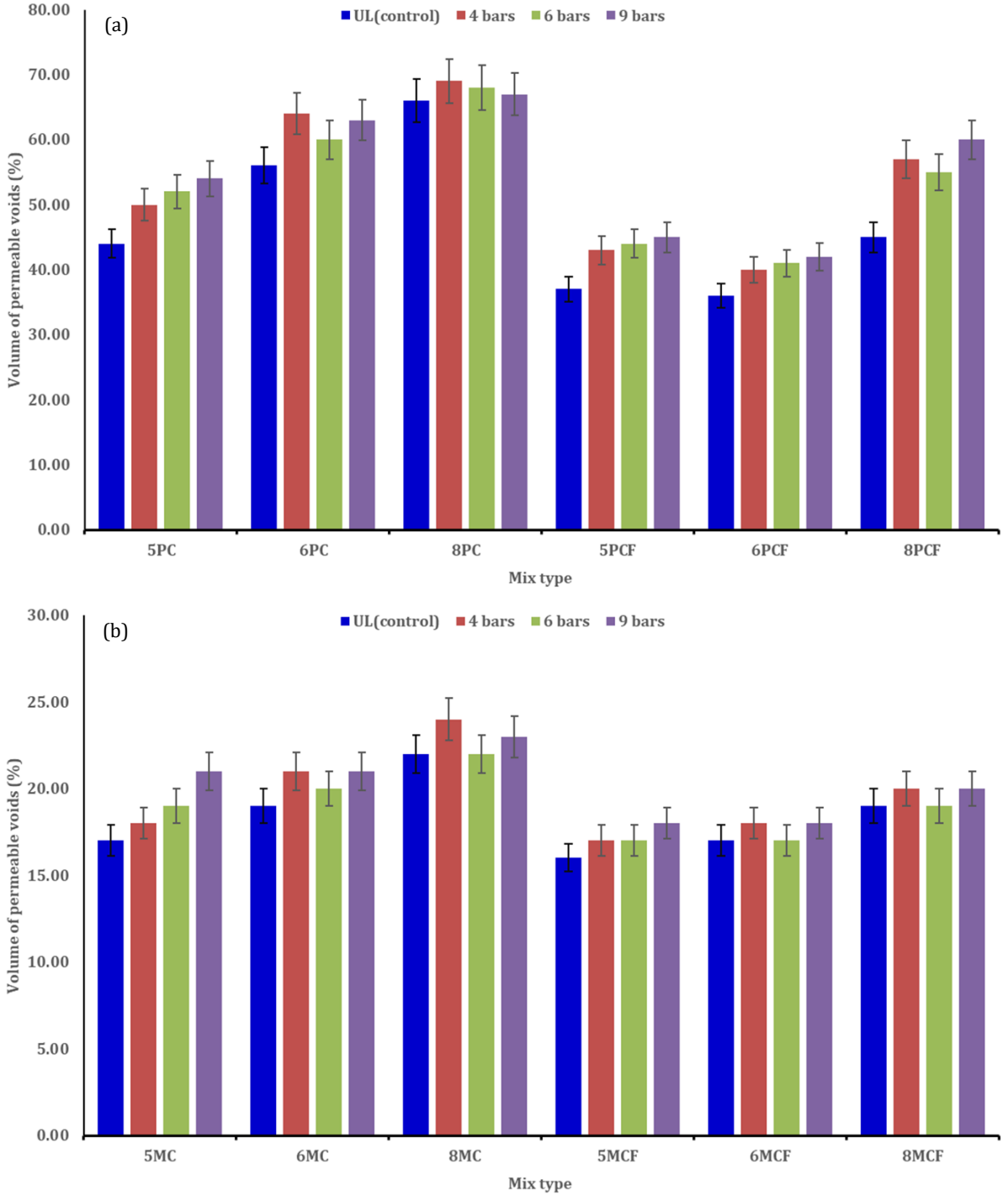

Fig. 5. (continued)

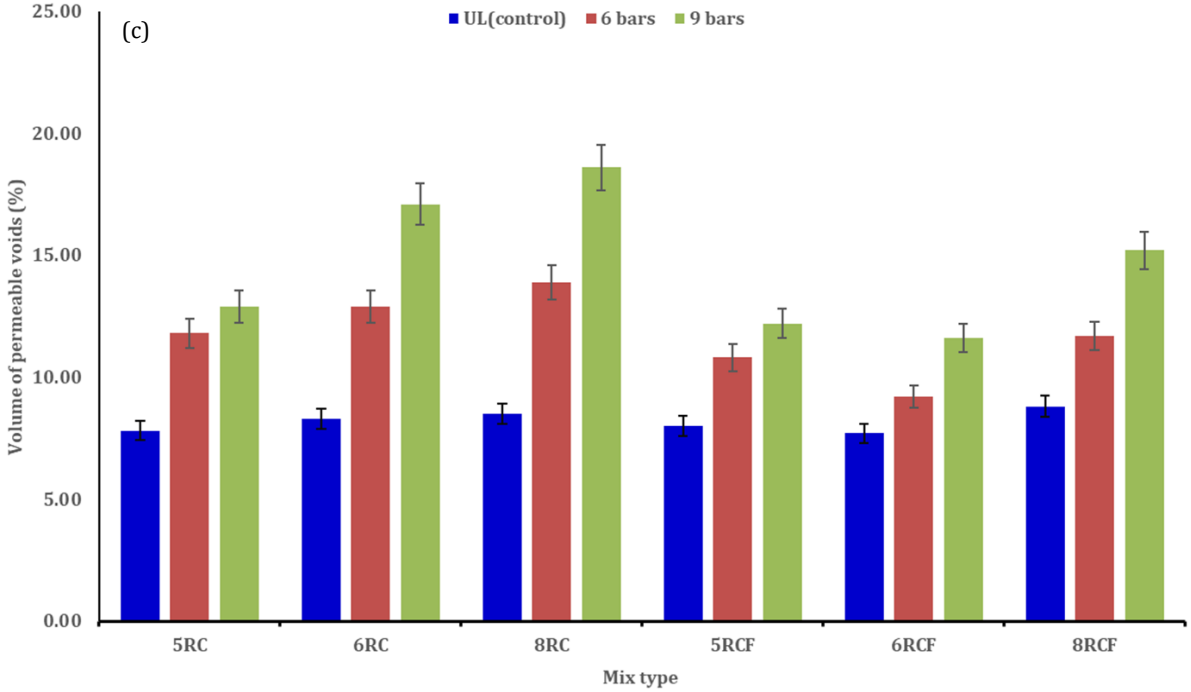

Fig. 5. The relationship of pore volume and applied leaching pressure: (a) Paste; (b) Mortar; (c) RCC.

3.3. Microstructural analysis

The microstructural characteristics of the paste specimens after calcium leaching were examined using SEM, as shown in Fig. 6. The SEM images illustrate comparative microstructural trends caused by calcium leaching. They are not intended to provide quantitative measurements of pore structure. The unleached specimens show a dense and continuous hydration matrix. Abundant C–S–H gel and well-distributed crystalline phases occupy the binder. In contrast, the leached specimens show clear degradation. Porosity increases, and microcracks become visible.

At a leaching pressure of 4 bars, the microstructure remains relatively compact. Specimens with low water-to-binder ratios (w/b = 0.5 and 0.6) show limited dissolution of calcium hydroxide. The C–S–H framework remains largely preserved, and microcracks are rare. Specimens with a higher w/b ratio (w/b = 0.8) contain small voids, but the matrix still maintains overall continuity. At a leaching pressure of 6 bars, microstructural damage becomes more evident. Voids and microcracks increase in all mixtures. Specimens with lower w/b ratios retain a partially connected C–S–H structure. Specimens with a higher w/b ratio exhibit a less dense and more fragmented matrix. Enlarged pores and localized cracking become more pronounced as w/b increases. At a leaching pressure of 9 bars, severe degradation occurs. Extensive voids and connected crack networks appear in all specimens. Damage remains limited in mixtures with low w/b ratios, but it becomes severe in the specimen with w/b = 0.8. In this case, the cement matrix appears highly porous and discontinuous.

Microstructural deterioration increases with both leaching pressure and water-to-binder ratio. At lower pressure, dissolution mainly affects localized regions of the matrix. At higher pressure and higher w/b ratios, calcium dissolution becomes widespread. This process accelerates pore connectivity and leads to a significant loss of structural integrity. These observations link directly to changes in the Ca/Si ratio of the C–S–H gel. In the unleached state, portlandite acts as a calcium reservoir and stabilizes the hydration system. Calcium leaching first dissolves portlandite, and this reduces calcium concentration in the pore solution. The equilibrium then shifts, and calcium begins to extract from the C–S–H gel. The Ca/Si ratio decreases, and the gel undergoes decalcification. The gel contracts, loses cohesion, and becomes more porous. This chemical transformation appears in the SEM images as gel fragmentation and pore opening.

The rate of Ca/Si reduction depends strongly on the initial pore structure. Low w/b mixtures restrict calcium transport and slow the decalcification process. High w/b mixtures contain interconnected pore networks that accelerate ion migration. As a result, the Ca/Si ratio drops throughout the matrix, and structural breakdown spreads rapidly. The SEM damage patterns therefore represent a direct microstructural expression of Ca/Si evolution in the binder phase. As the Ca/Si ratio decreases, the load-bearing capacity of the C–S–H gel declines, and the matrix transitions from a cohesive framework to a porous skeletal structure.

The calcium ion analysis obtained from EDS is shown in Fig. 7 At a low applied pressure of 4 bars, the percentage decrease of Ca^{2+} relative to the unleached specimens was 8%, 4%, and 8% for 5PCF, 6PCF, and 8PCF, respectively. At a moderate applied pressure of 6 bars, the Ca^{2+} reduction increased to 27%, 10%, and 45%. At a high applied pressure of 9 bars, the corresponding reductions further increased to 42%, 29%, and 50%.

The results indicate that Ca^{2+} leaching increased with applied pressure. The effect was more pronounced in specimens with higher water-to-binder ratios. This behavior suggests that pressure-induced microstructural changes enhanced calcium leaching in high w/b specimens compared with those with lower w/b ratios.

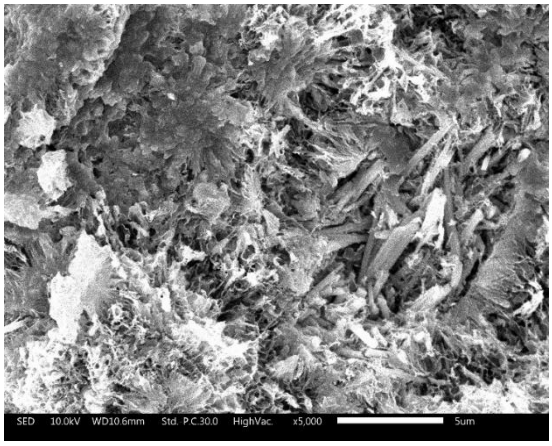

5 bar PCF-UL

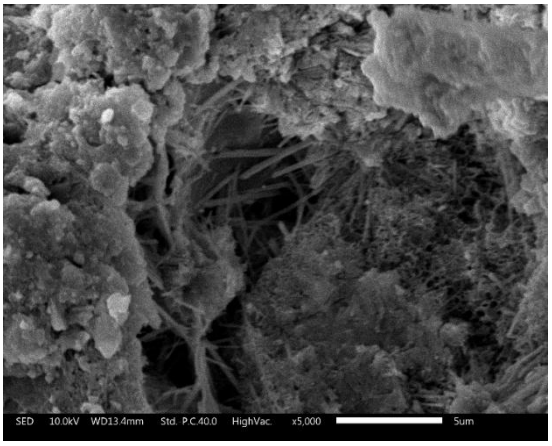

4 bar 5PCF

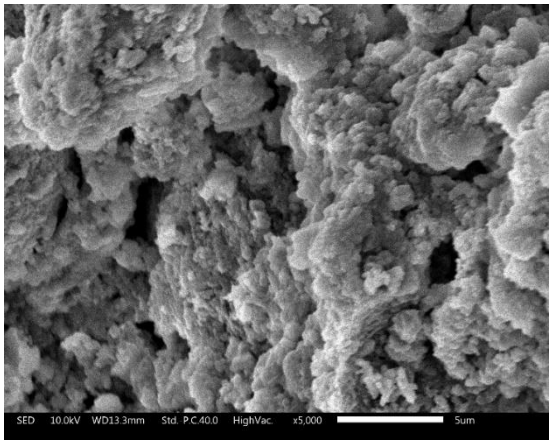

6 bar 5PCF

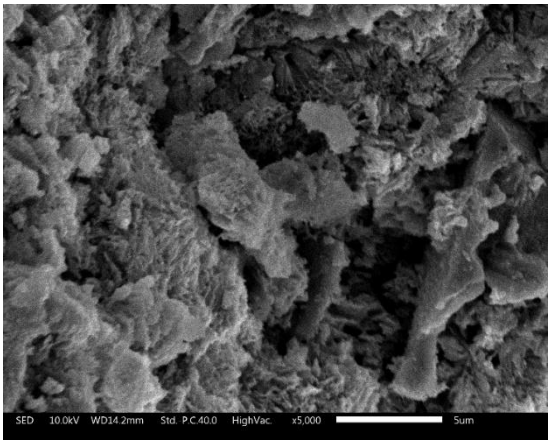

9 bar 5PCF

(a) w/b = 0.5

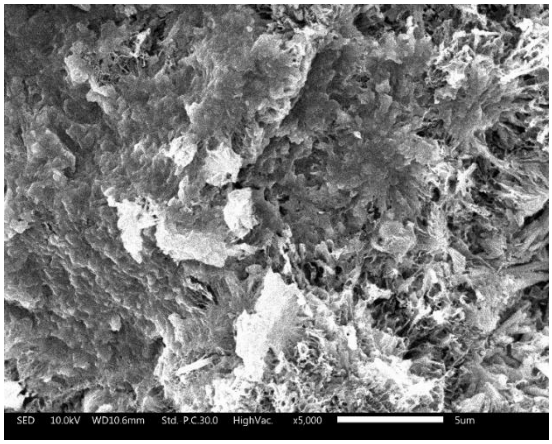

6 bar PCF-UL

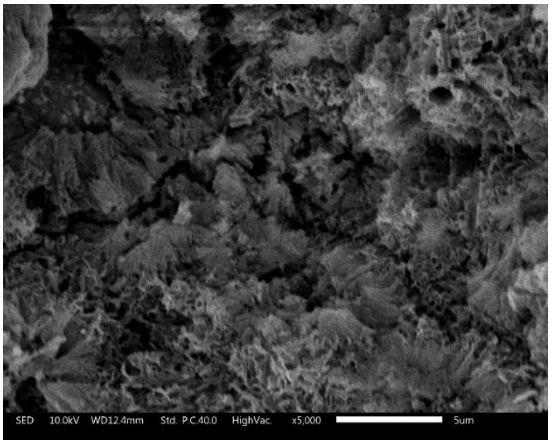

4 bar 6PCF

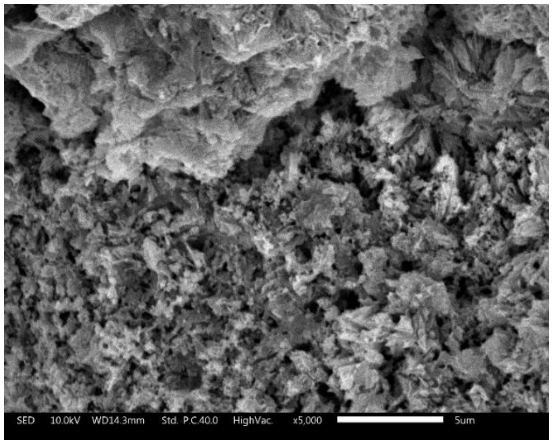

6 bar 6PCF

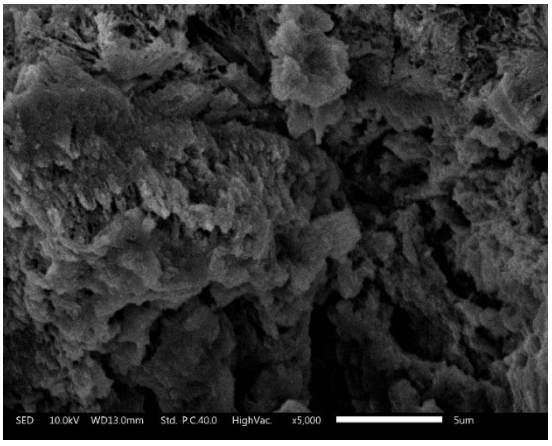

9 bar 6PCF

(b) w/b = 0.6

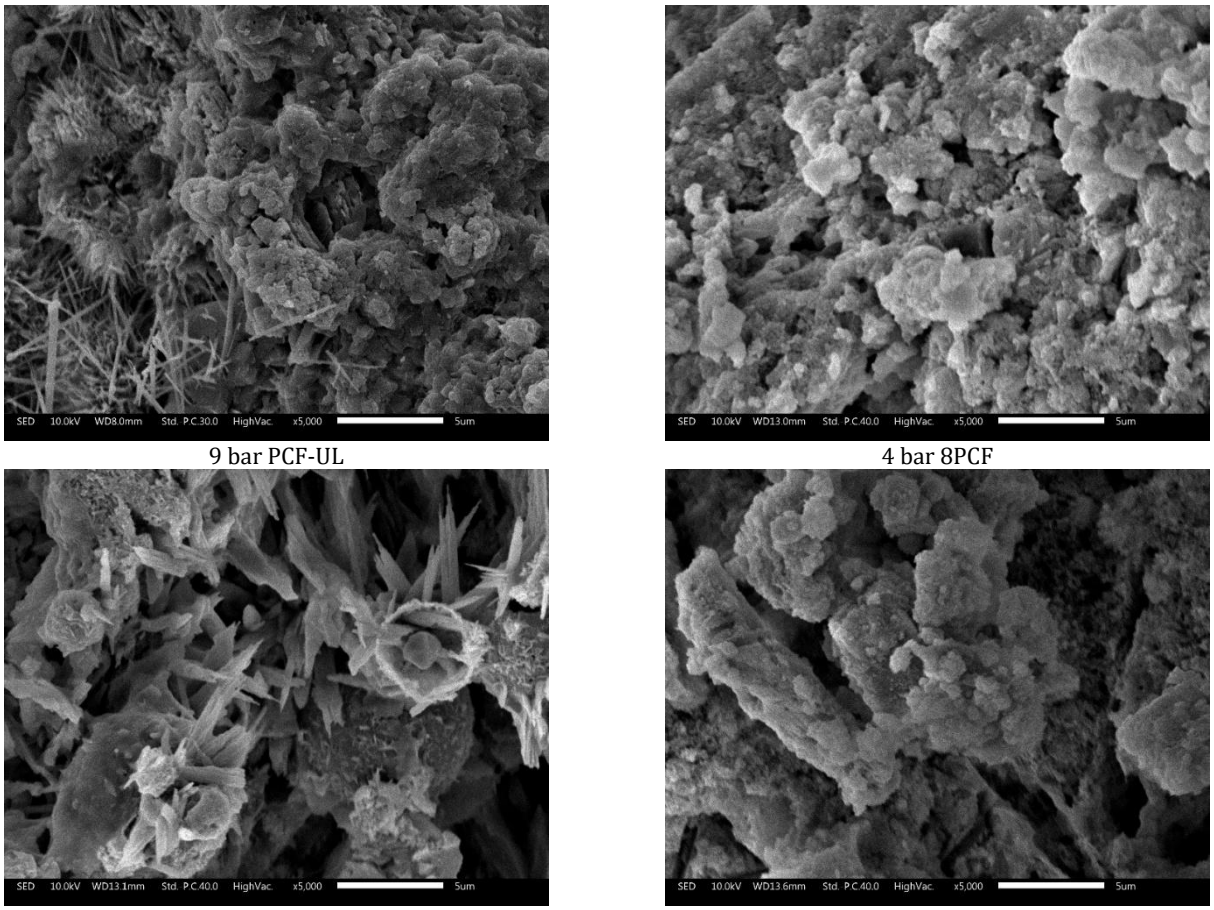

(c) w/b = 0.8

Fig. 6. The microstructure of the paste (w/b = 0.5, 0.6, and 0.8) under pressure of 4, 6, and 9 bars.

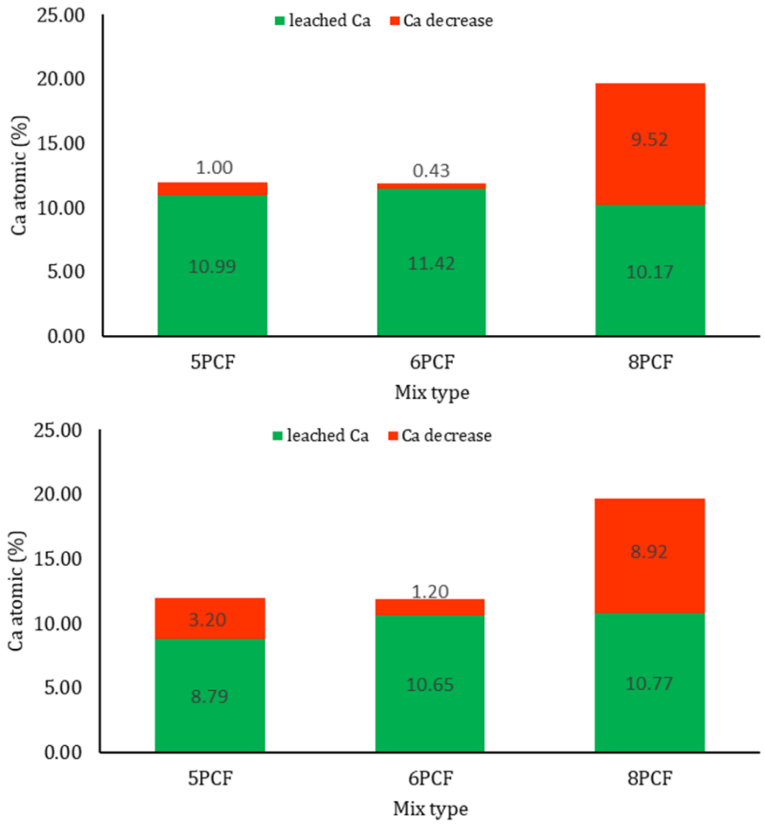

Fig. 7. (continued)

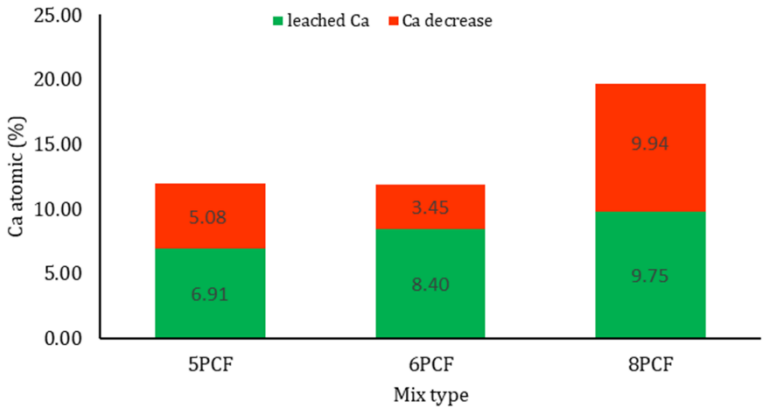

Fig. 7. The results of SEM/EDS of calcium leaching from pastes under pressure: (a) 4 bars; (b) 6 bars; (c) 9 bars.

The leaching results obtained from XRD analysis are presented in Fig. 8. The figure shows differences in calcium-bearing phases of fly ash–cement paste between unleached and leached specimens under different pressures. A significant reduction in the intensity of the portlandite (CH) peak was observed in the leached specimens. A slight reduction in the C–S–H-related peak was also detected.

The reduction in CH peak intensity increased with applied pressure. Specimens with a water-to-binder ratio of 0.8 exhibited the largest decrease in CH intensity. This result indicates that high w/b specimens were more strongly affected by the leaching process. This microstructural deterioration corresponds well with the observed increase in porosity and pore connectivity under pressure-driven leaching conditions. These changes directly explain the reduction in compressive strength reported in the subsequent section.

In this study, transport behavior was not measured directly using permeability or diffusion coefficients. Instead, it was inferred from permeability trends, porosity evolution, and microstructural features such as pore connectivity and cracking. These indicators collectively reflect changes in transport pathways governing pressure-driven calcium leaching.

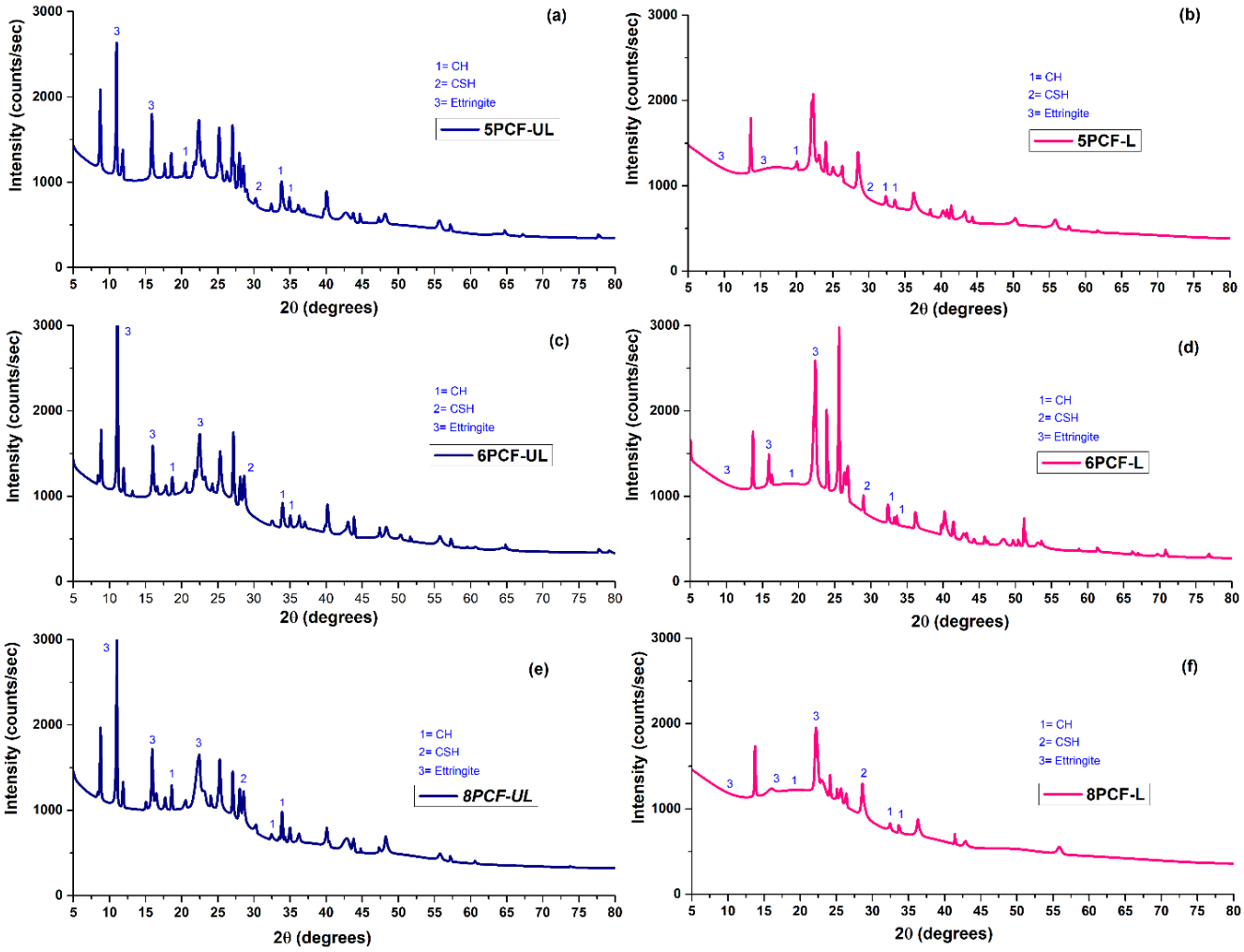

Fig. 8. The results of XRD fly ash cement pastes, unleached condition, and leached condition under pressure of 6 bars.

3.4. Compressive strength

The observed strength degradation can therefore be interpreted as a direct consequence of calcium leaching–induced microstructural weakening, including pore coarsening and degradation of the ITZ. The compressive strengths of leached paste specimens are presented in Fig. 9. For water-to-binder (w/b) ratios of 0.5 and 0.6, the plain cement paste exhibited higher compressive strength than the corresponding fly ash–cement paste, whereas a slight increase in compressive strength was observed for both paste types at a w/b ratio of 0.8. Leaching under pressures of 4, 6, and 9 bars reduced the compressive strength of plain cement paste by approximately 28–31%, 37–74%, and 49–79%, respectively. For fly ash–cement paste specimens, the corresponding strength reductions were about 43–60%, 49–62%, and 47–61% relative to the unleached specimens. Although higher leaching pressure resulted in greater compressive strength loss, with the reduction being more pronounced at 9 bars than at 6 bars, the effect at 4 bars was comparatively limited.

The dissolution of calcium-bearing hydration products occurs during the leaching process. This process weakens the cement matrix and leads to a decrease in compressive strength. A smaller strength reduction was observed at lower pressure, while higher pressure resulted in more pronounced strength loss. The more pronounced strength loss at higher pressures indicates increased leaching intensity. Under certain conditions, plain cement paste exhibited slightly higher compressive strength than fly ash–cement paste. This behavior can be attributed to the higher initial calcium hydroxide content available before leaching.

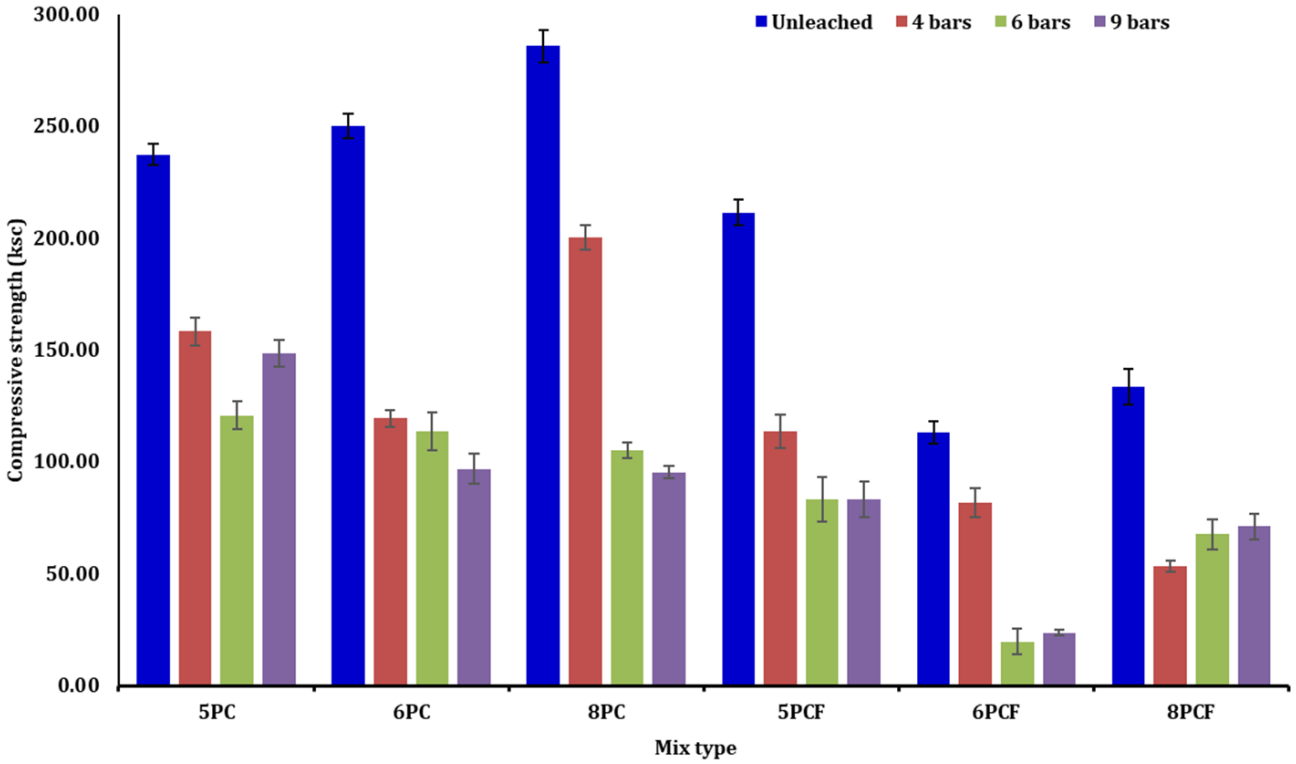

Fig. 9. Compressive strength and leaching pressure relationship of pastes.

For mortar specimens, the effects of calcium leaching on compressive strength are shown in Fig. 10. Under leaching pressures of 4, 6, and 9 bars, the compressive strength of plain cement mortar decreased by approximately 5–12%, 10–13%, and 24–43%, respectively. For fly ash–cement mortar, the corresponding reductions were about 4–16%, 7–22%, and 14–28%. Overall, greater leaching pressure resulted in larger compressive strength loss.

Higher leaching pressure caused greater compressive strength loss in the mortar specimens. At low pressure, leaching mainly occurred through percolation. Diffusion effects became more evident as pressure increased (Torrenti et al. 2008). The influence of fly ash under the same pressure level depended on the water-to-binder ratio. Strength reductions of approximately 2–29% were observed at w/b ratios of 0.5 and 0.6. Mortars with higher w/b ratios showed lower compressive strength. This behavior was related to changes in the fine aggregate-to-binder ratio and increased porosity. The pozzolanic reaction refined the pore structure. However, leaching-induced damage in the interfacial transition zone (ITZ) led to additional strength loss (Galle et al. 2008).

The compressive strength results of the concrete specimens are shown in Fig. 11. Calcium leaching reduced the compressive strength of concrete, and the strength loss increased with permeation pressure. Fly ash–cement concrete showed relatively small strength reductions of about 5–15% and 5–19% under leaching pressures of 6 and 9 bars, respectively, compared to the unleached specimens. At a high water-to-binder ratio (w/b=0.8), the compressive strength dropped to about 133 kg/cm^2. This corresponds to a strength reduction of approximately 37–54%.

Calcium leaching reduced the compressive strength of concrete under permeation pressure. This strength loss was associated with damage to the concrete microstructure. Fly ash–cement concrete showed a smaller strength reduction than plain cement concrete. At high water-to-binder ratios, increased porosity made the concrete more vulnerable to leaching. This led to severe strength loss. The use of fly ash reduced calcium hydroxide content and refined the pore structure through pozzolanic reactions. As a result, HVFA-RCC exhibited better resistance to calcium leaching when an appropriate binder composition and w/b ratio were used.

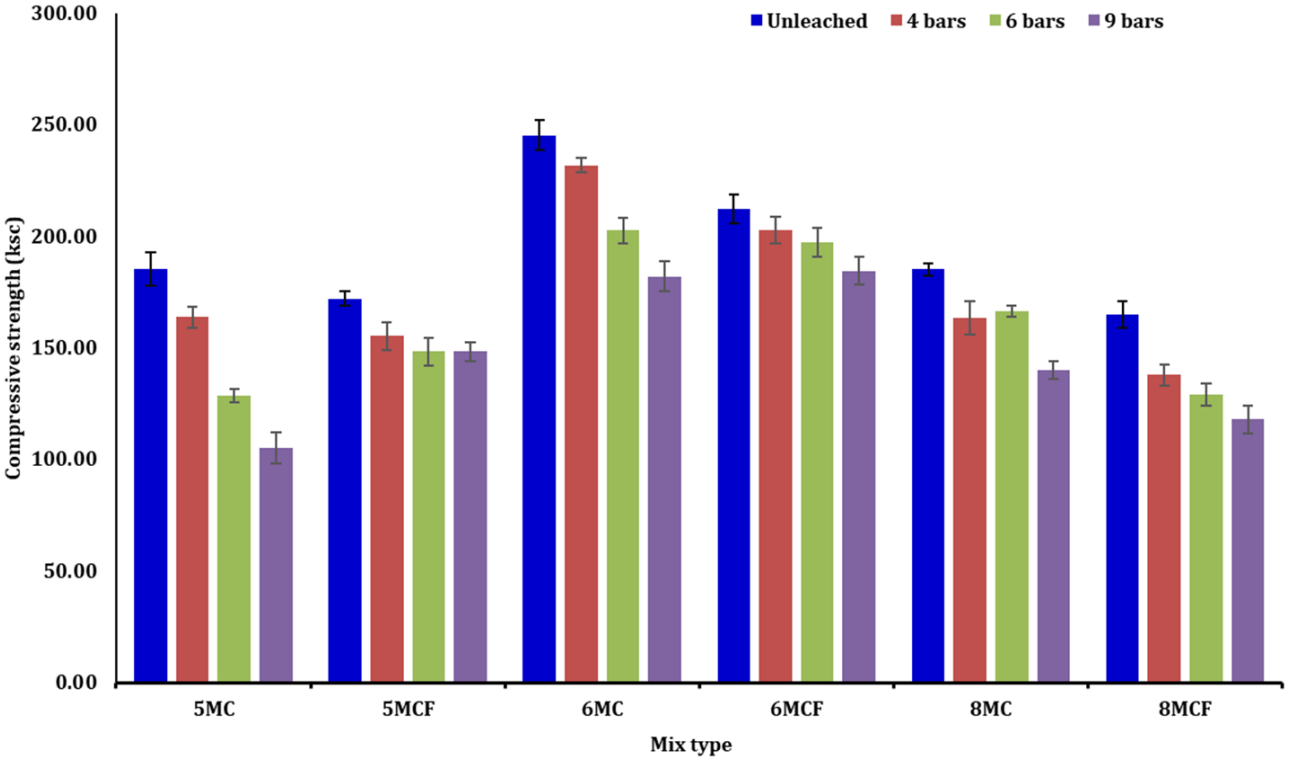

Fig. 10. Compressive strength and leaching pressure relationship of mortars.

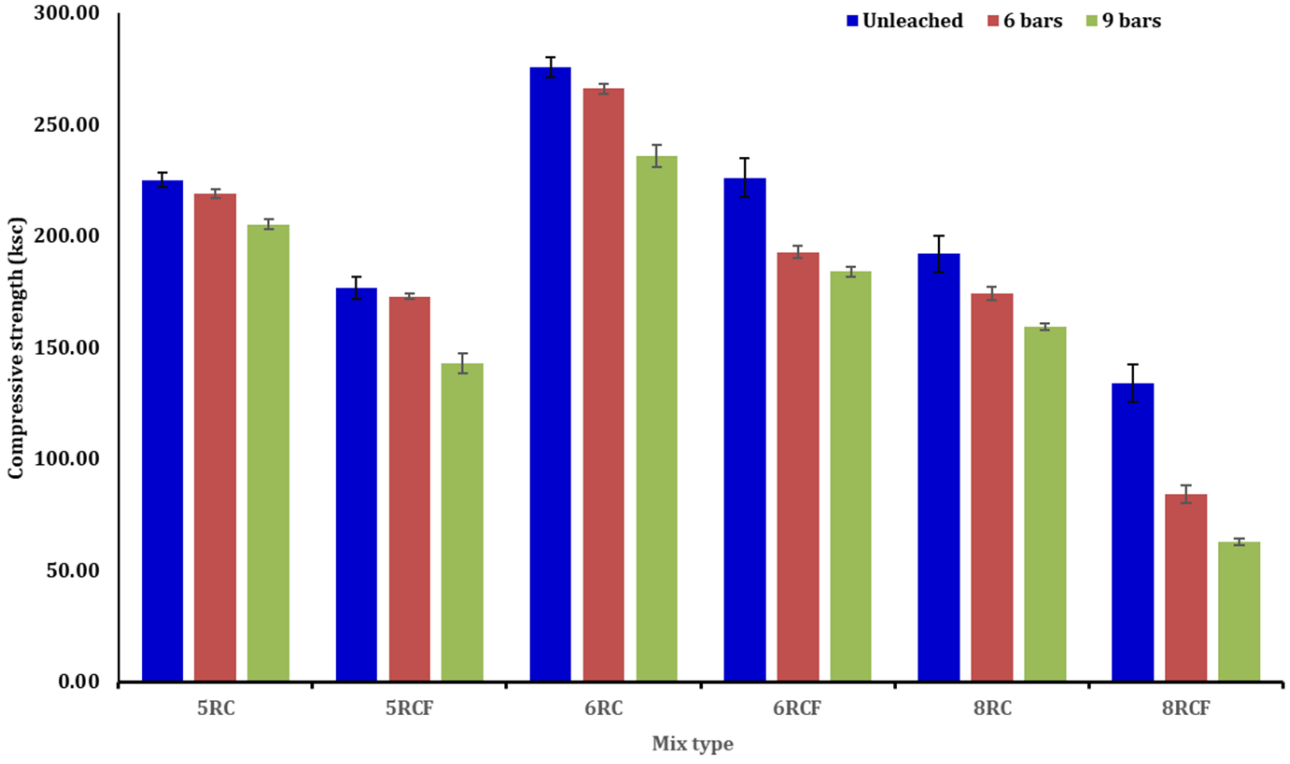

Fig. 11. Compressive strength and leaching pressure relationship of RCC.

4. Conclusions

This study presents a mechanistic evaluation of calcium leaching in high-volume fly ash roller-compacted concrete (HVFA-RCC) under pressure-driven permeation, with direct relevance to hydraulic structures such as RCC dams. The results show that calcium leaching in HVFA-RCC is controlled by the combined effects of chemical degradation and transport processes. This coupled behavior differs from diffusion-dominated or immersion-based leaching mechanisms commonly reported in previous studies. Pressure-driven permeation introduces an additional transport component. This component alters the progression of calcium loss. As a result, the governing leaching mechanisms are fundamentally different.

From a chemical perspective, HVFA-RCC contains a lower initial amount of portlandite and undergoes continued pozzolanic consumption of calcium hydroxide. These processes modify the chemistry of C–S–H toward lower Ca/Si ratios and improved phase stability. Calcium depletion from the cement matrix occurs at a slower rate. Microstructural degradation is less severe than in plain cement systems. Accordingly, HVFA-RCC shows smaller increases in porosity. These effects are directly associated with fly ash. Fly ash reduces portlandite availability, refines pore structure, and stabilizes the C–S–H phase under leaching conditions. Compressive strength loss is also reduced under identical permeation conditions.

From a transport standpoint, permeation pressure plays a key role in accelerating calcium leaching. Higher pressure enhances advective transport through connected pore networks. Calcium removal increases due to pressure-driven flow in addition to diffusion. Chemical decalcification intensifies as a result. Microstructural damage becomes more pronounced. This effect is especially evident in mixtures with higher water-to-binder ratios, where pore connectivity is greater. Mechanical degradation consistently follows both chemical decalcification and pressure-controlled transport intensity.

In RCC dams, continuous seepage and hydraulic pressure gradients develop along the dam height. Regions exposed to higher pressures are, therefore, more vulnerable to accelerated calcium leaching. Durability loss becomes more pronounced under these conditions. The incorporation of high-volume fly ash reduces the sensitivity of RCC to pressure-induced leaching. This behavior provides a durability advantage over plain cement systems.

Several limitations should be acknowledged. The accelerated NH_4Cl leaching method was employed to shorten the experimental duration and to promote controlled decalcification. However, this approach does not reproduce the chemical composition or timescale of natural seepage conditions, and the findings should therefore be interpreted in a mechanistic and comparative context. It differs from natural seepage water in RCC dams. Direct measurements of calcium flux were not conducted. The results should therefore be interpreted as a comparative and mechanistic assessment. Direct prediction of field leaching rates is not intended. Future studies should include direct calcium measurements and long-term exposure conditions. These efforts will further refine service-life evaluations of HVFA-RCC dams.

Acknowledgements
None declared.

Funding
The authors received no financial support for the research, authorship, and/or publication of this manuscript.

Conflict of Interest
The authors declare no potential conflicts of interest with respect to the research, authorship, and/or publication of this manuscript.

Data Availability
The datasets generated and/or analyzed during the current study are not publicly available but are available from the corresponding author upon reasonable request.

AI Assistance
No AI-based tools were used in the preparation of this manuscript.

Author Contributions
All authors made substantial contributions to the conception and design of the study, acquisition of data, analysis and interpretation of data; drafted or critically revised the manuscript for important intellectual content; and approved the final version to be published.

REFERENCES

Al-Safi S, Altharehi A, Alameri IA, Al-Jolahy A (2025). The mechanical properties of cement mortar reinforced with silica fume subjected to sulfate and chloride environment. *Challenge Journal of Structural Mechanics*, 11(1), 55-69.

ASTM C39 (2004). Standard test method for compressive strength of cylindrical concrete specimens. ASTM International, West Conshohocken, PA, USA.

ASTM C136 (2005). Standard test method for sieve analysis of fine and coarse aggregates. ASTM International, West Conshohocken, PA, USA.

ASTM C150 (1990). Standard specification for Portland cement. ASTM International, West Conshohocken, PA, USA.

ASTM C470 (2000). Standard specification for molds for forming concrete test cylinders vertically. ASTM International, West Conshohocken, PA, USA.

ASTM C642 (1997). Standard test method for density, absorption, and voids in hardened concrete. ASTM International, West Conshohocken, PA, USA.

ASTM C1170 (1998). Standard test methods for determining consistency and density of roller compacted concrete using a vibrating table. ASTM International, West Conshohocken, PA, USA.

Bache HH, Idorn GM, Nepper-Christensen P, Nielsen J (1966). Morphology of calcium hydroxide in cement paste. *Proceedings of the Symposium on Structure of Portland Cement Paste and Concrete*, Washington, D.C., USA, 154-174.

Carde C, François R (1997). Effect of the leaching of calcium hydroxide from cement paste on mechanical and physical properties. *Cement and Concrete Research*, 27(4), 539-550.

Chaisiwamongcol N (2008). Behaviors of Khun Dan Prakarnchon Dam During Construction and Initial Impounding. *M.Sc. thesis*, Kasetsart University, Bangkok, Thailand. (in Thai)

Chen X, Zhou M, Liu J, Wang Y (2023). Coupled transport-chemical degradation of cement-based materials under pressure-driven flow. *Cement and Concrete Composites*, 137, 104889.

Cheng A, Chao SJ, Lin WT (2013). Effects of leaching behavior of calcium ions on compression and durability of cement-based materials with mineral admixtures. *Materials*, 6(5), 1851-1872.

Choi YS, Yang EI (2013). Effect of calcium leaching on the pore structure, strength, and chloride penetration resistance in concrete specimens. *Nuclear Engineering and Design*, 259, 126-136.

Ekström T (2003). The Leaching Process and Its Effects. *Ph.D. thesis*, Lund University, Lund, Sweden.

Fanghui H, Rengguang L, Peiyu Y (2014). Effect of freshwater leaching on the microstructure of hardened composite binder pastes. *Construction and Building Materials*, 68, 630-636.

Galle C, Peycelon H, Le Bescop P (2008). Effect of accelerated chemical degradation on water permeability. *Cement and Concrete Research*, 38(4), 455-469.

Harirchian E (2024). Predicting compressive strength of AAC blocks through machine learning advancements. *Challenge Journal of Concrete Research Letters*, 15(2), 56-68.

Hu Y, Jiang L, Zhang Y, Pu Q, Xu Y (2012). Predicting the calcium leaching behavior of cement pastes in aggressive environments. *Construction and Building Materials*, 29, 88-96.

Inmala N, Soralump S (2010). Safety analysis of RCC dam from seepage through dam model case study. *Proceedings of the 15th National Convention on Civil Engineering*, Ubon Ratchathani, Thailand.

Kadhim AL, Keskin SB (2024). Calcium aluminate cement based high early strength engineered cementitious composites with recycled artificial flaws. *Challenge Journal of Concrete Research Letters*, 15(4), 120-133.

Lin L, Wang X, Zhou J, Chu H, Shen D, Chen H, Qin S (2018). Investigation of pore structure and mechanical property of cement paste subjected to the coupled action of freezing/thawing and calcium leaching. *Cement and Concrete Research*, 109, 133-146.

Liu J, Zhang Y, Wang Y, Jiang L (2022). Transport properties and calcium leaching of cementitious materials under seepage conditions. *Construction and Building Materials*, 318, 125960.

Mahmud H, Ahmed T, Islam MS (2025). Combined effect of rice husk ash and animal bone powder on strength and permeability of concrete. *Challenge Journal of Structural Mechanics*, 11(1), 1-13.

Marchand J, Bentz D, Samson E, Maltais Y (2001). Influence of calcium hydroxide dissolution on the transport properties of hydrated cement systems. In: Skalny JP, Gebauer J, Odler I, editors. *Materials Science of Concrete: Calcium Hydroxide in Concrete*. American Ceramic Society, Westerville, OH, USA, 113-129.

Mindess S, Young JF, Darwin D (2003). Concrete. 2nd ed. Pearson Education Inc., Upper Saddle River, NJ, USA.

Pandimani (2025). Assessment of stresses and vibration behavior of concrete gravity dam under fluctuating hydrostatic force. *Challenge Journal of Concrete Research Letters*, 16(1), 1-14.

Rozière E, Loukili A, El Hachem R, Grondin F (2009). Durability of concrete exposed to leaching and external sulfate attacks. *Cement and Concrete Research*, 39, 1188-1198.

Şermet F, Kartal ME, Yiğit ME, Hökelekli E (2024). The effect of the gravity on the earthquake performance of roller compacted concrete dams. *Challenge Journal of Concrete Research Letters*, 15(1), 20-29.

Shaheen YBI, Etman ZA, Sabiha HL (2025). Design of reactive powder concrete mortar mixes through high strength and durability. *Challenge Journal of Concrete Research Letters*, 16(3), 142-154.

Shi C, Wang D, Wu Z, Wu L (2019). Calcium leaching behavior of cementitious materials with supplementary cementitious materials. *Construction and Building Materials*, 221, 196-206.

Soysal BF (2025). A discrete element method for evaluating the seismic performance of concrete gravity dam-reservoir systems under main shock-aftershock events. *Challenge Journal of Structural Mechanics*, 11(4), 229-244.

Torrenti JM, Nguyen VH, Colina H, Le Maou F, Benboudjema F, Deleruyelle F (2008). Coupling between leaching and creep of concrete. *Cement and Concrete Research*, 38(6), 816-821.

Turan E, Alameri IA, Oltulu M (2025). Long-term durability of red mud-modified cement mortars: Effects of high temperature and freeze-thaw cycles. *Challenge Journal of Structural Mechanics*, 11(3), 116-127.

Wang Y, Liu J, Zhang J, Jiang L (2021). Effect of fly ash on calcium leaching properties of cement pastes in ammonium chloride solution. *Materials*, 14(19), 5935.

Zhang Y, Liu Z, Jiang Y, Guo L, Song Z (2020). Determination of calcium leaching behavior of cement pastes exposed to ammonium chloride aqueous solution. *Cement and Concrete Research*, 134, 106086.

Challenge Journal of CONCRETE RESEARCH LETTERS

Research Article

Structural performance of biaxially-loaded slender hybrid self-compacting concrete columns with RPC shells

Alaa Ali Salman Al-Taai [a,*], Waleed A. Waryosh [a]

[a] *Department of Civil Engineering, Mustansiriyah University, 10052 Baghdad, Iraq*

ABSTRACT

The response of slender hybrid reinforced concrete columns composed of two advanced cementitious composites, self-compacting concrete (SCC) and reactive powder concrete (RPC), under biaxial eccentric compression has not been adequately documented. This study addresses this gap by comparing conventional SCC columns with hybrid SCC columns and examining the development of steel strains and lateral deformations. Six 140 × 140 mm square columns with an overall height of 1260 mm were tested at three eccentricity levels: low, medium, and high. The investigated variables were the outer-shell material, namely self-compacting normal concrete (SC-NC) or self-compacting reactive powder concrete (SC-RPC), and the eccentricity level. In the hybrid specimens, the SC-NC core and SC-RPC outer shell were cast concentrically under fresh-to-fresh conditions to ensure full interaction. The results showed that the use of SC-RPC as the outer-shell material significantly increased the ultimate load and moment capacities and improved the deformation and failure responses, particularly at high eccentricity. Therefore, SC-RPC shells can substantially enhance the structural performance and safety of slender hybrid reinforced concrete columns subjected to biaxial eccentric loading.

ARTICLE INFO

Article history:
Received – November 25, 2025
Revision requested – January 16, 2026
Revision received – February 16, 2026
Accepted – February 25, 2026

Keywords:
Reactive powder concrete
Self-compacting concrete
Biaxial loading
Hybrid concrete columns
Slender columns

Citation: Al-Taai AAS, Waryosh WA (2026). Structural performance of biaxially-loaded slender hybrid self-compacting concrete columns with RPC shells. *Challenge Journal of Concrete Research Letters*, 17(2), 109–121.

1. Introduction

From a structural perspective, reinforced concrete columns are generally classified as short or slender members. Slender columns are increasingly used in modern construction, including tall buildings, large-span arenas, shopping centers, and multilevel parking facilities. However, their high slenderness ratios amplify second-order effects and lateral deflections under combined axial compression and bending, which may compromise structural safety and serviceability (Al-Taai et al. 2018; ACI 318M-19 2019; Al-Taai 2025). Accordingly, understanding the response of slender columns under combined loading is essential for the development of safer and more efficient structural systems.

To overcome the limitations of conventional slender columns, researchers have investigated composite and hybrid reinforced concrete systems in which the interaction between different materials can improve structural efficiency and economy. Experimental studies on concrete-filled steel members have shown that effective composite interaction can increase load-carrying capacity and delay local instability (Sancıoğlu et al. 2025). At the structural-system level, steel-concrete composite columns have also been reported to increase lateral rigidity and reduce storey displacements relative to conventional reinforced concrete columns (Yıldız and Şermet 2025). Composite columns containing steel I-sections encased in concrete have been widely investigated (Begum et al. 2013; Lai et al. 2019a, 2019b; Xie et al. 2019; Mao et al. 2021; Chen et al. 2022; Yuan et al. 2022; Hu et al. 2023; Liu et al. 2023). Concrete-filled steel and aluminum tubes have likewise been studied extensively, while external CFRP confinement has been used to im-

* *Corresponding author*. E-mail address: alaaalisalman@uomustansiriyah.edu.iq (A. A. S. Al-Taai)
ISSN: 2548-0928 / DOI: https://doi.org/10.20528/cjcrl.2026.02.003

prove the strength and ductility of short square columns (Wang et al. 2019; Patel et al. 2020; Deng et al. 2021; Bu et al. 2023; Rong 2023; Xu et al. 2024).

A hybrid concrete column combines two concrete types within a common cross-section, typically a high-strength outer shell and a normal-strength core (Resheq 2018; Al-Zuhairi 2021). The high-strength shell can contribute substantially to load resistance while also protecting the core against environmental and thermal effects. Because the structural response depends on the integrity of the outer layer, cracking or damage to the shell may adversely affect the performance of the entire cross-section (Richart and Brown 1934).

In hybrid concrete columns, the two concrete layers may act together through either full or partial interfacial bond. Several studies have examined the effect of this interaction on the behavior of short hybrid columns (Ali and Mohammed 2018; Mohammed Ali 2020). Ali and Mohammed (2018) investigated eccentrically loaded columns composed of a precast RPC shell and a normal-strength concrete core. Increasing the shell thickness from 25 to 50 mm increased the load capacity by approximately 11%, while the combined use of longitudinal and transverse reinforcement enhanced ductility compared with unreinforced specimens.

Mohammed Ali (2020) evaluated the concentric and eccentric performance of hybrid columns comprising a high-strength RPC shell and a low-strength concrete core bonded with epoxy resin. Under concentric loading, the ultimate capacity increased by 28-80%, depending on the shell strength, while the eccentrically loaded columns also exhibited stable and satisfactory behavior.

Several studies have investigated short hybrid columns designed with full bond between the outer and inner concrete layers (Latief 2018; Resheq 2018; Hamid et al. 2020; Mohammed et al. 2022; Mufja 2024). These studies have improved understanding of how full composite interaction affects cross-sectional response and overall load-carrying capacity.

Latief (2018) studied hybrid columns composed of high-strength concrete (HSC) and steel fiber-reinforced concrete (SFRC) and reported that both the outer-shell material and the eccentricity ratio (e/h) strongly affected the structural response. For eccentricity ratios of 1/3 and 1/2, the ultimate capacities of columns with HSC shells increased by 3.74% and 21.08%, respectively, while those of columns with SFRC shells increased by 3.74% and 11.11%, respectively. Resheq (2018) examined the effects of concrete type and sectional configuration on axial capacity. The load capacity increased by 70% when the diameter of the normal-concrete core was reduced and that of the SCC shell was increased, whereas the reverse configuration produced an increase of 20%. Al-Zuhairi (2021) investigated the axial capacity of short hybrid columns under biaxial loading and reported a 33.5% increase relative to conventional columns. The capacity increased by 38% when the hybrid ratio decreased from 0.36 to 0.16, and the lower hybrid ratio also reduced the axial strain at a given load level.

Hamid et al. (2020) assessed the influence of reinforcement detailing on short hybrid columns comprising a normal-concrete core and a 40 mm thick RPC outer shell. The combined use of the two concretes increased the ultimate load by 179% relative to the conventional concrete specimens, and transverse reinforcement had a greater influence on the response than longitudinal reinforcement. Mohammed et al. (2022) subsequently examined the effects of transverse-bar diameter and spacing in columns with the same 40 mm RPC shell. Increasing the bar diameter produced the greatest strength improvement, with an increase of 203% in ultimate load, while reducing the spacing increased the load by approximately 179% relative to the reference specimen. Mufja (2024) investigated the effects of eccentricity and outer-shell thicknesses of 25 and 50 mm in hybrid columns with a high-strength concrete core and an RPC shell. Three RPC mixtures were examined: 1% steel fiber (SF), 0.5% SF plus 0.5% polypropylene fiber (PPF), and 1% PPF. The mixture containing 1% SF exhibited the greatest axial stiffness and energy absorption. The ultimate loads increased by 12-28% for square sections and 26-35% for circular sections relative to the reference specimens. Overall, previous studies indicate two principal fabrication strategies: using a normal- or low-strength core confined by a high-strength or fiber-reinforced shell, and combining two concretes with markedly different mechanical properties. Because numerical predictions of reinforced concrete strength can vary with the adopted constitutive model, experimental studies remain essential for reliable characterization of hybrid systems (Polat and Karaman 2025).

The authors' previous studies provided detailed experimental assessments of slender hybrid SCC columns with normal-concrete cores and RPC outer shells under uniaxial eccentric loading (Al-Taai and Waryosh 2025, 2026). In the uniaxial loading study, replacing the outer shell with RPC increased the axial load capacity by 57.8% and the flexural moment capacity by 56%, while improving energy dissipation and reducing lateral deformation (Al-Taai and Waryosh 2026). In the related strengthening study, the hybrid columns were externally strengthened using near-surface-mounted (NSM) GFRP bars in combination with CFRP sheets. The strengthened specimens achieved approximately 80% greater axial load capacity and more than a 100% increase in flexural moment capacity relative to the unstrengthened specimens (Al-Taai and Waryosh 2025). These findings demonstrate the effectiveness of RPC shells and NSM strengthening in improving the strength, ductility, and overall response of slender SCC columns under eccentric compression.

The use of two concretes within a single hybrid cross-section requires both mixtures to possess sufficient flowability and cohesion so that the outer shell can fully encapsulate the inner core and develop a continuous interface without segregation or weak zones (Hassan 2015; Danha et al. 2020; Hussein et al. 2020; Al-Taai et al. 2025). Consequently, using two self-compacting concretes is a practical fabrication approach. Nevertheless, hybrid sections formed entirely from self-compacting concretes, particularly those incorporating RPC as an outer shell, have not been examined in sufficient detail. Research on slender hybrid SCC columns under biaxial eccentric loading is also scarce. The present study therefore experimentally investigates the structural performance of slender hybrid SCC columns subjected to biaxial eccentric compression, with full bond between the core and outer shell.

2. Experimental Details

2.1. Specimen description

Six slender reinforced concrete columns were prepared, each with a square cross-section of 140 × 140 mm and an overall height of 1260 mm, corresponding to a slenderness ratio of approximately 30. The longitudinal reinforcement comprised four 10 mm diameter deformed bars, providing a reinforcement ratio (ρ) of 1.6%, with a concrete cover of 22.5 mm. The detailing satisfied the minimum column reinforcement requirements of ACI 318-19 (ACI 318M-19 2019). The longitudinal bars had a yield strength of 630 MPa and an elastic modulus of 200 GPa. Closed 6 mm diameter stirrups spaced at 140 mm along the column height were used as transverse reinforcement. The column geometry and reinforcement layout are shown in Fig. 1. Two corbels were cast at the ends of each column to introduce biaxial eccentricity. The corbels were designed to resist the full test load and ensure that failure occurred within the intended test region. Each corbel had plan dimensions of 260 × 260 mm and a depth of 280 mm.

A loading system was specifically designed to apply biaxially eccentric compression to the slender columns and to promote failure within the central test region rather than near the ends. Each specimen was positioned near one corner of the corbels to provide the required offsets for the eccentric load. The load was applied horizontally in a biaxial configuration.

2.2. Test matrix

The experimental program comprised the six slender column specimens summarized in Table 1. All specimens had identical geometric and reinforcement details, while the investigated variables were the outer-shell concrete type and the biaxial eccentricity level. Three eccentricity ratios were considered: low (e_x/b_x=e_y/b_y=0.25), medium (e_x/b_x=e_y/b_y=0.65), and high (e_x/b_x=e_y/b_y= 0.90), corresponding to Groups 1, 2, and 3, respectively. Here, e_x and e_y denote the load eccentricities about the two principal axes, while b_x and b_y are the corresponding section dimensions. Each group included one reference column cast entirely with SC-NC and one hybrid column composed of an SC-NC core and an SC-RPC outer shell. The reference specimens were designated NBE1, NBE2, and NBE3, whereas the hybrid specimens were designated RBE1, RBE2, and RBE3.

The experimental program was designed to determine how biaxial eccentricity influences the load capacity, stiffness, and deformation response of slender hybrid columns and to evaluate the contribution of the RPC shell as a confining and load-resisting layer. The selected eccentricity ratios represent compression-controlled, near-balanced, and tension-controlled response conditions.

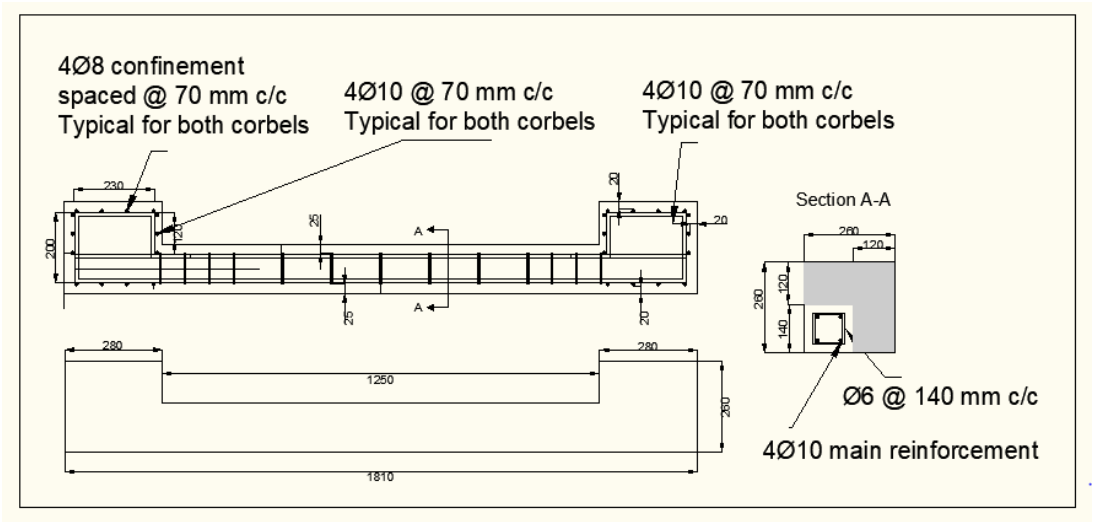

Fig. 1. Reinforcement layout of the hybrid SCC columns.

Table 1. Test matrix for biaxial loading.

Group	Eccentricity ratio	Self-compacting hybrid concrete (SC-HC)				Specimen designation
		Outer-shell concrete		Inner-core concrete		
		Concrete type	Grade (MPa)	Concrete type	Grade (MPa)	
1	e_x/b_x = 0.25	SC-NC	33.79	SC-NC	33.79	NBE1
		SC-RPC	100.16			RBE1
2	e_x/b_x = 0.65	SC-NC	33.79			NBE2
		SC-RPC	100.16			RBE2
3	e_x/b_x = 0.9	SC-NC	33.79			NBE3
		SC-RPC	100.16			RBE3

2.3. Specimen instrumentation

The biaxial loading tests were conducted using a servo-controlled testing machine with a maximum capacity of 3000 kN. Each specimen was subjected to monotonically increasing static load until failure. The instrumentation arrangement is shown in Fig. 2. Three linear variable differential transformers (LVDTs) were positioned at the lower, middle, and upper levels of each specimen to measure lateral displacement. Two strain gauges were installed on the longitudinal reinforcement at mid-height: SG1 on the tension side of the loaded axis and SG2 on the compression side of the opposite axis. The load was applied in 10 kN increments until failure. Load, strain, and displacement data were recorded automatically using a computer-based data acquisition system.

2.4. Test setup and procedure

The compressive load was applied using a hydraulic jack positioned between two steel loading caps. Each cap consisted of a 270 × 270 × 40 mm steel plate and four 270 × 150 × 10 mm side plates, which ensured uniform load distribution and reduced local stress concentrations. A semicircular knife edge was attached to the loading assembly, and the upper cap contained grooves aligned with the calculated eccentricity directions about the principal axes. This arrangement transferred the biaxially eccentric load through the knife-edge lines. A hinge connection permitted free rotation and prevented the development of unintended end moments. The loading caps, hinge arrangement, and complete test setup are shown in Fig. 3.

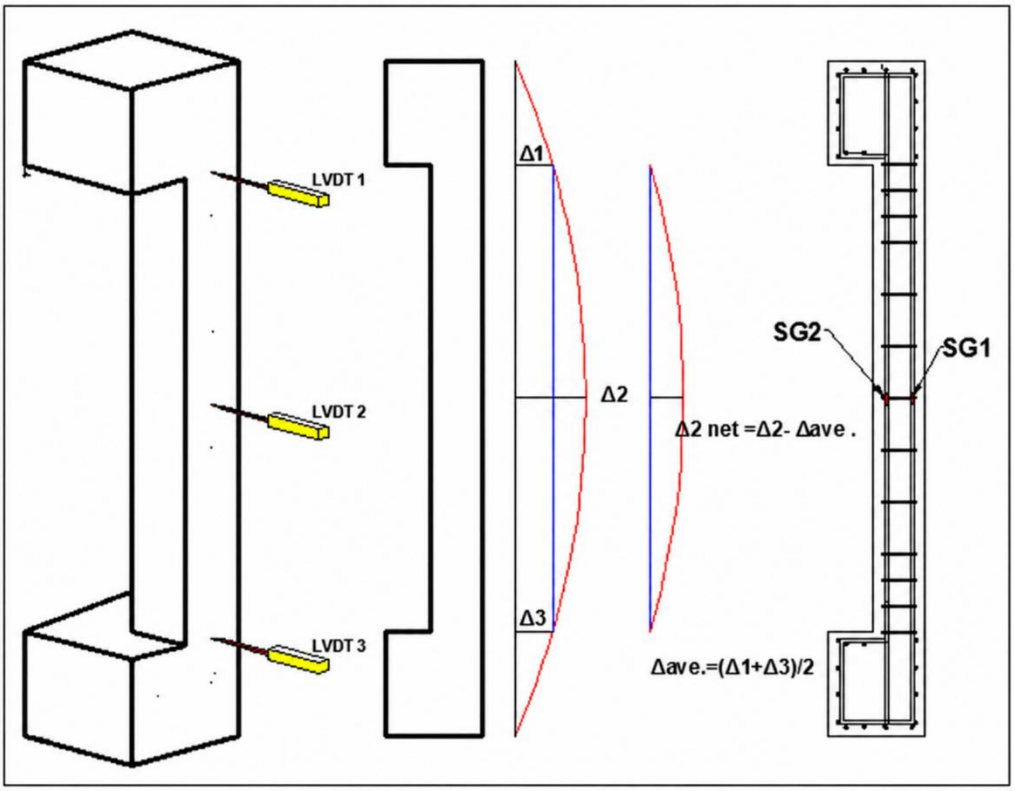

Fig. 2. Layout of the LVDTs and strain gauges installed on the longitudinal bars.

2.5. Materials

A series of trial mixtures was prepared to determine suitable self-compacting concrete compositions for the present study. The selected mixtures were required to possess adequate filling ability, passing ability, and resistance to segregation so that they could flow and consolidate under their own weight while producing uniform specimens.

The trial program produced the mixtures listed in Table 2. The specimens examined in the present study were cast using SC-NC and SC-RPC, with target compressive strengths of approximately 30 and 90 MPa, respectively.

All concrete mixtures were produced using ordinary Portland cement complying with Iraqi Specification No. 5 (IQS No. 5 2019). Crushed natural stone with a nominal maximum size of 10 mm and a sulfate content of 0.06% was used as the coarse aggregate, while crushed-stone sand with a sulfate content of 0.12% was used as the fine aggregate. Silica fume containing approximately 92% SiO_2 was incorporated to improve strength and durability. Previous experimental findings have shown that silica fume improves the mechanical performance of RPC by enhancing particle packing and promoting additional C-S-H formation, thereby producing a denser and less porous matrix (Shaheen et al. 2025). Straight steel fibers with a length of 13 mm, a diameter of 0.2 mm, and a tensile strength of 2500 MPa were used, corresponding to an aspect ratio of 65.

A high-performance superplasticizer (MasterGlenium 54) based on modified polycarboxylic ether chemistry was used in all SCC mixtures to achieve the required workability without compromising strength. The admixture, supplied by MBCC Group, was light brown, had a

specific gravity of approximately 1.07 and a pH of 5-8, and complied with ASTM C494 Types F and G (ASTM C494/C494M-19 2019).

The adopted dosage produced a slump flow greater than 600 mm and satisfied the EFNARC (2002) criteria for self-compacting concrete.

At 28 days, the measured compressive strengths were 33.79 MPa for Mix 1 and 88.86 MPa for Mix 2.

Deformed bars with a diameter of 10 mm (Grade 520) and a measured yield strength of 630 MPa were used as longitudinal reinforcement, while 6 mm diameter plain bars of the same grade were used as transverse reinforcement. The measured mechanical properties of the reinforcement are summarized in Table 3.

2.6. Casting and preparation of the test columns

Each specimen was cast vertically to maintain uniform placement and proper integration of the concrete layers. For the hybrid columns, an aluminum tube measuring 100 × 100 × 1.5 mm was installed within the steel mold to separate the inner core from the outer shell during casting. The tube was secured at its upper edges to prevent movement during placement and to facilitate removal after both concretes had been poured.

The reference reinforced concrete columns were cast in a single pour without an internal separator. In the hybrid specimens, the core and shell concretes were placed successively under fresh-to-fresh conditions to ensure full bond and composite interaction. Fig. 4 presents the cross-sectional configurations, and Fig. 5 shows the principal fabrication stages.

Fig. 3. Test setup and loading configuration.

Table 2. Mixture proportions of the self-compacting concretes.

Mixture	Cement (kg/m^3)	Sand (kg/m^3)	Gravel (kg/m^3)	Water (kg/m^3)	MasterGlenium 54 (kg/m^3)	Water/binder ratio	Silica fume (kg/m^3)	Steel fiber (kg/m^3)	28-day compressive strength (MPa)
SC-NC	360	780	830	158.50	6.40	0.440	–	–	33.79
SC-HSC	500	840	871	167.50	10.45	0.304	50	–	55.22
SC-RPC	950	1050	–	209.76	45.60	0.184	190	78.5	88.86

Table 3. Mechanical properties of the reinforcement.

Reinforcement diameter	Yield strength (MPa)	Ultimate strength (MPa)	Elongation (%)
6 mm	526	580	13.9
8 mm	354	561	24.1
10 mm	630	691	9.8

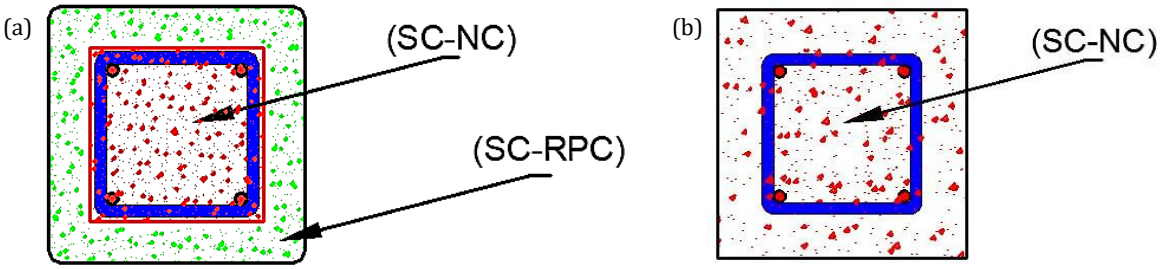

Fig. 4. Cross-sectional details of (a) hybrid self-compacting concrete columns and (b) normal self-compacting concrete columns.

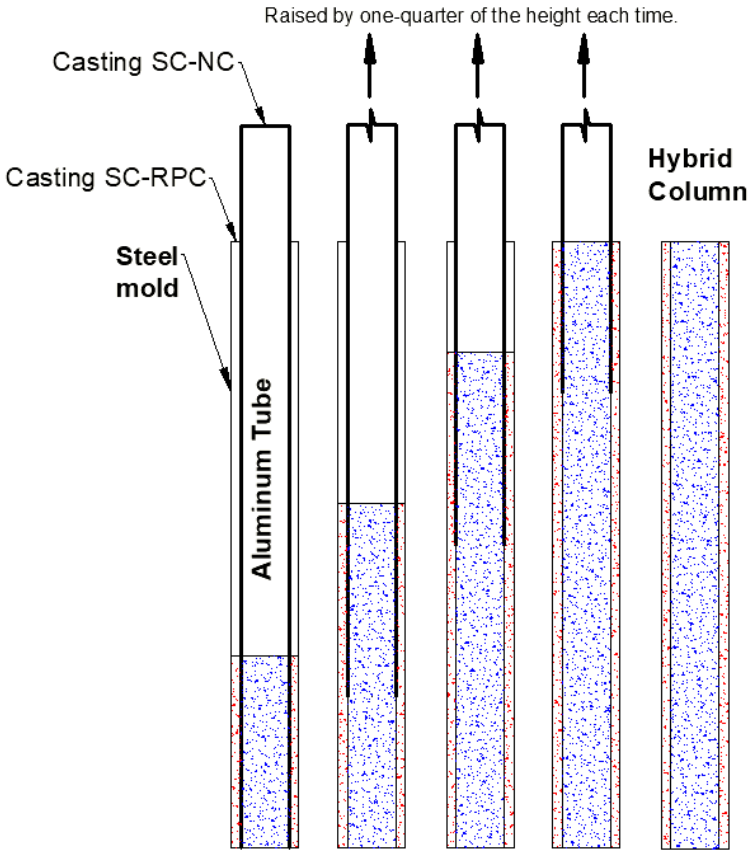

Fig. 5. Main stages of hybrid column fabrication.

3. Experimental Results

3.1. Load-lateral deflection relationships

Figs. 6–8 show the load-lateral deflection responses of the columns at eccentricity ratios of 0.25, 0.65, and 0.90, respectively. The results demonstrate that the outer-shell strength significantly influenced the lateral response of the hybrid columns under biaxial eccentric loading.

The outer layer was varied between SC-NC and SC-RPC to assess the effect of material strength. Lateral displacement was measured using three LVDTs positioned near the two ends and at mid-height, and the mid-height response was used for the load-deflection curves. The response of each specimen was approximately linear at the initial loading stage, followed by a reduction in stiffness and a rapid increase in lateral deflection near the ultimate load. The post-peak branches showed decreasing load with continued deformation. Table 4 summarizes the ultimate loads and corresponding lateral deflections. Relative to the reference specimens, the use of an SC-RPC shell increased the ultimate load by 45.96% for RBE1 (e_x/b_x=0.25), 59.67% for RBE2 (e_x/b_x=0.65), and 80.53% for RBE3 (e_x/b_x=0.90). This behavior is attributed to the higher compressive strength and elastic modulus of RPC, which increase the flexural stiffness of the section, delay cracking and stiffness degradation, and improve load-carrying capacity, particularly at high eccentricity where bending effects dominate.

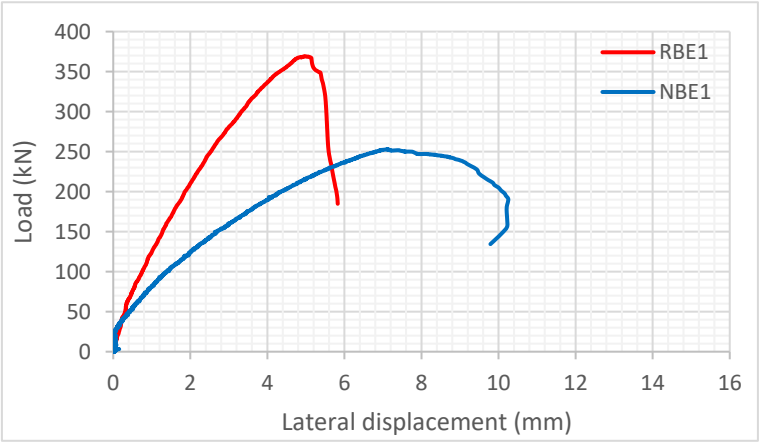

Fig. 6. Load-lateral deflection relationship at the low eccentricity ratio.

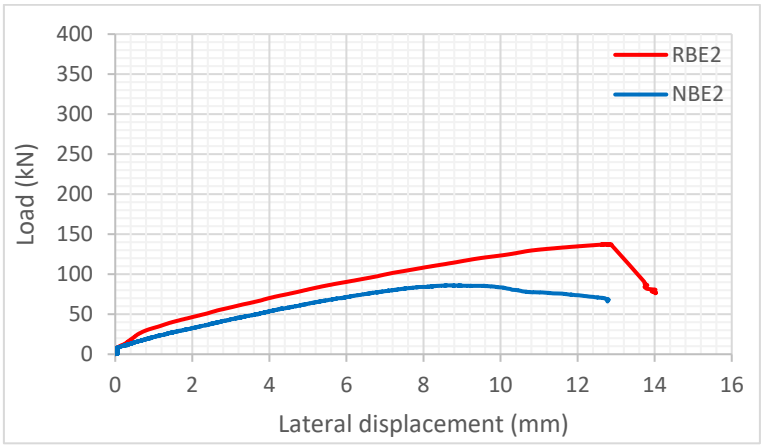

Fig. 7. Load-lateral deflection relationship at the medium eccentricity ratio.

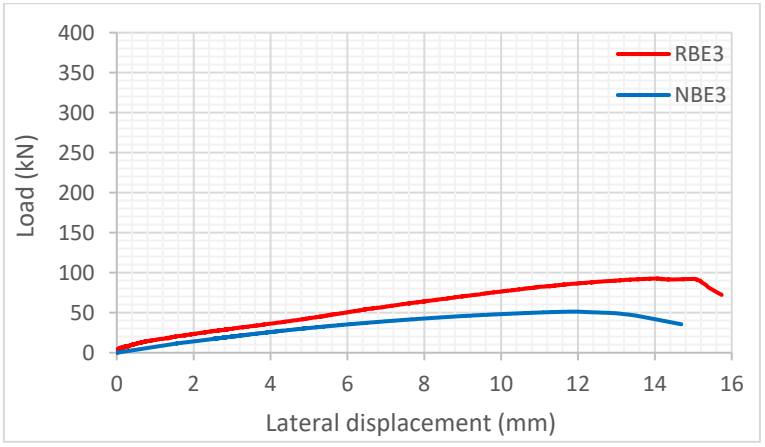

Fig. 8. Load-lateral deflection relationship at the high eccentricity ratio.

Table 4. Ultimate loads and lateral displacements of the biaxially loaded specimens.

No.	Specimen	P_u (kN)	Lateral deflection, Δ_u (mm)	Increase in P_u (%)
1	NBE1	252.86	7.116	0
2	RBE1	369.08	4.973	45.964
3	NBE2	86.034	8.699	0
4	RBE2	137.37	12.79	59.671
5	NBE3	51.348	11.92	0
6	RBE3	92.701	14.07	80.534

3.2. Load-longitudinal steel strain relationships

Figs. 9–11 illustrate the longitudinal steel strain responses at the mid-height of the specimens. In all biaxially loaded columns, the tensile reinforcement reached its yield strain before failure. At the low eccentricity ratio (e_x/b_x=0.25), yielding occurred at approximately 92% and 97% of the ultimate load for NBE1 and RBE1, respectively. At the medium eccentricity ratio (e_x/b_x=0.65), yielding occurred at 87% and 88% of the ultimate load for NBE2 and RBE2, respectively, accompanied by greater sectional rotation and lateral deflection. At the high eccentricity ratio (e_x/b_x=0.90), yielding occurred at 81% and 76% of the ultimate load for NBE3 and RBE3, respectively, with larger curvature and deformation beyond the balanced condition.

The compression reinforcement did not reach yield in any specimen, confirming that the response was governed primarily by tension-controlled behavior. The columns therefore exhibited ductile characteristics influenced by the applied eccentricity and the location of the outermost tensile reinforcement. Consequently, the tension bars yielded before significant compression failure developed in the concrete.

As the eccentricity increased, the bending moment, curvature, and tensile strains in the longitudinal reinforcement also increased. The neutral axis shifted toward the compression face, causing the tensile reinforce-

ment to yield at a smaller proportion of the ultimate load. This trend is consistent with the expected response of eccentrically loaded slender columns, in which flexural effects become increasingly dominant.

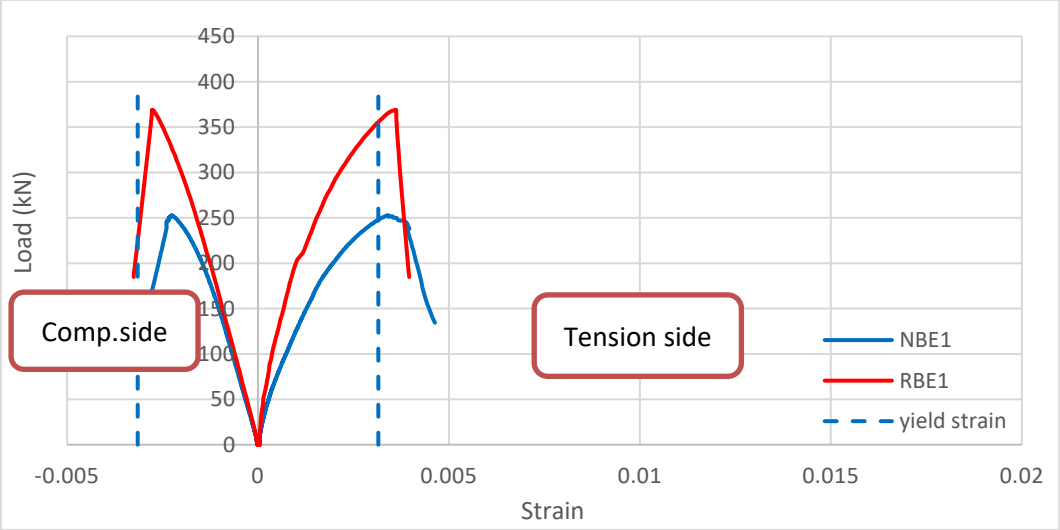

Fig. 9. Load-longitudinal steel strain relationship at the low eccentricity ratio.

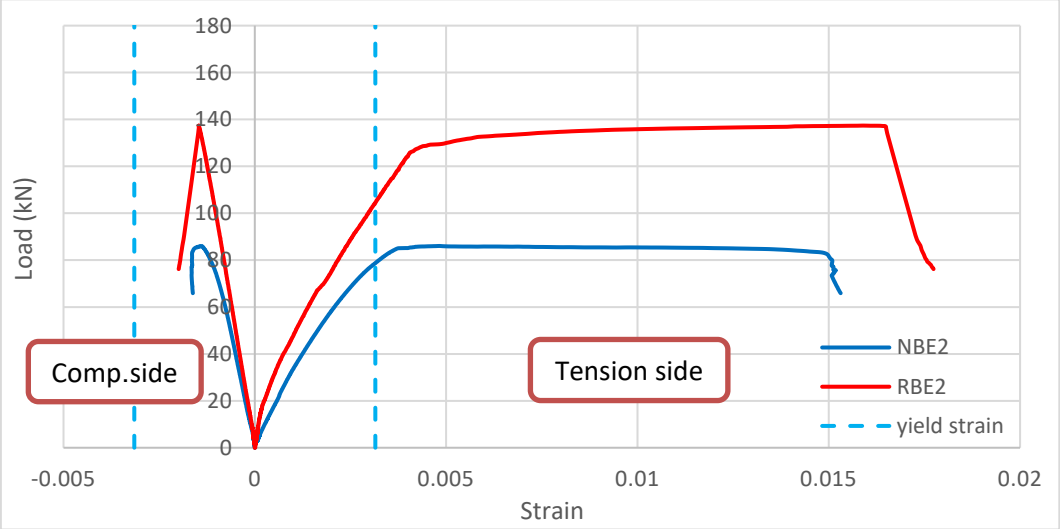

Fig. 10. Load-longitudinal steel strain relationship at the medium eccentricity ratio.

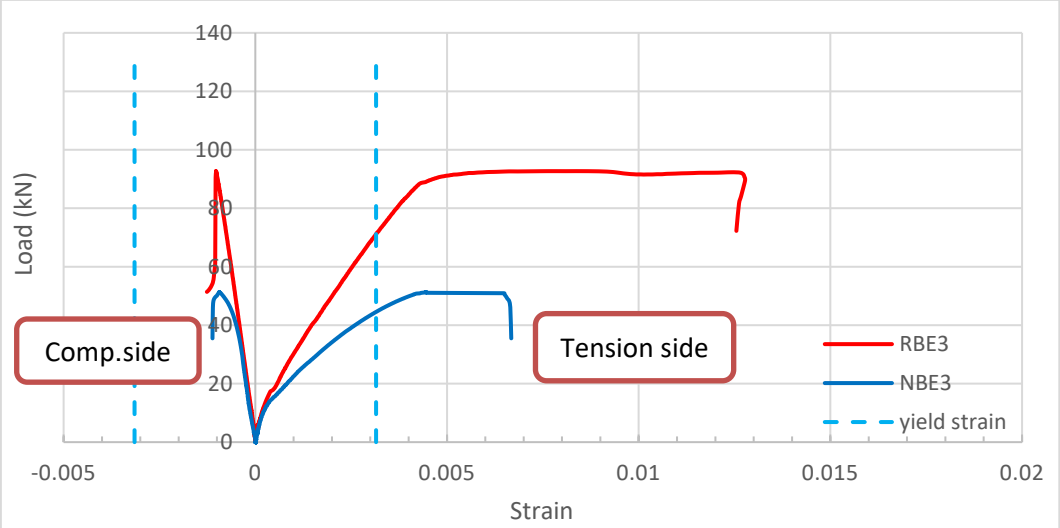

Fig. 11. Load-longitudinal steel strain relationship at the high eccentricity ratio.

3.3. Moment-curvature response

All specimens were subjected to eccentric compressive loading, resulting in biaxial bending about the principal axes. The moment-curvature relationships for the three experimental groups are shown in Figs. 12–14. At each load increment, the bending moment (M) was calculated as the product of the applied load (P) and the effective eccentricity, defined as the sum of the initial eccentricity (e) and the lateral deflection (Δ) measured at mid-height, as expressed in Eq. (1):

$$M_u = P(e + \Delta) \quad (1)$$

Curvature varied across the section during testing. It was evaluated using the plane-sections assumption, under which the longitudinal strain distribution is linear through the section depth. The curvature was therefore calculated using Eq. (2):

$$\phi_i = \frac{\varepsilon_{sti} - \varepsilon_{sci}}{d} \quad (2)$$

where ε_{sti} and ε_{sci} denote the measured strains in the tensile and compressive longitudinal reinforcement, respectively, and d is the distance between the two reinforcement layers. This distance remained constant at 289 mm for all tested columns. Table 5 summarizes the ultimate axial load, the corresponding lateral displacement, and the ultimate bending moment calculated as $M_u = P_u\ (e + \Delta_u)$. Replacing the SC-NC shell with SC-RPC increased the ultimate moment by 38.54% for RBE1, 66.64% for RBE2, and 83.47% for RBE3 relative to the corresponding reference specimens. The higher compressive strength and elastic modulus of RPC increased the flexural stiffness of the section, delayed cracking and stiffness degradation, and enabled the columns to sustain greater moments and curvatures before failure. This effect became more pronounced at higher eccentricity ratios, where flexural action governed the response.

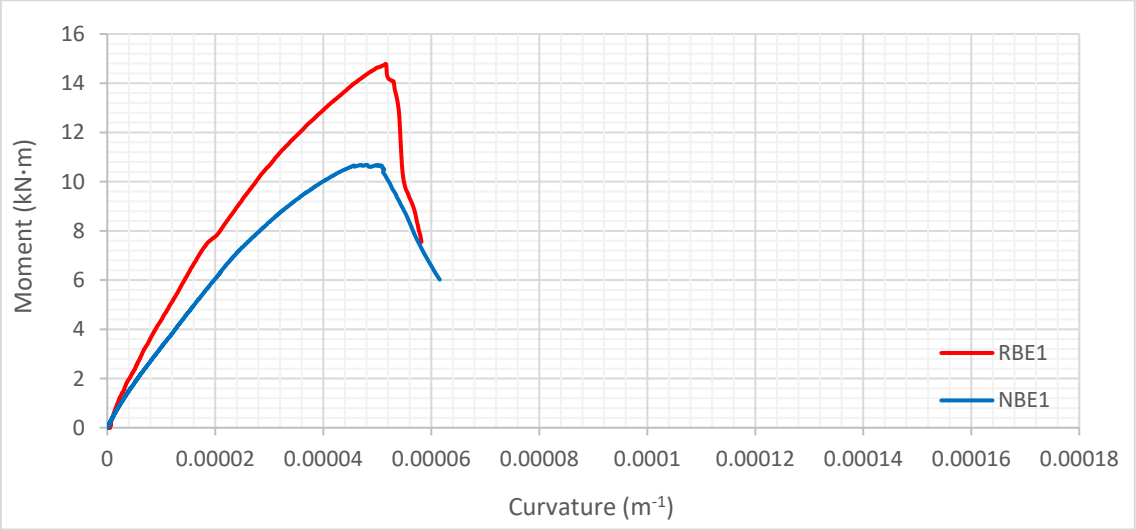

Fig. 12. Moment-curvature relationship at the low eccentricity ratio.

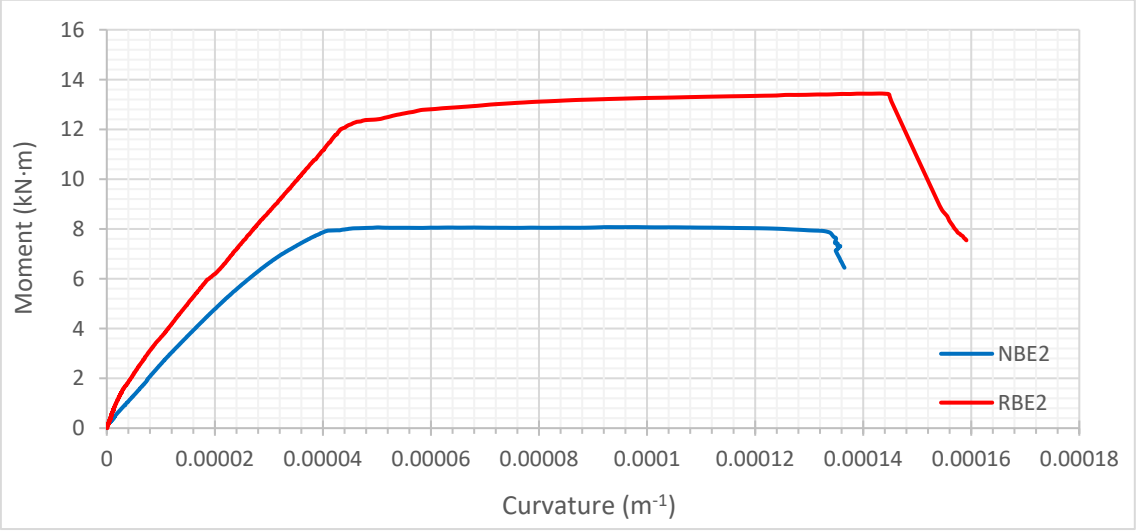

Fig. 13. Moment-curvature relationship at the medium eccentricity ratio.

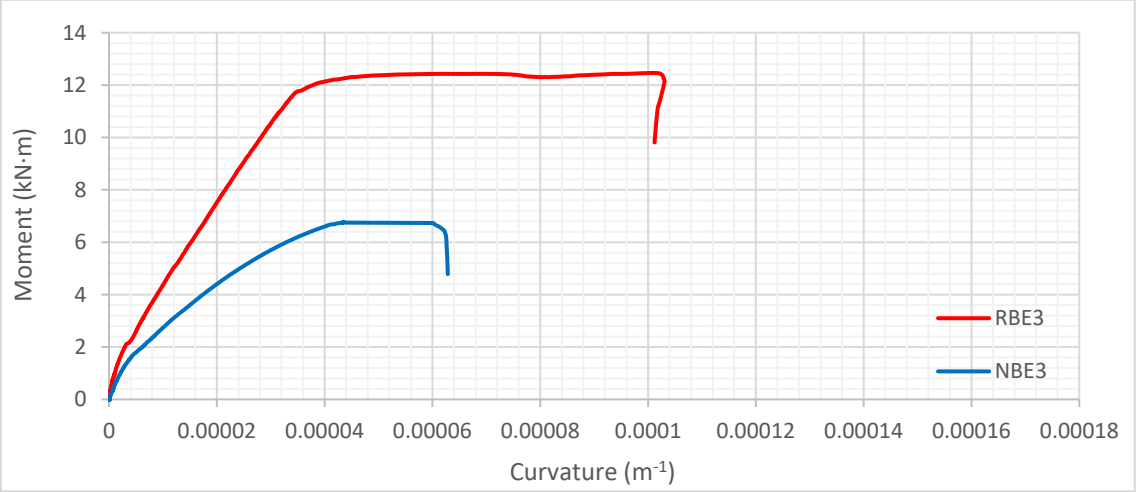

Fig. 14. Moment-curvature relationship at the high eccentricity ratio.

Table 5. Ultimate moment-curvature results for the biaxially loaded specimens.

No.	Specimen	P_u (kN)	Δ_u (mm)	$M_u = P_u\,(e + \Delta_u)$ (kN·m)	Curvature (1/mm)	Increase in M_u (%)
1	NBE1	252.86	7.116	10.649	4.56E-05	0
2	RBE1	369.08	4.973	14.753	5.14E-05	38.538
3	NBE2	86.034	8.699	8.061	5.02E-05	0
4	RBE2	137.37	12.79	13.433	1.40E-04	66.641
5	NBE3	51.348	11.92	6.774	4.35E-05	0
6	RBE3	92.701	14.07	12.428	6.15E-05	83.466

3.4. Curvature ductility, flexural stiffness, and energy absorption

Flexural stiffness is a key parameter governing the resistance of a column to lateral deformation and second-order effects. The effective flexural stiffness (EI_{eff}) of each tested column was derived from its moment-curvature response using the procedure described below:

$$EI_{eff} = \frac{M_{ty}}{\phi_y} \quad (3)$$

$$\mu_\phi = \frac{\phi_u}{\phi_y} \quad (4)$$

Fig. 15 schematically illustrates the procedure used to determine the yield curvature, ultimate curvature, and curvature ductility ratio. In this analysis, EI_{eff} denotes the effective flexural stiffness, and M_{ty} is the moment corresponding to initial yielding of the longitudinal reinforcement. The parameters ϕ_y and ϕ_u represent the curvatures at yielding and at 80% of the post-peak moment, respectively. To estimate ϕ_y, a line was drawn from the origin of the M-ϕ curve to the point corresponding to $0.75M_u$. The intersection of this line with the tangent at the ultimate moment was taken as the yield curvature, following the procedure proposed by El-Tawil and Deierlein (1999).

The comparisons in Table 6 show that the effect of the RPC shell on curvature ductility depended on the eccentricity level. At low eccentricity, the ductility ratio decreased slightly from 1.333 for NBE1 to 1.313 for RBE1. At medium eccentricity, it increased from 2.594 to 3.125, while at high eccentricity it increased markedly from 1.37 to 2.94. The hybrid specimens also exhibited greater flexural stiffness than the corresponding reference columns at all three eccentricity levels, indicating that the RPC shell improved deformation control under biaxial bending. Energy absorption increased from 1.725 to 1.771 at low eccentricity, from 2.389 to 3.769 at medium eccentricity, and from 1.803 to 4.094 at high eccentricity. Thus, the RPC outer shell consistently improved stiffness and energy absorption, while its influence on ductility became more beneficial as the eccentricity increased.

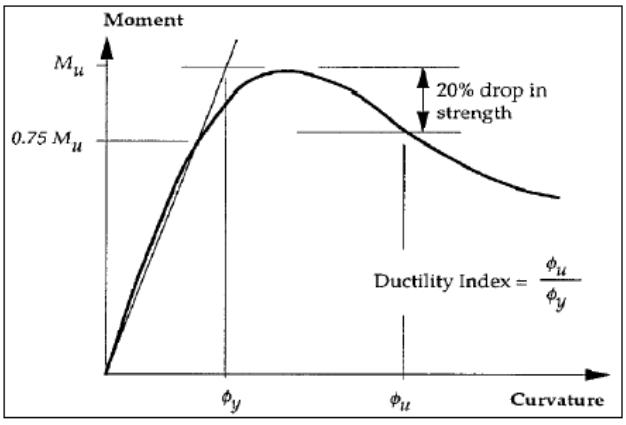

Fig. 15. Definition of the curvature ductility ratio according to El-Tawil and Deierlein (1999).

Table 6. Flexural stiffness, curvature ductility, and energy absorption of the biaxially loaded specimens.

No.	Specimen	M_u (kN·m)	ϕ_u (1/mm)	ϕ at $0.80M_u$ (1/mm)	ϕ at $0.75M_u$ (1/mm)	Curvature ductility	Flexural stiffness (kN·mm^2)	Energy absorption
1	NBE1	10.649	4.56E-05	0.000056	0.000042	1.333	373.710	1.725
2	RBE1	14.753	5.14E-05	0.000055	0.000042	1.313	478.553	1.771
3	NBE2	8.061	5.02E-05	0.000093	0.000036	2.594	396.060	2.389
4	RBE2	13.433	1.40E-04	0.000015	0.000048	3.125	415.215	3.769
5	NBE3	6.774	4.35E-05	0.000046	0.000034	1.370	246.619	1.803
6	RBE3	12.428	6.15E-05	0.000010	0.000034	2.940	303.819	4.094

Table 7. Observed failure modes of the tested specimens.

No.	Specimen	Failure mode	Description
1	NBE1	Compression failure	Sudden concrete crushing between the upper and middle thirds of the column, with visible cracking on the opposite tension face.
2	RBE1	Compression failure	Sudden concrete crushing in the upper third of the column, with visible cracking on the opposite tension face.
3	NBE2	Flexural failure	A wide crack developed in the middle third of the tension zone, accompanied by crushing in the middle third of the compression zone.
4	RBE2	Flexural failure	Cracks developed along the column, including a wide crack between the upper and middle thirds.
5	NBE3	Flexural-compression failure	Visible cracks developed on the tension side and widened with increasing load, while slow, localized concrete crushing occurred near mid-height on the opposite face.
6	RBE3	Flexural failure	A wide crack developed in the lower third of the tension zone, accompanied by slight crushing on the opposite face.

Fig. 16. Observed failure modes of the tested specimens.

4. Conclusions

- Replacing the SC-NC outer shell with SC-RPC substantially increased the ultimate load capacity of the hybrid columns under biaxial eccentric loading. The increases were 45.96%, 59.67%, and 80.53% at low, medium, and high eccentricity, respectively, indicating that the contribution of the RPC shell became more pronounced as the eccentricity increased.
- All specimens exhibited nonlinear load-deflection behavior. The RPC-shell columns sustained higher peak loads and generally maintained greater stiffness, demonstrating improved resistance to deformation and delayed stiffness degradation.
- The RPC-shell columns exhibited enhanced post-peak deformation capacity and energy absorption relative to the reference specimens, particularly at medium and high eccentricity. These results show that RPC improved not only strength but also the ability of the columns to sustain deformation before failure.
- The SC-RPC outer shell increased the ultimate flexural moment capacity by 38.54%, 66.64%, and 83.47% at low, medium, and high eccentricity, respectively, relative to the corresponding reference specimens.
- The influence of the RPC shell on curvature ductility depended on eccentricity. A slight reduction was observed at low eccentricity, whereas substantial improvements occurred at medium and high eccentricity.
- Although stiffness decreased as eccentricity increased, the hybrid columns retained greater stiffness and absorbed more energy than the corresponding reference columns. This response suggests that RPC shells may be beneficial in applications involving severe deformation demands, although dedicated cyclic or dynamic tests are required to confirm their seismic performance.
- The columns failed in compression, flexure, or combined flexural-compression modes, depending on eccentricity. The hybrid specimens generally exhibited more distributed cracking and less abrupt localized crushing, providing a more gradual failure response and an improved safety margin.

Acknowledgements

None declared.

Funding

The authors received no financial support for the research, authorship, and/or publication of this manuscript.

Conflict of Interest

The authors declare no potential conflicts of interest with respect to the research, authorship, and/or publication of this manuscript.

Data Availability

The datasets generated and/or analyzed during the current study are not publicly available but are available from the corresponding author upon reasonable request.

AI Assistance

No AI-based tools were used in the preparation of this manuscript.

Author Contributions

All authors made substantial contributions to the conception and design of the study, acquisition of data, analysis and interpretation of data; drafted or critically revised the manuscript for important intellectual content; and approved the final version to be published.

REFERENCES

ACI 318M-19 (2019). Building code requirements for structural concrete and commentary. American Concrete Institute, Farmington Hills, MI, USA.

Ali A, Mohammed Z (2018). Strength evaluation of hybrid reinforced concrete columns under eccentric loads. *Engineering and Technology Journal*, 36(4A), 449-455.

Al-Taai AAS (2025). Finite element analysis of concrete filled circular steel tube short columns subjected to axial compression load. *Mathematical Modelling of Engineering Problems*, 12(5), 1687-1694.

Al-Taai AAS, Al-Ibadi AHD, Al-Bayati JK (2025). Behavior of fibrous concrete slabs under static and impact loads. *Mathematical Modelling of Engineering Problems*, 12(6), 2148-2156.

Al-Taai AAS, Hassan SA, Hussein LF (2018). Finite element analysis of corner strengthening of CFRP-confined concrete column. *IOP Conference Series: Materials Science and Engineering*, 454(1), 012088.

Al-Taai AAS, Waryosh WA (2025). Structural behavior of slender hybrid self-compacting concrete columns with RPC shells and NSM technique. *Journal of Building Pathology and Rehabilitation*, 11(1), 42.

Al-Taai AAS, Waryosh WA (2026). Influence of load eccentricity on structural response of slender hybrid self-compacting concrete columns with reactive powder concrete shells under uniaxial loading. *International Journal of Engineering*, 39(8), 2022-2034.

Al-Zuhairi AH (2021). Structural behavior of reinforced hybrid concrete columns under biaxial loading. *Latin American Journal of Solids and Structures*, 18(6), 1-18.

ASTM C494/C494M-19 (2019). Standard specification for chemical admixtures for concrete. ASTM International, West Conshohocken, PA, USA.

Begum M, Driver RG, Elwi AE (2013). Behaviour of partially encased composite columns with high strength concrete. *Engineering Structures*, 56, 1718-1727.

Bu J, Liu Q, Yu Y, Qiu Q (2023). Axial compression performance and bearing capacity calculation of round-ended concrete-filled aluminum tube column. *Applied Sciences*, 13(13), 7918.

Chen Z, Ning F, Song C, Liang Y (2022). Study on axial compression bearing capacity of novel concrete-filled square steel tube columns. *Journal of Building Engineering*, 51, 104298.

Danha LS, Abdul-Hussien ZA, Abduljabbar MS, Yassin LAG (2020). Flexural behavior of hybrid ultra-high-performance concrete. *IOP Conference Series: Materials Science and Engineering*, 737(1), 012008.

Deng ZH, Guo JH, Yu JJ, Liu B (2021). Axial compression performance of coral concrete-filled aluminium tube (CCFAT) square stub columns. *Case Studies in Construction Materials*, 15, e00697.

EFNARC (2002). Specifications and guidelines for self-compacting concrete. European Federation for Specialist Construction Chemicals and Concrete Systems, Warrington, UK.

El-Tawil S, Deierlein GG (1999). Strength and ductility of concrete encased composite columns. *Journal of Structural Engineering*, 125(9), 1009-1019.

Hamid MM, Yassin LAG, Mohammed AH (2020). Behavior of hybrid reinforced concrete columns. *IOP Conference Series: Materials Science and Engineering*, 737(1), 012033.

Hassan FH (2015). Behavior of hybrid deep beams containing ultra high performance and conventional concretes. *Engineering and Technology Journal*, 33(1A), 30-50.

Hu HS, Yang ZJ, Xu L, Zhang YX, Gao YC (2023). Axial compressive behavior of square concrete-filled steel tube columns with high-strength steel fiber-reinforced concrete. *Engineering Structures*, 285, 116047.

Hussein LF, Al-Taai AAS, Khudhur ID (2020). Sustainability achieved by using voided slab system. *AIP Conference Proceedings*, 2213(1), 020071.

IQS No. 5 (2019). Iraqi specification no. 5: Portland cement. Central Organization for Standardization and Quality Control, Baghdad, Iraq.

Kandil K, El-Shami M, Hekal GM, ElGouhary OM (2025). Behavior of multi-cell steel columns under impact loading. *Challenge Journal of Concrete Research Letters*, 16(2), 95-114.

Lai B, Liew JYR, Hoang AL (2019). Behavior of high strength concrete encased steel composite stub columns with C130 concrete and S690 steel. *Engineering Structures*, 200, 109743.

Lai B, Liew JYR, Wang T (2019). Buckling behaviour of high strength concrete encased steel composite columns. *Journal of Constructional Steel Research*, 154, 27-42.

Latief AF (2018). Structural behavior of hybrid reinforced concrete columns. University of Babylon, El-Hille, Iraq.

Liu J, Gao P, Lin X, Wang X, Zhou X, Chen YF (2023). Experimental assessment on the size effects of circular concrete-filled steel tubular columns under axial compression. *Engineering Structures*, 275, 115247.

Mao WJ, Wang WD, Zhou K, Du EF (2021). Experimental study on steel-reinforced concrete-filled steel tubular columns under the fire. *Journal of Constructional Steel Research*, 185, 106867.

Mohammed AH, Yassin LAG, Hamid MM (2022). Experimental investigation on the ultimate capacity of rectangular reinforced hybrid concrete columns under axial load. *International Journal of GEOMATE*, 23(95), 112-118.

Mohammed Ali TK (2020). Experimental behavior and analysis of hybrid low-high strength reinforced concrete columns. *Journal of Materials and Engineering Structures*, 7(2), 203-214.

Mufja GF (2024). Experimental evaluation of hybrid reinforced concrete columns under eccentric loads externally strengthened with carbon fibre reinforced polymer. University of Babylon, El-Hille, Iraq.

Patel VI, Liang QQ, Hadi MNS (2020). Numerical simulations of circular high strength concrete-filled aluminum tubular short columns incorporating new concrete confinement model. *Thin-Walled Structures*, 147, 106492.

Polat E, Karaman G (2025). Predicting shear strength in reinforced concrete deep beams through finite element modeling of diverse concrete materials. *Challenge Journal of Structural Mechanics*, 11(1), 24-41.

Resheq A (2018). Behaviour of hybrid concrete columns under axial compression loads. *MATEC Web of Conferences*, 162, 1-6.

Richart FE, Brown RL (1934). An investigation of reinforced concrete columns. Engineering Experiment Station, University of Illinois, Urbana, IL, USA.

Rong B (2023). Study on axial compression behavior of 7A04-T6 concrete-filled aluminum tubular columns. *Journal of Building Engineering*, 76, 107118.

Sancıoğlu S, İlgün A, Çarbaş S (2025). Experimental performance analysis of concrete-filled steel column to concrete-filled steel beam connections. *Challenge Journal of Concrete Research Letters*, 16(4), 215-224.

Shaheen YBI, Etman ZA, Sabiha HL (2025). Design of reactive powder concrete mortar mixes through high strength and durability. *Challenge Journal of Concrete Research Letters*, 16(3), 142-154.

Wang FC, Zhao HY, Han LH (2019). Analytical behavior of concrete-filled aluminum tubular stub columns under axial compression. *Thin-Walled Structures*, 140, 21-30.

Xie F, Chen J, Yu QQ, Dong X (2019). Behavior of cross arms inserted in concrete-filled circular GFRP tubular columns. *Materials*, 12(14), 2280.

Xu W, Zhang J, Liu F, Ma Z (2024). Axial compression behavior of assembled aluminum alloy-concrete-carbon steel double-skin tubular column. *Structures*, 69, 107278.

Yıldız Y, Şermet F (2025). Impact of composite columns on soft and weak storey irregularities in buildings without ground floor infill walls. *Challenge Journal of Structural Mechanics*, 11(2), 70-81.

Yuan F, Cao L, Li H (2022). Axial compressive behaviour of high-strength steel spiral-confined square concrete-filled steel tubular columns. *Journal of Constructional Steel Research*, 192, 107245.

Challenge Journal of CONCRETE RESEARCH LETTERS

Research Article

Performance assessment of polypropylene fiber-reinforced engineered cementitious composites using experimental investigation and ANN modeling

Vinoda Rudrappa Chethan [a], Marilinge Rame Gowda [a], Bangalore Rajshekar Kavya [a], Balluru Thammannagowda Ashwini [a,*], Avant Srinivas Shrikanth [b]

[a] *Department of Civil Engineering, Adichunchanagiri Institute of Technology (Affiliated to Visvesvaraya Technological University), Chikkamagaluru 577102, Karnataka, India*

[b] *Department of Mathematics, Adichunchanagiri Institute of Technology (Affiliated to Visvesvaraya Technological University), Chikkamagaluru 577102, Karnataka, India*

ABSTRACT

The use of engineered cementitious composites (ECC) in structural repair and rehabilitation is becoming more and more common because of their strain-hardening behavior, controlled cracking, and better durability. Polypropylene fiber-reinforced ECC has even more benefits like being resistant to corrosion and saving money, however its mechanical performance is very much affected by the changes in mix composition and the amount of fiber used in the mix. The traditional approaches in mix design are mostly based on either carrying out large-scale experimental trials or using complex micromechanics-based formulations, which are both time-consuming and not very applicable in practice. On the other hand, although the use of Artificial Neural Networks (ANNs) for modeling the behavior of different cement-based materials has been successful, its use in the case of polypropylene fiber-reinforced ECC is still limited. The present study aims to develop an ANN-based predictive framework to predict compressive and flexural strength of polypropylene fiber-reinforced ECC by using the parameters of the mix design. A detailed experimental program with compressive strength and three-point bending tests was performed with different polypropylene fiber contents to study the ECC mixtures. ECC mixtures containing 0–2.0% PP fibers were experimentally tested at curing ages of 14, 28, and 56 days. The results indicate that an optimum PP fiber content of 1.5% yielded the highest mechanical performance, achieving compressive strengths of 31.95 MPa, 47.95 MPa, and 50.61 MPa, and corresponding flexural strengths of 13.41 MPa, 17.50 MPa, and 24.12 MPa at 14, 28, and 56 days, respectively. For making the model more robust and generally applicable, the experimental results were merged with the data from published literature that was carefully selected for ANN training and validation. An ANN model trained using 105 datasets (experimental and literature-based) demonstrated strong predictive capability, with coefficients of determination (R^2) of 0.955 and 0.963 for compressive and flexural strength during training, and 0.953 and 0.975 during testing, respectively. The mean absolute percentage error remained below 8.2% for both strength parameters. The proposed model shows a very strong agreement between the values of strength predicted and those measured in the experiments, as it is able to capture the non-linear relationship between the composition of ECC and its mechanical performance. The framework that has been developed is a practical tool for the optimization of ECC mixes and assessment of their performance, particularly for applications involving the rehabilitation of buildings where accurate predictions and efficient design of materials are of utmost importance.

ARTICLE INFO

Article history:
Received – January 7, 2026
Revision requested – February 9, 2026
Revision received – February 17, 2026
Accepted – February 25, 2026

Keywords:
Engineered cementitious composites
Polypropylene fibers
Compressive strength
Flexural strength
Artificial neural network

Citation: Chethan VR, Rame Gowda M, Kavya BR, Ashwini BT, Shrikanth AS (2026). Performance assessment of polypropylene fiber-reinforced engineered cementitious composites using experimental investigation and ANN modeling. *Challenge Journal of Concrete Research Letters*, 17(2), 122–134.

* *Corresponding author*. E-mail address: ashuchweetu88@gmail.com (B. T. Ashwini)
ISSN: 2548-0928 / DOI: https://doi.org/10.20528/cjcrl.2026.02.004

1. Introduction

Critical infrastructure construction is greatly relying on cementitious materials, which are the most easily available, least costly, and strongest in compression among all construction materials. However, traditional cement-based concretes display a quasi-brittle behavior with very low tensile strength, thus they crack and fail suddenly under dynamic and impact loads. The above shortcomings have a negative impact on the lifespan of the structure, maintenance, and serviceability, therefore the search for new cementitious materials with better ductility, crack control, and damage tolerance is encouraged.

Concrete has been in great demand and the construction industry has been developing so fast that its demand is now even higher. The use of concrete in infrastructures and buildings is a factor that has led to its massive global production. Ordinary concrete is made mainly of cement, fine and coarse aggregates and is characterized by its very good compressive strength but at the same time very weak tension. That is why different methods for strengthening concrete, such as using steel reinforcement, are widely applied in making the material able to withstand tension and cracks. The scenario of concrete has changed and the need for high-strength concrete has also increased very quickly due to modern construction practices with their own performance demands. On the contrary, research has shown that conventional concrete becomes more brittle as its compressive strength increases, which limits its application to non-ductile areas. The need to counter this problem has led to the introduction of new advanced cementitious materials with superior ductile behavior, such as the use of engineered cementitious composites (ECC), which are now being considered for structural and rehabilitation purposes (Uddin et al. 2024).

Engineered cementitious composites have turned out to be a new type of high-performance material that can effectively eliminate the drawbacks of the traditional construction materials (Li et al. 2001). ECC is one of the very few composite that can withstand high tensile strain and at the same time develop many tiny microcracks with precisely controlled widths, instead of large localized cracks. In contrast to regular concrete, ECC generally does not contain any coarse aggregates and depends on a very carefully controlled mixture of cementitious binders, fine aggregates, and short discrete fibers to attain the desired enhancement in mechanical performance. Because of these characteristics, ECC, which is often known as flexible concrete, has not only been that much utilized in the above-mentioned fields but also in structures, bridge decks, seismic-resistant systems, and repair and refurbishment where ductility and durability are the main requirements.

Extensive studies have demonstrated that fiber-reinforced ECC exhibits superior tensile strength, pseudo strain-hardening behavior, and high energy absorption capacity when compared to conventional fiber-reinforced concretes (Liu et al. 2023). The mechanical performance of ECC is highly influenced by the properties of the fibers and the composition of the mix (Wang and Li 2006; Yu et al. 2015). As a result, research has been conducted on the performance enhancement of ECC under compression and tension loading with the addition of polypropylene fiber (PP) (ChiaHwan and JianBo 2014; Hossain et al. 2024; Zhu et al. 2021). Among various fiber types, polypropylene fibers have attracted increasing attention due to their low density, corrosion resistance, cost-effectiveness, and favourable interaction with the cementitious matrix. ECC mixtures incorporating polypropylene fibers in the range of 0–2.0% by volume has been reported to show notable improvements in flexural performance, ductility, and crack resistance. In addition, ECC systems incorporating functional fibers have demonstrated self-sensing and multifunctional capabilities, further expanding their application potential (Han et al. 2015).

Despite these advances, the mechanical and functional properties of ECC remain highly sensitive to variations in mix design parameters, fiber volume fraction, and constituent material proportions. The exact forecasting of prominent performance measures like compressive strength, flexural strength, and crack behavior based solely on mix composition remains one of the hardest problems to solve. Nevertheless, micromechanics-based theories do help in the design of ECC somewhat by connecting fiber–matrix interactions to macroscopic behavior (Fischer and Li 2007), however, their application in practice is frequently restricted by requirements such as detailed microstructural calibration, huge experimental validation, and numerical simulations.

The research on engineered cementitious composites has moved from purely strength enhancement to much more diverse fields including crack control, durability, multifunctionality, and data-driven material design. At the same time, the enhancement of the mix optimization methods, supplementary cementitious materials, and microstructural tailoring have all contributed to the sustainability and applicability of ECC. The material innovations are not the only factor, there is also the growing adoption of artificial intelligence techniques, such as neural networks and machine learning regression models, which have been used to predict the mechanical and durability properties of cement-based materials. The use of these techniques has proven to be highly effective in identifying nonlinear relationships, which are usually difficult to pinpoint with either analytical or empirical models. This study is moving the field of ECC forward by combining experimental research with ANN-based modeling, thus making ECC research relevant to contemporary data-driven material design and simultaneously solving the issue of performance prediction.

In the past few years, Artificial Neural Networks (ANN) have been acknowledged as the best means for modeling intricate and non-linear relationships among materials based on cement. The brain-inspired development and the ability of ANN to perform tasks simultaneously make it ideal for handling problems with analytical models that are not competent enough. Models that are built using ANN approach have already been tested and proven to predict mechanical properties of a number of cementitious systems, such as confined concrete columns (Oreta and Kawashima 2003), self-compacting concrete (Nehdi et al. 2001), elastic modulus and con-

crete strength (Demir 2008), autoclaved aerated concrete (Michelini et al. 2023), fiber-reinforced concrete (Ashwini et al. 2024; Kavya et al. 2022) and GGBS-based concrete composites (Bilim et al. 2009; Kavya et al. 2025). These works are the testimony of the capability of ANN models to accurately represent the nonlinear behavior of materials. However, the direct application of ANN techniques to engineered cementitious composites, particularly polypropylene fiber-reinforced ECC (Haque et al. 2024), remains limited. Unlike conventional and generic fiber-reinforced concretes, ECC behavior is governed by distributed micro-cracking and strain-hardening mechanisms, which are not explicitly addressed in most existing ANN studies.

Recent research on ECC has focused on expanding its mechanical performance, sustainability, and predictive modelling capabilities. A recent comprehensive review highlights advancements in ECC properties, design strategies, ductility performance, sustainability measures, and applications in structural engineering, including tensile strain capacities up to 8% and improved crack control behavior (Odeyemi et al. 2025). Statistical evaluations of ECC mixes with various fiber types, including polypropylene, PVA, and glass fibers at different percentages, have provided insights into the influence of fiber type and dosage on mechanical and fracture performance (Shabakhty et al. 2024). Sustainable ECC formulations using high slag and polypropylene fiber contents have demonstrated tensile strain exceeding 3% and improved energy absorption with additional mesh reinforcements (Saljoughian et al. 2024). In parallel, recent machine-learning approaches have been developed to predict ECC mechanical behavior beyond conventional strength measures, including ANN-based models for full tensile stress–strain curves and ANN predictions for polyethylene fiber–based ECC performance. These studies reflect emerging trends in ECC research, incorporating advanced materials, sustainability considerations, and data-driven predictive modelling (Riaz et al. 2023).

The innovation of this research is to the extent of the combined experimental and soft computing methods that were used to assess and forecast the mechanical performance of polypropylene fiber-reinforced ECC. The current study carries out systematic integration of experimentally generated data with chosen literature data to create a strong and all-encompassing dataset. An ANN based predictive model is created and statistically verified for the purpose of providing an accurate estimate of compressive and flexural strengths, based on the parameters of mix design. The nonlinear influence of key mix design parameters on compressive and flexural strength is captured by the proposed model in a way that reflects ECC-specific deformation mechanisms through the integration of these data sources. This framework establishes a direct data-driven relationship between the composition of ECC and its mechanical performance without the need for complex micromechanical assumptions or extensive trial-and-error testing.

Despite extensive research on engineered cementitious composites, limited studies have systematically investigated the combined effects of polypropylene fiber content on mechanical performance, microstructural behavior, and predictive modeling within a unified framework. In particular, the majority of existing studies focus either on experimental strength characterization or on data-driven modeling, with minimal integration of SEM-based microstructural evidence to explain strength enhancement mechanisms. Furthermore, ANN models specifically developed for polypropylene fiber-reinforced ECC remain scarce. Therefore, the present study addresses this gap by experimentally evaluating compressive and flexural behavior, correlating microstructural observations with mechanical performance, and developing an ANN-based predictive model, thereby providing a comprehensive understanding of polypropylene fiber-reinforced ECC.

2. Materials and Method

The mechanical properties of bendable concrete are influenced by the combination of the fiber strength, its elastic modulus, interaction between the fiber and matrix, fine particles and cement paste. To carry out the experimental inquiry, multiple ratios of cement, fly ash and fine aggregates were adopted as per the relevant Indian Standards. Moreover, high-range water-reducing agent was added to the concrete mix for the purpose of improving the workability and the durability of the concrete. This ensured that the compatibility with building components was optimized for the water content. Polypropylene fibers are incorporated in the concrete to minimize cracking due to drying shrinkage as well as plastic. The fine dispersion of fiber helps to limit water percolation by clogging channels like pores and capillaries, thus restricting the movement of water through the concrete matrix. The properties of the polypropylene fiber are detailed in Table 1.

Table 1. Properties of polypropylene fiber.

Fiber type	Tensile strength (MPa)	Young's modulus (GPa)	Fiber elongation (%)	Specific gravity
Polypropylene	500~700	6~7	20	0.91

3. Experimental Procedure

In the initial stage of ECC preparation, the dry constituents Portland cement, fly ash, and fine sand were proportioned by weight in the ratio of 0.8:1.0:1.1, respectively. A high-range water-reducing admixture was added at a dosage of 0.1 by weight of cement. The water content was maintained separately using a constant water–cement ratio of 0.46 for all mixes to ensure adequate workability and uniform dispersion of polypropylene fi-

bers. Finally, polypropylene fibers were incorporated into the mix as the third step of the composite preparation process which varies between 0 and 2%. For each mix proportion and curing age (14, 28, and 56 days), three identical cube specimens (70×70×70 mm) were tested to determine compressive strength, and three identical beam specimens (304.8×76.2×12.2 mm) were tested to determine flexural strength. Beam specimens with an overall length of 304.8 mm were prepared using the specified mix proportions and cast in steel molds. After 24 hours, the specimens were demolded and spray cured at a controlled laboratory temperature of 27 ± 2 °C for 14, 28 and 56 days prior to testing. Flexural behavior was evaluated using a three-point bending test under simply supported conditions. The effective support span (L) was maintained at 254 mm using two roller supports. A single concentrated load was applied vertically at the mid-span of the beam through a loading nose. The tests were conducted under displacement-controlled loading at a constant rate of 0.5 mm/min using a calibrated universal testing machine. Mid-span deflection was measured using a linear variable differential transformer (LVDT) mounted at the bottom center of the specimen directly below the loading point to eliminate the influence of support settlement. Load and corresponding deflection data were continuously recorded using the testing machine data acquisition system until specimen failure. The reported compressive and flexural strength values represent the average of three specimens. Table 2 displays the compressive strength of polypropylene fiber reinforced engineered cementitious concrete at 14, 28, and 56 days, while Table 3 provides specifics on the flexural strength values at the same curing ages.

Table 2. Compression strength test.

Polypropylene fiber content in (%)	Dimension		Compression strength (N/mm²)		
	L (mm)	B (mm)	14 days	28 days	56 days
0.00	70	70	23.46	30.20	34.40
1.00	70	70	27.67	36.42	36.55
1.25	70	70	29.97	39.48	41.04
1.50	70	70	31.95	47.95	50.61
1.75	70	70	31.12	46.83	46.44
2.00	70	70	29.93	43.97	43.87

Table 3. Flexural strength test.

Polypropylene fiber content in (%)	Dimension			Flexural strength (N/mm²)		
	L (mm)	B (mm)	D (mm)	14 days	28 days	56 days
0.00	304.2	76.2	12.2	03.31	04.64	07.08
1.00	304.2	76.2	12.2	08.36	10.01	12.19
1.25	304.2	76.2	12.2	10.19	12.67	14.80
1.50	304.2	76.2	12.2	13.41	17.50	24.12
1.75	304.2	76.2	12.2	11.83	16.23	17.27
2.00	304.2	76.2	12.2	11.03	15.72	16.72

To enhance the clarity of the experimental methodology, representative photographs illustrating the experimental program are presented in Fig. 1. These include the preparation and mixing of ECC constituents, casting of cube and beam specimens, curing process, compressive strength testing of cube specimens, bending test setup for flexural strength evaluation. The inclusion of these figures provides a clear visual representation of the experimental workflow and testing procedures adopted in the present study.

Fig. 2 illustrates the compressive and flexural strength development of ECC specimens containing various proportions of polypropylene fibers, evaluated at curing ages of 14, 28, and 56 days. The data clearly indicate that a polypropylene fiber content of 1.5% yields the most substantial augmentation in mechanical functionality. At 14 days, the maximum compressive and flexural strengths recorded were 31.95 MPa and 13.41 MPa, respectively. Similarly, at 28 days, specimens with 1.5% PP fiber achieved peak compressive strengths of 47.95 MPa and flexural strength of 17.50 MPa. At 56 days, the trend continued, with the highest strengths reaching 50.61 MPa and 24.12 MPa, respectively. The results, thus, underline the advantage of mixing 1.5% PP fibers with ECC, which has already been indicated as the best ratio for strengthening the compressive and flexural characteristics of the material.

Fig. 1. Experimental program illustrating: (a) ECC mixing and specimen preparation; (b) Casting of cube; (c) Beam specimens; (d) Curing of specimen; (e) Compressive strength testing setup; (f) Bending test setup.

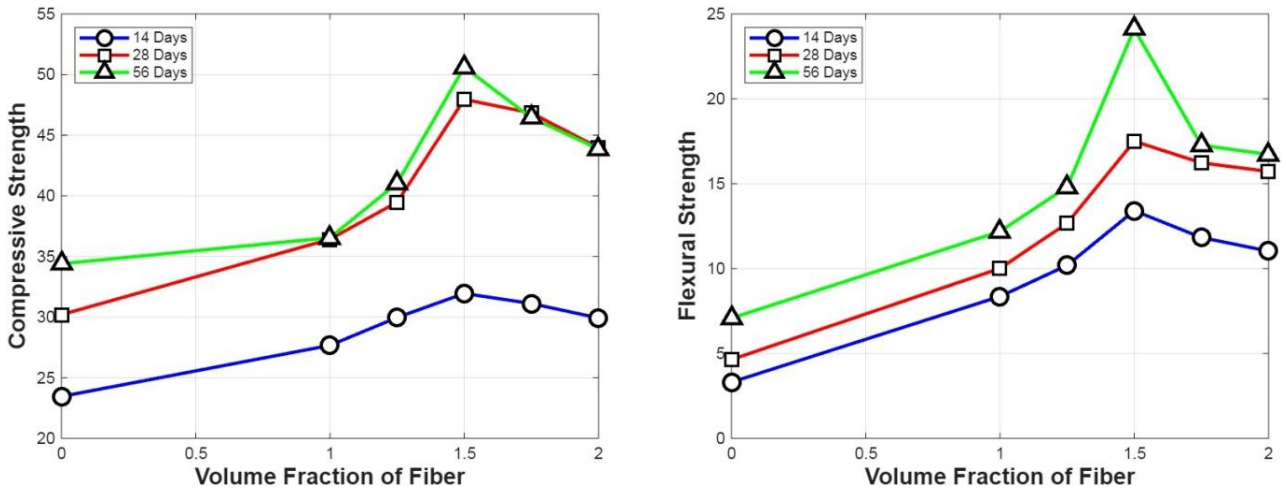

Fig. 2. Compressive and flexural strengths with respect to fiber volume fraction for different curing period.

4. Scanning Electron Microscopy (SEM) Analysis

Scanning electron microscopy (SEM) is an outstanding method that permits the imaging of material surfaces at very high resolution. This technique involves a very fine electron beam that is pointed at the specimen inside the vacuum enclosure. Scanning Electron Microscopy (SEM) analysis was performed using a scanning electron microscope operated at an accelerating voltage of 15 kV, with magnifications ranging from 500x to 5000x. Small fragments obtained from the fractured surfaces of tested specimens were oven-dried, mounted on aluminum stubs, and coated with a thin layer of gold to ensure surface conductivity. The interaction of the electrons with the surface atoms generates various signals, the most common of which being backscattered and secondary electrons, and these signals are the ones used producing the final images. The images produced contain vital information about surface roughness, microstructure, and general morphology of the investigated material represented in Fig. 3.

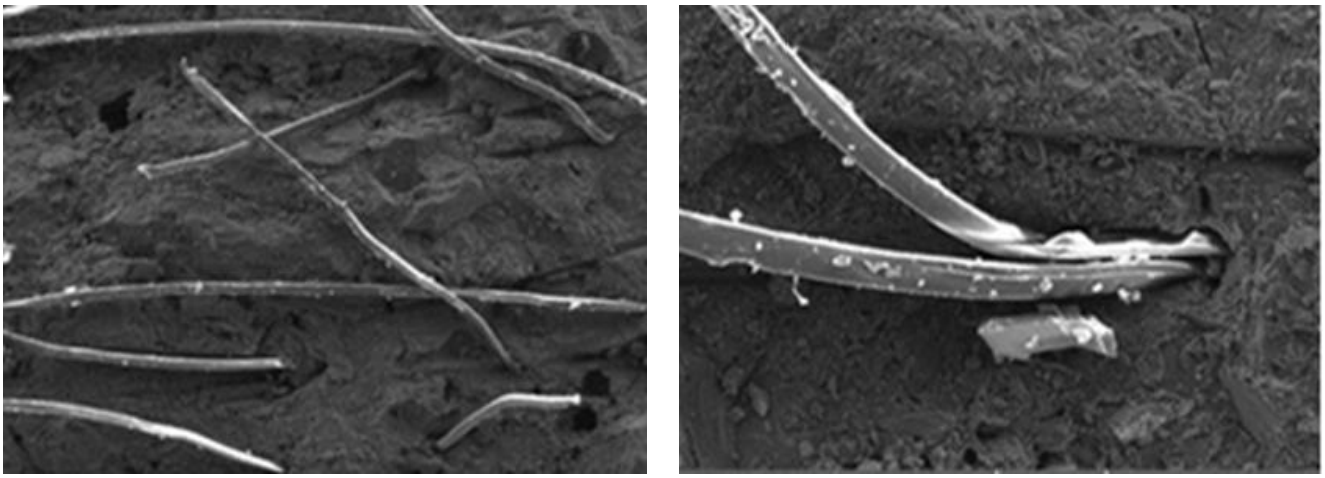

Fig. 3. SEM micrographs of ECC containing 1.5% polypropylene fiber showing fiber–matrix interaction and microstructural morphology (magnification: 2000x; accelerating voltage: 15 kV).

The SEM micrograph very clearly reveals that long and thin polypropylene fibers were embedded in the cement composite. The texture of the surface around the fibers suggests a dense microstructure with a low volume of pores, while the background, which is rough, indicates the presence of sand particles that have been incorporated in the paste. The fibers that are well distributed across the matrix indicate that they are controlling the micro cracks and thus contributing to the overall toughness of the composite. The rough and compact background indicates the existence of hydration products and sand particles, but tiny pores can also be seen. The fibers look to be very well anchored and bonded, and this shows their role in preventing cracks from spreading and thus increasing the overall toughness of the composite.

5. Energy Dispersive X-ray (EDAX) Analysis

Energy X-ray Dispersive Analysis, an also known as EDAX is advanced microscopic analytical method that allows to know the elemental composition of a material. It is usually coupled with electron microscopes like SEM or TEM. Energy Dispersive X-ray (EDAX) analysis was conducted using an attached EDAX detector to determine the elemental composition of the ECC matrix. The analyses were carried out at selected regions of interest to correlate microstructural features with mechanical performance is represented in Fig. 4 and results are shown in Table 4. When the electron beam is concentrated on the specimen, it knocks out an electron from the inner shell, and an electron from the outer shell occupies the site.

The transition of electrons emits an X-ray photon that has an energy corresponding to a particular element. The X-rays are detected and a spectrum is generated by the system, where the peak positions correspond to the types of elements present, and the peak heights indicate their estimated concentrations. EDAX is a non-destructive method that provides both qualitative and quantitative information, therefore, it is very useful for understanding microstructural composition. In ECC, it plays a role in confirming the occurrence and dispersal of materials such as cement, fly ash, and other ingredients that influence the strength and durability traits of the composite.

Table 4. EDAX results of ECC with 1.5% polypropylene fiber.

Element	CO_2	MgO	Al_2O_3	SiO_2	SO_3	K_2O	CaO	Fe_2O_3
Weight (%)	40.37	0.47	3.08	17.61	0.88	0.15	35.23	2.22
Atomic	48.11	0.61	1.58	15.37	0.57	0.08	32.94	0.73

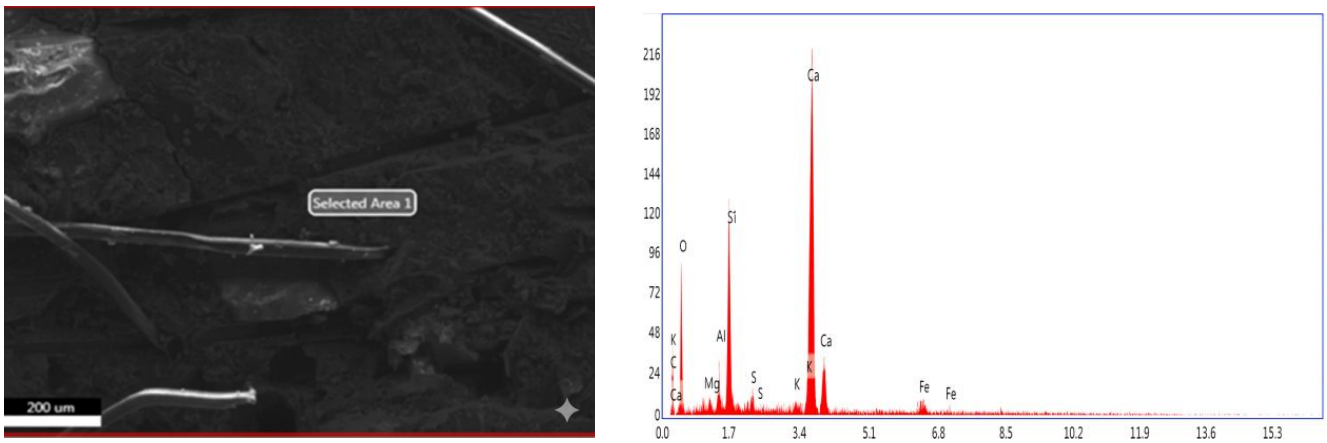

Fig. 4. SEM-EDAX micrograph of ECC with 1.5% polypropylene fiber (Selected Area 1).

6. Artificial Neural Network

Neural networks are computational models guided by the architecture and operation of the human brain. They are designed to manage tasks involving estimation and prediction with multiple input variables. ANN has demonstrated remarkable efficacy in tackling intricate and nonlinear problems. An input layer, one or more Processing layers where learning takes place through weight adjustments, and a prediction layer make up a standard ANN. In accordance with the requirements of the design, the network uses numerous types of activation functions, including tan-sigmoid, log-sigmoid, and ReLU.

As illustrated in Fig. 5(a), the core constituents of a neural network include input values, connection strengths, a summation function, an activation function, and an output. Each neuron receives inputs often derived from external features, which are processed during the training and evaluation phases. These neurons then pass their output as input to the subsequent layer. ANN typically utilizes a feed-forward architecture, where information flows in one direction. Fig. 5(b) illustrates a typical configuration, which corresponds to a multilayer feed-forward neural network. Currently, there is no definitive formula for determining the optimal number of neurons for a specific problem; rather, this is usually identified through empirical testing and iterative refinement.

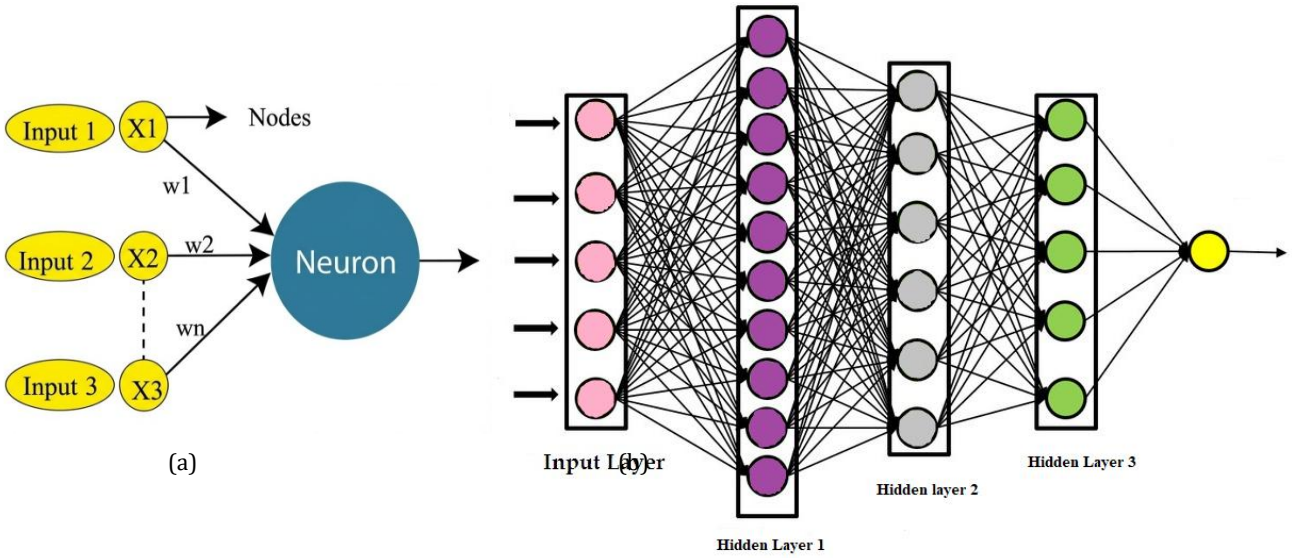

Fig. 5. Structures of (a) Artificial Neuron and (b) Artificial Neural Network.

Since ANN can learn intricate relationships and patterns from data, they are frequently used in prediction tasks across a variety of domains. ANN techniques have been used to predict mechanical properties of concrete based on mix design parameters. Because of their capacity to capture and depict complex and nonlinear connections between the inputs and outputs in the realm of concrete technology, ANN have gained a lot of attention recently.

Prior to ANN training, all input and output variables were normalized using a min–max scaling technique to map the data within a dimensionless range. As a result, the values presented in Table 5 represent normalized inputs rather than raw experimental quantities. For clarity, the original physical ranges of key parameters were as follows: curing age (7, 28 and 56 days), polypropylene fiber volume fraction (0–1.5%), and mechanical strength values expressed in MPa. Data normalization was

adopted to enhance model convergence, prevent numerical dominance of higher-magnitude variables, and improve prediction.

Several ANN models have been developed based on mix design parameters to predict the mechanical properties of concrete. Öztaş et al. (2006) highlighted the capability of NN in estimating both compressive strength and slump of high-strength concrete by utilizing various mix design data reported in the literature. Rofooei et al. (2011) utilized an ANN model to predict the vulnerability of conventional reinforced moment-resisting frames and to estimate the associated seismic damage index. Topçu and Saridemir (2008) employed ANN and fuzzy logic approaches to forecast the compressive strength of concrete incorporating high- and low-lime fly ash at curing ages of 7, 28, and 90 days. Mashhadban et al. (2016) looked into the influence of fibers on self-compacting concrete through ANN modeling, relying on experimental datasets. In a different investigation, Belalia Douma et al. (2017) attempted to find the level of the ANN models' accuracy in predicting the properties of fly ash self-compacting concrete in part replacing cement.

7. Database

The decision about how well a deep learning model is to predict the properties of ECC concrete mainly relies on the quality and quantity of the training data provided to the network. This research focuses on cement, fly ash, fine aggregate, and polypropylene fiber content percentages. 105 ECC samples were gathered from the comprehensive literature survey and the experimental setup from past research (Ahmed et al. 2025; Chethan et al. 2015; Marushchak et al. 2023; Ranjith et al. 2017; Saljoughian et al. 2024). The statistical parameters of the collected data are summarized in Table 5.

Table 5. Statistical measures of the data.

	Max.	Min.	Mean	Mode	Median	STD	Skewness	Kurtosis
Cement	1.00	0.80	0.97	1.00	1.00	0.07	–2.19	2.840
Fly ash/cement ratio	1.50	0.00	0.88	1.50	0.80	0.48	–0.22	–1.190
Crush sand/cement ratio	1.00	0.400	0.671	0.80	0.60	0.176	0.011	–0.776
Water/cement ratio	0.86	0.300	0.463	0.42	0.42	0.138	1.20	1.734
Water reducer/cement ratio	0.70	0.002	0.077	0.084	0.07	0.126	3.930	16.576
Volume fraction	7.50	0.000	1.744	2.00	1.500	1.554	2.026	4.972
Tensile strength	6.00	4.00	4.79	4.00	5.00	0.80	0.27	–1.560
Young's modulus	5.00	1.400	3.382	3.80	3.80	1.230	–0.684	–1.096
Length of fiber	120	5.0	10.038	12.0	10.00	2.283	–0.879	–0.358
Compressive strength	86.20	14.25	40.55	29.50	38.70	12.50	0.960	2.160
Flexural strength	28.40	1.98	13.30	18.90	13.25	6.110	0.067	–0.616

8. Model Training and Testing

Data preprocessing is an essential step prior to ANN training, as it enhances the accuracy and reliability of the predictive model. This step has to do with removing duplicate records, dealing with missing data, and applying normalization or standardization techniques to make sure that all the input features are properly scaled. For the neural network to make a correct prediction about the material properties, it has to first learn using a dataset where different ECC mix components such as cement, fly ash, crushed sand, water, high-range water-reducing admixture, volume fraction of polypropylene fibers, tensile strength, Young's modulus, and fiber length are taken as inputs and the resulting mechanical properties, namely compressive and flexural strengths, are treated as outputs. The back propagation algorithm is used to modify the connection weights and minimize the prediction errors during the training phase, which basically is the most critical phase in the formation of an ANN. A multilayer feed-forward neural network with two hidden layers of 22 and 30 neurons each was built and trained for this research using MATLAB. Training and Testing Plots of ANN model for compressive and flexural strength prediction is displayed in Fig. 6.

A total of 105 experimental data points were considered for model development, where 90 samples were used for training and the remaining 15 samples were set aside for evaluating the model performance. To improve learning efficiency, the connection was adjoined with a nonlinear sigmoid activation function. To determine the optimal model, over 500 different neural network configurations were evaluated. The ANN model performance was evaluated using regression-based statistical metrics, including the coefficient of determination (R^2), root mean square error (RMSE), and mean absolute error (MAE). The dataset was randomly divided into training (70%), validation (15%), and testing (15%) subsets to ensure reliable model generalization. Model effectiveness was assessed by comparing predicted and experimental values on the independent testing dataset (Figs. 7 and 8).

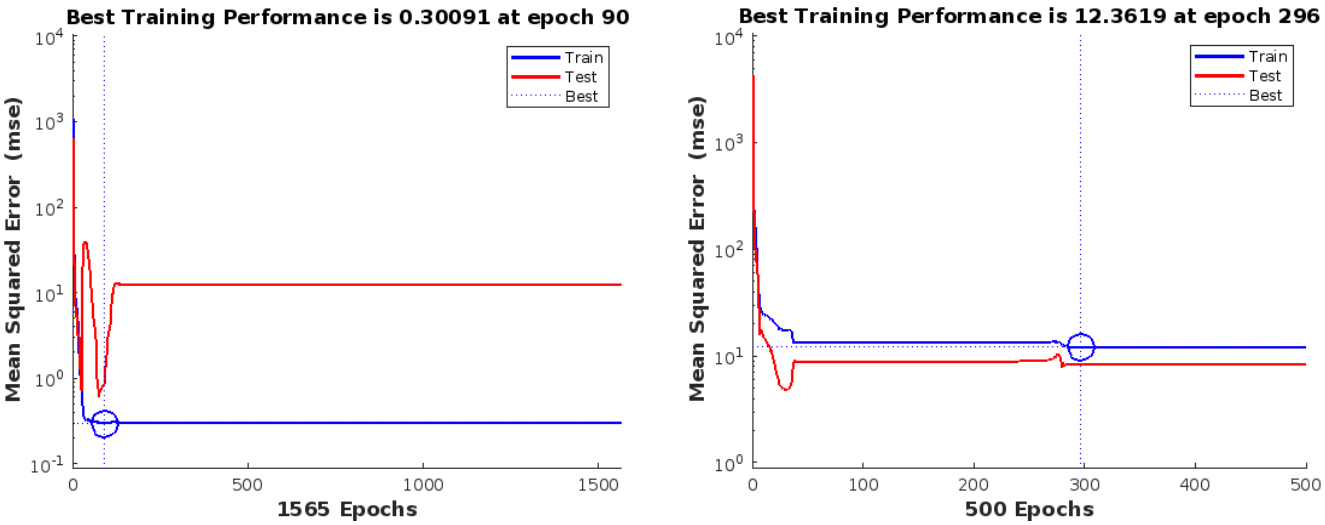

Fig. 6. Training and testing plots of ANN.

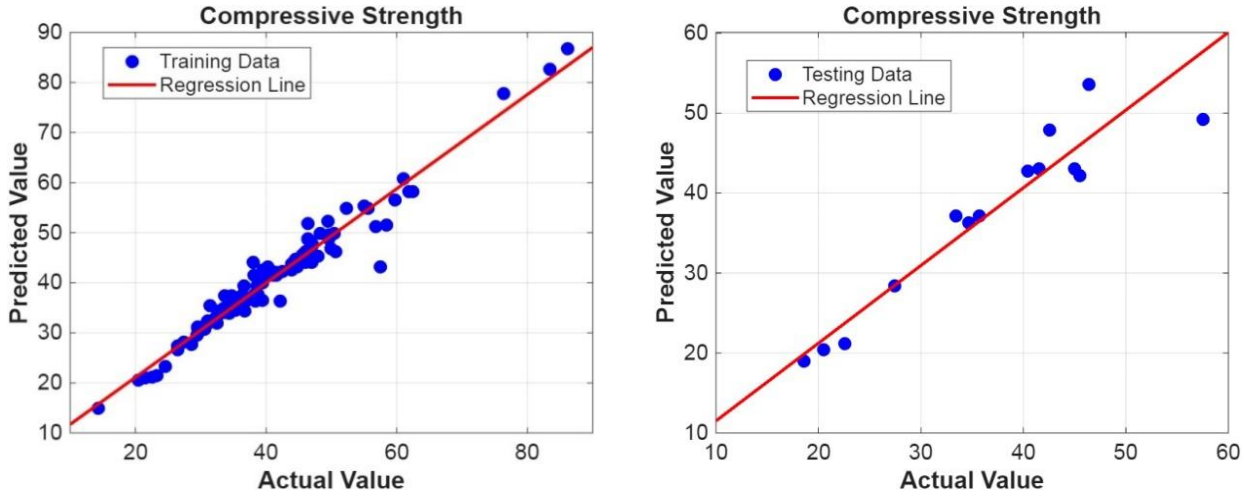

Fig. 7. The assessment of trained and tested data in 28 days compressive strength.

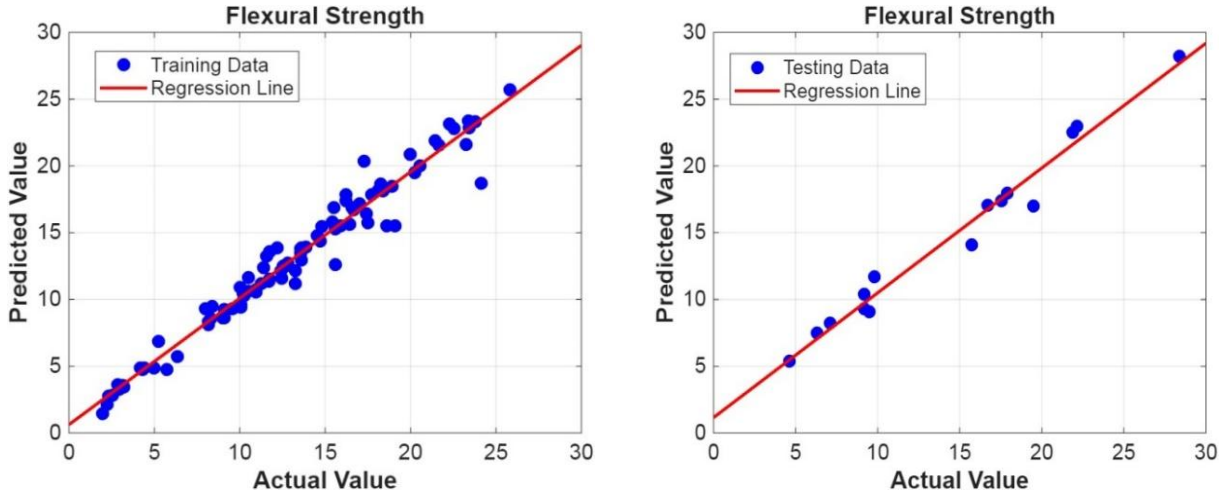

Fig. 8. The assessment of trained and tested data in 28 days flexural strength.

9. Statistical Inference

The accuracy of the predictions was determined using the statistical metrics namely, mean absolute percent error (MAPE), root mean square error (RMSE), and mean absolute error (MAE). The statistical values of RMSE, MAE, and MAPE for the training and testing datasets were displayed in Tables 6 and 7. The highest relative errors for 28-day compressive and flexural strengths during training were recorded as 24.92% and 30.558%, re-

spectively, while the lowest relative errors were only 0.003% and 0.098%. In the testing phase, the maximum relative errors for 28-day compressive and flexural strengths were measured at 15.58% and 19.10%, with the corresponding minimum relative errors being 0.384% and 0.367%.

Table 6. Relative errors of training data.

	Max. relative error (%)	Min. relative error (%)	MAPE (%)	RMSE	MAE	R^2
Compressive strength	24.920	0.0003	4.120	2.675	1.754	0.955
Flexural strength	30.558	0.0980	6.656	1.149	0.735	0.963

Table 7. Relative errors of testing data.

	Max. relative error (%)	Min. relative error (%)	MAPE (%)	RMSE	MAE	R^2
Compressive strength	15.58	0.384	6.409	3.593	2.67556	0.953
Flexural strength	19.10	0.367	8.181	1.119	0.86913	0.975

The histograms in Figs. 9 and 10 show the relative percentage error distribution for the 28 days compressive and flexural strengths. It is worth noting that nearly 70% of the samples were found to have prediction errors not higher than 10%, thus confirming the predicting power of ANN model and reliability in terms of ECC strength parameters. The statistical data demonstrates that, the ANN model has properly learned the relation between input parameters and mechanical properties and it has good generalization ability and high predictive accuracy.

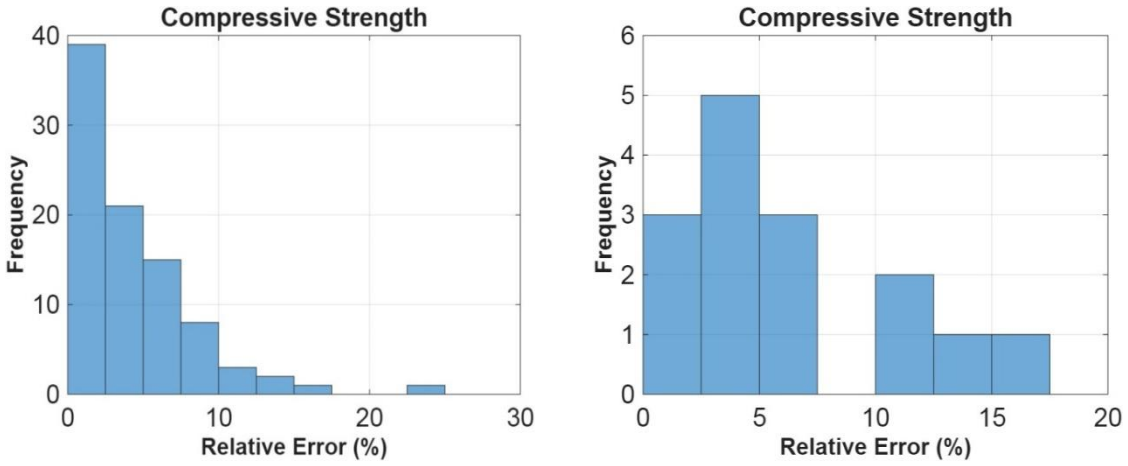

Fig. 9. Histogram of relative error percentage of 28 days compressive strength for training and testing.

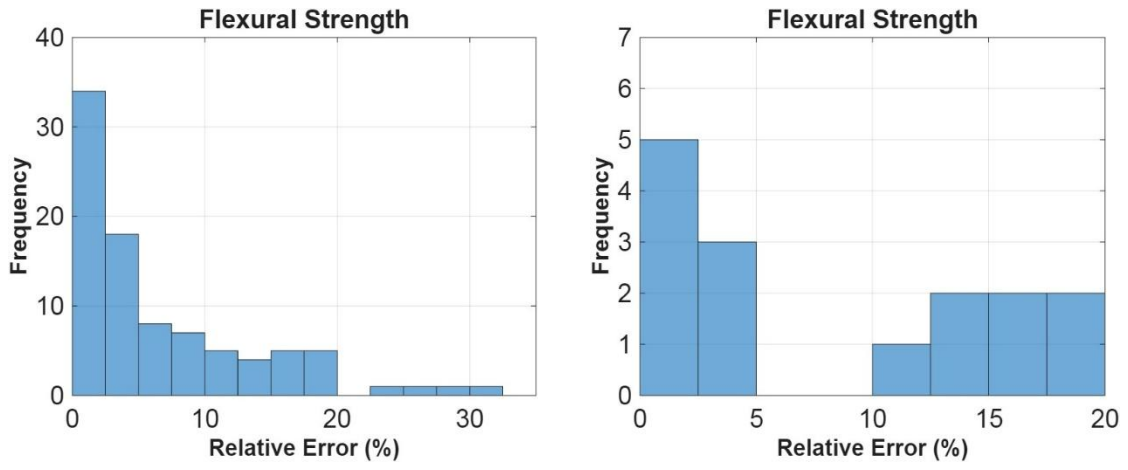

Fig. 10. Histogram of relative error percentage of 28 days flexural strength for training and testing.

10. Results and Discussion

The experimental results demonstrate that the incorporation of polypropylene fibers significantly influences the mechanical performance of engineered cementitious composites. The relationship between compressive strength and polypropylene fiber volume fraction, shown in Fig. 4 indicates that the compressive strength rose slowly but surely with the addition of fiber until optimal fiber content was reached, after which only a slight increase was noted. This pattern suggests that the polypropylene fibers indirectly provide compressive strength by preventing microcracks from forming and spreading instead of by bearing the compressive force. An appreciable increase in flexural strength was observed with increasing polypropylene fiber volume fraction, confirming the effectiveness of fibers under tensile and bending stresses. During three-point bending tests, ECC specimens exhibited multiple fine cracks instead of a single dominant crack, demonstrating the characteristic pseudo strain-hardening behavior of ECC.

The mechanical performance obtained in the present study is consistent with trends reported in the existing ECC literature. Several studies have shown that polypropylene fiber contents in the range of 1.0–2.0% lead to significant improvements in flexural strength and ductility due to effective fiber bridging and multiple microcracking behavior. For instance, ChiaHwan and JianBo (2014) reported optimum PP fiber contents between 1.2% and 1.6%, beyond which fiber agglomeration and workability loss resulted in marginal or reduced strength gains. A similar trend was observed in the present study, where the maximum compressive and flexural strengths were achieved at 1.5% PP fiber content, followed by a slight reduction at higher dosages.

In terms of flexural performance, the 28-day flexural strength of 17.50 MPa obtained in this study at 1.5% fiber content is comparable to the values reported by Marushchak et al. (2023) and Saljoughian et al. (2024) for polypropylene fiber-based ECC systems, confirming the effectiveness of PP fibers in enhancing tensile and bending resistance. The observed multiple fine cracks and stable post-cracking response are also in agreement with the strain-hardening behavior reported in earlier ECC studies.

Regarding predictive modeling, the ANN developed in the present study achieved R^2 values exceeding 0.95 for both compressive and flexural strength prediction, which is comparable to or slightly higher than those reported in recent ANN-based studies on fiber-reinforced and ECC-type composites. For example, Kavya et al. (2022) and Hossain et al. (2024) reported R^2 values in the range of 0.90–0.96 for strength prediction using ANN models. This comparison indicates that the proposed ANN framework provides reliable predictive capability while being specifically tailored to polypropylene fiber-reinforced ECC.

The EDAX analysis of ECC containing 1.5% polypropylene fiber, as presented in Table 4, confirms the presence of major cementitious oxides such as CaO, SiO_2, and Al_2O_3, which play a critical role in hydration reactions and strength development of cement-based materials. Minor oxides such as MgO, SO_3, and K_2O detected in the present study fall within typical ranges reported for cementitious composites and are not considered detrimental at low concentrations. The relatively uniform elemental distribution observed in the polypropylene fiber-reinforced ECC indicates good matrix continuity and compatibility between the fibers and the cementitious phase.

The ANN provide an effective and reliable approach for predicting the compressive and flexural strength of polypropylene fiber-reinforced engineered cementitious composites. The developed multilayer feed-forward model, trained using the back-propagation algorithm, exhibited strong agreement between predicted and experimental strength values for both training and testing datasets. For the training data, the ANN achieved R^2 values of 0.955 and 0.963 for compressive and flexural strength, respectively, with low MAPE values of 4.12% and 6.66%, as summarized in Table 5. In like manner, the R^2 values of 0.953 for compressive strength and 0.975 for flexural strength were obtained for the testing dataset along with MAPE values of 6.41% and 8.18%, respectively in Table 6, which demonstrates great predictive power and excellent generalization performance of the model.

11. Conclusions

According to the data, the addition of 1.5% polypropylene fiber seemed to be the most effective way to improve the mechanical performance of concrete. The dosage offered the highest compressive strength of 31.95 MPa and the highest flexural strength of 13.41 MPa after 14 days of curing, 47.95 MPa and 17.50 MPa after 28 days of curing and 50.61 MPa and 24.12 MPa after 56 days of curing. It can be inferred that polypropylene fiber at a dosage of 1.5% not only enhances the strength of ECC but also serves as a feasible and optimal percentage for mechanical property enhancement.

The microstructural examination strengthened the experimental and modeling results. Scanning electron microscopy uncovered the cementitious matrix to contain polypropylene fibers that had been perfectly embedded, as well as numerous cracks that were very fine but fiber-bridged, thus validating the strain-hardening mechanism typical of ECC. The observed presence of adhered matrix particles on fiber surfaces is a sign of strong fiber-matrix interfacial bonding that leads to better control over cracks and increased ductility. Energy-dispersive X-ray analysis not only verified the existence of pivotal cementitious oxides like CaO, SiO_2, and Al_2O_3 but also revealed a homogeneous elemental distribution in fiber-reinforced specimens, which in turn implies good matrix-fiber compatibility.

The current research provided evidence that Artificial Neural Network is the best choice for the prediction of compressive and flexural strength of polypropylene fiber-reinforced engineered cementitious composites. The multilayer feed-forward ANN constructed and trained by the back-propagation algorithm had almost the same predicted and measured strength values for both the training and testing groups of data. The small prediction inaccuracies suggest that the model has managed to depict the nonlinear connection between the design parameters and the mechanical performance, thus allowing for prompt strength estimation of ECC mixtures that fall within the specified range of the training data.

Acknowledgements
None declared.

Funding
The authors received no financial support for the research, authorship, and/or publication of this manuscript.

Conflict of Interest
The authors declare no potential conflicts of interest with respect to the research, authorship, and/or publication of this manuscript.

Data Availability
The datasets generated and/or analyzed during the current study are not publicly available but are available from the corresponding author upon reasonable request.

AI Assistance
No AI-based tools were used in the preparation of this manuscript.

Author Contributions
All authors made substantial contributions to the conception and design of the study, acquisition of data, analysis and interpretation of data; drafted or critically revised the manuscript for important intellectual content; and approved the final version to be published.

REFERENCES

Ahmed AH, Hübner J, Junger D, Signorini C, Butler M, Liebscher M, Scheffler C, Mechtcherine V (2025). Engineering low clinker strain-hardening cementitious composites (SHCC) using polyethylene and cost-effective polypropylene fibers: An experimental scale-linking analysis. *Materials & Design*, 254, 114051.

Ashwini BT, Kumar YMV, Gowda BSK, Kumar DTN (2024). Prognostication of mechanical properties of banana and jute fiber reinforced concrete using ANN. *Asian Journal of Civil Engineering*, 25(6), 4429-4449.

Belalia Douma O, Boukhatem B, Ghrici M, Tagnit-Hamou A (2017). Prediction of properties of self-compacting concrete containing fly ash using artificial neural network. *Neural Computing and Applications*, 28, 707-718.

Bilim C, Atis CD, Tanyildizi H, Karahan O (2009). Predicting the compressive strength of ground granulated blast furnace slag concrete using artificial neural network. *Advances in Engineering Software*, 40(5), 334-340.

Chethan VR, Gokul SL, Neelaveni SK, Dilip CH (2015). Experimental studies on ECC by using poly propylene fibers. *International Research Journal of Engineering and Technology*, 2(5), 130-136.

ChiaHwan Y, JianBo H (2014). The mechanical behavior of fiber reinforced PP ECC beams under reverse cyclic loading. *Advances in Materials Science and Engineering*, 2014, 1-9.

Demir F (2008). Prediction of elastic modulus of normal and high strength concrete by artificial neural networks. *Construction and Building Materials*, 22(7), 1428-1435.

Fischer G, Li VC (2007). Effect of fiber reinforcement on the response of structural members. *Engineering Fracture Mechanics*, 74(1-2), 258-272.

Han B, Ding S, Yu X (2015). Intrinsic self-sensing concrete and structures: A review. *Measurement*, 59, 110-128.

Haque MA, Dai JG, Zhao XL (2024). Magnesium cements and their carbonation curing: A state-of-the-art review. *Low-Carbon Materials and Green Construction*, 2(1), 2.

Hossain S, Uddin MN, Yan K (2024). Prediction of the mechanical performance of polyethylene fiber-based engineered cementitious composite (PE-ECC). *Low-Carbon Materials and Green Construction*, 2(1), 9.

Kavya BR, Naveen Kumar SM, Rahul N, Shrikanth AS (2025). Comparative study on the mechanical properties of geopolymer concrete containing GGBS and fly ash using experimental analysis and artificial neural network. *Asian Journal of Civil Engineering*, 26(8), 3233-3244.

Kavya BR, Sureshchandra HS, Prashantha SJ, Shrikanth AS (2022). Prediction of mechanical properties of glass and basalt fiber reinforced concrete using ANN. *Asian Journal of Civil Engineering*, 23(6), 877-886.

Li VC, Wang S, Wu C (2001). Tensile strain-hardening behavior of polyvinyl alcohol engineered cementitious composite (PVA-ECC). *ACI Materials Journal*, 98(6), 483-492.

Liu D, Yu J, Qin F, Zhang K, Zhang Z (2023). Mechanical performance of high-strength engineering cementitious composites (ECC) with hybriding PE and steel fibers. *Case Studies in Construction Materials*, 18, e01961.

Marushchak U, Sydor N, Margal I (2023). Impact of polypropylene fibers on the properties of engineered cementitious composites. In: Blikharskyy Z, editor. *EcoComfort 2022*. Springer, Cham, Switzerland, 262-269.

Mashhadban H, Kutanaei SS, Sayarinejad MA (2016). Prediction and modeling of mechanical properties in fiber reinforced self-compacting concrete using particle swarm optimization algorithm and artificial neural network. *Construction and Building Materials*, 119, 277-287.

Michelini E, Ferretti D, Miccoli L, Parisi F (2023). Autoclaved aerated concrete masonry for energy efficient buildings: State of the art and future developments. *Construction and Building Materials*, 402, 132996.

Nehdi M, El Chabib H, El Naggar MH (2001). Predicting performance of self-compacting concrete mixtures using artificial neural networks. *ACI Materials Journal*, 98, 394-401.

Odeyemi SO, Sholagberu MS, Atoyebi OD, Adesina A (2025). Engineered cementitious composites (ECC): A review on properties, design, sustainability and applications. *Discover Concrete and Cement*, 1(1), 9.

Oreta AWC, Kawashima K (2003). Neural network modeling of confined compressive strength and strain of circular concrete columns. *Journal of Structural Engineering*, 129(4), 554-561.

Öztas A, Pala M, Özbay E, Kanca E, Çağlar N, Bhatti MA (2006). Predicting the compressive strength and slump of high strength concrete using neural network. *Construction and Building Materials*, 20(9), 769-775.

Ranjith S, Venkatasubramani R, Sreevidya V (2017). Comparative study on durability properties of engineered cementitious composites with polypropylene fiber and glass fiber. *Archives of Civil Engineering*, 63(4), 83-101.

Riaz RD, Malik UJ, Shah MU, Usman M, Najam FA (2023). Enhancing seismic resilience of existing reinforced concrete building using non-linear viscous dampers: A comparative study. *Actuators*, 12(4), 175.

Rofooei FR, Kaveh A, Farahani FM (2011). Estimating the vulnerability of the concrete moment resisting frame structures using artificial neural networks. *International Journal of Optimization in Civil Engineering*, 3, 433-448.

Saljoughian A, Bahmani H, Ansari Z, Jafari N, Mostofinejad D (2024). An eco-friendly ECC with high slag and polypropylene fiber content for high-tensile strain applications. *Journal of Building Engineering*, 91, 109726.

Shabakhty N, Karimi HR, Bakhtiary AY (2024). Statistical evaluation of fracture and mechanical performance of engineered cementitious composites (ECC), containing different percentages of glass, polypropylene, polyvinyl-alcohol fibers, and fly ash. *Construction and Building Materials*, 417, 135247.

Topcu IB, Saridemir M (2008). Prediction of compressive strength of concrete containing fly ash using artificial neural networks and fuzzy logic. *Computational Materials Science*, 41(3), 305-311.

Uddin MN, Al-Amin, Hossain S (2024). Revolutionizing engineered cementitious composite materials (ECC): The impact of XGBoost-SHAP analysis on polyvinyl alcohol (PVA) based ECC predictions. *Low-Carbon Materials and Green Construction*, 2(1), 11.

Wang S, Li VC (2006). Polyvinyl alcohol fiber reinforced engineered cementitious composites: Material design and performances. In: Fischer G, Li VC, editors. *International RILEM Workshop on High Performance Fiber Reinforced Cementitious Composites in Struc-*

tural Applications. RILEM Publications SARL, Bagneux, France, 65-73.

Yu J, Lin J, Zhang Z, Li VC (2015). Mechanical performance of ECC with high-volume fly ash after sub-elevated temperatures. *Construction and Building Materials*, 99, 82-89.

Zhu H, Yu K, Li VC (2021). Sprayable engineered cementitious composites (ECC) using calcined clay limestone cement (LC3) and PP fiber. *Cement and Concrete Composites*, 115, 103868.

Challenge Journal of CONCRETE RESEARCH LETTERS

Research Article

The effect of tincal-added cement on the attenuation of gamma rays and neutrons

Hayrettin Eroğlu [a,*], İhsan İş [b], Mustafa Engin Kocadağistan [c], Ali Gürol [d]

[a] *Department of Chemical Engineering, Erzurum Technical University, 25050 Erzurum, Türkiye*
[b] *Department of Biomedical Engineering, Erzurum Technical University, 25050 Erzurum, Türkiye*
[c] *Department of Metallurgical and Materials Engineering, Atatürk University, 25240 Erzurum, Türkiye*
[d] *Department of Physics, Atatürk University, 25240 Erzurum, Türkiye*

ABSTRACT

The increasing use of ionizing radiation in nuclear energy, medical diagnostics, radiotherapy, and industrial applications necessitates the development of effective and sustainable radiation shielding materials. In this study, the gamma-ray and fast neutron attenuation properties of cement-based composites incorporating anhydrous tincal obtained from the Balıkesir–Bigadiç region were experimentally investigated. Tincal was dehydrated at 650 °C to remove crystal water and added to Portland cement at ratios of 1%, 5%, and 10% by weight. The research includes gamma and neutron attenuation experiments, compressive strength tests, SEM, and XRD analyses under different parameters. Based on the evaluation of the obtained results, it was concluded that tincal has no effect on gamma attenuation. In contrast, neutron attenuation performance improved significantly with increasing tincal content. However, compressive strength values decreased significantly in tincal-added samples, which presents limitations for structural applications. It is thought that it cannot be used as a load-bearing element in construction, but rather as a cladding material. When considered overall, the effectiveness of the material in terms of neutron attenuation suggests potential applications in the fields of nuclear safety, radiation protection and construction materials. It is predicted that radiation-attenuating composites developed with natural minerals could contribute to the widespread adoption of environmentally friendly material technologies aimed at minimizing toxic waste production.

ARTICLE INFO

Article history:
Received – December 23, 2025
Revision requested – January 22, 2026
Revision received – February 22, 2026
Accepted – March 2, 2026

Keywords:
Cement
Tincal
Boron
Radiation
Neutron attenuation
Gamma attenuation

Citation: Eroğlu H, İş İ, Kocadağistan ME, Gürol A (2026). The effect of tincal-added cement on the attenuation of gamma rays and neutrons. *Challenge Journal of Concrete Research Letters*, 17(2), 135–146.

1. Introduction

Radiation can be defined as the emission of energy from a source in the form of particles or electromagnetic waves that travel in straight lines. Its utilization has been increasing in a variety of fields, ranging from medical applications to industrial operations (Sehhatigdiri 2014). Radiation is generally categorized into two distinct classifications: ionising and non-ionising. It is well established that exposure to ionising radiation, such as alpha and beta particles, X-rays, and gamma rays, poses a significant risk to human health.

The use of X-rays and gamma rays, in particular, for diagnostic and therapeutic purposes in medicine, such as radiation oncology, nuclear medicine, cardiology, and radiology, is quite widespread. Furthermore, nuclear energy is employed as a substantial source of electrical energy generation. Radiation is also utilized in industrial applications across various regions. Furthermore, radiation is utilized in the destruction of microorganisms during the sterilization process. Radiation is employed in the preservation of foodstuffs, the extension of their shelf life, and the eradication of potentially harmful microorganisms. Radioisotopes find application in a variety

* *Corresponding author*. E-mail address: hayrettin.eroglu@erzurum.edu.tr (H. Eroğlu)
ISSN: 2548-0928 / DOI: https://doi.org/10.20528/cjcrl.2026.02.005

of fields, including materials analysis, archaeological research, and the monitoring and control of industrial processes. A variety of legal permits related to radiation are utilized in research settings. Radiation techniques and methods are utilized in research across a wide range of disciplines, including physics, chemistry, biology, archaeology, and materials science. Radiation safety and control are of crucial importance (Karakoç 2024; Yılmaz 2011).

Gamma rays, which are electromagnetic radiation emitted during transitions between nuclear energy levels, have much higher energy and penetration capability than alpha or beta particles. For this reason, high-density materials are generally used for gamma-ray shielding.

As the use of radiation continues to increase, measures to protect against its potentially harmful effects have become imperative. Ionizing radiation has been demonstrated to induce DNA damage, cellular malfunctions, acute effects at high doses, and stochastic effects such as cancer at lower chronic exposures (Eroglu 2009; Görpe 1992). There are three fundamental methods of protection against the harmful effects of radiation: time, distance and shielding.

- Time: In long-term exposures, the exposure dose increases as time increases, resulting in a directly proportional effect. Therefore, the time spent in the environment near the source should be kept as short as possible. Reducing the exposure time is important for direct exposures, but keeping the exposure time short is even more crucial for fluoroscopy due to the high dose (Eroglu 2009; Keskin 2024).
- Distance: The dose exposure increases as one approaches the radiation source. Radiation intensity is inversely proportional to the square of the distance, a phenomenon known as the inverse square law. Appropriate warnings and signs should be installed in areas close to the radiation source (Eroglu 2009; Keskin 2024).
- Shielding: Materials placed between the radiation source and the exposed area, thereby reducing its intensity, are referred to as shielding materials. Protection is achieved by creating a barrier with materials that prevent the passage of the radiation source. Shielding should be made with materials and thickness appropriate to the type, energy, and intensity of each radiation. Lead shielding should be used to protect against ionizing radiation. Special lead-lined extraction rooms, lead barriers, and leaded personal protective equipment can effectively block ionizing radiation (Eroglu 2009; Keskin 2024). In addition, Yılmaz (2011) investigated the gamma attenuation potential of tincal-based concrete, an alternative to lead shielding.

Concrete is one of the most widely used construction materials owing to its engineering performance, cost efficiency, and durability. Nevertheless, cement-based materials are increasingly being reconsidered from a sustainability perspective because Portland cement production is associated with considerable environmental impacts. Accordingly, mineral additives, industrial by-products, nano-additions, and alternative binder systems have attracted growing attention for improving the mechanical, durability-related, and functional performance of cement-based composites (Abutaha and Çelik 2025; Tarhan and Tarhan 2025; Srivastava et al. 2025). These materials can be tailored through binder composition, particle grading, and admixture selection; however, their effectiveness strongly depends on chemical compatibility, replacement level, particle packing, and their influence on hydration-related products (Al-Safi et al. 2025; Turan et al. 2025; Shaheen et al. 2025). Therefore, when natural mineral additives are incorporated into cementitious systems for specific functional purposes, such as radiation shielding, their contribution must be evaluated together with their possible effects on mechanical integrity and material performance.

Tincal, also known as borax, a boron mineral, appears colorless and transparent in its pure form. However, in areas where it is layered with clay and in fine-grained form, it can turn pale pink, yellowish-orange, and gray under the influence of external substances (Durak 2011). A review of scientific literature suggests that boron oxide may have radiation shielding properties. Studies have shown that:

In a previous study, Erdoğan (1998) produced different types of cement by adding ground boron minerals to cement and examined their physical and mechanical properties. In addition, an evaluation was conducted of the shielding potential of boron minerals when employed in concrete, utilizing theoretical approaches. In light of the findings, it was concluded that boron mineral addition exerted a favorable influence on shielding performance (Erdoğan 1998).

Kharita et al. (2008) investigated the attenuation coefficients of concrete produced from aggregates commonly used in Syria for gamma rays (^{137}Cs and ^{60}Co isotopes) and neutrons (Am-Be source). The concretes were produced by mixing black beach sand, hematite, dolomite, and serpentine with beach sand in varying proportions. The results showed that concretes containing hematite were more effective in providing protection against both types of radiation.

Experiments were conducted by Henrie (1962) on concrete samples containing boron oxide, colemanite, and boron, and the radiation shielding capacity of the concrete's chemical components was analyzed. The study demonstrated that boron-added heavyweight concretes offered advantages not only in terms of effective shielding performance but also in terms of cost.

In a study conducted by Sychev (1967), the shielding potential of concrete samples prepared using hematite minerals against neutrons emitted from a beryllium source were investigated. In this context, evaluations were made considering five different neutron energy levels ranging from 170 MeV to 660 MeV (Sychev 1967).

Erdoğmuş et al. (2011) investigated the effects of adding different mixtures of colemanite concentrator waste and Karabük slag to Portland cement on the mechanical properties of the cement. Additionally, the effect of adding different ratios of Na_2CO_3 to Portland cement on the mechanical properties of the cement were investigated. The colemanite concentrator waste, slag, gypsum, and clinker used in the experiments were chemically analyzed using XRF. The mechanical properties examined in the study included compressive strength, setting time, volumetric expansion, and normal consistency water.

The findings were compared with Turkish Standards (TS), and the research concluded that colemanite concentrator waste and Karabük slag can be utilized appropriately in cement production.

Uğurlu et al. (2004) investigated the usability of solid waste, called "clay paste," generated during the concentration of borax mineral during tincal production, in cement. For the cement study, ground clay paste waste was added to Portland cement mortar at different ratios, and fresh and hardened concrete tests were conducted on the resulting mortar samples. These tests investigated the behavior of clay paste in cement and its effect on cement mortar samples. The results were compared with reference samples and Turkish Standards (TS). The results indicate that borax-containing clay paste waste can be used as a retarder in mortar or concrete, and that low percentages of clay paste waste can increase the impermeability of concrete.

Akkurt et al. (2010) conducted a study using heavyweight concretes produced using barite and lead. They measured linear attenuation coefficients using radioactive sources with energies of 0.662 MeV, 1.173 MeV, and 1.332 MeV using a NaI(Tl) detector. The results were compared with XCOM data. The results revealed that barite and barite-added heavyweight concretes are good gamma-ray absorbers, but their shielding properties are lower than those of lead.

Korkut et al. (2012) carried out a theoretical and experimental investigation in order to ascertain the neutron attenuation properties of colemanite, ulexite and tincal. The researchers discovered that the attenuation of neutrons in these materials is predominantly determined by the density of boron atoms within them. This is due to the fact that boron, particularly the ^{10}B isotope, exhibits a high thermal neutron capture cross-section. The total macroscopic neutron cross sections, denoted by Σ, exhibited a systematic increase with increasing boron content, thereby confirming the predominant role of boron in neutron attenuation.

A study published by Yang et al. (2024) investigated the neutron shielding performance of various boron-containing particles within aluminum-based composites for proton therapy and boron neutron capture therapy (BNCT) applications using Monte Carlo simulations, and showed that increasing boron content significantly improved neutron attenuation efficiency.

Furthermore, Kim et al. (2025) found that high-density boron nitride nanotube (BNNT) composites provide effective shielding against solar-space radiation; this study demonstrates that BNNTs represent a step forward in both mechanical and neutron shielding performance.

In addition, another study by Kiani et al. (2025) addresses the design of multifunctional polymer-nanocomposites and reveals that nanodispersion of boron carbide improves neutron shielding properties.

When boron ore is used in an anhydrous form, the boron compound directly participates in chemical reactions, resulting in lower energy consumption and improved process efficiency. Anhydrous boron exhibits higher chemical activity, enabling more controlled reactions, reduced processing time, and lower overall costs. In contrast, hydrated boron minerals may release crystal water abruptly during heating, leading to foaming, cracking, and volume expansion, which can cause defects in products, particularly in glass, ceramic, and metallurgical applications. The anhydrous form significantly minimizes these risks. From a logistical perspective, crystal water represents unnecessary mass and increases transportation and storage costs. Anhydrous boron ores are lighter, more stable, and less sensitive to moisture. Moreover, industrial processes require water to be introduced separately and in a controlled manner; the uncontrolled presence of crystal water can negatively affect reaction balance, viscosity, and melting behavior. Use of Anhydrous Boron in Cement; in cement systems, boron compounds act as strong setting retarders. When hydrated boron is used, the sudden release of crystal water disrupts cement hydration, causing excessive and unpredictable setting delay. The use of anhydrous boron provides a more predictable and controllable setting behavior. Cement hydration primarily involves the reaction of C_3S and C_2S phases with water. Hydrated boron minerals introduce irregular water into the system, delay C–S–H gel formation, and reduce early-age strength. Anhydrous boron enables precise control of the water-to-cement ratio, leading to a more homogeneous microstructure and improved compressive strength. In addition, anhydrous boron is more compatible with standards such as TS EN and ASTM, facilitating quality control (Jiri et al. 2014; Davraz 2010; Özdemir and Öztürk 2003; Olgun et al. 2007; Filazi et al. 2022).

The present study is concerned with the preparation of tincal-added cement samples, the determination of their physical and mechanical properties, and the experimental investigation of their X- and gamma-ray and neutron attenuation capacity.

2. Materials and Methods

2.1. Materials

In this study, tincal ($Na_2B_4O_7{\cdot}10H_2O$), a primary boron mineral, was used to investigate its neutron beam attenuation properties. The cement used in the experiments was Portland cement (CEM I 42.5 R) supplied by the Aşkale Cement Factory. No additional analysis was performed, as commercially available cement with a known composition was used.

Tincal, a natural borate mineral with a high boron content, was obtained from the Balıkesir-Bigadiç/Türkiye region. Before being used in experimental studies, it underwent preliminary preparation processes such as grinding, drying, and sieve analysis. The tincal ore to be used in the heat treatment experiments was first reduced to 500 grams by taking 1 kg samples from 2 kg of run-of-mine ore using appropriate sampling methods as preparation for particle size reduction. Crushing was performed in a jaw crusher to reduce the particle size to 250 microns (60 mesh), and grinding was performed in a ball mill to obtain a particle size of 45 microns (325 mesh). After obtaining samples with the desired particle size, they were subjected to sieving in 200 g portions. The tincal ore samples were sieved using a mechanical sieve, and the resulting samples were prepared for heat

treatment experiments. The reason for using a particle size of 45 microns is to ensure a similar size to the cement used and to obtain a more homogeneous composition during mixing. Following these processes, the samples were reduced to a particle size of 45 μm and finally heat-treated at 650 °C to remove the crystal water, resulting in anhydrous sodium tetraborate.

The chemical analysis of the ore was determined at Atatürk University DAYTAM using the XPS method. Using the data obtained from the XPS results, the amounts of B_2O_3, H_2O, Na_2O, and CaO in the ore composition were compared and verified with the stoichiometrically calculated amounts and the analysis results of the ore source (Table 1). According to XPS and chemical analysis results of tincal ore, it was determined that tincal contains 47.12% H_2O. As a result of weight difference calculations, H_2O content was reduced to 1% after heat treatment and used in experiments.

Table 1. XPS analysis results of tincal ore.

Compound	Tincal (%)
B_2O_3	36.65
Na_2O	16.23
H_2O	47.12

2.2. Methods

2.2.1. Production of concrete

The concretes examined in this study were produced at the Civil Engineering Department Laboratory of Erzurum Technical University. Three types of concrete were produced in this study: standard concrete and tincal-added concrete. First, cement-only samples were prepared for comparison. Then, 1%, 5%, and 10% tincal were added to each cement sample, sequentially and separately. The water/binder ratio was set at 0.20 in the experiments. The temperature of the sample was measured with a digital thermometer, and the mixing water temperature was determined to be between 25-30 °C. The prepared samples were placed in 5x5x5cm cube sample molds. The samples were kept in their molds for 24 hours and then removed from the molds. During the curing process, the samples were maintained in a constant temperature environment (24 °C), and the ambient temperature and relative humidity were regularly monitored with a digital thermometer. The standard used for determining the setting time is TS EN 196-3 (2016), and the experiments were carried out according to this standard.

2.2.2. Unconfined pressure test

The compressive strength of the concrete produced within the scope of this study was measured at the Department of Civil Engineering, Erzurum Technical University (Fig. 1). Experimental studies were carried out in accordance with the TS EN 12390-3 (2010) standard, and compression was applied to the samples with a constant loading rate until the maximum load capacity was reached (TS EN 12390-3 (2010), is an official standard that specifies the methods of compressive testing performed to measure the strength of concrete). The test sample was placed between the loading head of the testing machine and the test head, and care was taken to ensure that the samples were placed perpendicular to the direction of concrete pouring. The samples were placed centrally on the lower loading head of the machine. The highest load read from the indicator was recorded, and the compressive strength was calculated using the following formula (Uzbaş 2019).

$$\sigma = \frac{P}{A} \tag{1}$$

Here, compressive strength (σ) is the ratio of the maximum load (P) the sample carries at the moment of fracture to the cross-sectional area (A) subjected to compression.

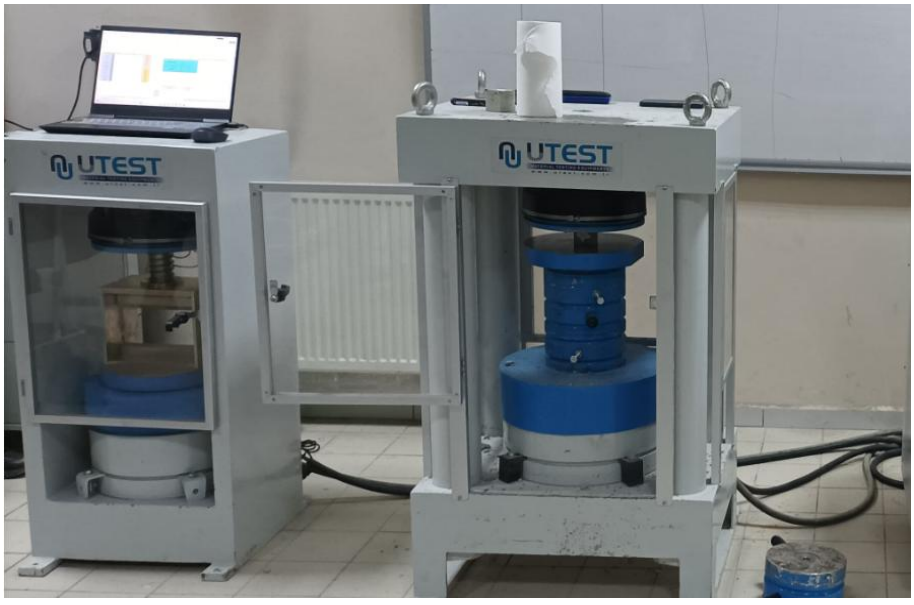

Fig. 1. Unconfined pressure testing apparatus.

2.2.3. Gamma measurements

The experimental measurements undertaken in relation to the attenuation coefficient of the concrete produced as part of the study were conducted at the High Energy Spectroscopy Laboratory, which is housed within the Physics Department at Atatürk University's Faculty of Science. The experimental setup utilized in the study is illustrated in Fig. 2. In the experiment, the VEX (variable energy source) and Ba-133 radioisotope were utilized as the source. In the experiments utilising VEX, the distances between the source and the sample, and between the sample and the detector, were 4.0 cm and 6.0 cm, respectively. The live time in all measurements was set to 1800 s in order to obtain sufficient counting statistics. The Rb, Mo, Ag and Tb K X-rays, as well as the 59.54 gamma rays, are emitted from Am-241 radioisotopes and subsequently scattered elastically from a Cu foil on a VEX source were used in the calculations. The Ba-133 source has a specific activity of approximately 2.73 mCi, emitting gamma rays with energies of 53.155 keV, 81 keV, 276.39 keV, 302.85 keV, 356.01 keV, and 385.851 keV. The distances between the source and the sample, and between the sample and the detector, were 10 cm and 6 cm, respectively.

The intensity of a photon flux, I_0, decreases with increasing thickness, t, of an absorbing material. The decrease in intensity is described by the Lambert-Beer law (Yılmaz 2011) as the linear attenuation coefficient (LAC), given by the following equation:

$$\mu = -\frac{1}{t}\ln\left(\frac{I}{I_0}\right) \quad (\text{cm}^{-1}) \tag{2}$$

However, the mass attenuation coefficient (μ/ρ), defined as the ratio of the linear attenuation coefficient (μ) to the sample density (ρ) and does not change depending on the phase of the material, is more commonly used. The mass attenuation coefficients (MACs) are determined using the intensity values measured experimentally in the experimental geometry shown in Fig. 2 from the equation:

$$\left(\frac{\mu}{\rho}\right) = -\frac{1}{\rho t}\ln\left(\frac{I}{I_0}\right) \tag{3}$$

where ρt is called the mass thickness (g/cm^2). The unit of the mass attenuation coefficients is cm^2/g.

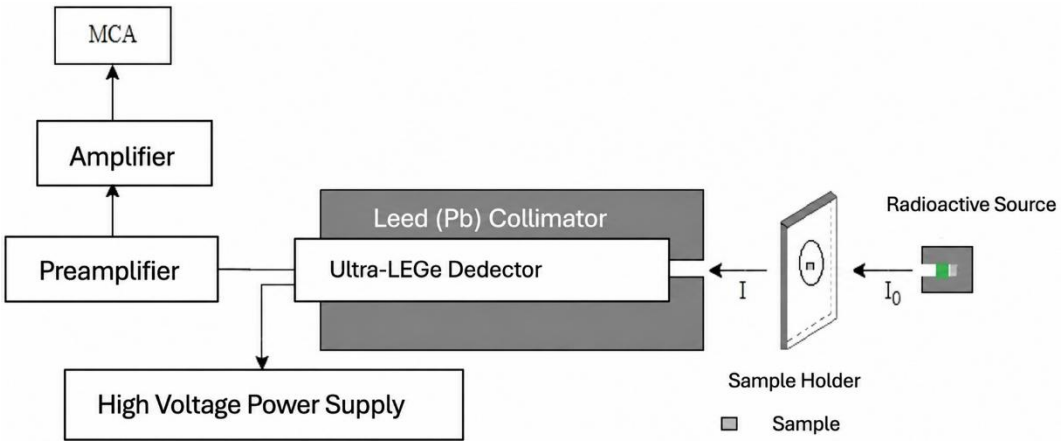

Fig. 2. Experimental setup for gamma ray attenuation.

2.2.4. Neutron attenuation experiments

The experimental measurements undertaken in relation to the attenuation coefficient of the concrete produced as part of the study were conducted at the High Energy Spectroscopy Laboratory, which is housed within the Physics Department, Faculty of Science, Atatürk University.

The measurement of the neutron absorbed dose rate was conducted using a ^{241}Am/Be fast neutron source, which emits 2–11 MeV neutrons. The Canberra NP100B-BF_3 gaseous neutron detector and the Canberra ADM606 series of digital rate meters (RADACs) were utilized in the experiments. The experimental set-up for neutron dose rate measurements is illustrated in Fig. 3. A comprehensive explanation of the properties of the neutron source, detector, and experimental set-up is provided by Korkut et al. (2012).

Neutron experiments are evaluated experimentally by using

$$\Sigma_t = -\frac{1}{Bt}\ln\left(\frac{I}{I_0}\right) \tag{4}$$

where t is thickness of the sample (cm), B is the buildup factor (equal to 5 for Am-Be fast neutron source) Σ_t is the macroscopic removal cross-section which is a measure of the neutron shielding ability for the mean energy of neutron flux having incident dose rate I_0 (μSv/h) and I is dose rate of the transmitted neutron flux (μSv/h) (Wang et al. 2015).

The effective removal cross-section, $\sum R$ (cm^2/g), is a measure of the probability of a fast or fission energy neutron's first collision with the shielding material it faces (Singh and Badiger 2014). The value of $\sum R$ can be calculated by dividing $\sum_t$ by density ρ for an element and evaluated by the mixture rule for a compound or mixture, theoretically. Besides, the effective removal cross-section, $\sum R$ (cm^2/g) is experimentally given by

$$\Sigma R = \frac{\Sigma_t}{\rho} = -\frac{1}{B\rho t}\ln\left(\frac{I}{I_0}\right) \tag{5}$$

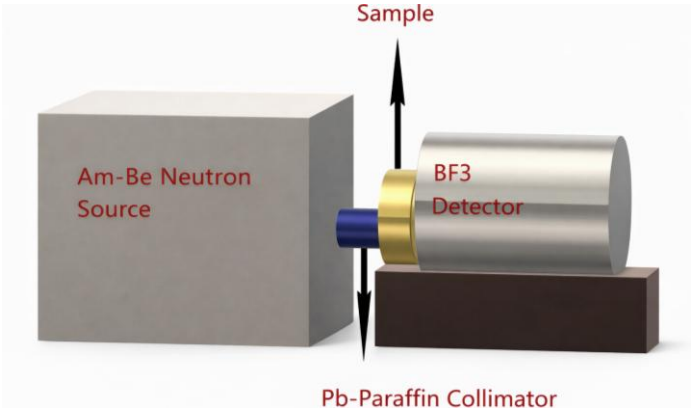

Fig. 3. Experimental setup for neutron attenuation experiments.

2.2.5. X-ray diffraction (XRD)

XRD analysis of the concretes produced within the scope of this study was measured using a GNR-Explorer device at High Technology Application and Research Center (YUTAM), Erzurum Technical University.

Calculating compound or phase compositions from oxide components can be accomplished using both theoretical and experimental methods. X-ray diffraction (XRD) has been successfully used for many years to determine mineral concentrations. Since 1958, various studies have been conducted on the use of XRD analysis in determining cement compositions (Winter 2012).

Concrete, a composite material, exhibits complex behavior due to its high cement content. Microstructural differences from the cement paste have been observed, particularly at the cement-aggregate interface. The formation of new compounds as a result of exposure to various aggressive environmental conditions and the formation of characteristic structures during the natural deterioration processes of concrete have made X-ray diffraction (XRD) analysis an important and essential method for investigating service life, durability, and related product performance (Ramachandran et al. 2000).

2.2.6. Scanning electron microscope (SEM)

SEM/EDX (Scanning Electron Microscopy with Energy Dispersive X-ray Spectroscopy) analyses were performed using FEI QUANTA FEG 250 devices at Erzurum Technical University, High Technology Application and Research Center (YUTAM). SEM images were acquired under the following conditions: kV: 15, Magnification: 10000, Takeoff: 30.1, Amp. Time (µs): 7.68, Resolution: (eV)125. SEM, thanks to its equipment that allows X-ray microanalysis and digital image analysis, enables three basic processes to be carried out on a sample. These processes are; examination of the microstructure of the sample through SEM images, determination of chemical components through X-ray microanalysis, and dimensional measurements through digital image analysis (Winter 2012).

A dosage analysis was performed using SEM and XRD because, according to the analysis results, XRD analysis was performed on the sample that yielded the most suitable result. It is known that the microstructure results cannot be generalized to other dosages.

2.2.7. Heat treatment

The use of boron in the cement sector has become widespread, but boron ores are suitable for use up to a maximum of 2% water content (Kocadağistan and Arslan 2024). Tincal was dewatered in a muffle furnace at 650 °C for 6 hours. Following the heat treatment, the chemically bound water removal rate was calculated by taking the weight differences of tincal ores. According to the calculations, 98% water removal was achieved in both ores (Ataç 2024).

3. Research Findings and Discussion

Cement and tincal mixtures with 1%, 5%, and 10% dehydrated tincal were investigated, and their gamma and neutron attenuation values are given below. Analysis of these values revealed that the best values were obtained with 5% tincal, and SEM and XRD analyses were performed based on these values (Fig. 4). Furthermore, unconfined compression tests of the samples giving the best attenuation values were examined, and their suitability as building materials was evaluated.

3.1. Gamma attenuation tests of tincal additive cement

The Gamma ray attenuation results of the samples of the mixtures are given in Table 2.

Table 2 presents the mass attenuation coefficients μ/ρ at different incident photon energy (E, keV) for samples with different tincal doping ratios (1%, 5%, and 10%). When the data are evaluated in the context of the material's interaction with electromagnetic radiation, it is observed that the linear attenuation coefficient systematically decreases with increasing dopant content. This suggests that the photon attenuation capacity of the material decreases with increasing tincal doping.

The PyMCA software (Sole et al. 2007) was utilized for the determination of I and I_0. The peaks were modelled as being fitted to a Gaussian function with an exponential background. It was determined that the minimum counts of both I and I_0 exceeded 10^4. In order to obtain the background under all peak regions, an exponential polynomial background was utilised, and the software simultaneously calculated both the Gaussian and background at the peak region.

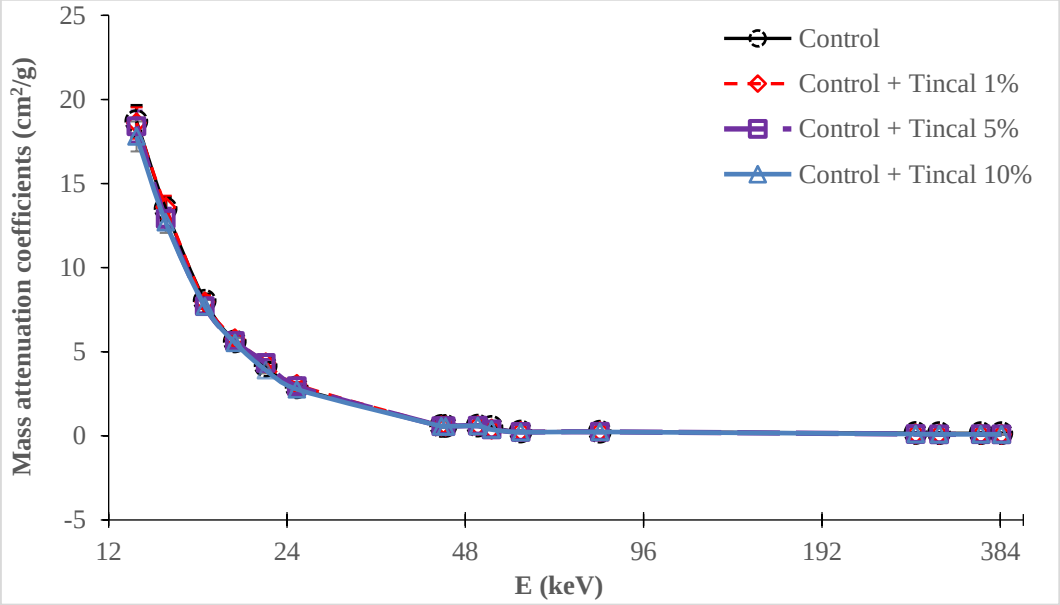

Fig. 4. Mass attenuation coefficients changes of cement samples including tincal with incident X or gamma rays.

Table 2. Measured mass attenuation coefficients μ/ρ (cm²/g) of samples.

E (keV)	Control	Control + 1% Tincal	Control + 5% Tincal	Control + 10% Tincal
13.375	18.7	18.6	18.4	17.8
14.980	13.5	13.6	12.9	12.7
17.443	8.02	7.95	7.71	7.70
19.607	5.60	5.77	5.63	5.53
22.103	4.16	4.34	4.33	3.91
24.942	2.87	3.05	2.95	2.77
43.737	0.580	0.589	0.570	0.568
44.470	0.575	0.583	0.573	0.562
50.391	0.596	0.605	0.598	0.586
53.155	0.521	0.400	0.379	0.375
59.537	0.243	0.260	0.232	0.222
81.000	0.236	0.256	0.240	0.233
276.390	0.160	0.113	0.107	0.107
302.850	0.154	0.091	0.089	0.090
356.010	0.153	0.091	0.090	0.090
385.851	0.148	0.085	0.087	0.086

In our experiments, the standard deviations of peak areas were approximately 1%. The thickness of the samples, which were shaped as rectangular prisms, was measured using a Vernier. The mass of each sample was measured using a high-precision scale. Finally, the thickness uncertainties were found to be less than 1%.

A quantitative analysis was conducted on the density of each sample. This involved calculating the measured mass and volume of the samples, using their known dimensions. It was evident that each measurement reflected its associated uncertainty with respect to the density value. The maximum uncertainties in mass thickness (ρt) employed in the calculations were approximately 2%. It is important to note that the final uncertainties are such that the mass attenuation coefficients listed in Table 2 are less than 3%.

The μ/ρ values demonstrate different behaviors for different energies. In order to proceed, it is necessary to engage in a discussion regarding the alterations in μ/ρ values across three distinct energy domains.

- Low Energy Range (13.375 – 25.942 keV): Tincal dopant has been demonstrated to exhibit a more significant effect on the mass attenuation coefficient μ/ρ. For instance, at 13.375 keV, the undoped control sample displays a value of 18.7, whereas this value diminishes to 17.8 in the 10% tincal-doped sample. This finding

suggests that the tincal doping may impede the interaction of low-energy photons within the material.

- Mid-Energy Range (43.737–81 keV): The tincal dopant effect remains consistent, yet the disparities are more constrained. Within this range, an increase in the doping rate results in a slight decrease in the mass attenuation coefficient μ/ρ.
- High Energy Range (276.39 – 385.851 keV): The tincal dopant effect has reached a minimal level, and the difference between the measured mass attenuation coefficients μ/ρ has decreased considerably.

A general assessment reveals that tincal additions alter the photon absorption properties of cement-based composite materials, and that this change varies with photon energy. It appears that increasing tincal content leads to a decrease in the material's photon absorption capacity, particularly for low-energy photons. These findings provide important insights into the potential role of tincal additions in radiation permeability and structural shielding applications.

3.2. Neutron experiments

The results of the neutron attenuation experiments are given in Table 3 and Fig. 5. The detector measures the dose rate for 100 seconds (one measurement per second and 100 measurement). We repeat the measurements ten times for each sample. We then calculate the mean values of I and I_0 and their standard deviations, which are used as uncertainties. These uncertainties are less than 1% for each sample. The uncertainties at the macroscopic and effective removal cross sections are 2% and 3%, respectively.

The data in Table 3 demonstrate the effects of tincal addition on the neutron attenuation behavior of cement-based samples. As tincal addition increases, a decrease in transmitted light intensity is observed, indicating that the material becomes more effective attenuator against neutrons. Particularly with 5% and 10% tincal additions, the macroscopic and effective removal cross sections increase significantly. This phenomenon is the result of interactions between neutrons and boron nuclei, particularly those of the ^{10}B isotopes. Consequently, in addition to cement, tincal has the potential to enhance the attenuation performance of cement-based composites against neutron radiation.

3.3. XRD analysis evaluation (5% tincal added sample)

The X-ray diffraction (XRD) pattern of a tincal-added cement sample allows the determination of its crystal structure and mineralogical composition. The graph presents intensity values corresponding to the 2θ angle, and these data are used to identify the crystalline phases within the sample (Fig. 6).

Table 3. Tincal neutron attenuation experiment results.

Sample	t (cm)	ρ (g/cm³)	Σ_t (cm^{-1})	ΣR (cm^2/g)
Control	0.540	1.8245	0.248	0.136
Control + Tincal 1%	0.540	1.8087	0.313	0.173
Control + Tincal 5%	0.540	2.1424	0.381	0.178
Control + Tincal 10%	0.540	1.8476	0.373	0.202

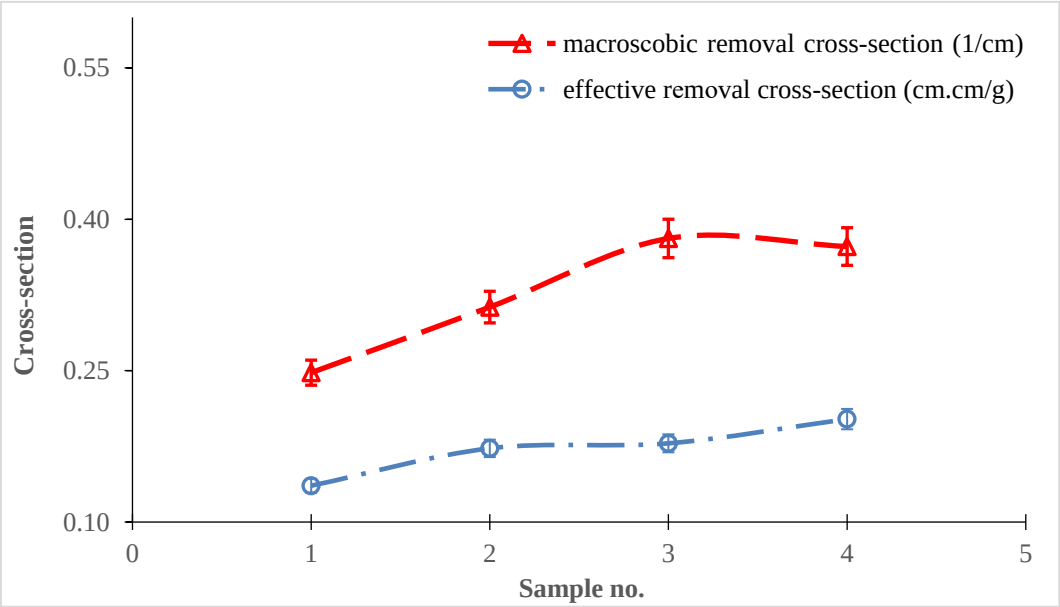

Fig. 5. Neutron experiment results. On the horizontal axis, 1 represents plain cement, and 2, 3, and 4 represent cement with 1%, 5%, and 10% tincal additive, respectively.

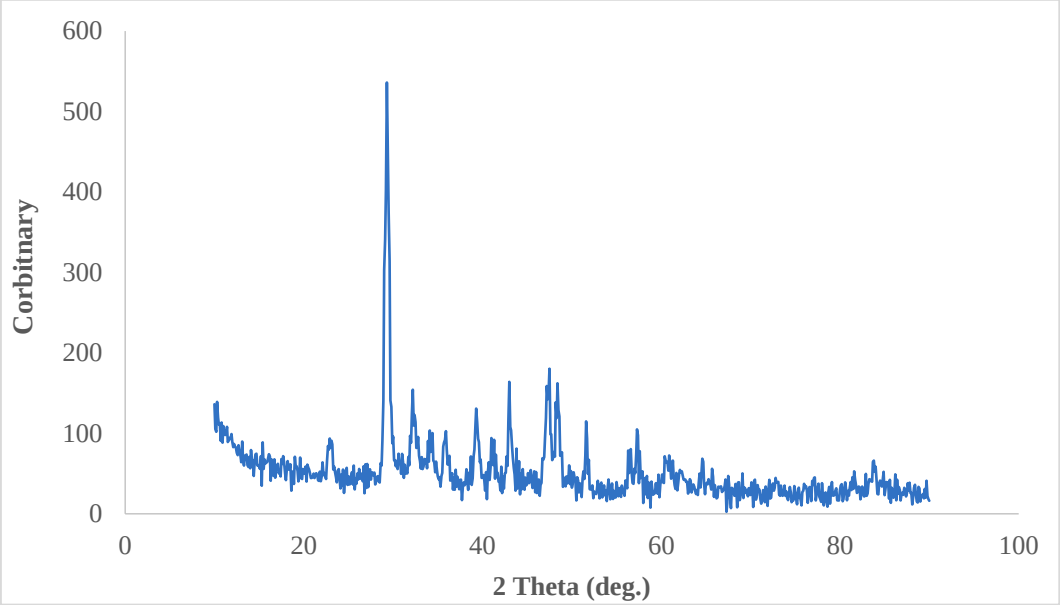

Fig. 6. XRD analysis of the 5% tincal added sample.

Tincal, dolomite, smectite, and calcite are observed in the planes corresponding to the prominent peaks in the XRD spectrum of tincal ore. The high-intensity peak observed at approximately 29° 2θ in the obtained diffractogram reveals the dominant presence of tincal ($Na_2B_4O_7.10H_2O$) and calcite ($CaCO_3$) phases in the sample. Calcite is a common component in the cement matrix, and its presence may be due to either the clinker structure or the carbonation process of the cement matrix. In addition, other intense peaks observed in the 32–34° 2θ range indicate the presence of calcium silicate hydrate (C-S-H) and ettringite phases, which are cement hydration products.

Some intense peaks detected in the graph with low intensity but distinct levels can be associated with X-ray reflections of the crystal structure of the mineral tincal ($Na_2B_4O_7{\cdot}10H_2O$), which is used as an additive. This suggests that the additive is preserved either physically or chemically within the cement matrix and integrated into the structure. However, diffraction intense peaks appearing between 40° and 50° 2θ suggest that tincal may have interacted with cement hydration products, triggering the formation of new mineral phases.

These data indicate that a 5% tincal addition can lead to the formation of specific crystalline phases in the cement matrix, thereby inducing structural changes in the cement microstructure. Such structural changes have the potential to directly affect the mechanical and physical properties (e.g., compressive strength, durability, and impermeability) of cement-based composites.

3.4. SEM analysis findings (5% tincal added sample)

The SEM image of a cement sample containing 5% Tincal additive, obtained after a 7-day curing period, provides important data about the microstructural characteristics of the material. Images a) were obtained at 1000x magnification with a 100 µm scale bar, b) at 2500x magnification with a 50 µm scale bar, c) at 5000x magnification with a 20 µm scale bar, and d) at 10000x magnification with a 10 µm scale bar. The SEM images show that the the tincal ore structure generally consists of short prismatic crystals, partly platy and flat crystals, and the grains have smooth surfaces (Fig. 7).

Table 4. Average compressive strengths of the mixtures.

Group no	Group number	Compressive strength (MPa)	Avg. comp. strength (MPa)
1	Control-1	31.54	
2	Control-2	33.14	32.4
3	Control-3	32.53	
4	Control + Tincal 5%	2.01	
5	Control + Tincal 5%	2.02	2.02
6	Control + Tincal 5%	2.03	

3.5. Unconfined compression test of tincal-added cement

After a 7-day curing period in saturated water, 3 samples were taken from each mixture and subjected to compressive strength testing. The average compressive strength values of the samples from the mixtures are given in Table 4 and Fig. 8.

The data in Table 4 allows for the comparative evaluation of the compressive strength performance of cement-based concrete samples containing 5% Tincal additive with the control group. While the average compressive strength in the control group samples was determined as 32.4 MPa, this value remained at only 2.02 MPa in the Tincal-added concrete samples prepared under the same conditions. This result shows that Tincal additive has a significantly adverse effect on mechanical strength at early ages.

This significant loss of strength suggests that Tincal interferes with the cement hydration process or negatively affects the formation of the binder matrix. Possible causes include reactive incompatibility of Tincal's chemical composition with the cement or its role in inhibiting the development of hydration products. The findings indicate that Tincal should be investigated comprehensively, not only in terms of its photon or neutron attenuating potential, but also in terms of its effects on the structural performance of concrete.

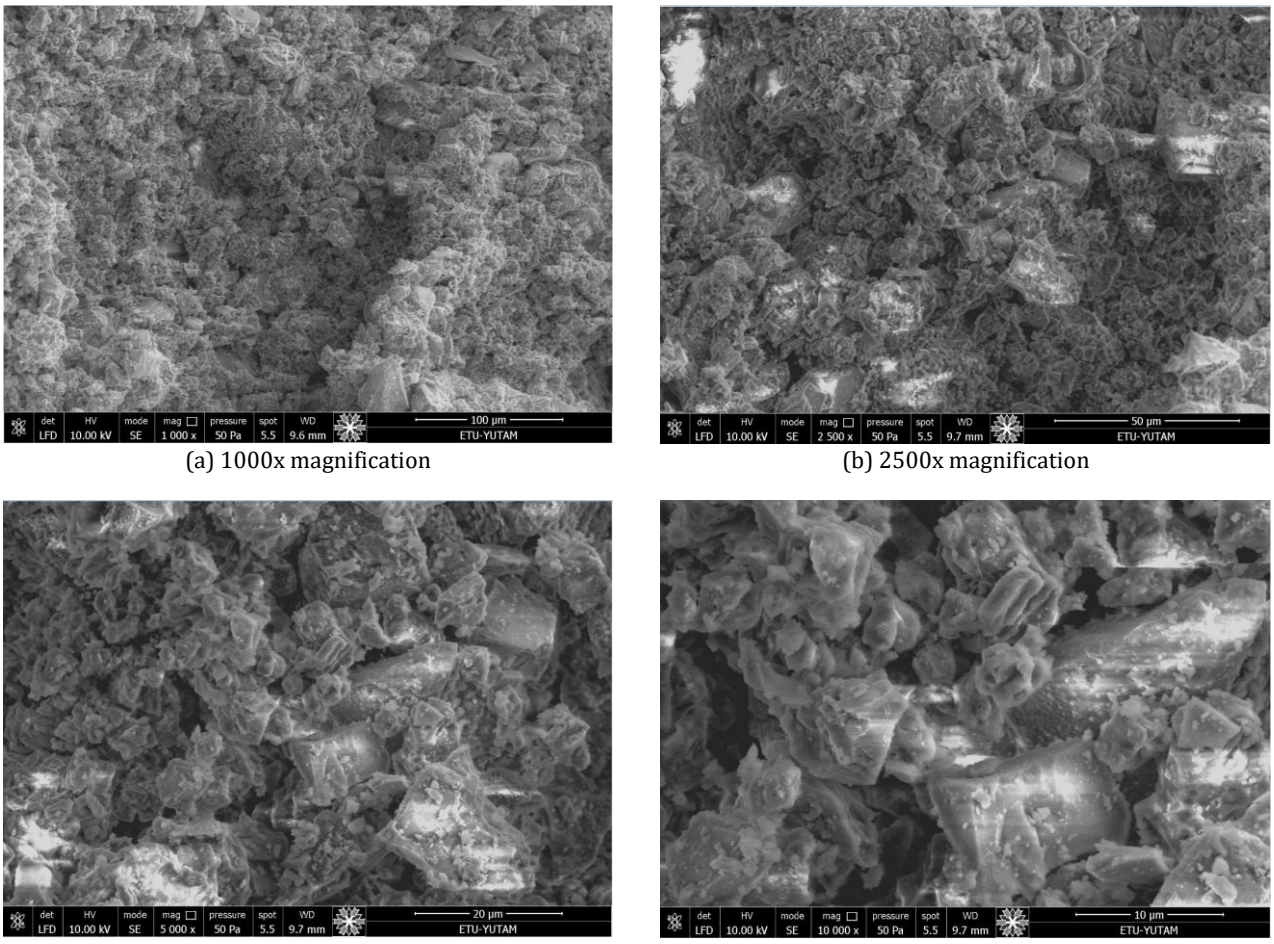

(a) 1000x magnification (b) 2500x magnification

(c) 5000x magnification (d) 10000x magnification

Fig. 7. SEM image of the tincal-doped sample at different scales.

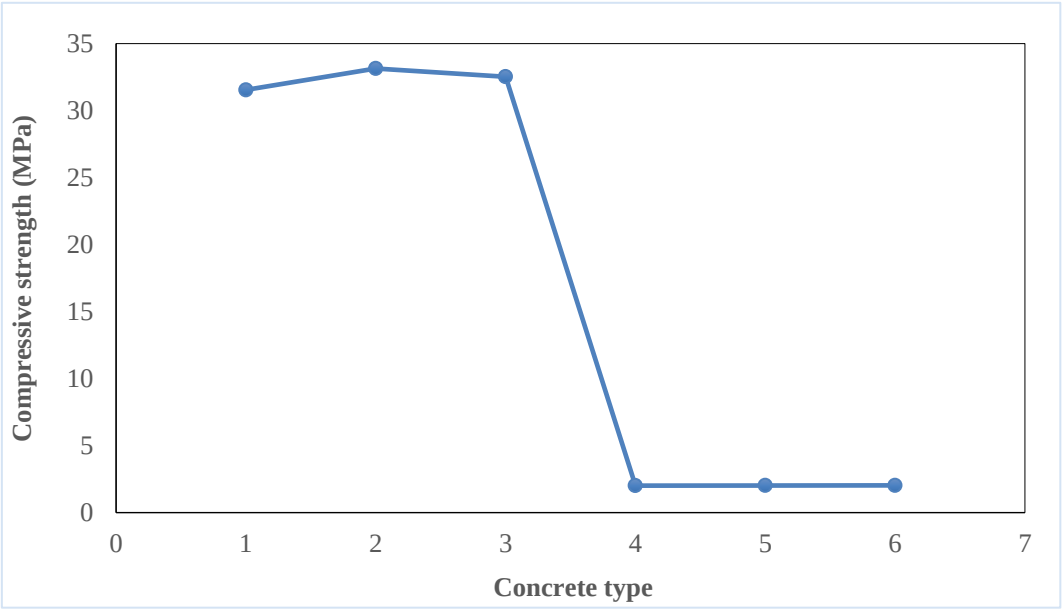

Fig. 8. Compressive strength according to mix type.

4. Conclusions

In this study, the gamma and neutron attenuation properties of tincal ores obtained from the Balıkesir-Bigadiç region were investigated using various experimental methods. The experimental studies included gamma and neutron attenuation experiments under different parameters, compressive strength tests, and scanning electron microscopy (SEM) and X-ray diffraction (XRD) analyses. The results of these analyses provided a detailed evaluation of the gamma and neutron attenuation properties of the tincal ore, and the findings are presented below.

- The mass attenuation coefficients (μ/ρ) of composite samples formed by doping tincal ore at different rates were investigated experimentally. As a result of measurements carried out at energy range of 13.375 keV and 385.851 keV, it was determined that the additives had significant effects on radiation permeability, especially in the low and medium energy ranges.
- Tincal-doped samples were found to generally have higher gamma ray transmittance, leading to lower attenuation performance. A decreasing trend in the mass attenuation coefficient of the sample was observed with increasing doping ratio, and this was particularly evident in the high-energy gamma rays.
- The neutron attenuation properties of composite samples formed by adding tincal ore at different rates were experimentally investigated. It was observed that as the tincal addition rate increased, the transmitted radiation intensity decreased, while at the same time, the attenuation properties became more effective against neutrons. This obviously attribute to high nuclear reaction cross sections between boron nuclei, especially ^{10}B isotopes, and fast neutrons. It is the result of interactions between neutrons and boron nuclei.
- Demonstrating the attenuation performance of tincal ore against neutron radiation with varying amounts of additives suggests that these natural minerals can be considered alternative shielding materials in radiation protection applications. As a result, the utilization of tincal ore obtained from the Bigadiç region, one of Türkiye's important boron reserves, allows for the transformation of domestic mineral resources into value-added products. This contributes to economic sustainability and provides a strategic contribution to reducing external dependence.
- The attenuation coefficients obtained over a wide energy range constitute an important database that can be used in the design and development of next-generation radiation shielding materials. These data are a reference for the scientific literature as they form the basis for advanced research.
- The development of attenuating composites using natural minerals minimizes the production of toxic waste, contributing to the widespread adoption of environmentally friendly material technologies. In this respect, the study can be evaluated within the scope of sustainable engineering practices.
- The neutron attenuation coefficients obtained in this study were quantitatively compared with boron-based materials commonly used in the literature. The mass neutron attenuation coefficients (0.095–0.110 cm^2/g) of cement samples containing 5% tincal additive are found to be of the same order of magnitude as the values reported for concrete containing colemanite and ulexite additives (Erdoğan et al. 1998; Erdoğmuş et al. 2011; Kharita et al. 2008).
- Boron carbide (B_4C) offers higher neutron removal coefficient due to its high boron content; however, its high cost, processing difficulties, and problems with homogeneous distribution in the cement matrix limit its use in building materials (Henrie 1962). In contrast, natural boron minerals such as tincal represent an important alternative for concrete and cement-based radiation shielding applications due to their economic, environmental, and sustainable properties.
- In this context, the neutron attenuation performance of tincal-modified cement is competitive with boron-based systems in the literature, not only in terms of absolute values but also in terms of applicability and cost-effectiveness criteria.

Consequently, unless new evidence is provided demonstrating that tincal or similar boron mineral additives can match or exceed the neutron attenuation performance of these more effective boron compounds under comparable conditions, the suitability of the tested material for structural applications remains questionable. This conclusion is of particular pertinence when considering design criteria that must balance radiation shielding efficacy with mechanical integrity and durability in load-bearing concrete structures. After evaluating all the data, it was concluded that the developed structural material would be more suitable as a surface coating material rather than for use in load-bearing elements.

Since the aim of this study was to investigate the radiation permeability of cement-boron mixtures, mechanical strength was not investigated in detail. While other studies are being conducted on that topic, this information is not included in this work.

Acknowledgements

This research has previously been presented at the 8th International Eurasian Conference on Biological and Chemical Sciences (EurasianBioChem 2025) held in Ankara, Türkiye, on December 17-19, 2025. Extended version of the research has been submitted to Challenge Journal of Concrete Research Letters and has been peer-reviewed prior to the publication.

Funding

The authors received no financial support for the research, authorship, and/or publication of this manuscript.

Conflict of Interest

The authors declare no potential conflicts of interest with respect to the research, authorship, and/or publication of this manuscript.

Data Availability

The datasets generated and/or analyzed during the current study are not publicly available but are available from the corresponding author upon reasonable request.

AI Assistance

No AI-based tools were used in the preparation of this manuscript.

Author Contributions

All authors made substantial contributions to the conception and design of the study, acquisition of data, analysis and interpretation of data; drafted or critically revised the manuscript for important intellectual content; and approved the final version to be published.

REFERENCES

Abutaha F, Çelik Aİ (2025). The engineering properties of silica fume and GGBS-based geopolymer mortars cured in elevated temperature. *Challenge Journal of Concrete Research Letters*, 16(2), 69-84.

Akkurt I, Akyildirim H, Mavi B, Kilincarslan S, Basyigit C (2010). Radiation shielding of concrete containing zeolite. *Radiation Measurements*, 45(7), 827-830.

Al-Safi S, Altharehi A, Alameri IA, Al-Jolahy A (2025). The mechanical properties of cement mortar reinforced with silica fume subjected to sulfate and chloride environment. *Challenge Journal of Structural Mechanics*, 11(1), 55-69.

Ataç E (2024). The Effect of Heating Speed on the Decomposition Temperature of Tincal Ore and Calcination. *M.Sc. thesis*, Atatürk University, Erzurum, Türkiye.

Davraz M (2010). The effects of boron compounds on the properties of cementitious composites. *Science and Engineering of Composite Materials*, 17(1), 1-18.

EN 196-3 (2016). Methods of testing cement. Part 3: Determination of setting times and soundness. European Committee for Standardization, Brussels, Belgium.

Erdoğan Y, Zeybek MS, Demirbaş A (1998). Cement mixes containing colemanite from concentrator wastes. *Cement and Concrete Research*, 28, 605-609.

Erdoğmuş E, Erdoğan Y, Gencel O, Targan S, Avcıata U (2011). Influence of colemanite admixture on Portland cement durability. *Advances in Cement Research*, 24, 155-164.

Eroğlu H (2009). Adsorption of Radioactive Thallium-201 and Gallium-67 Used in Nuclear Medicine. *Ph.D. thesis*, Atatürk University, Erzurum, Türkiye.

Filazi A, Pul M (2022). Boraks pentahidrat ikamesinin çimento harcının ses geçirme ve mekanik özelliklerine etkisi. *Uluslararası Mühendislik Araştırma ve Geliştirme Dergisi*, 14(2), 604-610. (in Turkish)

Görpe A, Cantez S (1992). Temel fizik. In: Görpe A, Cantez S, editors. *Pratik Nükleer Tıp*. İstanbul Tıp Fakültesi Vakfı, İstanbul, Türkiye, 1-42. (in Turkish)

Henrie JO (1962). Concrete for Radiation Shielding. 2nd ed. American Concrete Institute, Detroit, MI, USA.

Karakoç A (2024). Making Radiation Detector and Radiation Measurement of Various Materials. *M.Sc. thesis*, Erzincan Binali Yıldırım University, Erzincan, Türkiye.

Keskin N (2024). Evaluation of the Knowledge Levels and Attitudes of Anesthesia Technicians Working in Türkiye about Protection from Ionizing Radiation. *M.Sc. thesis*, Ufuk University, Ankara, Türkiye.

Kharita MH, Takeyeddin M, Alnassar M, Yousef S (2008). Development of special radiation shielding concretes using natural local materials and evaluation of their shielding characteristics. *Progress in Nuclear Energy*, 50, 33-36.

Kiani MA, Outokesh M, Ahmadi SJ (2025). Development of a new multifunctional polymer-based nanocomposite for neutron shielding applications. *Scientific Reports*, 15(1), 45137.

Kim YK, Lim IJ, Lim H, Joo Y, Park J, Hossain MM, Cho H, You NH, Ahn S, Lee H, Lee SS, Joo Y, Moon SY, Yoo HI, Lum C, Park C, Choi SQ (2025). High-density boron nitride nanotube composites via surfactant-stabilized lyotropic liquid crystals for enhanced space radiation shielding. *Advanced Functional Materials*, 35(52), e10716.

Kocadağistan ME, Arslan H (2024). Advantageous approach for boron ores used in cement production: Optimization of dehydration. *Challenge Journal of Concrete Research Letters*, 15(1), 7-19.

Korkut T, Karabulut A, Budak G, Aygün B, Gencel O, Hançerlioğulları A (2012). Investigation of neutron shielding properties depending on number of boron atoms for colemanite, ulexite and tincal ores by experiments and FLUKA Monte Carlo simulations. *Applied Radiation and Isotopes*, 70, 341-345.

Kratochvíl J, Opravil T, Diviš P (2014). The effect of boron and its compounds on setting of Portland cement. *Advanced Materials Research*, 1000, 16-19.

Olgun A, Kavas T, Erdogan Y, Once G (2007). Physico-chemical characteristics of chemically activated cement containing boron. *Building and Environment*, 42(6), 2384-2395.

Özdemir M, Öztürk NU (2003). Utilization of clay wastes containing boron as cement additives. *Cement and Concrete Research*, 33(10), 1659-1661.

Ramachandran VS, Beaudoin JJ (2001). Handbook of Analytical Techniques in Concrete Science and Technology. Noyes Publications, Norwich, NY, USA.

Sehhatigdiri A (2014). Experimental Investigation of the Shielding Properties of Different Clays against Radioactive Materials. *M.Sc. thesis*, Atatürk University, Erzurum, Türkiye.

Shaheen YBI, Etman ZA, Sabiha HL (2025). Design of reactive powder concrete mortar mixes through high strength and durability. *Challenge Journal of Concrete Research Letters*, 16(3), 142-154.

Singh VP, Badiger NM (2014). Gamma ray and neutron shielding properties of some alloy materials. *Annals of Nuclear Energy*, 64, 301-310.

Solé VA, Papillon E, Cotte M, Walter P, Susini J (2007). A multiplatform code for the analysis of energy-dispersive X-ray fluorescence spectra. *Spectrochimica Acta Part B: Atomic Spectroscopy*, 62, 63-68.

Srivastava A, Mishra A, Singh SK (2025). Mechanical and durability study of nano-SiO2 and nano-TiO2 on fiber reinforced concrete. *Challenge Journal of Concrete Research Letters*, 16(1), 33-39.

Sychev BS, Mal'kov VV, Komochkov MM, Zaitsev LI (1967). Penetration of heavy concrete shields by high-energy neutrons. *Journal of Nuclear Energy*, 21(3), 315-317.

Tarhan İH, Tarhan Y (2025). Nonlinear in-plane response of 3D-printed concrete walls with varied infill patterns: Experimental mix design and numerical structural assessment. *Challenge Journal of Structural Mechanics*, 11(3), 160-173.

Turan E, Alameri IA, Oltulu M (2025). Long-term durability of red mud-modified cement mortars: Effects of high temperature and freeze-thaw cycles. *Challenge Journal of Structural Mechanics*, 11(3), 116-127.

Uğurlu A, Özdemir M, Topçu İ (2004). Evaluation of boron containing clay wastes in cement. *Proceedings of the 2nd International Boron Symposium*, Eskişehir, Türkiye, 405-411.

Uzbaş B (2019). Modeling of SEM and XRD-Supported Visual Analyses of Cement-Based Composites Containing Silica Fume and Fly Ash Using Artificial Neural Networks. *Ph.D. thesis*, Atatürk University, Erzurum, Türkiye.

Wang P, Tang X, Chai H, Chen D, Qiu Y (2015). Design, fabrication, and properties of a continuous carbon-fiber reinforced Sm_2O_3/polyimide gamma ray/neutron shielding material. *Fusion Engineering and Design*, 101, 218-225.

Winter NB (2012). Scanning Electron Microscopy of Cement and Concrete. WHD Microanalysis Consultants Ltd., Woodbridge, UK.

Yang S, Yao Y, Wang H, Huang H (2024). A comparative study of neutron shielding performance in Al-based composites reinforced with various boron-containing particles for radiotherapy: A Monte Carlo simulation. *Nanomaterials*, 14(21), 1696.

Yılmaz E (2011). Determination of Gamma Ray Attenuation Coefficients and Neutron Removal Cross Sections in Some Building Materials. *M.Sc. thesis*, Rize University, Rize, Türkiye.

Challenge Journal of CONCRETE RESEARCH LETTERS

Research Article

Experimental study on the effect of polypropylene fiber on bond behavior, corrosion resistance, and microstructural characteristics of high-strength flowable concrete

Komala Nandaraju [a,*], Ramalingam Mourougane [a]

[a] *Department of Civil Engineering, Ramaiah Institute of Technology, Bengaluru 560054, Karnataka, India*

ABSTRACT

This study experimentally assesses the effects of polypropylene fibers (PPFs) on the mechanical, bond, durability, and microstructural performance of high-strength concrete (HSC) and high-strength flowable concrete (HSFC). A total of six M70-grade concrete mixes, with a characteristic compressive strength of 70 N/mm^2 at 28 days, were prepared: three HSC mixes and three HSFC mixes containing PPF at volume fractions of 0%, 0.1%, and 0.2%. Mechanical performance was evaluated through compressive, splitting tensile, and flexural strength tests at 3, 7, and 28 days. Bond behavior was examined using pull-out tests on deformed steel bars, while corrosion resistance was assessed using accelerated electrolytic corrosion testing. Microstructural changes during hydration were characterized by X-ray diffraction (XRD) and Fourier-transform infrared spectroscopy (FTIR). The results show that PPF improves tensile, flexural, and bond strength, with an optimum volume fraction of approximately 0.1%. The HSFC mixes exhibited slightly better post-cracking performance and bond strength than the HSC mixes, which can be attributed to more uniform fiber distribution and a denser matrix. Accelerated corrosion tests indicated that the fiber-reinforced mixes experienced lower steel mass loss and delayed crack initiation. XRD and FTIR analyses confirmed ongoing hydration and increasing microstructural density over time. The measured bond strengths exceeded the values predicted by IS 456:2000 and BS 8110, indicating that these code provisions are conservative for the studied fiber-reinforced high-strength concretes.

ARTICLE INFO

Article history:
Received – January 9, 2026
Revision requested – February 12, 2026
Revision received – March 11, 2026
Accepted – March 28, 2026

Keywords:
High-strength concrete
Microstructural characterization
Accelerated corrosion
Bond behavior
Polypropylene fibers

Citation: Nandaraju K, Mourougane R (2026). Experimental study on the effect of polypropylene fiber on bond behavior, corrosion resistance, and microstructural characteristics of high-strength flowable concrete. *Challenge Journal of Concrete Research Letters*, 17(2), 147–161.

1. Introduction

Plain concrete and reinforced concrete (RC) are widely used in civil engineering because of their strength, stiffness, cost efficiency, and suitability for various structural applications. Fig. 1 summarizes the main performance-related properties of concrete. However, the increasing use of cement-based materials has raised sustainability concerns related to Portland cement production, encouraging the incorporation of supplementary cementitious materials and industrial by-products as partial binder replacements (Mohamad et al. 2025; Tanash et al. 2025). At the same time, the long-term performance of RC structures is often limited by deterioration mechanisms such as reinforcement corrosion, drying shrinkage, and cracking, which may reduce load-carrying capacity and shorten service life. In this context, high-strength concrete (HSC) and high-strength flowable concrete (HSFC) have been developed to provide higher load capacity, improved durability, and better construction efficiency, particularly in structural members where dense reinforcement, bond performance,

* *Corresponding author*. E-mail address: komala.n@msrit.edu (K. Nandaraju)
ISSN: 2548-0928 / DOI: https://doi.org/10.20528/cjcrl.2026.02.006

and resistance to aggressive environments are critical. The high compressive strength of HSC, which is achieved by using very low water-to-binder ratios and developing dense microstructures, is far greater than that of conventional concrete (Hasan et al. 2025; Torres-Ortega et al. 2021). However, the dense microstructure and high strength of HSC may reduce workability, making placement and compaction more difficult in heavily reinforced or complex formwork (De Alencar Monteiro et al. 2018; Mazaheripour et al. 2011). HSFC addresses these workability limitations through high-range water-reducing admixtures, supplementary cementitious materials, and fine-particle packing, which together produce a flowable and self-compacting mix without vibration (Abdraimov 2024; Mazaheripour et al. 2011; Uysal and Tanyildizi 2012).

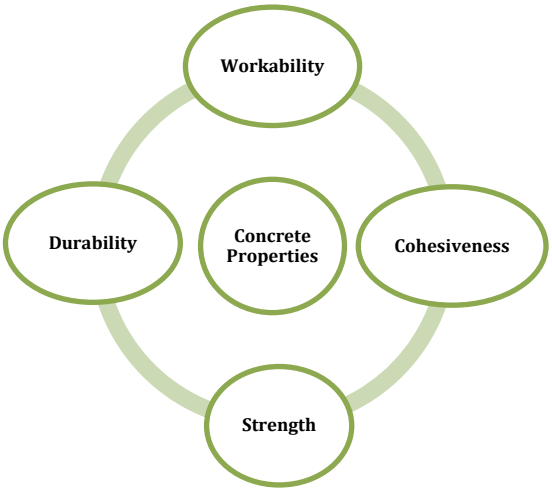

Fig. 1. Main properties of concrete.

PPFs are increasingly used in HSC and HSFC to improve tensile resistance, post-cracking behavior, crack control, and energy absorption (De Alencar Monteiro et al. 2018; Khaloo et al. 2022; Qin et al. 2019; Resende et al. 2022). Their low elastic modulus, chemical stability, and high elongation capacity allow properly dosed PPFs to bridge microcracks and improve ductility without causing a substantial reduction in compressive strength or fresh-state performance. This effect is particularly important in high-strength and flowable concrete systems, where dense matrices provide high strength but may also increase brittleness and create placement difficulties in heavily reinforced or complex structural members.

The performance of PPF-reinforced HSC and HSFC is also strongly influenced by the binder system and mixture proportioning. When PPFs are combined with mineral admixtures, nano-additions, or pozzolanic industrial by-products, these additions can improve strength, refine the pore structure, promote additional hydration products, increase durability, and help maintain adequate workability when used at suitable dosages (Abdraimov 2024; Al-Safi et al. 2025; Hasan et al. 2025; Mohamad et al. 2025; Srivastava et al. 2025; Tanash et al. 2025; Uysal and Tanyildizi 2012). However, excessive replacement levels, unsuitable particle dispersion, or increased water demand may reduce workability, increase porosity, and weaken fiber-matrix interaction, indicating that mixture proportioning remains critical for fiber-reinforced high-strength systems (Mohamad et al. 2025; Srivastava et al. 2025; Tanash et al. 2025). Previous studies have also shown that the use of PPF in self-compacting or flowable concrete can affect slump flow, passing ability, viscosity, and superplasticizer demand, especially when mineral additives, micro-silica, or alternative fine aggregates are incorporated into the mixture (Abdraimov 2024; Dubal and Naktode 2024; Mazaheripour et al. 2011; Uysal and Tanyildizi 2012).

Previous research further indicates that PPF and hybrid fiber systems can improve fracture resistance, deformability, residual load capacity, ductility, post-peak behavior, and crack control in high-strength concretes (Bakhita et al. 2025; De Alencar Monteiro et al. 2018; Hima Bindu et al. 2024; Khaloo et al. 2022). Under elevated temperature or other severe exposure conditions, PPF has been reported to reduce explosive spalling, support residual mechanical performance, and contribute to strength retention, while fiber type and post-exposure treatment can further influence the recovery and durability of fiber-reinforced concretes (Resende et al. 2022; Urtekin and Çelik 2025; Zhao et al. 2022). In addition, recycled polypropylene particles and combined fiber-SCM systems have been associated with improved sustainability, chloride resistance, microstructural densification, and cost-effective crack control (Faraj et al. 2019; Hasan et al. 2025; Labaran et al. 2024). Overall, these findings support the use of PPF-reinforced HSC and HSFC in structural applications where mechanical performance, durability, bond behavior, and resistance to aggressive environments are required.

1.1. X-ray diffraction (XRD) and Fourier-transform infrared spectroscopy (FTIR) analysis

Microstructural characterization methods such as XRD and FTIR are increasingly used as complementary tests alongside mechanical and durability assessments of advanced concretes. These techniques provide information on hydration phases, crystalline and amorphous contents, and chemical interactions among fibers, the cement matrix, and supplementary cementitious materials (SCMs) (Hasan et al. 2025; Resende et al. 2022). XRD analysis identifies crystalline hydration products, such as portlandite ($Ca(OH)_2$), ettringite, and calcium silicate hydrate (C-S-H), as well as secondary phases associated with SCMs such as silica fume or nano-silica additions (Abdraimov 2024; Hasan et al. 2025). In PPF systems, XRD can reveal changes caused by high-temperature exposure or fiber addition that may alter hydration rates or lead to decomposition or dehydration of phase-transition products. At elevated temperatures, XRD patterns have indicated phase changes such as portlandite decomposition and the transformation of C-S-H zones into more crystalline transitional phases, which are related to residual-strength changes (Resende et al. 2022; Zhao et al. 2022).

In fiber-reinforced HSC and HSFC, FTIR spectra typically show prominent peaks corresponding to Si-O stretching in the C-S-H gel phase, hydroxyl groups associated with portlandite, and carbonate ($CaCO_3$) formed

through carbonation. Combined microstructural and fracture-property analyses show how PPF affects crack networks at the micro-level (Torres-Ortega et al. 2021). Therefore, changes in the intensity or position of these peaks can indicate modifications in hydration products caused by fiber inclusion, SCM content, or environmental exposure. For example, Resende et al. (2022) showed that FTIR can detect signals related to polymer degradation and changes in cement-matrix chemistry after thermal loading, confirming the onset of polypropylene melting and the associated microstructural changes. Hasan et al. (2025) reported that FTIR observations, together with mineralogical densification detected by XRD and increased resistance to chloride penetration, support improved durability at higher SCM contents. Thus, combined XRD, FTIR, mechanical, and durability results can provide a more comprehensive understanding of the performance mechanisms of HSC and HSFC.

The bond behavior between reinforcing steel and concrete is crucial because it enables composite action and transfers stress between the two materials. Loss of bond performance directly affects crack spacing, deflection, anchorage length, and ultimately structural integrity. Bond degradation is influenced by the physical and mechanical properties of the reinforcing steel and concrete, environmental exposure, and time-dependent deformations caused by drying, corrosion-induced expansion, and shrinkage.

Fiber reinforcement is an effective approach for improving the strength, durability, and post-cracking behavior of concrete. Fibers bridge cracks after their formation, provide additional confinement around reinforcing bars, and can therefore influence the bond between steel reinforcement and the surrounding concrete (Ranjbar et al. 2016; Varghese et al. 2019). Pull-out-based studies have also shown that bond resistance and stress transfer are strongly affected by matrix composition, fiber surface condition, and interfacial compatibility, even in different fiber-reinforced cementitious or earth-based composite systems (Tarhan et al. 2025). In reinforced concrete, both metallic and non-metallic fibers have been reported to increase bond strength and delay splitting failure in pull-out tests (Deng and Yang 2024; Tsiotsias and Pantazopoulou 2021).

PPF, basalt, cellulose, and other synthetic fibers have gained attention because of their corrosion resistance, low density, and ability to control microcracking (Ahmed et al. 2021; Chen et al. 2024; Touahri et al. 2021). Experimental studies have shown that PPF helps retain bond strength under wet conditions by limiting cracking and maintaining support around the steel bar (Deng and Yang 2024; Ranjbar et al. 2016). Hybrid and coarse synthetic fibers are also being evaluated as possible replacements for steel fibers and have shown tensile and bond-strength performance comparable to that of high-performance and ultra-high-performance concrete, while offering durability and sustainability benefits (Lin et al. 2024; Sangkeaw et al. 2025).

The bond between reinforcing steel and concrete is essential for ensuring composite action and effective stress transfer in RC members. The bond between ribbed steel bars and the surrounding cementitious matrix depends on mechanical interlocking and friction between the bar ribs and the matrix (Diab et al. 2014; Tastani and Pantazopoulou 2010). Several factors influence bond performance, including concrete compressive strength, bar diameter, embedment length, bar surface deformation, and confinement type (Burdziński and Niedostatkiewicz 2022; Hadi 2008; Torre-Casanova et al. 2013). High-strength and high-performance concretes generally provide higher bond strength because of their dense microstructures and superior mechanical properties. However, they are also more susceptible to brittle splitting because of their lower deformation capacity (Hadi 2008; Tsiotsias and Pantazopoulou 2021). Previous studies have observed reductions in bond strength and shifts in pull-out failure modes as reinforcement corrosion increases. Accelerated corrosion tests further show that bond deterioration decreases peak bond strength and increases slip, thereby reducing structural ductility (Hou et al. 2019; Leporace-Guimil et al. 2021). Drying-shrinkage cracking also affects bond behavior because reduced confinement pressure around the reinforcing steel increases slip and decreases bond strength (Hou et al. 2019).

Corrosion of steel reinforcement is a major cause of premature deterioration in concrete structures, especially in environments with high chloride-ion concentrations, such as marine environments or structures exposed to de-icing salts. Chloride ions migrate through concrete and reach the steel reinforcement, where they damage the passive film and initiate electrochemical corrosion (Sola et al. 2019; Song and Saraswathy 2007). The volume of corrosion products exceeds that of the original steel, generating stresses in the surrounding concrete and leading to cracking, spalling, and reduced bond strength. Electrochemical methods allow the initiation and progression of corrosion in reinforced concrete to be detected through techniques such as half-cell potential measurements, corrosion-current-density measurements, and accelerated corrosion tests (Pan et al. 2020; Song and Saraswathy 2007). In addition to electrochemical techniques, acoustic emission monitoring has been used as a non-invasive method to detect corrosion-induced microcracking and to develop corrosion-rate prediction models based on recorded signal parameters (Patil 2025). These methods provide quantitative real-time information on corrosion activity and facilitate the evaluation of different concrete types, synthetic materials, fibers, SCMs, and corrosion inhibitors (Aguirre-Guerrero et al. 2021; Fahmy et al. 2022; Ouda 2024). Recent research shows that high-performance concrete and fiber-reinforced concrete can reduce corrosion rates and improve electrochemical performance by controlling cracking and refining pore structure, thereby limiting chloride transport (Bajić et al. 2025; Deng and Yang 2024; Leporace-Guimil et al. 2021). Nevertheless, corrosion-related bond deterioration remains critical when shrinkage cracking and sustained loading affect bond development (Hou et al. 2019). Fig. 2 illustrates the effects of PPF in hardened concrete.

Although fiber-reinforced concrete has been widely studied, most investigations treat mechanical behavior and durability as separate topics. Previous studies have examined the effects of PPF on tensile strength, flexural performance, and crack control, whereas other studies

have addressed corrosion resistance or microstructural properties using separate test methods. However, the relationships among mechanical performance, bond behavior, durability, and microstructural change remain insufficiently integrated. In addition, only a limited number of studies have directly compared HSC and HSFC reinforced with PPF under similar mix proportions. The improved workability of HSFC may influence fiber distribution and interfacial transition-zone properties, thereby affecting bond strength and corrosion resistance.

This study provides an integrated evaluation of mechanical properties, pull-out bond behavior, corrosion resistance, and microstructural characteristics using XRD and FTIR within the same experimental framework for both HSC and HSFC systems at identical fiber dosages. It also assesses bond-strength predictions according to BS 8110 (1997) and IS 456 (2000).

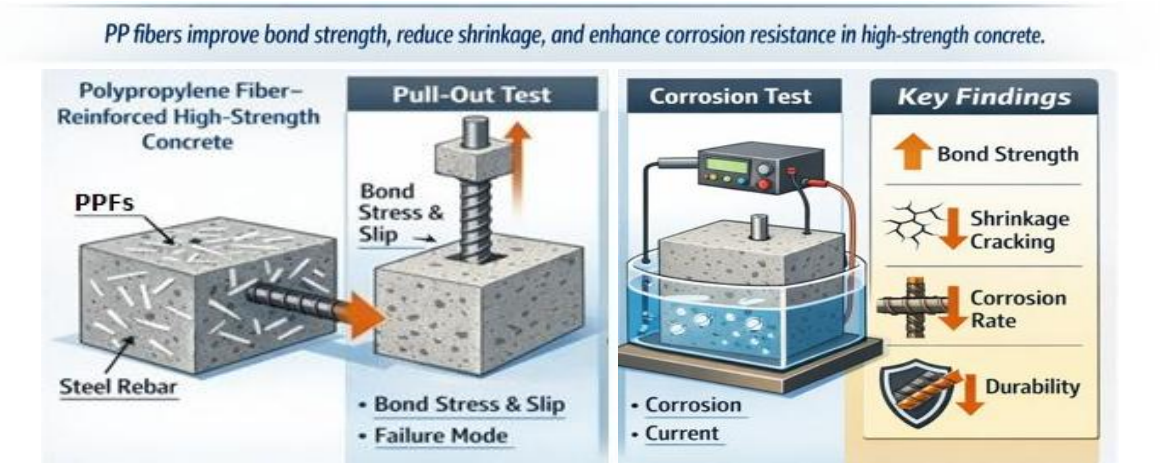

Fig. 2. Effects of PPF in pull-out and accelerated corrosion tests.

2. Research Gap and Novelty

Current research generally focuses on three separate areas: mechanical performance of PPF-reinforced HSC, corrosion resistance, and microstructural characterization. Direct quantitative comparisons between HSC and HSFC containing identical PPF dosages remain limited. Therefore, this study compares HSC and HSFC using the same fiber contents and evaluates mechanical, bond, corrosion, and microstructural responses within a single experimental framework.

The present study aims to:

- Compare the mechanical properties of HSC and HSFC containing identical PPF contents of 0%, 0.1%, and 0.2%.
- Examine the bond behavior between reinforcing steel and fiber-reinforced high-strength concrete using pull-out tests.
- Assess the corrosion resistance of reinforced concrete using an accelerated electrolytic corrosion test.
- Investigate microstructural changes using XRD and FTIR techniques.
- Evaluate the reliability of IS 456:2000 and BS 8110 predictions for bond strength in polypropylene-fiber-reinforced high-strength concrete systems.

3. Materials and Methods

The experimental program used 53-grade ordinary Portland cement (OPC) conforming to IS 12269 (2013), manufactured sand as fine aggregate, and crushed coarse aggregate with a maximum nominal size of 12.5 mm. The HSFC mixes contained both a superplasticizer and a viscosity-modifying agent (VMA), whereas the HSC mixes contained only a polycarboxylate ether (PCE)-based superplasticizer. Table 1 presents the physical properties of the synthetic micro-PPF used in this study. Fly ash and silica fume were used as SCMs; fly ash was incorporated at 15% by weight for HSC and 20% for HSFC, while silica fume was used at 5% by weight for both HSC and HSFC. Fig. 3 shows the materials used in concrete preparation. Concrete mix preparation was carried out in accordance with IS 10262 (2019), and six mixes were produced: three HSC mixes and three HSFC mixes with and without fibers. Basic material tests and fresh-property assessments were performed in accordance with the relevant standards, and all results were within acceptable limits. Mechanical performance was evaluated through compressive, splitting tensile, and flexural strength tests at 3, 7, and 28 days. Water absorption was measured in accordance with ASTM C1585 (2020). Microstructural analysis was conducted using XRD and FTIR after 28 days of curing.

Table 1. Physical properties of polypropylene fibers.

Property	Value
Shape	Triangular
Cut length	12 mm
Effective diameter	30 μm
Specific gravity	0.91
Melting point	160-165 °C
Elongation	90%
Young's modulus	4000 MPa

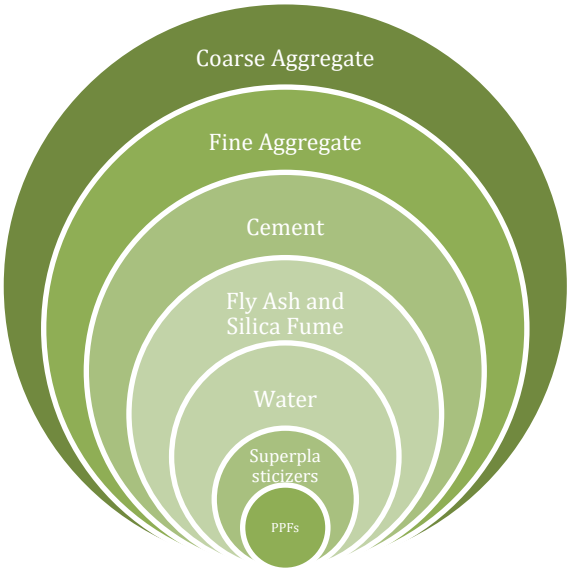

Fig. 3. Materials used in concrete preparation.

4. Experimental Work

4.1. Mechanical properties

The compressive, splitting tensile, and flexural strengths of HSC and HSFC with and without PPF were evaluated at 3, 7, and 28 days of curing for mixes M1-M6, as defined in Table 2. Compressive tests were performed on 100×100×100 mm cube specimens using a calibrated compression testing machine in accordance with IS 516 (1959). Splitting tensile strength was determined in accordance with IS 5816 (1999) using 100×200 mm cylindrical specimens subjected to diametral loading until failure. Flexural strength was assessed using a two-point loading setup on 75×75×450 mm prism specimens in accordance with IS 516 (1959). Fig. 4 illustrates the mechanical strength testing setup.

Table 2. Mix codes used in the study.

M1-HSC (0% PPF)	High-strength concrete
M2-HSC (0.1% PPF)	High-strength concrete
M3-HSC (0.2% PPF)	High-strength concrete
M4-HSFC (0% PPF)	High-strength flowable concrete
M5-HSFC (0.1% PPF)	High-strength flowable concrete
M6-HSFC (0.2% PPF)	High-strength flowable concrete

4.2. Accelerated corrosion test

To determine concrete resistance to corrosion, an accelerated electrolytic corrosion test was performed on specimens prepared from mixes M1-M6. Cylindrical specimens with a diameter of 100 mm and a height of 200 mm contained a 10 mm diameter steel bar at the center, providing a concrete cover of 45 mm, and were cured for 28 days, as shown in Fig. 5. The specimens were then submerged in a 5% sodium chloride solution, where the steel bar served as the anode and an external stainless-steel plate served as the cathode. The system was operated under direct current (DC), with voltage maintained throughout the test while current variations were monitored. Fig. 6 illustrates the testing procedure. Corrosion initiation was identified by a sudden increase in current and the appearance of visible surface cracks. After testing, the specimens were broken open, and the reinforcement bars were extracted, cleaned with Clark's solution, dried, and weighed to determine corrosion-related mass loss.

Fig. 4. Mechanical strength testing setup.

4.3. Pull-out bond strength test

To evaluate the bond strength between deformed reinforcing bars and concrete, pull-out tests were performed on specimens from mixes M1-M6. Each specimen consisted of a 150×150×150 mm concrete cube with a central 12 mm diameter deformed bar. The embedment length was 150 mm to ensure a consistent bond length during testing. After 24 h, the specimens were demolded and subjected to 28 days of water curing. Before testing, the protruding ends of the embedded bars were cleaned and prepared for placement in the mounting fixture, as shown in Fig. 7. The specimens were mounted in a 400 kN universal testing machine (UTM), which held the cubes securely while the bars were pulled axially from the concrete.

Fig. 5. Specimens used for accelerated corrosion testing during curing and after corrosion.

Fig. 6. Accelerated corrosion test setup.

Fig. 7. Test setup for pull-out test.

The steel bar was pulled at a constant loading rate of 0.5 mm/min until failure occurred by either bar slip or concrete splitting. At failure, the maximum applied load (P_{max}) was recorded. The average bond stress (τ_b) was calculated using Eq. (1).

$$\tau_b = \frac{P_{max}}{\pi d l} \quad (1)$$

where P_{max} is the peak pull-out load, d is the rebar diameter (12 mm), and l is the embedded length of the rebar (150 mm). This procedure follows the recommendations of IS 2770 (1967) for evaluating the bond performance of steel reinforcement in fiber-reinforced concrete.

5. Results and Discussion

5.1. Mechanical properties

All concrete mixtures achieved the characteristic strength of 70 MPa at 28 days, with ultimate compressive strengths ranging from 75.7 to 77.9 MPa for mixes M1-M6. Strength development followed a typical hydration pattern, with approximately 55-60% of the 28-day strength reached at 3 days and approximately 70-80% reached at 7 days. The addition of PPF caused only minor fluctuations in compressive strength, within approximately ±3%. A slight increase was observed at the 0.1% fiber dosage, which may be attributed to improved microcrack control and matrix integrity. At 0.2% PPF, the improvement was limited, possibly because of fiber agglomeration and reduced workability. The HSFC mixes showed slightly better performance than the HSC mixes, which may be related to better packing density and more uniform fiber distribution. Overall, PPF had a limited effect on compressive strength.

In the splitting tensile strength test, the control mix reached 5.7 MPa at 28 days, while 0.1% PPF increased the strength to 6.3-6.5 MPa, corresponding to an improvement of approximately 10-18%. The increase at 0.2% PPF was smaller but still noticeable. The improvement is attributed to crack-bridging action and stress redistribution, which enhance energy absorption. The HSFC mixes exhibited slightly higher tensile strength than the HSC mixes because of their superior fiber distribution and denser microstructure. Based on these results, the optimum fiber dosage was 0.1% by volume.

Flexural strength also improved in the HSC and HSFC mixes containing PPF. The control mixes reached 7.1-7.3 MPa at 28 days, while 0.1% PPF increased flexural strength to approximately 7.9 MPa, corresponding to an improvement of 8-12%. The increase at 0.2% PPF was less pronounced. The fibers improved crack resistance, post-cracking ductility, and toughness during bending. The HSFC mixes performed better than the HSC mixes because of improved fiber-matrix bonding and better structural integrity. Fig. 8 presents the mechanical strength test results.

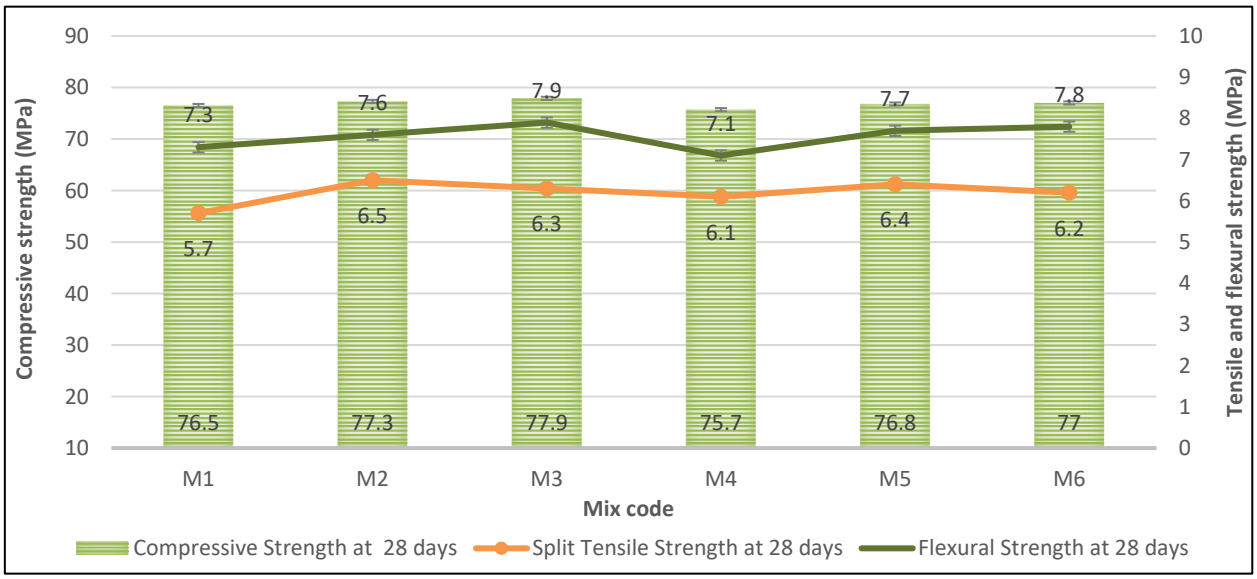

Fig. 8. Mechanical strength test results.

5.2. FTIR and XRD analyses

Fig. 9 shows the FTIR spectrum in the region of approximately 3640-3700 cm^{-1}, where the sharp band at about 3640 cm^{-1} is associated with O-H stretching of structural hydroxyl groups from portlandite or bound water in ettringite. The broad feature at about 3400 cm^{-1} and the bending mode at about 1650 cm^{-1} are associated with molecular water. The asymmetric stretching of carbonate ions (CO_3^{2-}) appears at about 1410-1480 cm^{-1}, with an out-of-plane bending mode at about 875 cm^{-1}. These bands increased in intensity from early to late samples, suggesting increased calcite formation. Bands related to S-O stretching in sulfate phases at about 1100-1130 cm^{-1} decreased over time as ettringite and gypsum were consumed during carbonation. The Si-O stretching modes at about 980-1000 cm^{-1} and Si-O-Si bending modes at about 450-500 cm^{-1} remained largely unchanged, confirming the non-reactive nature of quartz. The band at about 3400 cm^{-1} broadened at intermediate hydration stages, possibly because of increased hydroxyl disorder in hydroxyl-containing phases and bound wa-

ter, and then decreased toward the final stage. These spectral trends agree with the XRD results, where the ettringite peak diminished, calcite reflections increased from M1 to M6, sulfate bands decreased, and carbonate modes developed, indicating a more crystalline and carbonate-rich end product.

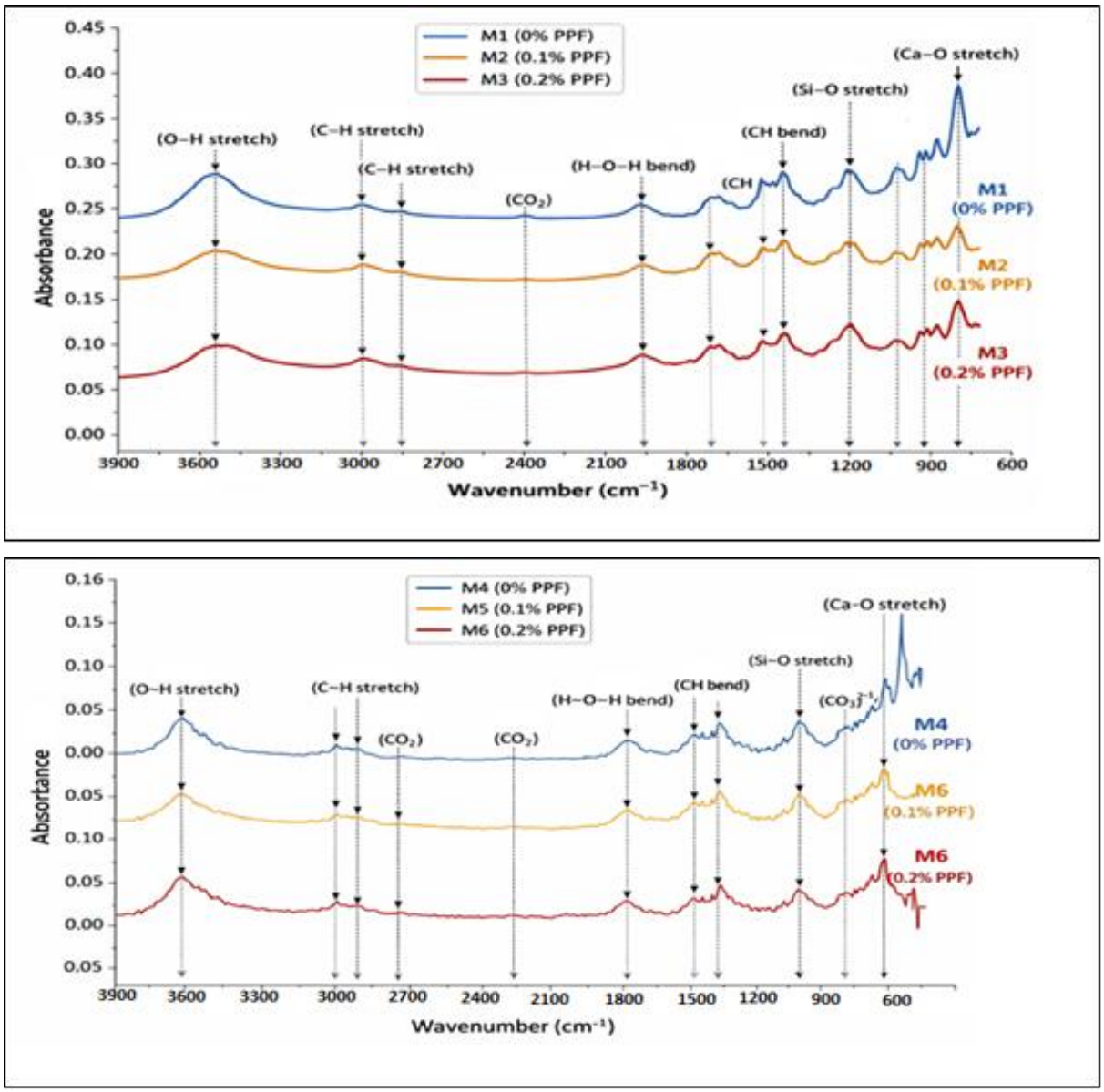

Fig. 9. FTIR analysis results.

The XRD data shown in Fig. 10 for phases M1-M6 indicate clear mineralogical evolution caused by carbonation or phase transformation in the stable samples.

The M1 and M5 specimens exhibited a quartz-dominated crystalline framework. Although this framework provides structural support, the limited development of hydration products may increase interfacial porosity and reduce bond strength. M3 showed reduced quartz intensity and the development of ettringite at approximately 10.3° and C-S-H between 29° and 35°, indicating advanced chemical conversion. The M2 group exhibited higher bond strength because ettringite needle growth and C-S-H gel formation occurred within the capillary pores. This mineralogical evolution enhanced mechanical interlocking at the reinforcement interface. FTIR analysis confirmed silicate polymerization, indicating the formation of a stronger binder matrix with improved resistance to pull-out forces compared with the siliceous matrix of M1. Electrochemical performance depends on the physical barrier provided by hydrated phases. M4 exhibited amorphous characteristics, resulting in a dense structure that blocked ionic diffusion through more complex pathways, as indicated by the absence of distinct crystalline peaks. This micro-densification delayed corrosion initiation. The presence of calcite in M6 indicates that carbonation may depassivate the embedded steel; thus, XRD can help evaluate the electrochemical stability of the reinforcement. Table 3 presents the XRD and FTIR results.

- Calcite formation resulted in pore refinement and reduced chloride transport.
- Reduced ettringite indicated stabilization of the matrix.
- Dense C-S-H improved the ITZ and increased bond strength.

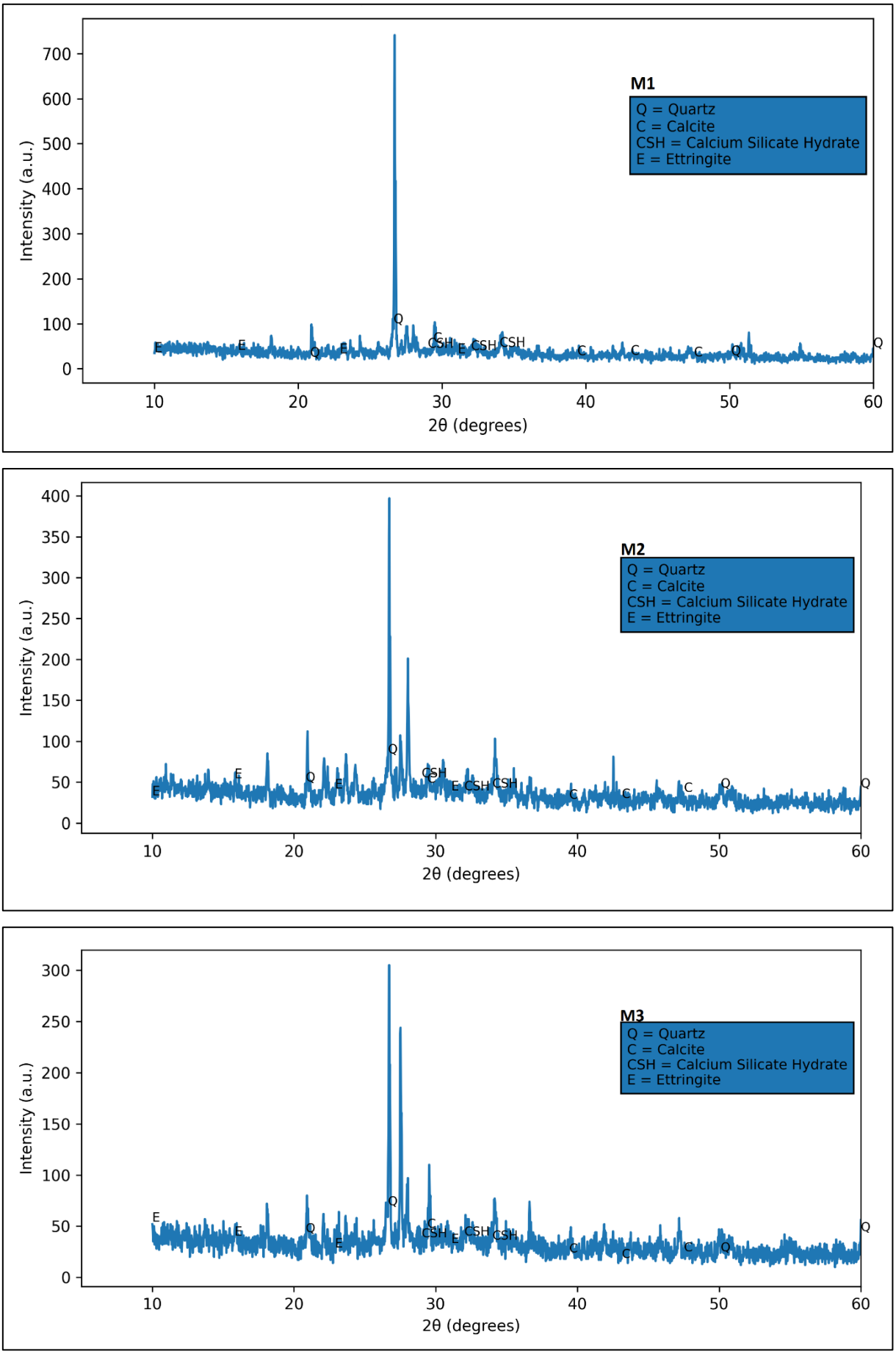

Fig. 10. (continued)

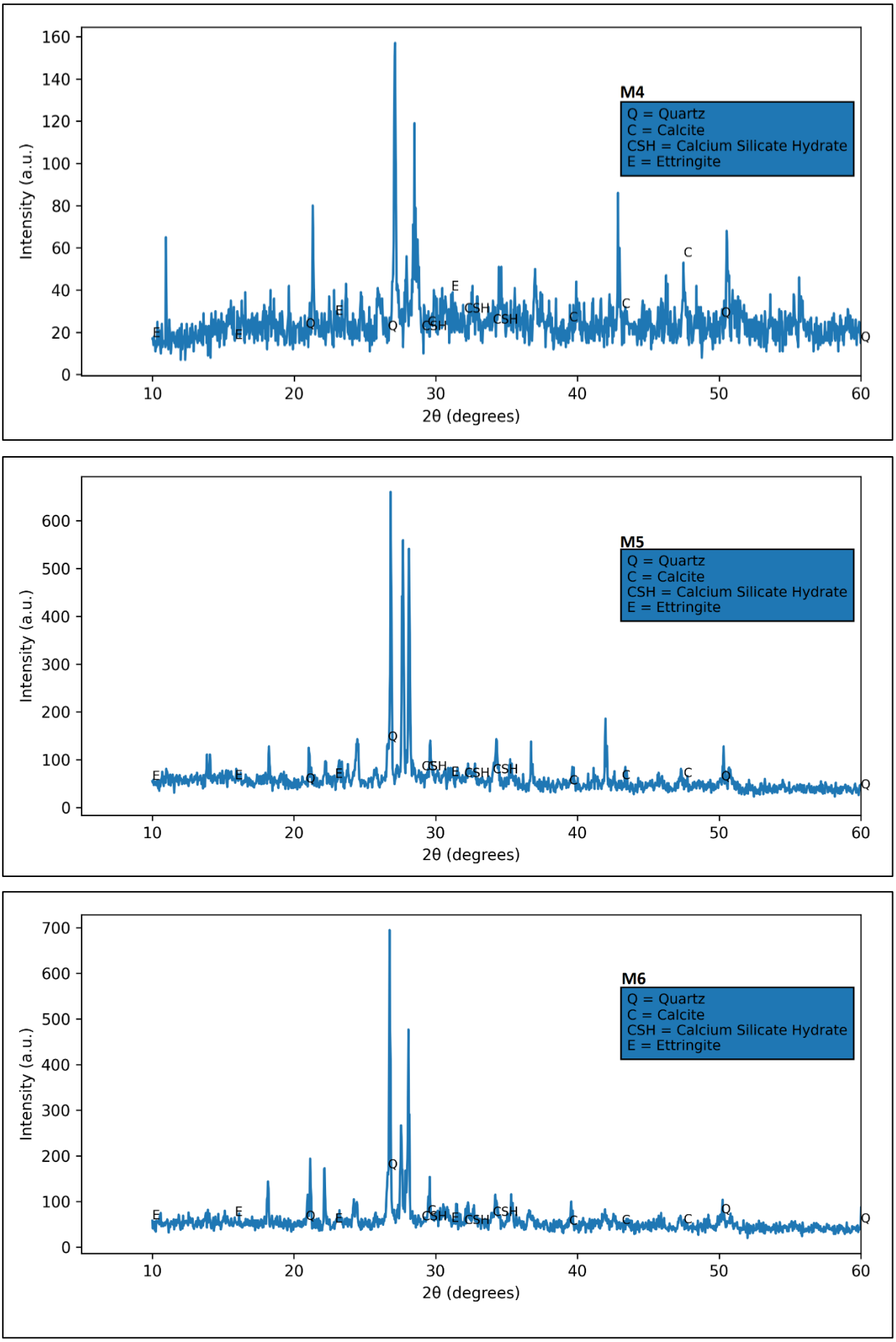

Fig. 10. XRD analysis results for M1-M6.

Table 3. XRD and FTIR analysis results.

Mix code	XRD points	FTIR points	Bond-strength mechanism	Corrosion-resistance basis
M1, M5	Quartz peaks with hydration products.	Low silicate polymerization indicated by the main Si-O stretching and Si-O bond-configuration bands.	The interfacial transition zone (ITZ) shows relatively weak mechanical interlocking because of its porous structure, limited C-S-H development, and the presence of less-reactive filler material.	Interconnected pores permit chloride-ion ingress because the hydration products do not sufficiently block pore pathways.
M2, M3	Main C-S-H diffraction pattern and ettringite-related diffraction pattern, together with vanadium oxide and silicate-based polymer materials.	High silicate polymerization indicated by silica-oxygen stretching and silicon-oxygen bond-stretching bands.	The fiber-concrete interface shows improved chemical adhesion and mechanical interlocking through the combined presence of dense C-S-H and ettringite.	The improved pore structure increases ionic tortuosity and electrical resistivity, resulting in a lower chloride-diffusion rate.
M4	Broad amorphous hump with minimal crystalline peaks and the lowest peak intensity.	Broad Al-O-Si asymmetric stretching bands are the dominant spectral feature.	The highly adhesive amorphous gel establishes continuous matrix links, although the limited crystalline content may reduce mechanical bonding.	The dense amorphous gel matrix acts as a barrier that limits chloride and moisture ingress.
M6	Distinct calcite diffraction peaks indicating carbonation.	Two carbonate absorption bands with strong absorption intensity.	The filler material increases matrix stiffness and confinement, whereas brittle interfaces may reduce ductility and bond strength.	Carbonation decreases pore-solution pH, removes the protective film on reinforcing steel, and may initiate corrosion damage.

5.3. Accelerated corrosion test

The accelerated corrosion test was used to assess the corrosion resistance of fiber-reinforced concrete by measuring reinforcement mass loss over time. The initial and final steel masses for mixes M1-M6 are presented in Table 4. The control mix M1 showed no mass loss during the first 45-90 min of testing. Reinforcement mass began to decrease after 120 min, indicating the onset of corrosion. The increasing mass loss over time suggests that microcracks and ionic-transport pathways developed, allowing chloride ions to enter and induce corrosion in plain HSC.

The addition of PPF reduced corrosion-related mass loss. Mix M2 showed significantly lower mass loss than the control mix, indicating improved corrosion resistance. Mix M3 also provided better corrosion protection than M1, although its performance was slightly lower than that of M2, possibly because the higher fiber content increased pore connectivity and reduced the uniformity of fiber dispersion. The HSFC mixes showed similar trends. M4 experienced moderate reinforcement mass loss after longer exposure, whereas the fiber-reinforced mixes M5 and M6 provided improved protection. M5 exhibited the lowest mass loss and therefore showed the best corrosion performance. Overall, the HSFC mixes demonstrated improved durability through enhanced resistance to environmental attack.

Some studies suggest that accelerated corrosion tests reproduce certain features of natural corrosion processes observed in the field. However, the applied DC voltage substantially increases the corrosion rate and does not fully represent chloride diffusion, moisture variation, and electrochemical-potential changes in real structures. Therefore, the data should be considered relative indicators of corrosion resistance rather than direct predictions of long-term service life. Future studies should include long-term natural-exposure tests and chloride-diffusion measurements to evaluate durability under realistic conditions.

5.4. Pull-out bond strength test

The peak bond stress of the HSC mixes increased from 13.61 MPa for M1 with 0% PPF to 14.15 MPa for M2 with 0.1% PPF and 14.32 MPa for M3 with 0.2% PPF. This improvement is attributed to the crack-bridging effect of PPF, which increases the tensile resistance of the concrete matrix and limits the development of microcracks from the reinforcing bar. The fibers provide additional confinement around the bar ribs, resulting in more effective mechanical interlock and higher bond resistance. They also help control splitting cracks, which commonly govern failure in pull-out tests of high-strength concrete.

The HSFC mixes showed a similar trend. Bond stress increased from 13.44 MPa for M4 with 0% PPF to 14.50 MPa for M5 with 0.1% PPF and 16.27 MPa for M6 with 0.2% PPF. The higher bond strength of the fiber-reinforced HSFC mixes may be attributed to improved particle packing and better consolidation, which enhance contact between the steel surface and the surrounding matrix. The combination of fiber reinforcement and flowable concrete produced a denser interfacial transition zone (ITZ), thereby improving resistance to radial cracking. The slip at peak bond stress increased with fiber content, from 0.65 mm in M1 to 1.29 mm in M6. These results indicate that fiber-reinforced mixes exhibit higher ductility and require greater energy for pull-out failure. PPF bridges cracks and allows stress transfer to continue through cracked regions, enabling the concrete matrix to sustain larger deformations before bond failure. Fig. 11 shows the pull-out test results.

Table 4. Accelerated corrosion test results.

M1			
Mix code	Time	Initial mass	Final mass
M1 - 1	(45 min)	0.195	0.195
M1 - 2	(60 min)	0.203	0.203
M1 - 3	(90 min)	0.177	0.177
M1 - 4	(120 min)	0.207	0.205
M1 - 5	(150 min)	0.179	0.176
M1 - 6	(180 min)	0.184	0.179
M2			
Mix code	Time	Initial mass	Final mass
M2 - 1	(45 min)	0.191	0.191
M2 - 2	(60 min)	0.204	0.204
M2 - 3	(90 min)	0.201	0.199
M2 - 4	(120 min)	0.196	0.195
M2 - 5	(150 min)	0.201	0.197
M2 - 6	(180 min)	0.205	0.201
M3			
Mix code	Time	Initial mass	Final mass
M3 - 1	(45 min)	0.205	0.205
M3 - 2	(60 min)	0.204	0.204
M3 - 3	(90 min)	0.203	0.202
M3 - 4	(120 min)	0.193	0.191
M3 - 5	(150 min)	0.203	0.199
M3 - 6	(180 min)	0.203	0.198

M4			
Mix code	Time	Initial mass	Final mass
M4 - 1	(45 min)	0.202	0.202
M4 - 2	(60 min)	0.192	0.192
M4 - 3	(90 min)	0.194	0.194
M4 - 4	(120 min)	0.206	0.204
M4 - 5	(150 min)	0.195	0.193
M4 - 6	(180 min)	0.194	0.191
M5			
Mix code	Time	Initial mass	Final mass
M5 - 1	(45 min)	0.195	0.195
M5 - 2	(60 min)	0.195	0.195
M5 - 3	(90 min)	0.205	0.205
M5 - 4	(120 min)	0.198	0.197
M5 - 5	(150 min)	0.207	0.204
M5 - 6	(180 min)	0.204	0.202
M6			
Mix code	Time	Initial mass	Final mass
M6 - 1	(45 min)	0.206	0.206
M6 - 2	(60 min)	0.205	0.205
M6 - 3	(90 min)	0.204	0.204
M6 - 4	(120 min)	0.205	0.203
M6 - 5	(150 min)	0.204	0.201
M6 - 6	(180 min)	0.204	0.202

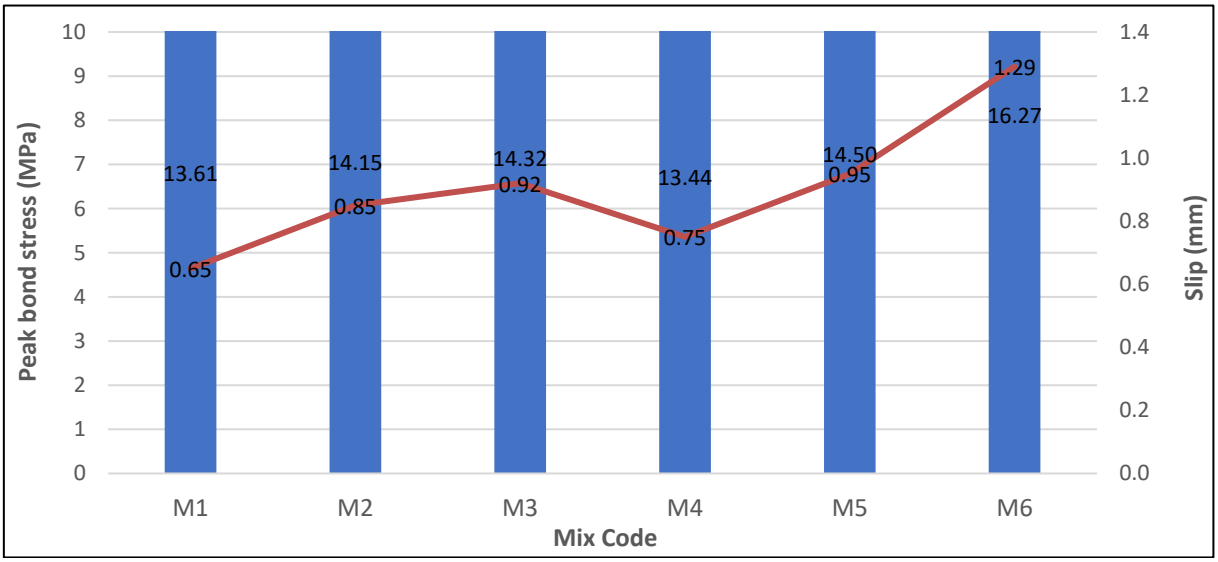

Fig. 11. Pull-out test results.

The experimental bond-strength values were higher than the values predicted by the design codes, as calculated using Eqs. (2) and (3). This difference is expected because the code equations are intended for safe design and include conservative assumptions. In addition, pull-out tests are conducted under controlled conditions, whereas structural members may also be affected by bending stresses, cracking, confinement variation, and other service conditions. Therefore, although the PPF-reinforced mixes showed improved bond performance, the results should be interpreted within the limitations of the test method.

The theoretical bond strength was evaluated according to BS 8110 (1997) and IS 456 (2000), and the results are tabulated in Table 5. According to BS 8110 (1997), the ultimate bond strength is expressed by Eq. (2).

$$f_{bu} = 0.50\sqrt{f_{cu}} \rightarrow f_{bu} = 0.50\sqrt{70} = 4.18 \text{ N/mm}^2 \quad (2)$$

where f_{bu} is the theoretical bond strength (N/mm^2), β is the bond coefficient (0.28 for plain bars and 0.50 for deformed bars), and f_{cu} is the cube compressive strength of concrete (N/mm^2).

According to IS 456:2000, the theoretical bond strength for plain bars is 1.9 N/mm^2. For deformed bars, this value is increased by 60%, as shown in Eq. (3).

$$\tau_{bd} = 1.9 \cdot 1.6 = 3.04 \text{ N/mm}^2 \quad (3)$$

Table 5. Bond strength test results.

Mix code	Peak stress (MPa)	Slip at peak (mm)	Stress at 0.25 mm slip	IS 456 design value	BS 8110 theoretical value
M1	13.61	0.65	5.44 MPa	3.04 MPa	4.18 MPa
M2	14.15	0.85	4.86 MPa	3.04 MPa	4.18 MPa
M3	14.32	0.92	4.42 MPa	3.04 MPa	4.18 MPa
M4	13.44	0.75	4.48 MPa	3.04 MPa	4.18 MPa
M5	14.50	0.95	3.31 MPa	3.04 MPa	4.18 MPa
M6	16.27	1.29	3.15 MPa	3.04 MPa	4.18 MPa

6. Conclusions

This experimental investigation examined the influence of PPF on the mechanical properties, bond behavior, corrosion resistance, and microstructural characteristics of HSC and HSFC. The main conclusions are as follows:

- Overall, the results showed that adding PPF had a negligible effect on compressive strength, with a variation of approximately ±3%, while notable improvements were observed in tensile and flexural strengths. The increase in splitting tensile strength ranged from 10% to 18% at 0.1% PPF, and flexural strength increased by 8% to 12%.
- The optimum fiber content was 0.1% by volume. Although 0.2% PPF improved tensile and bond properties, the additional benefits were limited, possibly because of fiber agglomeration.
- Pull-out test results indicated that adding fibers improved the bond between reinforcing bars and concrete. Bond strength increased from 13.61 MPa for M1 to 14.32 MPa for M3 and 16.27 MPa for M6. This improvement resulted from crack bridging and enhanced protection against splitting around the reinforcing bars, which improved mechanical interlocking.
- HSFC showed superior mechanical properties and bond strength compared with HSC. Improved particle arrangement and more uniform fiber distribution enhanced workability and produced a denser interfacial transition zone (ITZ).
- Steel mass loss during accelerated corrosion testing was lower in the fiber-reinforced mixes, whereas the control specimens exhibited earlier crack development. The fiber-reinforced system therefore provided better corrosion protection by reducing crack size and crack number and by limiting chloride ingress through a more resistant pore structure.
- XRD and FTIR analyses revealed the formation and development of hydration products such as C-S-H gel, ettringite, and calcite, as well as ongoing densification of the cement matrix over time. These results also indicated improved mechanical and long-term performance of the fiber-reinforced mixes owing to enhanced silicate polymerization and microstructural development.
- The measured bond strengths exceeded the predictions of IS 456:2000 and BS 8110, suggesting that current code provisions are conservative for fiber-reinforced high-strength concrete systems.
- The findings demonstrate that PPF-reinforced HSFC provides a balanced combination of strength, bond improvement, and durability, making it a suitable material for reinforced concrete structures exposed to aggressive environments.

Acknowledgements

The authors would like to thank MSRIT, Bengaluru for their support and contribution to this study.

Funding

The authors received no financial support for the research, authorship, and/or publication of this manuscript.

Conflict of Interest

The authors declare(s) no potential conflicts of interest with respect to the research, authorship, and/or publication of this manuscript.

Data Availability

The datasets generated and/or analyzed during the current study are not publicly available but are available from the corresponding author upon reasonable request.

AI Assistance

During the preparation of this manuscript, Grammarly, Gemini and ChatGPT were used exclusively for language editing and stylistic refinement. The authors take full responsibility for the content, interpretation, and conclusions of the published article.

Author Contributions

All authors made substantial contributions to the conception and design of the study, acquisition of data, analysis and interpretation of data; drafted or critically revised the manuscript for important intellectual content; and approved the final version to be published.

References

Abdraimov I (2024). Strength and durability effect of self-compacting concrete reinforcement with micro-silica and volume fiber. *International Journal of GEOMATE*, 27(119), 1-8.

Aguirre-Guerrero AM, Robayo-Salazar RA, Mejía De Gutiérrez R (2021). Corrosion resistance of alkali-activated binary reinforced concrete based on natural volcanic pozzolan exposed to chlorides. *Journal of Building Engineering*, 33, 101593.

Ahmed TW, Aljubory NH, Zidan RS (2021). Properties and performance of polypropylene fiber reinforced concrete: A review. *Tikrit Journal of Engineering Sciences*, 27(2), 82-97.

Al-Safi S, Altharehi A, Alameri IA, Al-Jolahy A (2025). The mechanical properties of cement mortar reinforced with silica fume subjected to sulfate and chloride environment. *Challenge Journal of Structural Mechanics*, 11(1), 55–69.

ASTM C1585 (2020). Standard test method for measurement of rate of absorption of water by hydraulic-cement concretes. ASTM International, West Conshohocken, PA, USA.

Bajić P, Leporace-Guimil B, Andrade C, Tošić N, De La Fuente A (2025). Chloride-induced corrosion effects on the structural performance of concrete with rebar and fibres: A review. *Applied Sciences*, 15(12), 6457.

Bakhita CD, Kanali C, Onchiri RO (2025). Mechanical properties of high-strength concrete reinforced with basalt and polypropylene fibers. *Engineering, Technology & Applied Science Research*, 15(3), 22725-22733.

BS 8110 (1997). Structural use of concrete. Part 1: Code of practice for design and construction. British Standards Institution, London, UK.

Burdziński M, Niedostatkiewicz M (2022). Experimental-numerical analysis of the effect of bar diameter on bond in pull-out test. *Buildings*, 12(9), 1392.

Chen Y, Waheed MS, Iqbal S, Rizwan M, Room S (2024). Durability properties of macro-polypropylene fiber reinforced self-compacting concrete. *Materials*, 17(2), 284.

De Alencar Monteiro VM, Lima LR, De Andrade Silva F (2018). On the mechanical behavior of polypropylene, steel and hybrid fiber reinforced self-consolidating concrete. *Construction and Building Materials*, 188, 280-291.

Deng Y, Yang Y (2024). An experimental study on corrosion resistance and bond behavior of reinforced concrete structures with various fibers. *KSCE Journal of Civil Engineering*, 28(12), 5593-5603.

Diab AM, Elyamany HE, Hussein MA, Al Ashy HM (2014). Properties of pull-out bond strength and concept to assess ultimate bond stress of NSC and HSC. *Magazine of Concrete Research*, 66(17), 877-895.

Dubal AC, Naktode PL (2024). Effect of polypropylene fiber on the properties of self-compacting concrete with M-sand. *Educational Administration Theory and Practice*, 30(2), 1-8.

Fahmy NG, Hussien RM, Abd El-Hafez LM, Mohamed RAS, Faried AS (2022). Comparative study on fresh, mechanical, microstructure properties and corrosion resistance of self-compacted concrete incorporating nanoparticles extracted from industrial wastes under various curing conditions. *Journal of Building Engineering*, 57, 104874.

Faraj RH, Sherwani AFH, Daraei A (2019). Mechanical, fracture and durability properties of self-compacting high-strength concrete containing recycled polypropylene plastic particles. *Journal of Building Engineering*, 25, 100808.

Hadi MNS (2008). Bond of high strength concrete with high strength reinforcing steel. *The Open Civil Engineering Journal*, 2(1), 143-147.

Hasan M, Alkhaly YR, Hamzani, Fikri R, Saidi T (2025). Properties of high-strength concrete incorporating calcined diatomaceous earth, polypropylene and glass fibers. *Buildings*, 15(2), 225.

Hima Bindu K, Rathna Chary M, Haranatti JS, Rao LV, Dev PV, Kotov EV (2024). Behavior of high strength reinforced cement concrete with polypropylene and steel fibres. *MATEC Web of Conferences*, 392, 01011.

Hou L, Zhou B, Guo S, Aslani F, Chen D (2019). Corrosion behavior and flexural performance of reinforced concrete/ultrahigh toughness cementitious composite beams under sustained loading and shrinkage cracking. *Construction and Building Materials*, 198, 278-287.

IS 456 (2000). Plain and reinforced concrete. Code of practice. Bureau of Indian Standards, New Delhi, India.

IS 516 (1959). Methods of tests for strength of concrete. Bureau of Indian Standards, New Delhi, India.

IS 2770 (1967). Methods of testing bond in reinforced concrete. Part 1: Pull-out test. Bureau of Indian Standards, New Delhi, India.

IS 5816 (1999). Method of test for splitting tensile strength of concrete. Bureau of Indian Standards, New Delhi, India.

IS 10262 (2019). Concrete mix proportioning. Guidelines. Bureau of Indian Standards, New Delhi, India.

IS 12269 (2013). Ordinary Portland cement, 53 grade. Specification. Bureau of Indian Standards, New Delhi, India.

Khaloo A, Daneshyar A, Rezaei B, Fartash A (2022). Fiber bridging in polypropylene-reinforced high-strength concrete: An experimental and numerical survey. *Structural Concrete*, 23(1), 457-472.

Labaran YH, Atmaca N, Tan M, Atmaca K (2024). High-strength fiber-reinforced concrete: Assessing the impact of polyvinyl alcohol, glass and polypropylene fibers on structural integrity and cost efficiency. *Discover Civil Engineering*, 1(1), 37.

Leporace-Guimil B, Conforti A, Zerbino R, Plizzari GA (2021). Chloride-induced corrosion in reinforced concrete and fiber reinforced concrete elements under tensile service loads. *Cement and Concrete Composites*, 124, 104245.

Lin JX, Luo RH, Su JY, Guo YC, Chen WS (2024). Coarse synthetic fibers as a replacement to steel fibers in UHPC: Tensile behavior, environmental and economic assessment. *Construction and Building Materials*, 412, 134654.

Mazaheripour H, Ghanbarpour S, Mirmoradi SH, Hosseinpour I (2011). The effect of polypropylene fibers on the properties of fresh and hardened lightweight self-compacting concrete. *Construction and Building Materials*, 25(1), 351-358.

Mohamad N, Embong R, Othman NH, Muthusamy K, Jaafar MFM (2025). Flowability and compressive strength of ternary blended cement mortar of coal bottom ash and ground cockle shell ash. *Challenge Journal of Concrete Research Letters*, 16(1), 25–32.

Ouda AS (2024). Insights into the physico-mechanical characteristics and corrosion behavior of high-performance heavy density concrete used in the construction of electro-nuclear power facilities. *Construction and Building Materials*, 443, 137838.

Pan C, Chen N, He J, Liu S, Chen K, Wang P, Xu P (2020). Effects of corrosion inhibitor and functional components on the electrochemical and mechanical properties of concrete subject to chloride environment. *Construction and Building Materials*, 260, 119724.

Patil SV (2025). Predictive modelling of acoustic emission signal data for corrosion assessment: A modified dimensional analysis based approach. *Challenge Journal of Concrete Research Letters*, 16(3), 125–132.

Qin Y, Zhang X, Chai J, Xu Z, Li S (2019). Experimental study of compressive behavior of polypropylene-fiber-reinforced and polypropylene-fiber-fabric-reinforced concrete. *Construction and Building Materials*, 194, 216-225.

Ranjbar N, Talebian S, Mehrali M, Kuenzel C, Metselaar HSC, Jumaat MZ (2016). Mechanisms of interfacial bond in steel and polypropylene fiber reinforced geopolymer composites. *Composites Science and Technology*, 122, 73-81.

Resende HF, Reis ED, Arroyo FN, De Moraes MHM, Dos Santos HF, Da Silva EG, Lahr FAR (2022). Residual mechanical properties and durability of high-strength concrete with polypropylene fibers in high temperatures. *Materials*, 15(13), 4711.

Sangkeaw P, Thongchom C, Keawsawasvong S, Prasittisopin L (2025). Mechanical properties and microstructure of cellulose fiber and synthetic fiber reinforced high-strength concrete. *Arabian Journal for Science and Engineering*, 50(3), 2149-2168.

Sola E, Ožbolt J, Balabanić G, Mir ZM (2019). Experimental and numerical study of accelerated corrosion of steel reinforcement in concrete: Transport of corrosion products. *Cement and Concrete Research*, 120, 119-131.

Song HW, Saraswathy V (2007). Corrosion monitoring of reinforced concrete structures: A review. *International Journal of Electrochemical Science*, 2(1), 1-28.

Srivastava A, Mishra A, Singh SK (2025). Mechanical and durability study of nano TiO2 and nano SiO2 on fiber reinforced concrete. *Challenge Journal of Concrete Research Letters*, 16(1), 33–39.

Tanash AO, Budiea AMA, Md Jaafar MF, Muthusamy K, Zulkarnain F (2025). Experimental study on the mechanical performance of polypropylene fiber-reinforced concrete incorporating palm oil fuel ash as partial cement replacement. *Challenge Journal of Concrete Research Letters*, 16(3), 115–124.

Tarhan Y, Tarhan İH, Perrot A (2025). Improving bond performance of 3D-printable earth-based mortar reinforced with jute fibers. *Challenge Journal of Structural Mechanics*, 11(2), 99–105.

Tastani SP, Pantazopoulou SJ (2010). Direct tension pullout bond test: Experimental results. *Journal of Structural Engineering*, 136(6), 731-743.

Torre-Casanova A, Jason L, Davenne L, Pinelli X (2013). Confinement effects on the steel-concrete bond strength and pull-out failure. *Engineering Fracture Mechanics*, 97, 92-104.

Torres-Ortega R, Quiñonez-Bolaños E, Tejada-Tovar C, García-Díaz Y, Cabarcas-Torres I (2021). High-strength concrete with natural aggregates, silica fume and polypropylene macrofibers. *Ciencia e Ingeniería Neogranadina*, 31(2), 27-40.

Touahri A, Branci T, Yahia A, Ezziane K (2021). Effect of recycled polypropylene fiber on high strength concrete and normal strength concrete properties. *Advances in Materials Research*, 10(4), 267-281.

Tsiotsias K, Pantazopoulou SJ (2021). Bond behavior of high-performance fiber reinforced concrete under direct tension pullout. *Engineering Structures*, 243, 112701.

Urtekin Y, Çelik Z (2025). Investigation of the effects of re-curing on mechanical properties of basalt-polypropylene hybrid fiber concretes after exposure to high temperature. *Challenge Journal of Structural Mechanics*, 11(1), 14–23.

Uysal M, Tanyildizi H (2012). Estimation of compressive strength of self-compacting concrete containing polypropylene fiber and mineral additives exposed to high temperature using artificial neural network. *Construction and Building Materials*, 27(1), 404-414.

Varghese A, Anand N, Arulraj GP, Alengaram UJ (2019). Influence of fibers on bond strength of concrete exposed to elevated temperature. *Journal of Adhesion Science and Technology*, 33(14), 1521-1543.

Zhao J, Yang X, Fan J, Gao S, Ma H (2022). Research on dynamic compressive performance of polypropylene fiber reinforced high-strength concrete under freeze-thaw environment. *Advances in Materials Science and Engineering*, 2022, 9079019.

Challenge Journal of CONCRETE RESEARCH LETTERS

Research Article

Bio-based cementitious composites reinforced with natural fibers derived from Cedrus libani A.Rich. acicular leaf: Extraction, microstructural characterization, and mechanical performance after thermal exposure

Fatih Şamdan [a,*], Canan Şamdan [b], Mehmet Canbaz [a]

[a] *Department of Civil Engineering, Eskişehir Osmangazi University, 26040 Eskişehir, Türkiye*
[b] *Department of Chemical Engineering, Eskişehir Osmangazi University, 26040 Eskişehir, Türkiye*

ABSTRACT

This study investigates the physical and mechanical performance of bio-based cementitious composites produced with natural fibers obtained from dried, fallen acicular leaf of Cedrus libani A.Rich. The fibers underwent a multi-stage pre-treatment prior to composite production, including hot water extraction, alkaline treatment (NaOH), and $Ca(OH)_2$ mineralization. Changes in surface morphology and chemical composition were confirmed by SEM and EDS analyses, and significant calcium enrichment and increased roughness were observed on the fiber surface after mineralization. Specimens produced with aggregate- and additive-free mixtures were exposed to temperatures of 20, 200, and 400 °C for 3 hours at the end of the curing periods. Unit volume weight, ultrasonic pulse velocity, compressive, flexural, and splitting tensile strengths were determined, and the dynamic modulus of elasticity was calculated. The results showed that limited losses in mechanical properties occurred up to 200 °C, while more significant reductions in strength and stiffness occurred at 400 °C due to microcrack formation and weakening of the fiber-matrix interface. It was determined that mixtures with a high fiber/cement ratio partially limit crack progression and reduce strength loss in certain temperature ranges. The findings reveal the mechanical properties of Cedrus libani acicular leaf fibers as reinforcement in cementitious composites after thermal exposure.

ARTICLE INFO

Article history:
Received – February 14, 2026
Revision requested – March 12, 2026
Revision received – March 15, 2026
Accepted – March 28, 2026

Keywords:
Extraction
Characterization
Cementitious composites
Natural fiber
Mechanical performance
Thermal exposure

Citation: Şamdan F, Şamdan C, Canbaz M (2026). Bio-based cementitious composites reinforced with natural fibers derived from Cedrus libani A.Rich. acicular leaf: Extraction, microstructural characterization, and mechanical performance after thermal exposure. *Challenge Journal of Concrete Research Letters*, 17(2), 162–176.

1. Introduction

Composite materials are engineering materials that cannot be obtained from matrix and reinforcement components alone, but superior mechanical and physical properties are provided by using them together. When building materials are evaluated, cementitious composites are widely used, and detailed academic studies are conducted on this subject. In cementitious composite production, the aim is not only to provide high compressive strength but also to meet various purposes, such as lightness, workability, improved physical properties, resource efficiency, sustainability, and recycling. Fiber-reinforced cementitious composites are preferred to eliminate problems such as brittleness and crack formation and to highlight features such as crack bridging. These composites have been intensively researched in the literature for their contributions, including limiting brittle

* *Corresponding author*. E-mail address: fatihsamdan@eskisehir.edu.tr (F. Şamdan)
ISSN: 2548-0928 / DOI: https://doi.org/10.20528/cjcrl.2026.02.007

behavior, controlling crack formation and progression, and increasing ductility. The incorporation of fibers into the cement paste matrix directly affects the composite's mechanical behavior through adhesion, charge-transfer mechanisms, and microcrack-bridging effects at the fiber-matrix interface. These mechanisms suppress sudden fracture behavior, thereby increasing the composite's energy absorption capacity. Thus, fiber reinforcement stands out as an effective material design approach that improves the internal structural continuity of cementitious composites and enables controlled damage development.

Reinforcing cementitious composites with fibers is an effective method that significantly improves the matrix's mechanical performance and damage tolerance. Fiber reinforcement increases tensile and flexural strengths, suppresses brittle fracture behavior, and provides a more ductile deformation process (Bentur and Mindess 2007). It has been experimentally demonstrated that the crack-bridging mechanism formed by fibers in the matrix limits the progression of microcracks and reduces the rate of crack propagation (Li 2003). Similarly, the adhesion developed at the fiber–matrix interface is noted to increase residual bearing capacity and toughness by regulating charge transfer (Banthia and Trottier 1995). The positive effect of fiber supplementation on the energy absorption capacity of composites has been extensively evaluated, leading to marked improvements in impact and fatigue strength (Naaman 2003). It has also been reported that cementitious composites containing fibers exhibit superior properties compared to conventional concretes in reducing shrinkage cracks, controlling crack widths, and improving overall performance (Yousefieh et al. 2017). Taken together, these studies indicate that fiber reinforcement offers an effective material design approach that enables controlled damage development in cementitious composites and improves structural safety.

Fibers are classified as natural, synthetic, and metallic based on their origin, and each type affects the mechanical and physical behavior of cementitious composites through distinct mechanisms. This broad use is also reflected in recent studies on fiber-reinforced construction materials, where fibers are used to improve crack control, flexural response, load transfer, and overall mechanical performance in cementitious and other composite-based systems (Çelik et al. 2024; Ünal and Canbaz 2025; Baş 2025; Alshabrawi and Uysal 2025; Ünal et al. 2025). Natural fibers, in particular, are considered alternative or complementary reinforcing elements in certain applications within fiber-reinforced cementitious composites due to their lower density compared with synthetic and steel fibers, derivation from renewable raw materials, and relatively limited environmental impact. For natural fiber-reinforced lightweight cementitious materials, this contribution is strongly dosage-dependent: suitable contents can improve compressive and flexural performance, whereas excessive fiber incorporation may reduce workability, disturb fiber distribution, and limit hydration because of the high water absorption capacity of plant-based fibers (Uzun 2024). Although natural fibers are classified by origin as vegetable (lignocellulosic), animal, and mineral, vegetable fibers constitute the main body of the literature on cementitious composites. In this group, jute, flax, hemp, kenaf, sisal, coconut fiber (coir), abaca, cotton, and wood/cellulose-origin fibers stand out (Onuaguluchi and Banthia 2016). Studies show that natural fibers limit crack formation and progression through microcrack bridging in the cementitious matrix, thereby reducing shrinkage-induced cracking, especially in early-age behavior; for example, kenaf and jute fibers have been reported to significantly reduce plastic shrinkage crack width at certain dosages (Lura et al. 2025). In terms of mechanical performance, the use of vegetable fibers such as jute, in appropriate proportions, has been shown to affect fresh and hardened properties and crack control (Islam and Ahmed 2018). Similarly, studies with sisal fibers have reported increases in splitting tensile and flexural strengths and, at suitable dosages, prevention of plastic-shrinkage cracking compared with fiber-free mixtures (Veigas et al. 2022). However, because natural fibers pose risks related to interfacial adhesion and durability in alkaline environments and under wet-drying cycles, the literature emphasizes design strategies such as fiber surface modification, coating, or reducing matrix alkalinity to improve fiber/matrix compatibility. This is also supported by pull-out-based studies on natural fiber-reinforced mineral matrices, which show that fiber surface condition, matrix composition, and interfacial compatibility strongly influence bond resistance and stress transfer at the fiber-matrix interface (Tarhan et al. 2025). For example, post-crack behavior changes due to weakening of the fiber-matrix bond over time have been reported in alkaline-treated natural fiber-reinforced composite systems exposed to natural weathering conditions (Zukowski et al. 2018). Forest-origin natural fibers and plant wastes have also been examined as reinforcement or filler materials, including branches, bark, leaves, cones, sawdust, and chips. The use of lignocellulosic resources associated with forest waste in cementitious composites can reduce unit weight and support crack control through a low-density renewable reinforcement or filler approach, while also influencing processability and fiber-matrix interface strength (Savastano Jr et al. 2003). In studies using bark and woody wastes in fiber or particle form, positive contributions have been reported in terms of thermal insulation, shrinkage behavior, and crack control, although limited decreases in mechanical strength can be observed (Fiore et al. 2015; Merta and Tschegg 2013). Experimental research on cementitious composites with sawdust and wood meal additives has revealed that fiber-matrix adherence improves and performance can be increased when the fiber surface is harmonized with alkaline treatment or mineral additives (Pacheco-Torgal and Jalali 2011; Bilba and Arsène 2008). In studies on leaf-based lignocellulosic supplements, it has been reported that coniferous and broad-leaved plant wastes limit the spread of microcracks and support ductile behavior thanks to their low elastic modulus (Toledo Filho et al. 2005; Silva et al. 2010). In a study in which pine needle leaf fiber (after alkaline pretreatment) was used,

the compressive strength, tensile and splitting tensile strength, and ductility/toughness values of the composite concrete produced increased; it is reported that the effect is explained through fiber–matrix adherence and bridging capacity (Long and Wang 2021).

Exposure of cementitious composites reinforced with natural fibers to elevated temperatures can affect fiber-matrix interaction and the continuity of the internal structure, leading to temperature-dependent changes in mechanical properties. More generally, high-temperature studies on fiber-reinforced concretes indicate that residual mechanical properties and ultrasonic pulse velocity are affected by fiber type, thermal stability, crack development, and fiber-matrix interface changes after heating (Urtekin and Çelik 2025). For this reason, studies have examined the behavior of natural fiber-reinforced cementitious composites under high temperatures. In most of these studies, samples were heated to temperatures in the range of 200–800 °C and evaluated based on compressive, flexural, and tensile strength; mass loss; crack development; and spalling tendency after cooling. The general trend is that as temperature increases, mechanical properties decrease due to dehydration of hydrate products and increased porosity. In addition, because vegetable fibers are organic, degradation at the fiber-matrix interface and thermal degradation of the fibers are reported as critical mechanisms. It has been determined that the high-temperature performance and critical temperature band in plant-based fiber-reinforced concretes are concentrated around 350–450 °C, with damage accelerating above this range. It has also been reported that certain fiber types and geometries may help limit microcracks and reduce the risk of spalling (Al-Dala'ien et al. 2025). In an experimental study on UHPC, exploratory spalling was observed only at 600 °C in steel-fiber mixtures; however, a jute fiber + micro/macro steel fiber hybrid was effective in preventing spalling at 600 °C and provided better results in tensile/flexural strength and toughness parameters (Ridha 2024). In a study of Kenaf fiber-reinforced concretes, experiments conducted between 100 and 800 °C showed a significant deterioration in physical and mechanical properties as temperature increased, highlighting the critical role of thermal damage at the fiber-matrix interface (Aluko et al. 2023). Another study reported that natural fibers can limit spalling by facilitating vapor-pressure discharge as temperature rises, and that the use of sisal+steel hybrid fibers can suppress spalling through a permeability/channel formation mechanism (Ren et al. 2022). Similarly, bamboo fibers regulate internal pressure and crack propagation by creating a "channel" effect through carbonization in the range of 200–800 °C; it has been shown that the hybrid bamboo/steel fiber design can reduce the risk of spalling and maintain residual strength better than steel-fiber-only systems (Zhao et al. 2025). It was also emphasized that natural fibers do not increase strength in all cases; in hemp fiber concretes heated to 400 °C, the strength effect of the fibers may be limited, and a micromechanism that reduces crack propagation occurs despite partial fiber decomposition (Grubeša et al. 2018). It has been reported that the compressive strength of hemp fiber alkali-activated cement foam can improve in the 100–200 °C band depending on the fiber dosage, but the loss of strength becomes evident with thermal degradation of the fiber at 400 °C and 800 °C (Dhasindrakrishna et al. 2023).

When the behavior of cementitious composites reinforced with forest wastes under temperature is examined, the literature reports that strength and mass loss occur in samples directly exposed to high temperatures. In a study on samples reinforced with date palm fiber, it was reported that exposure to 200–300 °C caused a decrease of approximately 6.4–14.8% in compressive strength and 2.1–3.7% in unit volume weight. It has been stated that at these temperature levels, the fibers partially maintain the microcrack-bridging effect, and losses in tensile strength in bending and splitting generally remain in the range of 5.6–9.3%. With the increase in temperature to the range of 400–600 °C, significant thermal degradation was observed in the lignocellulosic structure of the fibers; this situation led to a decrease of 32.4–48.7% in compressive strength and 37.2–58.9% in flexural strength, while unit weight losses were reported to reach 6.5-9.8%. At temperatures above 600 °C, compressive and tensile strength decreased by 61.3–79.6% due to major carbonization or decomposition of the fibers; on the other hand, it has been emphasized that the voids formed by the decomposition of the fibers can relieve vapor pressure, limiting the risk of explosive spalling in some mixtures (Kareem 2025). Another study on date palm fiber shows that as temperature increases, overall mass loss rises and strength decreases due to degradation of the binder hydrate products and increased porosity. In mixtures containing palm leaf-derived fiber, samples were examined after 2 hours of heat exposure; mass loss in the control mixture increased from 0.59% to 4.47% over 200–800 °C, while compressive strength decreased by 46.7% after 800 °C. With higher fiber content, compressive strength decreased by up to 61.8% after 800 °C. These results indicate that fiber addition can increase microstructural gapping and that damage is accelerated by high-temperature water loss and crack network growth; however, strength is retained at moderate temperatures such as 200–400 °C with appropriate mineral additive/binder design (Adamu et al. 2023). Similarly, in another study focusing on mass loss and compressive strength under high temperature, date palm fiber concretes were evaluated over 300–900 °C; it has been reported that the optimum design yields 25.17 MPa strength and 9.84% mass loss at 800 °C, and that approximately 53.5% strength loss occurs as the compressive strength of 54.13 MPa at 24 °C decreases to 25.17 MPa at 800 °C (Adamu et al. 2025). In summary, literature findings show that the mechanical contribution of natural fibers occurs mainly through crack control, and that this contributes positively to mechanical performance. However, fiber-reinforced cementitious composites exposed to different temperatures change in their physical and mechanical properties after temperature, just like normal cementitious composites.

According to the General Directorate of Forestry's 2024 records, cedar (Cedrus) is distributed across ap-

proximately 580 thousand hectares in Turkey (General Directorate of Forestry 2025). Cedrus libani A.Rich., a species of the genus Cedrus, has acicular leaf about 15–35 mm long and is characterized by its rhomboidal cross-sectional geometry and relatively high specific surface area. Unique to the Pinaceae family, it has a distinct wax layer on the leaf surface, and its chemical structure consists mainly of lignocellulosic components, including cellulose, hemicellulose, lignin, and resin. Over time, the natural aging process gradually degrades this wax layer, resulting in increased surface roughness (Güney et al. 2016). Thanks to their high specific surface area and age-related increase in roughness, Cedrus libani fibers have the potential to reduce unit weight in the composite, limit microcrack formation, and improve strength and durability by forming an isotropic fiber network in the cemented matrix.

Today, various cement-based composite systems are being developed that utilize forest products and forest-based wastes. These materials are widely used, especially in the construction sector and in the production of different architectural elements. Examples of this approach include wood-precast concrete composites containing wood-based aggregates or fibers, as well as wood-cement-based pressed board products. In such composite systems, mineral aggregate is often not used. Additionally, to better examine the structural characteristics of the material and the fiber-matrix interaction, a fiber-reinforced structure is preferred within the cement matrix. In this study, natural fibers were extracted from Cedrus libani A. Rich coniferous leaves, which are considered forest waste. After characterizing the fibers obtained, they were used to produce cement matrix-based composites with different fiber ratios. When reviewing the literature, similar studies have investigated the mechanical behavior of cement-bonded composites made from wood wastes and their performance, particularly under high temperatures (Canbaz et al. 2021; Garcez et al. 2016; Mahzabin et al. 2013). In this study, fiber-reinforced cementitious composites with different cement ratios were prepared using dried and spilled acicular leaf of Cedrus libani A.Rich as natural fibers. The specimens were then exposed to temperatures of 20, 200, and 400°C for 3 hours. The fibers were randomly distributed in all directions, creating an isotropic fiber arrangement. Aggregates and additives were not used in the mixture so that the physical and mechanical effects of the fibers, which change with temperature, were fully observed. At the end of the 7- and 28-day curing periods, unit weight, ultrasonic pulse velocity, compressive and flexural strength, and splitting tensile strength were measured for the specimens produced. After exposure to temperatures of 20, 200, and 400°C, the physical and mechanical properties of the specimens were examined.

Numerous studies in the literature explore the physical and mechanical behavior of cementitious wood composites. For instance, Garcez et al. (2016) analyzed how different wood species, particle treatments, and mixing ratios affect the density and mechanical properties of cement–wood composites, revealing that the type of wood and mixing ratio are key factors in composite performance. Similarly, Mahzabin et al. (2013) studied how chemical modification of wood fibers influences the physical and mechanical properties of the cement matrix, demonstrating that chemical treatments to boost fiber-matrix compatibility can markedly improve strength. Additionally, Canbaz et al. (2021) investigated the mechanical behavior of cement-bonded composites containing sawdust exposed to high temperatures, noting that increased temperature can lead to microcrack formation and reduced strength. However, most existing research focuses on wood waste in the form of sawdust or particles, and studies on the use of natural fibers from Cedrus libani acicular leaves in cement-based composites, particularly regarding their mechanical behavior under high temperature, are very limited. Therefore, fiber dosage, water absorption behavior, surface condition, and fiber-matrix bond quality should be considered together when evaluating crack-bridging capacity and mechanical performance in natural fiber-reinforced cementitious composites (Uzun 2024; Tarhan et al. 2025). In this context, this study extracts and characterizes natural fibers from Cedrus libani acicular leaves and examines their influence on the mechanical performance of cementitious composites, especially under high temperature conditions.

2. Materials and Methods

2.1. Materials

In this study, Çimsa CEM I 52.5 R cement was used, and its physical and chemical properties are presented in the table. As natural fibers, dried, fallen waste leaf of the Cedrus libani A.Rich tree were used. The properties of the fiber are presented in Table 2. City tap water was used as mixing water, and the results of the chemical analysis are presented in Table 3.

Table 1. Physical and chemical properties of CEM I 52.5 R cement.

Physical properties		
Density (g/cm³)	3.06	
Blaine (m²/g)	4300	
Compressive Strength (MPa)	7.day 50	28.day 60
Setting time (min)	Initial 95	Final 125

Chemical content (%)			
CaO	64.70	SiO_2	21.20
Al_2O_3	4.60	Fe_2O_3	0.28
MgO	1.35	Na_2O	0.38
SO_3	3.50	K_2O	0.20
Cl	0.01	LOI	3.50

Table 2. Physical properties of Cedrus libani A.Rich. and acicular leaf.

Length (mm)	15–35	Unit Weight (g/cm³)	0.13
Width (mm)	0.8–2.1	Density (g/cm³)	0.48–0.51*
Leaf type	Acicular	Modulus of elasticity (GPa)	0.67–7.80*
Leaf shape	Needle rhomboidal	Poisson ratio	0.052–0.522*
		Water absorption (%)	80.7*
Structure and composition		Lignocellulosic fibers (hemicellulose, cellulose, lignin, and wax)*	

* The data was obtained for Cedrus libani A. Rich (Efe 2021; Güney et al. 2016; Güntekin 2022; Şahin and Çam 2022).

Table 3. Chemical analysis report for the drinking water treatment plant.

Chemical analysis results (mg/L)					
pH	7.28	SO_4	70	Al	<0.012
Turbidity (NTU)	0.10	NO_3	7.5	Fe	<0.0075
Conductivity (µS/cm)	664	Cl	43	Mn	<0.0007
Hardness (Fr°)	32	NH_4	<0.05		

2.2. Method and tests

2.2.1. Fiber pretreatment

The dry, acicular leaf of Cedrus libani A. Rich., collected from the forest ecosystem, were subjected to a comprehensive multistage pretreatment prior to incorporation into cementitious composites. Initially, the materials were manually sorted to eliminate biological and environmental impurities, including soil particles, sand, ash, and fungal residues. First, the collected leaves were sieved to remove foreign substances. Then, to ensure the fiber size falls within a specific range, the material was passed through a sieve with a mesh opening of 2.36–0.60 mm and classified. This process guarantees that the fibers have a more uniform size distribution. The cleaned leaf was thoroughly rinsed with deionized water to remove superficial contaminants and subsequently oven-dried at 60 °C for 24 h. To remove water-soluble extractives, such as tannins and phenolic compounds, that may interfere with cement hydration, hot-water extraction was conducted at 80 °C for 4 h. This procedure was repeated twice using fresh deionized water to ensure effective removal of soluble organic constituents. After extraction, the residues were filtered and dried before undergoing chemical treatment. Alkaline pretreatment was performed by immersing the fibers in a 2.5 wt% NaOH aqueous solution under continuous stirring for 4 h. This step aimed to remove hemicellulosic components and partially increase surface roughness, thereby improving surface reactivity. The treated fibers were rinsed with deionized water until neutral pH was achieved and then oven-dried. For the mineralization stage, the fibers were immersed in a saturated $Ca(OH)_2$ solution at 30 °C for 12 h using a solid-to-liquid ratio of 2:10 (g mL^{-1}). The process was repeated twice with fresh $Ca(OH)_2$ solution to promote uniform mineral deposition on the fiber surface. Finally, the mineralized fibers were gently rinsed to remove excess surface deposits and dried at 60 °C prior to their incorporation into cementitious composite mixtures.

2.2.2. Preparation of specimens

In this study, specimens were produced using natural fibers obtained from the acicular leaf of Cedrus libani A.Rich in different proportions. After the natural fiber-reinforced cementitious composite specimens were exposed to temperatures of 20, 200, and 400°C for 3 hours, their physical and mechanical properties were examined. The cementitious composite mixture is given in Table 4. To observe the effect of the natural fiber, no additives or aggregates other than cement, water, and natural fiber were used. Various cement-based composite systems are being developed, incorporating forest products and waste materials. These materials are mainly used in construction and in making different architectural components. Current applications include wood-precast concrete composites with wood-based aggregates or fibers, as well as wood-cement-based pressed boards. Typically, mineral aggregate is not used in these composite systems, and a fiber-reinforced structure is preferred within the cement matrix to better understand the material's structural behavior and fiber-matrix interaction. In such systems, the performance is often assessed by comparing mixtures with different fiber contents. Therefore, this study compares mixtures with varying fiber-to-cement ratios and does not include a fiber-free control sample like other studies in the literature (Canbaz et al. 2021; Garcez et al. 2016; Mahzabin et al. 2013). The water/cement ratio and the amount of natural fiber were kept constant, while the cement content was increased.

The specimens were prepared by following the mixing and production procedures specified in the TS EN 196-1 (2016) standard. During production, special attention was given to achieving a homogeneous distribution of fibers within the cement matrix without agglomeration. This aims to ensure that fibers are evenly distributed in various directions within the composite structure, resulting in a more uniform and isotropic behavior of the material. Additionally, after placing the mixture into the formwork, pressure was applied, similar to the process used for manufacturing wood-cement-based pressed boards, to ensure the mixture was more uniformly and neatly placed within the formwork.

Cedrus libani A.Rich. The acicular-leaf mixture was symbolized by CL, and specimen types were identified by adding the amount of cement used to the codes. Standard specimens of 4x4x16 cm were produced and cured at 20 ± 2 °C for 28 days. Photographs of CL-type specimens are shown in Fig 1.

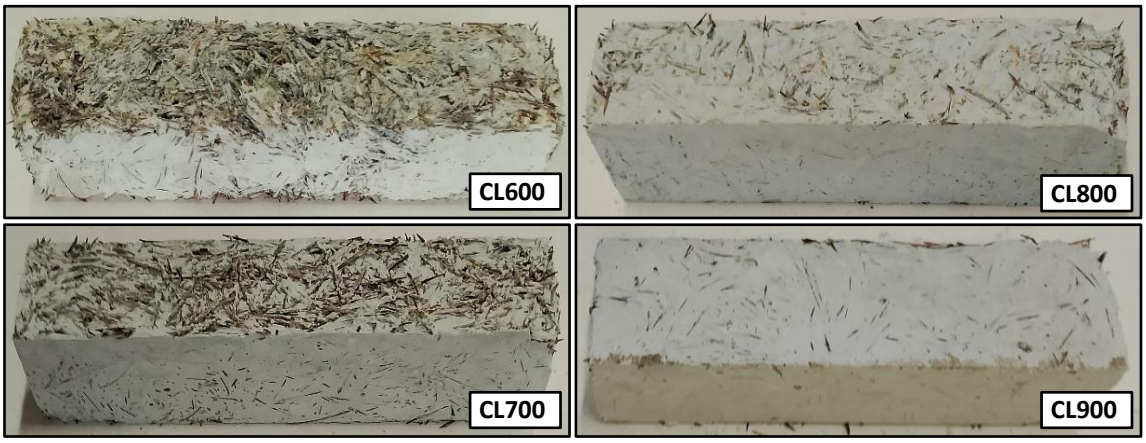

Fig. 1. Photographs of CL600–900 specimens after production.

Table 4. Proportions of materials as per the mixture.

Code	Water / Cement (by wt.)	Fiber (g)	Cement (g)	Fiber / Cement (by wt.)	(by vol.)
CL600	0.40	130	600	0.22	0.32
CL700			700	0.19	0.28
CL800			800	0.16	0.24
CL900			900	0.14	0.22

2.2.3. Thermal exposure of specimens

After curing, the specimens were kept in the laboratory oven for 1 hour to ensure they were dry. Then, thermal exposure was applied to the specimens using a Nevola Reis 110/10 thermocouple-controlled furnace. During thermal exposure, the temperature was gradually increased to an average rate of 80–100 °C/min. Because the furnace system has a control mechanism that minimizes temperature fluctuations, the target temperatures are reached more steadily. After reaching the target temperatures of 200 and 400 °C, the specimens were maintained at these levels for 3 hours. Once the thermal exposure was complete, the specimens were removed from the furnace and allowed to cool naturally at room temperature in a laboratory environment.

Temperature levels of 20, 200, and 400 °C were applied in the experimental program. These levels were chosen because 20 °C represents the reference condition at room temperature, 200 °C indicates a moderate thermal effect in cementitious materials where free water loss and initial microstructural changes occur, and 400 °C marks a critical temperature range nearing the thermal degradation and ignition points reported in the literature for lignocellulosic fibers.

The main goal of this study is to analyze how natural fiber reinforced cement-based composites behave under high temperatures and to identify the damage mechanisms, especially at the fiber-matrix interface. Natural fibers from plants have a lignocellulosic structure mainly made up of hemicellulose, cellulose, and lignin (Şahin and Çam 2022). These components degrade at different temperatures as the temperature rises, leading to significant changes in the fiber's structural integrity. The literature reports that the thermal degradation and ignition temperatures of lignocellulosic biomass components are about 370 °C for hemicellulose, 410 °C for cellulose, and 405 °C for lignin (Yang et al. 2007; Cao et al. 2019). This indicates that the fiber structure can quickly degrade at temperatures of 400 °C and above, greatly increasing the risk of burning or ignition. The study selected a temperature range where both fiber-matrix interactions and changes in mechanical performance could be observed, while still maintaining specimen integrity. Specifically, experiments were conducted at 20, 200, and 400 °C, with the upper limit of 400 °C chosen to account for the critical temperature zone where lignocellulosic fibers begin to ignite and degrade rapidly. This approach allowed for a safe and controlled evaluation of the thermal damage mechanisms and performance changes of natural fiber-reinforced cement-based composites at high temperatures.

2.2.4. Mechanical tests of specimens

Prismatic specimens, measuring 40×40×160 mm, were subjected to a three-point flexural test in accordance with the TS EN 196-1 (2016) standard after exposure to temperatures of 20, 200, and 400°C. During the experiments, loading was carried out using the clearance and loading speed specified in the standard. Samples produced at different fiber/cement ratios were examined for their mechanical behavior after exposure to different temperatures.

Cubic samples measuring 40×40×40 mm, produced with various fiber/cement ratios, were exposed to temperatures of 20, 200, and 400°C, and then a compression test was performed in accordance with TS EN 196-1 (2016). The experiments were performed on a universal test press, and the samples were loaded until they failed

under the established standard conditions. The mechanical properties of the samples produced at different fiber/cement ratios and exposed to various temperatures were evaluated.

To determine the splitting tensile strength of the specimens, loads were applied perpendicularly to the cross-sections, and the splitting tensile strengths generated along the sample cross-section were measured.

In the experimental program, specimens were produced considering three different temperature levels, four types of specimens, and three repetitions for each type. In this process, a total of 36 specimens were tested for each mechanical test. The average results of the experiments for each variable were calculated, and the standard deviation (SD) and coefficient of variation (CV) values are shown in Table 5.

Table 5. Statistical analysis of data.

Compressive strength (MPa)					Flexural strength (MPa)				
Temperature (°C)	Code	Mean	SD	CV (%)	Temperature (°C)	Code	Mean	SD	CV (%)
20	CL600	8.27	0.52	6.2	20	CL600	1.36	0.07	5.1
	CL700	9.40	0.49	5.2		CL700	2.25	0.18	7.8
	CL800	10.49	0.80	7.6		CL800	3.09	0.21	6.8
	CL900	11.10	0.75	6.7		CL900	3.45	0.26	7.5
200	CL600	7.84	0.58	7.4	200	CL600	1.23	0.07	5.3
	CL700	9.02	0.69	7.7		CL700	1.92	0.12	6.1
	CL800	9.69	0.61	6.3		CL800	2.70	0.17	6.2
	CL900	10.13	0.60	5.9		CL900	3.02	0.23	7.7
400	CL600	7.56	0.36	4.8	400	CL600	1.18	0.08	6.6
	CL700	8.35	0.43	5.2		CL700	1.74	0.12	7.0
	CL800	8.78	0.65	7.5		CL800	2.33	0.16	6.9
	CL900	9.09	0.42	4.6		CL900	2.52	0.16	6.5
Splitting tensile strength (MPa)					Unit weight (kg/dm^3)				
Temperature (°C)	Code	Mean	SD	CV (%)	Temperature (°C)	Code	Mean	SD	CV (%)
20	CL600	1.46	0.09	6.3	20	CL600	1.420	0.08	5.6
	CL700	1.55	0.07	4.4		CL700	1.473	0.09	6.0
	CL800	2.04	0.09	4.7		CL800	1.570	0.09	6.0
	CL900	2.28	0.16	7.2		CL900	1.596	0.07	4.4
200	CL600	1.38	0.07	5.3	200	CL600	1.280	0.07	5.8
	CL700	1.50	0.08	5.3		CL700	1.364	0.09	6.4
	CL800	1.94	0.10	5.0		CL800	1.500	0.06	4.1
	CL900	2.13	0.16	7.5		CL900	1.547	0.07	4.5
400	CL600	1.34	0.07	5.0	400	CL600	1.218	0.08	6.3
	CL700	1.38	0.07	5.0		CL700	1.282	0.09	7.1
	CL800	1.69	0.11	6.4		CL800	1.429	0.07	5.0
	CL900	1.84	0.08	4.5		CL900	1.456	0.09	5.9
UPV (km/h)					$E_{dynamic}$ (Gpa)				
Temperature (°C)	Code	Mean	SD	CV (%)	Temperature (°C)	Code	Mean	SD	CV (%)
20	CL600	2.38	0.15	6.3	20	CL600	8.16	0.57	7.0
	CL700	2.45	0.15	6.2		CL700	9.02	0.58	6.4
	CL800	2.62	0.14	5.4		CL800	10.98	0.53	4.8
	CL900	2.69	0.21	7.9		CL900	11.76	1.34	11.4
200	CL600	2.23	0.15	6.7	200	CL600	6.49	0.50	7.7
	CL700	2.28	0.13	5.7		CL700	7.24	0.36	5.0
	CL800	2.52	0.14	5.5		CL800	9.74	0.68	7.0
	CL900	2.63	0.11	4.2		CL900	10.90	0.43	3.9
400	CL600	2.08	0.10	4.8	400	CL600	5.38	0.17	3.2
	CL700	2.16	0.14	6.6		CL700	6.09	0.37	6.1
	CL800	2.42	0.17	7.0		CL800	8.53	0.77	9.0
	CL900	2.50	0.15	6.0		CL900	9.24	0.57	6.2

3. Results and Discussion

3.1. Microstructural and chemical characterization

As shown in Fig. 2a, the untreated fibers display a relatively smooth and dense surface structure common to lignocellulosic materials that maintain their waxy and hemicellulosic layers. These traits typically inhibit mechanical interlocking within cementitious matrices due to a reduction in surface roughness. Comparable morphological characteristics in unprocessed plant fibers were also documented, observed that fewer surface irregularities were linked to a decrease in interfacial bonding potential (Melichar et al. 2024).

In contrast, Fig. 2b shows that treatment with $Ca(OH)_2$ significantly alters the fiber surface. After undergoing alkaline treatment and subsequent mineralization, there is a notable increase in surface roughness along with the formation of localized mineral aggregates. Alkaline conditions can prompt structural rearrangements, which in turn boost surface reactivity. This mechanism aligns with the morphological changes observed in the present study, in which alkali-mediated surface activation increases the potential for fiber-matrix interactions. (Hu et al. 2024).

The EDS spectra show a distinct compositional shift following the mineralization process. As illustrated in Fig. 2c, the untreated fibers primarily exhibit peaks from carbon and oxygen, indicating their lignocellulosic composition, with carbon as the predominant element and oxygen as the secondary one. The absence of measurable calcium indicates that the untreated surface is entirely organic, consistent with the lignin–cellulose–hemicellulose structures observed in native biomass fibers (Das et al. 2024). After $Ca(OH)_2$ treatment (Fig. 2c), a pronounced calcium peak emerges, with Ca reaching approximately 50–53 wt%, while carbon decreases to around 19–20 wt% and oxygen increases to roughly 27–28 wt%. This marked shift from a carbon-dominated to a calcium-rich surface composition confirms successful mineral deposition. Similar calcium enrichment accompanied by relative carbon reduction has been documented following Ca-based surface mineralization of natural fibers, where inorganic precipitation partially masks the organic substrate and alters the surface chemistry (Li et al. 2025; Zhang et al. 2025).

Elemental mapping (Fig. 2d-e) further confirms that calcium is distributed across the treated fiber surface rather than uniformly embedded within the bulk structure. The formation of calcium-rich domains indicates surface precipitation and partial mineral coverage. This local mineralization has been associated with increased interfacial stiffness and improved load transfer in cemented composites in some studies (Feng et al. 2025; Melichar et al. 2024).

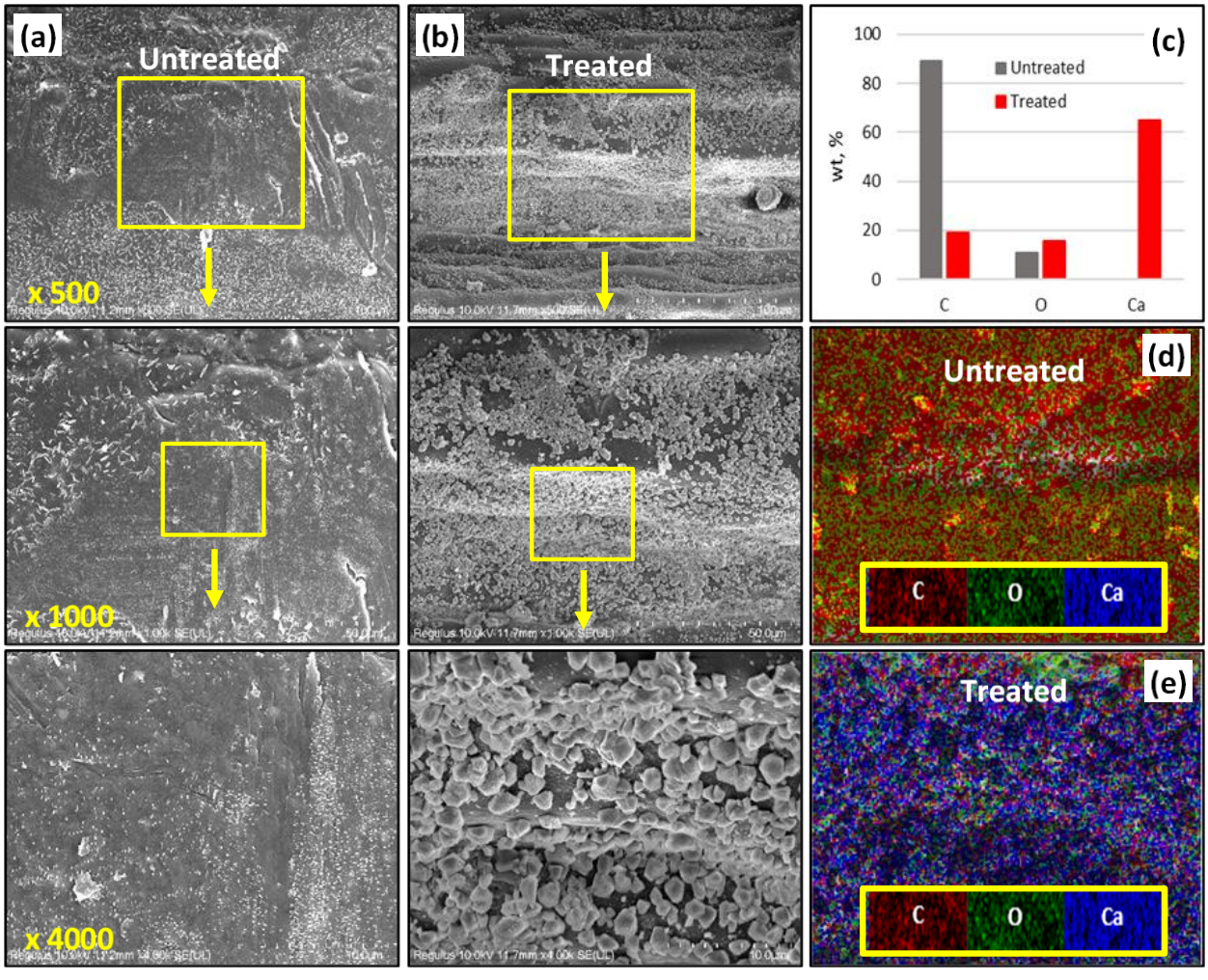

Fig. 2. Untreated (a) and treated (b) fiber SEM images; (c) EDS analysis; (d, e) Elemental mapping.

Changes in fiber morphology after surface treatments significantly influence the microstructural behavior of the composite material. Increased roughness on the fiber surface following alkaline and calcium hydroxide treatments, along with mineral phase deposits, promote mechanical interlocking at the fiber-matrix interface. This enhances the bond between cement hydration products and the fiber surface, leading to more efficient load transfer. Performance under high temperatures is affected not only by the reduction in mechanical properties but also by microstructural and chemical transformations within the composite. Natural fibers with lignocellulosic structures primarily contain hemicellulose, cellulose, and lignin, which degrade thermally at different temperature ranges. Partial degradation of the fiber structure, especially at elevated temperatures, can cause loss of adhesion, formation of microgaps, and development of microcracks at the fiber-matrix interface. In the cement-based matrix, processes such as hydrate phase dehydration, bond weakening, and internal stress buildup also occur as temperature rises. When considering these microstructural and thermochemical changes together, it becomes clear that the variation in mechanical performance of composite materials at high temperatures is closely linked to thermal degradation of the fiber structure and weakening of interfacial interactions.

On the other hand, the natural fibers in the composite structure play a crucial mechanical role, especially during crack propagation. The fibers act as a bridge between crack surfaces by restricting the progression of microcracks in the matrix and enabling charge transfer to continue through the fibers. The crack-bridging effect delays the sudden fracture of composite materials because the fibers show more ductile behavior than the matrix. Mechanical clamping of the fibers to the matrix and improved bonding at the interface reduce crack growth and enhance the composite's energy absorption capacity. This is also supported by fracture behavior observed, especially in flexural and splitting tensile tests. During these experiments, it was observed that the specimens did not break suddenly and destructively; instead, they formed a bridge between the cracked surfaces with the fibers, preventing complete separation. The fibers continued to carry loads between the cracked surfaces, causing the specimens to retain some integrity and display more ductile behavior even after fracture. This indicates that the fiber-matrix interaction in natural fiber-reinforced cement-based composites significantly contributes not only to initial mechanical strength but also to the fracture process and damage development.

3.2. Compressive strength

First of all, the cement-based composites developed in this study are designed for applications similar to wood-cement composites and wood-based cement binder products in terms of their intended use. These materials are widely used in producing different architectural elements, especially in the construction industry, with examples including wood-precast concrete composites containing wood-based aggregates or fibers and wood-cement-based pressed board products. Since these materials are not typically used as load-bearing structural elements, high compressive strength is not an expected characteristic of such composite systems. The compressive stresses measured in these products are generally low (Canbaz et al. 2021; Garcez et al. 2016; Mahzabin et al. 2013). The main reason for the low compressive stress is that the woody content in the mixture bonds weaker than cement, which increases the void ratio (Canbaz et al. 2021).

The compressive strength results presented in Fig. 3 show that cementitious composites reinforced with natural fibers from acicular Cedrus libani A.Rich exhibit a significant but gradual loss of strength with increasing temperature. For all mixtures, the decrease in compressive strength after 200 °C was limited; in specimens, it ranged from about 5.25% to 8.76%. Compressive strength is largely preserved due to the removal of free water and limited microstructural changes up to 200 °C. At 400 °C, total strength losses ranged from 8.58% to 18.08% compared with specimens at 20 °C. Compressive strength losses are mainly related to microcracks developing in the cement paste with increasing temperature, weakening of adhesion at the fiber-matrix interface, and gradual degradation of lignocellulosic coniferous fibers in the range of 200–400 °C. The higher strength loss at 400 °C (16.33–18.08%), especially in the CL800 and CL900 series with high cement content, indicates that a more rigid and dense matrix structure is more sensitive to crack development under thermal stresses.

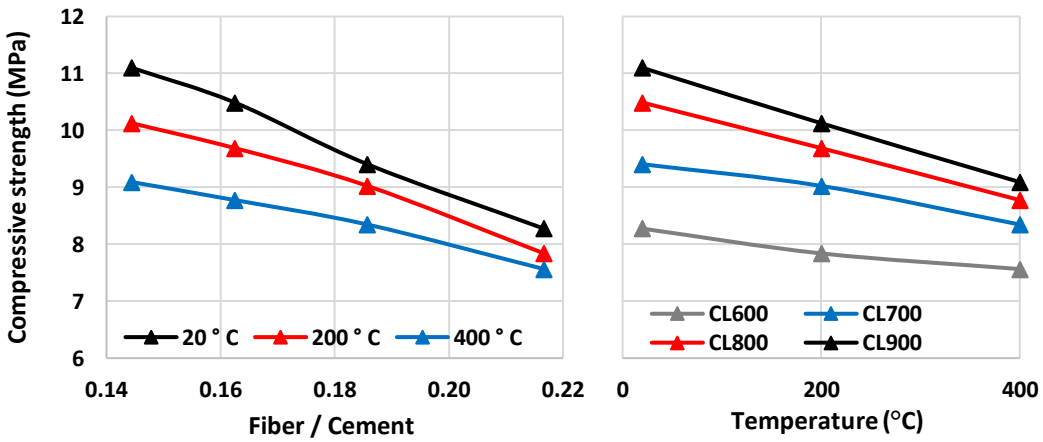

Fig. 3. Compressive strength of specimens based on changes in fiber/cement ratio and temperature after thermal exposure.

On the other hand, in CL600 and CL700 specimens, microcracks are partially limited thanks to the higher fiber/cement ratio, and the strength loss is more limited at 400 °C. These findings show that Cedrus libani needle-leaf fibers can contribute to the maintenance of compressive strength by delaying crack propagation at certain fiber/cement ratios under high temperature.

3.3. Flexural strength

The flexural strength results presented in Fig. 4 reveal a significant and systematic decrease in strength with increasing temperature in cementitious composites reinforced with Cedrus libani acicular leaf fiber. When flexural strengths measured at 20 °C are compared with those exposed to 200 °C, a loss of approximately 9.8-14.8% is observed. For samples exposed to 400 °C, the flexural strength loss ranges from 13.4% to 27.1%. This indicates that, with the fiber content held constant across temperature levels, increasing the cement dosage significantly increases flexural strength. Flexural strength is more sensitive to temperature increases than compressive strength, and this effect is particularly evident in the 200–400 °C range. Because flexural behavior is governed by tensile stresses, microcracks in the cement paste, along with weakening of adhesion at the fiber-matrix interface as temperature rises, lead to proportionally greater losses in flexural strength. The greater strength losses observed at 400 °C in CL800 and CL900 specimens with high cement content (24.6–27.1%) suggest that the denser, more rigid matrix structure is more susceptible to crack formation under thermal stresses. In contrast, the higher fiber/cement ratio in the CL600 and CL700 samples appears to partially limit microcrack development, and therefore the relative losses in flexural strength remain at lower levels. In this context, Cedrus libani acicular leaf fibers play a supporting role in flexural behavior at low and medium temperatures, but this contribution becomes limited as the fiber-matrix interaction weakens when the temperature reaches 400 °C.

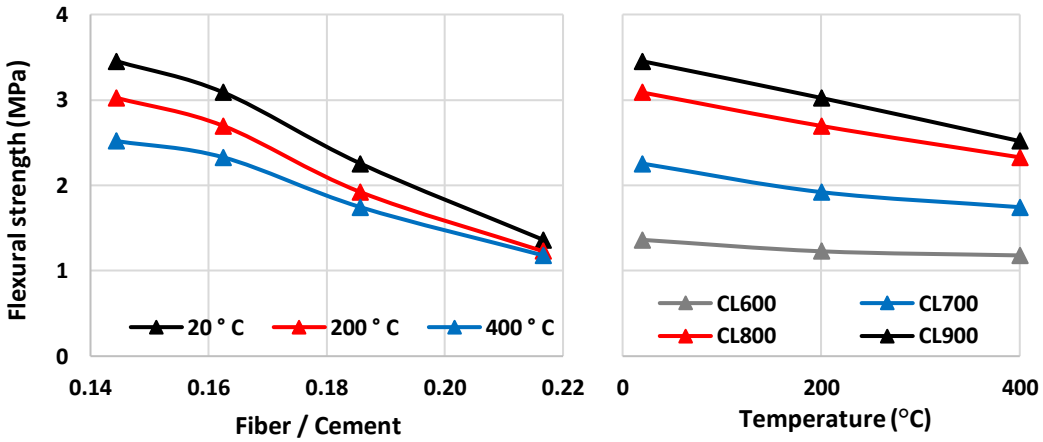

Fig. 4. Flexural strength of the specimens influenced by changes in fiber/cement ratio and temperature after thermal exposure.

3.4. Splitting tensile strength tests

The splitting tensile strength results presented in Fig. 5 show that the tensile behavior of Cedrus libani acicular leaf fiber-reinforced cementitious composites weakens systematically with increasing temperature. With the temperature increase to 200 °C, the strengths decreased by approximately 3.1–6.5% compared to the 20 °C reference, and after the application of 400 °C, the strength losses reached 8.6–19.1%. This trend in splitting tensile strength can be associated with the weakening of the fiber-matrix interaction, which is sensitive to tensile stresses, as the temperature increases. The occurrence of higher proportional strength losses (additional decrease in the range of 12.5–13.4%) in the CL800 and CL900 specimens, especially in the range of 200–400 °C, suggests that the more rigid and dense matrix structure exhibits a more sensitive response to microcrack formation under thermal stresses. On the other hand, it is seen that microcracks are partially limited in CL600 and CL700 mixtures thanks to the higher fiber/cement ratio, and the additional strength loss remains at lower levels after 400 °C. In this context, it was found that Cedrus libani acicular leaf fibers contribute to splitting tensile strength by delaying the progression of tensile cracks at low and medium temperatures; however, when the temperature reaches 400 °C, this contribution decreases significantly with increasing damage to the fiber-matrix interface.

3.5. Unit weight

The unit weight results after applying the temperature shown in Fig. 6 indicate that a significant density loss occurs as temperature increases in cementitious composites reinforced with Cedrus libani acicular leaf fiber. Unit weight values measured at 20 °C were 1,420–1,596 kg/dm^3. With the rise in temperature to 200 °C, unit weights decreased to 1,280–1,547 kg/dm^3. This corresponds to unit weight losses of approximately 9.9% for CL600, 7.4% for CL700, 4.4% for CL800, and 3.1% for CL900, compared with the 20 °C reference.

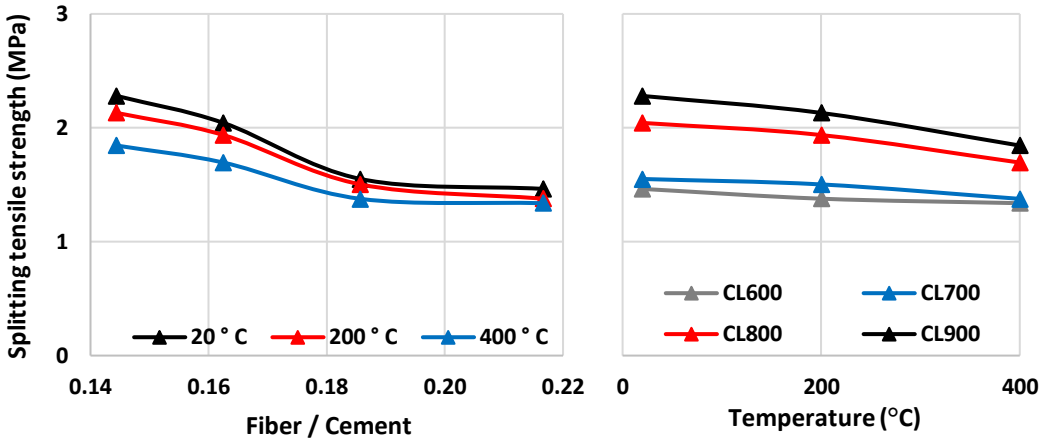

Fig. 5. Variation in the splitting tensile strength of the specimens concerning fiber/cement ratio and temperature after thermal exposure.

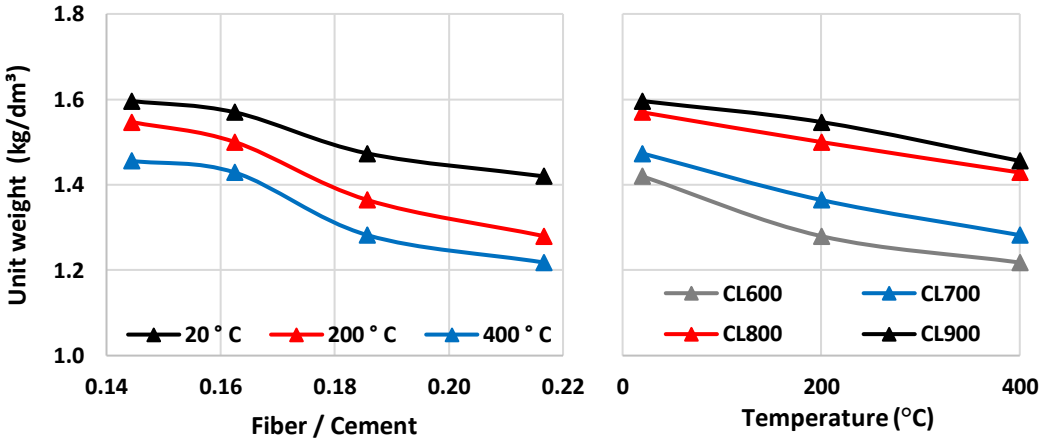

Fig. 6. Changes in the unit weight of specimens depending on the fiber/cement ratio and exposure temperature.

As seen in Fig. 6, unit weight loss was more limited after 200 °C in mixtures with a low fiber/cement ratio and higher cement content. With the increase in temperature to 400 °C, the decrease in unit weight became more pronounced, and the values were measured as 1,218–1,456 kg/dm^3. Accordingly, total unit weight losses compared with 20 °C reached approximately 14.2% in CL600, 13.0% in CL700, 9.0% in CL800, and 8.8% in CL900. The higher unit weight loss in the CL600 and CL700 samples with a higher fiber-to-cement ratio indicates that the continuity of the internal structure deteriorates more under temperature effects, and porosity increases more markedly. On the other hand, in CL800 and CL900 mixtures, the unit weight loss after temperature exposure is more limited due to the denser cement matrix; however, at 400 °C, it is evident that damage to the internal structure becomes apparent in all mixtures.

3.6. Ultrasonic pulse velocity

The ultrasonic pulse velocity (UPV) results after applying temperature are presented in Fig. 7. Cedrus libani clearly shows that the continuity of the internal structure gradually weakens with increasing temperature in cementitious composites reinforced with acicular leaf fiber. UPV values measured at 20 °C were 2.37–2.68 km/h. With the rise in temperature to 200 °C, UPV values decreased to 2.23–2.63 km/h; with the increase in temperature to 400 °C, the decrease in UPV became more pronounced, and the values were measured as 2.08–2.49 km/h. The change at 200 °C corresponded to a decrease in the range of approximately 6.2–4.1%, while the change at 400 °C corresponded to a decrease in the range of approximately 12.3–6.9%. For all mixtures, it is seen that the UPV decreases with increasing temperature; this shows that the density of microcracks and discontinuities in the internal structure of the concrete increases with the effect of temperature. The higher UPV losses in the CL600 and CL700 samples with higher fiber-to-cement ratios suggest that the continuity of the internal structure is more sensitive to temperature in these mixtures. In contrast, in the CL800 and CL900 specimens, it was found that the ultrasonic wave transmission paths could be partially conserved due to the denser cement matrix; however, it is understood that internal structural damage becomes evident for all mixtures at the level of 400 °C.

3.7. Dynamic modulus of elasticity

The dynamic modulus of elasticity results, as shown in Fig. 8, indicate that the stiffness of cementitious composites reinforced with Cedrus libani acicular leaf fiber decreases significantly with increasing temperature. The

dynamic modulus of elasticity, calculated from unit weight and ultrasonic pulse velocity (UPV), is highly sensitive to the continuity of the concrete's internal structure and microstructural damage. The formula used to calculate the dynamic modulus of elasticity is taken from the ASTM C597 (2020) standard and is shown in Eq. (1). The theoretical expression for the dynamic modulus of elasticity is based on the theory of elastic wave propagation. However, some studies accept a constant value because the Poisson's ratio in cementitious composites cannot always be determined experimentally. In the literature, the Poisson's ratios of composites made with forest wastes are given as 0.052–0.522 (Ibearugbulem et al. 2019; Güntekin 2022). Similarly, in this study, the Poisson's ratio was assumed to be 0.20, and this assumption was used to calculate the dynamic modulus of elasticity. Additionally, in this study, the dynamic modulus of elasticity was calculated using the unit weight (γ) parameter instead of density (ρ).

$$E_{\text{dynamic}} = V^2 \rho \frac{(1+\upsilon)(1-2\upsilon)}{(1-\upsilon)} \quad (1)$$

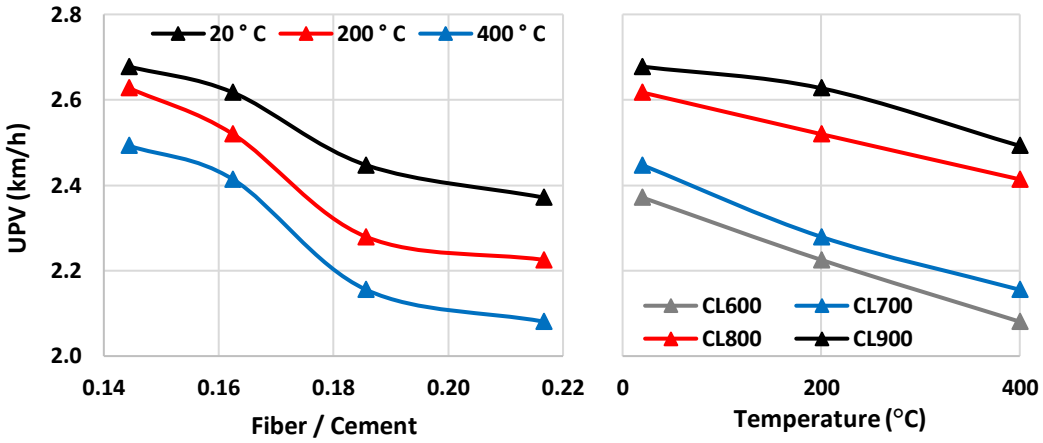

Fig. 7. Effect of fiber/cement ratio and temperature on the UPV of specimens after thermal exposure.

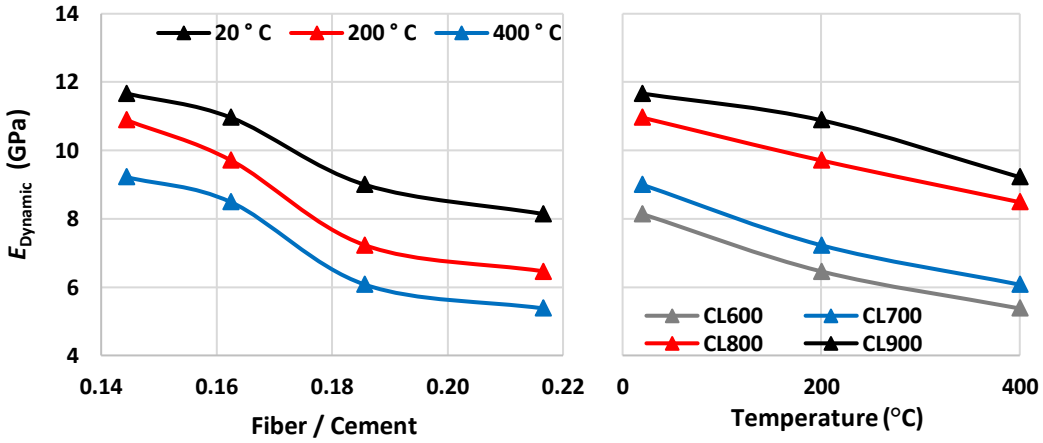

Fig. 8. E_{dynamic} of specimens depending on changes in fiber/cement ratio and temperature after thermal exposure.

As the temperature rose to 200 °C, the dynamic modulus of elasticity decreased to 6.2–9.1 GPa, corresponding to a stiffness loss of approximately 7–13% compared with specimens at 20 °C. As shown in Fig. 8, the decrease in the dynamic modulus of elasticity over this temperature range is consistent with the limited decreases observed in unit weight and UPV. As the temperature increased to 400 °C, the decrease in the dynamic modulus of elasticity became more pronounced, reaching 5.5–8.1 GPa. Accordingly, the total stiffness losses compared with the sample at 20 °C ranged from 22–19%. These discontinuities in the internal structure and the increase in microcrack density due to temperature are directly reflected in the dynamic modulus of elasticity through decreases in unit weight and UPV. The greater loss of dynamic modulus of elasticity in CL600 and CL700 mixtures with higher fiber/cement ratios suggests that the internal structure is more significantly disrupted after temperature exposure in these mixtures. In contrast, in the CL800 and CL900 specimens, ultrasonic wave transmission paths and unit weight were partially conserved due to the denser cement matrix; however, at 400 °C, rigidity decreased significantly for all mixtures.

4. Conclusions

In this study, the usability of natural fibers derived from dried, fallen acicular leaf of Cedrus libani A. Rich. as reinforcement in cementitious composites was extensively evaluated. The fibers underwent a multi-stage extraction and pretreatment process before composite

production; water-soluble components were removed by hot water extraction, the hemicellulosic structure was partially removed, and surface roughness was increased by alkaline treatment. In the mineralization phase with $Ca(OH)_2$, inorganic phase accumulation occurred on the fiber surface. This approach provided controlled surface modification to improve fiber-matrix interfacial interaction. Characterization results showed that the pretreatments induced significant changes in fiber morphology and chemical composition. Increased surface roughness and mineral aggregations were observed in SEM images after processing, and EDS analyses confirmed the transition from a carbon-weighted organic structure to a calcium-rich surface composition. Elemental mapping showed that calcium was inhomogeneous but widely distributed on the fiber surface. These findings support enhanced chemical and mechanical compatibility of the fibers with the cement matrix.

The effect of different fiber/cement ratios on high-temperature behavior was systematically studied in Cedrus libani acicular leaf fiber-reinforced cementitious composites produced with aggregate- and additive-free mixtures. Compressive strength results showed that losses were limited (5–9%) up to 200 °C, while at 400 °C, more significant reductions of 8–18% occurred due to microcrack formation and interface weakening. Mixtures with a high fiber/cement ratio were found to reduce strength loss by partially limiting crack progression, especially at 400 °C. Flexural strength results showed a more pronounced response to temperature rise than compressive strength. Strength losses of approximately 10–15% were observed at 200 °C and 13-27% at 400 °C. In mixtures with high cement dosage, proportional losses were higher at 400 °C, whereas in mixtures with a lower fiber/cement ratio, damage development was more controlled thanks to the crack-bridging effect of the fibers. Splitting tensile strength results showed a similar trend; reductions of 3–7% were recorded at 200 °C and 9–19% at 400 °C. In terms of physical properties, unit weight gradually decreased with increasing temperature, and total losses reached 9-14% at 400 °C. UPV results revealed that internal structural continuity weakened with temperature; decreases of 7–12% were observed at 400 °C. This trend is consistent with the increasing density of microcracks and void ratio in the internal structure. Dynamic modulus of elasticity results indicated significant stiffness losses with increasing temperature, consistent with unit weight and ultrasonic transition velocity data. Modulus reductions of approximately 7–13% at 200 °C and 19–22% at 400 °C were calculated. As a result, bio-based cementitious composites produced with Cedrus libani A.Rich. acicular leaf fibers largely maintained their mechanical performance at low and medium temperature levels, while fiber-matrix interface damage was decisive at high temperature. These findings show that it is possible to develop sustainable and thermally resistant cementitious composites with appropriate fiber/cement ratio design.

This study has shown that natural fibers from Cedrus libani A.Rich. acicular leaf not only offer a sustainable approach to waste assessment but also serve as a technically functional reinforcement material in cementitious composites. Thanks to multi-stage extraction and mineralization processes, a chemically and morphologically active structure was created on the fiber surface; this strengthened the fiber-matrix interface interaction and helped maintain mechanical performance, especially at low and medium temperatures. The results showed that when the appropriate fiber/cement ratio is selected, controlled damage development can be achieved in tensile strength under compression, flexural and splitting, and crack propagation is partially limited, while internal structural continuity can be maintained within certain temperature ranges. In addition, unit volume weight, UPV, and dynamic modulus of elasticity data clearly showed that fiber admixture is directly related to microstructural changes under the influence of temperature. This publication scientifically demonstrates that Cedrus libani A.Rich. acicular leaf, which are forest waste, constitute a rational alternative in the development of high-added-value, environmentally sustainable cementitious composites that are resistant to thermal effects to a certain extent.

Acknowledgements

None declared.

Funding

The authors received no financial support for the research, authorship, and/or publication of this manuscript.

Conflict of Interest

The authors declare no potential conflicts of interest with respect to the research, authorship, and/or publication of this manuscript.

Data Availability

The datasets generated and/or analyzed during the current study are not publicly available but are available from the corresponding author upon reasonable request.

AI Assistance

No AI-based tools were used in the preparation of this manuscript.

Author Contributions

All authors made substantial contributions to the conception and design of the study, acquisition of data, analysis and interpretation of data; drafted or critically revised the manuscript for important intellectual content; and approved the final version to be published.

REFERENCES

Adamu M, Rehman KU, Ibrahim YE, Shatanawi W (2023). Predicting the strengths of date fiber reinforced concrete subjected to elevated temperature using artificial neural network, and Weibull distribution. *Scientific Reports*, 13, 18649.

Adamu M, Ibrahim YE, Raut A (2025). High-temperature performance evaluation of sustainable date palm fiber concrete with activated carbon: An MCDM and Weibull analysis approach. *Results in Control and Optimization*, 20, 100602.

Al-Dala'ien RN, Zaid O, Al-Ezzi MJ, Wani SR (2025). State-of-the-art review on high-temperature performance of plant-based fiber reinforced concrete. *Discover Materials*, 5, 176.

Alshabrawi HAM, Uysal H (2025). Enhancing the mechanical performance of perforated steel plates through fiber-reinforced composite reinforcement: A finite element analysis study. *Challenge Journal of Structural Mechanics*, 11(4), 174-183.

Aluko OG, Yatim JM, Kadir MAA, Yahya K (2023). Experimental investigation of residual physical and mechanical properties of kenaf fibre

reinforced concrete exposed to elevated temperatures. *Fire Technology*, 59, 949-982.

ASTM C597-16 (2020). Standard test method for pulse velocity through concrete. ASTM International, West Conshohocken, PA, USA.

Banthia N, Trottier JF (1995). Concrete reinforced with deformed steel fibers, Part I: Bond-slip mechanisms. *ACI Materials Journal*, 92(4), 435-446.

Baş Fİ (2025). Investigating the effects of glass fiber in enhancing concrete pavement performance. *Challenge Journal of Structural Mechanics*, 11(1), 42-54.

Bentur A, Mindess S (2007). Fibre Reinforced Cementitious Composites. 2nd ed. Taylor & Francis, Abingdon, UK.

Bilba K, Arsène MA (2008). Silane treatment of bagasse fiber for reinforcement of cementitious composites. *Composites Part A*, 39(9), 1488-1495.

Canbaz M, Kara İ, Topçu İB (2021). Effect of high temperature on the mechanical behavior of cement-bonded wood composite produced with wood waste. *Challenge Journal of Structural Mechanics*, 7(1), 42-48.

Cao W, Li J, Marti-Rosselló T, Zhang X (2019). Experimental study on the ignition characteristics of cellulose, hemicellulose, lignin and their mixtures. *Journal of the Energy Institute*, 92(5), 1303-1312.

Çelik Z, Turan E, Oltulu M, Öner G (2024). Reinforcement of concrete beams using waste carbon-nanoclay-fiberglass laminate pieces. *Challenge Journal of Concrete Research Letters*, 15(1), 1-6.

Das AK, Agar DA, Rudolfsson M, Kilpeläinen P, Tienaho J, Fernando D (2024). Micromorphology and native extractive behaviour of wood powder. *Scientific Reports*, 14, 25548.

Dhasindrakrishna K, Pasupathy K, Ramakrishnan S, Sanjayan J (2023). The ambient and elevated temperature performance of hemp fibre reinforced alkali-activated cement foam: Effects of fibre dosage and alkali treatment. *Journal of Building Engineering*, 76, 107131.

Efe FT (2021). Sedir odununun bazı fiziksel ve mekanik özelliklerinin belirlenmesi üzerine bir araştırma. *Türk Tarım ve Doğa Bilimleri Dergisi*, 8(1), 43-52.

Feng H, Xia S, Guo A, Huang H, Dai K, Feng Z, Yu Z (2025). Mechanical properties of alkali-activated biomass power plant ash recycled concrete. *Construction and Building Materials*, 481, 141549.

Fiore V, Scalici T, Valenza A, Di Bella G (2015). A review on basalt fibre and its composites. *Composites Part B*, 74, 74-94.

Garcez MR, Oliari Garcez E, Machado AO, Gatto DA (2016). Cement-wood composites: Effects of wood species, particle treatments and mix proportion. *International Journal of Composite Materials*, 6(1), 1-8.

General Directorate of Forestry (2025). Forestry Statistics 2024. https://www.ogm.gov.tr/tr/e-kutuphane/resmi-istatistikler [accessed 30-12-2025].

Grubeša IN, Marković B, Gojević A, Brdarić J (2018). Effect of hemp fibers on fire resistance of concrete. *Construction and Building Materials*, 184, 473-484.

Güney A, Zimmermann R, Krupp A, Haas K (2016). Needle characteristics of Lebanon cedar (Cedrus libani A.Rich.): Degradation of epicuticular waxes and decrease of photosynthetic rates with increasing needle age. *Turkish Journal of Agriculture and Forestry*, 40(3), 386-396.

Güntekin E (2022). Sedir Odununun (Cedrus libani A.) Elastik Sabitleri. *Bartın Orman Fakültesi Dergisi*, 24(3), 436-443.

Hu M, Lv X, Wang Y, Ma L, Zhang Y, Dai H (2024). Recent advance on lignin-containing nanocelluloses: The key role of lignin. *Carbohydrate Polymers*, 343, 122460.

Ibearugbulem OM, Amaechi CK, Nwakwasi NL, Anyaogu L, Arimanwa JI, Onyechere IC (2019). Structural characteristics of sawdust-quarry dust composite. *SSRG International Journal of Civil Engineering*, 6(7), 7-12.

Islam MS, Ahmed SJU (2018). Influence of jute fiber on concrete properties. *Construction and Building Materials*, 189, 768-776.

Kareem A (2025). A review on date palm fiber as a sustainable reinforcement for concrete applications. *International Journal of Concrete Structures and Materials*, 19(1), 98.

Li VC (2003). On engineered cementitious composites (ECC). *Journal of Advanced Concrete Technology*, 1(3), 215-230.

Li K, Deng J, Zhu Y, Zhang W, Zhang T, Tian C, Ma J, Shao Y, Yang Y, Yanqiu S (2025). Utilization of municipal solid waste incineration fly ash with different pretreatments with gold tailings and coal fly ash for environmentally friendly geopolymers. *Waste Management*, 194, 342-352.

Long W, Wang Y (2021). Effect of pine needle fibre reinforcement on the mechanical properties of concrete. *Construction and Building Materials*, 278, 122333.

Lura P, Toropovs N, Justs J, Shakoorioskooie M, Münch B, Griffa M (2025). Mitigation of plastic shrinkage cracking with natural fibers: Kenaf, abaca, coir, jute and sisal. *Cement and Concrete Composites*, 155, 105827.

Maier D, Manea DL, Tămaş-Gavrea DR, Țiriac A, Costin P (2025). Long-term performance of wood-cement composites: Stabilization versus degradation driven by waste type. *Buildings*, 15(22), 4137.

Mahzabin MS, Hamid R, Badaruzzaman WHW (2013). Evaluation of chemicals incorporated wood fibre cement matrix properties. *Journal of Engineering Science and Technology*, 8(4), 385-398.

Melichar T, Dufka A, Dvořák K, Bayer P, Vasas S, Novakova I, Schwarzova I, Bydžovský J (2024). Durability of wood-cement composites with modified composition by limestone and stabilised spruce chips. *Materials*, 17, 6300.

Merta I, Tschegg EK (2013). Fracture energy of natural fibre reinforced concrete. *Construction and Building Materials*, 40, 991-997.

Naaman AE (2003). Engineered steel fibers with optimal properties for reinforcement of cement composites. *Journal of Advanced Concrete Technology*, 1(3), 241-252.

Onuaguluchi O, Banthia N (2016). Plant-based natural fibre reinforced cement composites: A review. *Cement and Concrete Composites*, 68, 96-108.

Pacheco-Torgal F, Jalali S (2011). Cementitious building materials reinforced with vegetable fibres. *Construction and Building Materials*, 25(2), 575-581.

Ren G, Gao X, Zhang H (2022). Utilization of hybrid sisal and steel fibers to improve elevated temperature resistance of ultra-high performance concrete. *Cement and Concrete Composites*, 130, 104555.

Ridha MMS (2024). Combined effect of natural fibre and steel fibre on the thermal-mechanical properties of UHPC subjected to high temperature. *Cement and Concrete Research*, 180, 107510.

Savastano Jr H, Warden PG, Coutts RS (2003). Potential of alternative fibre cements as building materials for developing areas. *Cement and Concrete Composites*, 25(6), 585-592.

Silva FA, Chawla N, Toledo Filho RD (2010). Tensile behavior of high performance natural (sisal) fibers. *Composites Science and Technology*, 68(15-16), 3438-3443.

Şahin HT, Çam E (2022). Properties of gypsum boards made with cedrus tree (Cedrus libani) components. Part 2: Chemical and technological properties. *Bartın Orman Fakültesi Dergisi*, 24(2), 202-210.

Tarhan Y, Tarhan İH, Perrot A (2025). Improving bond performance of 3D-printable earth-based mortar reinforced with jute fibers. *Challenge Journal of Structural Mechanics*, 11(2), 99-105.

Toledo Filho RD, Ghavami K, England GL, Scrivener K (2005). Development of vegetable fibre-mortar composites of improved durability. *Cement and Concrete Composites*, 27(2), 185-196.

TS EN 196-1 (2016). Methods of testing cement. Part 1: Determination of strength. Turkish Standards Institution, Ankara, Türkiye.

Urtekin Y, Çelik Z (2025). Investigation of the effects of re-curing on mechanical properties of basalt-polypropylene hybrid fiber concretes after exposure to high temperature. *Challenge Journal of Structural Mechanics*, 11(1), 14-23.

Uzun M (2024). Enhancing mechanical properties of foam concrete with sisal fiber reinforcement: An experimental investigation. *Challenge Journal of Concrete Research Letters*, 15(3), 82-89.

Ünal S, Canbaz M (2025). Photocatalytic activation of fibrous lightweight polymer concrete surfaces under artificial light source. *Challenge Journal of Concrete Research Letters*, 16(1), 15-24.

Ünal S, Kurt AB, Canbaz M (2025). Impact of wrap quantity on strength of damaged and undamaged CFRP-reinforced structural members. *Challenge Journal of Concrete Research Letters*, 16(3), 133-141.

Veigas MG, Najimi M, Shafei B (2022). Cementitious composites made with natural fibers: Investigation of uncoated and coated sisal fibers. *Case Studies in Construction Materials*, 16, e00788.

Yang H, Yan R, Chen H, Lee DH, Zheng C (2007). Characteristics of hemicellulose, cellulose and lignin pyrolysis. *Fuel*, 86(12-13), 1781-1788.

Yousefieh N, Joshaghani A, Hajibandeh E, Shekarchi M (2017). Influence of fibers on drying shrinkage in restrained concrete. *Construction and Building Materials*, 148, 833-845.

Zhang B, Yin X, Yu H, Zhang Z, Qin W, Hao X (2025). Effects of freezing-microwave assisted alkali treatment on physicochemical and thermomechanical properties of bamboo. *Polymer Testing*, 150, 108905.

Zhao H, Zhou T, Tang J, Li Z, Yao C, Gao X (2025). Temperature-adaptive mechanism of bamboo fibers for regulating elevated temperature performance of UHPC. *Construction and Building Materials*, 471, 140674.

Zukowski B, dos Santos ERF, dos Santos Mendonça YG, dos S Silva FDA, Toledo Filho RD (2018). The durability of SHCC with alkali treated curaua fiber exposed to natural weathering. *Cement and Concrete Composites*, 94, 116-125.

Challenge Journal of CONCRETE RESEARCH LETTERS

Research Article

Structural behavior of lightweight composite ferrocement plates

Yousry B. I. Shaheen [a], Noha Gamal Rady [a], Fatma M. Eid [a,*]

[a] *Department of Civil Engineering, Menoufia University, 32511 Shebin El-Kom, Menofia, Egypt*

ABSTRACT

Ferrocement is a reinforced cementitious composite consisting of layers of wire mesh or small-diameter steel rods embedded in cement mortar. Its structural efficiency depends mainly on reinforcement geometry and distribution rather than on material quantity alone. This study examines the flexural behavior of ten lightweight ferrocement plates reinforced with different mesh types, namely welded metal mesh, Gavazzi mesh, and Tenax mesh. All plate specimens had dimensions of 1200 mm × 500 mm × 120 mm and contained corrugated foam panels embedded at the mid-depth. Steel mesh with a wire diameter of 5.5 mm was provided at the top and bottom as the main reinforcement. The load-deflection response, cracking behavior, ductility, energy absorption, and overall flexural performance were evaluated to determine the effect of mesh type and mesh-layer arrangement on structural efficiency. The results showed that plates reinforced with four layers of welded metal mesh achieved the best ultimate strength and crack resistance. These plates reached ultimate and service loads that were 34% and 48.88% higher, respectively, than those of the control specimen without additional mesh. In contrast, the plate reinforced with one additional layer of Gavazzi mesh showed the highest energy absorption among all specimens, with a value 75.9% higher than that of the control specimen. Increasing the number of mesh layers improved cracking load, service load, ultimate load, and energy absorption. Welded metal mesh also outperformed Tenax mesh in energy absorption, making it preferable for structural elements requiring high toughness and resilience.

ARTICLE INFO

Article history:
Received – January 3, 2026
Revision requested – February 9, 2026
Revision received – March 25, 2026
Accepted – March 30, 2026

Keywords:
Lightweight concrete
Composite plates
Ferrocement
Flexural behavior
Welded metal mesh
Gavazzi mesh
Tenax mesh

Citation: Shaheen YBI, Rady NG, Eid FM (2026). Structural behavior of light weight composite ferrocement plates. *Challenge Journal of Concrete Research Letters*, 17(2), 177–191.

1. Introduction

Ferrocement is produced by layering continuous wire meshes that are tied together, with reinforcement ratios that may reach approximately 8%. The mortar cover over the meshes is typically between 3 and 5 mm, which promotes a uniform distribution of reinforcement. This configuration improves material homogeneity and enhances mechanical properties such as tensile strength, flexural performance, impact resistance, and crack control. The interconnected wire meshes are filled with cement mortar, forming a dense composite material that can be molded into thin, lightweight sections without losing structural integrity.

In ferrocement members, the structural response is strongly influenced by the mortar matrix, reinforcement ratio, and the type, stiffness, geometry, and distribution of the reinforcing mesh. Recent studies on ferrocement beams have shown that metallic and non-metallic mesh configurations can significantly affect first cracking load, ultimate load, ductility, energy absorption, crack distribution, and load-to-weight efficiency, particularly when material-efficient sections such as beams with openings or lightweight cores are considered (Hekal et al. 2024; Shaheen et al. 2024).

Shaheen et al. (2023a) studied the structural performance of ferrocement beams with longitudinal perforations filled with lightweight concrete. The experimental

* *Corresponding author*. E-mail address: fatma_elzahraa2002@yahoo.com (F. M. Eid)
ISSN: 2548-0928 / DOI: https://doi.org/10.20528/cjcrl.2026.02.008

program included two normal-weight concrete (NWC) beams and ten ferrocement (FC) beams with lightweight cores reinforced with welded steel mesh used as shear reinforcement and tested under three-point bending. The lightweight core concrete contained aerated autoclaved brick waste and expanded polystyrene. Compared with the control NWC beam, the FC beams with different filler materials and welded steel meshes instead of conventional stirrups increased ultimate load by 36.6-107.3%, ultimate deflection by 6-272%, and ductility by 89-1155%.

Qureshi et al. (2023) conducted four-point bending tests on 16 simply supported ferrocement panels measuring 1000 mm × 450 mm to evaluate the flexural performance of panels containing SBR latex. The results indicated that latex and polypropylene (PP) fibers mainly affected the initial stiffness and had limited influence on the final load. The control specimens had a lower peak load than specimens reinforced with welded iron mesh, whereas specimens with PVC mesh showed greater flexural toughness than those with welded iron mesh. This is consistent with recent observations that metallic meshes generally provide higher stiffness and strength contribution, whereas non-metallic meshes such as Gavazzi, Tensar, or polymer-based grids may improve crack distribution, deformation capacity, and energy absorption depending on their tensile stiffness, elongation capacity, and bond with the mortar matrix (Hekal et al. 2024). The PVC plastic mesh specimens also exhibited a smeared cracking pattern, indicating greater ductility than the iron mesh specimens.

Several additional studies have investigated ferrocement and ferrocement-related systems in different structural applications. These include lightweight ferrocement box columns, geopolymer ferrocement beams, reinforced concrete beams strengthened with U-shaped ferrocement jackets, sustainable high-performance mortar with natural sisal fibers, fiber-reinforced ferrocement beams under monotonic and repeated loading, ferrocement panels under flexural and impact loads, lightweight panels with expanded perlite, sandwich panel slabs under shear, ferrocement I-beams, composite ferrocement-concrete plates, and voided ferrocement channel sections (Eltaly et al. 2023; El-Sayed et al. 2023; Rajguru and Patkar 2022; Dawood et al. 2021; Naveen and Suresh 2020; Murali et al. 2020; Madadi et al. 2018; Shaheen et al. 2016; Acma et al. 2015; Shaheen et al. 2013; Rao et al. 2008). Collectively, these studies confirm the ability of ferrocement systems to improve strength, stiffness, cracking behavior, ductility, energy absorption, and weight efficiency.

Similarly, studies on ferrocement beams with web or circular openings have indicated that material reduction in selected regions may improve structural efficiency, but it can also alter stress flow, crack propagation, stiffness, ductility, and energy absorption depending on the opening configuration and mesh type (Hekal et al. 2024; Shaheen et al. 2024). These findings are directly relevant to lightweight ferrocement systems because reducing self-weight through voids, openings, or lightweight cores requires a balanced assessment of ultimate load, serviceability, deflection response, crack pattern, ductility, energy absorption, and load-to-weight ratio.

Abdel Tawab (2006) developed U-shaped ferrocement permanent formwork as a practical alternative to conventional wooden and metal forms for reinforced concrete beams. Shaheen et al. (2023b) studied ferrocement walls under vertical and horizontal loading. The walls consisted of two thin ferrocement layers reinforced with one, two, three, or four layers of welded wire mesh or expanded steel mesh, with a lightweight extruded foam core. Thirteen lightweight walls with dimensions of 100 mm × 650 mm × 1250 mm were cast and tested until failure, and ABAQUS finite element analysis was also performed. The results showed that walls reinforced with expanded wire meshes performed better than walls reinforced with welded wire meshes. Energy absorption increased by 40% in the specimens reinforced with expanded wire meshes compared with the corresponding welded wire mesh specimens.

Based on this review, the present study examines the structural behavior of ferrocement plates reinforced with different mesh types. The study also evaluates the effects of mesh type, number of mesh layers, and combinations of different mesh systems, together with the use of corrugated foam panels to reduce plate weight.

Although previous studies have examined ferrocement beams with openings and highlighted the effects of mesh type, opening configuration, and load-to-weight efficiency, limited information is available on lightweight ferrocement plates incorporating corrugated foam cores with different metallic and non-metallic mesh systems. Therefore, this study extends the existing ferrocement literature from beam-type members with openings to plate-type lightweight composite elements by focusing on flexural performance, cracking behavior, ductility, energy absorption, and structural efficiency.

This research introduces a new integration of ferrocement and corrugated foam-core systems for developing ultra-lightweight and sustainable structural elements. By evaluating welded, Gavazzi, and Tenax meshes, the study assesses the influence of hybrid reinforcement and bond-slip mechanisms in thin composite plates. The use of corrugated foam panels reduces self-weight without compromising flexural integrity, thereby providing a resource-efficient model for building envelope applications. The study also quantifies a 75.9% increase in energy absorption when Gavazzi mesh is used, indicating improved flexural toughness and energy dissipation capacity under monotonic loading. Overall, the proposed system supports sustainable construction by reducing concrete volume and improving thermal resistance within a single lightweight structural unit.

2. Experimental Materials

This section describes the materials used to develop the mortar mix and fabricate the tested plates, including cement, fine aggregate, water, superplasticizer, polypropylene fibers, silica fume, reinforcing meshes, and corrugated foam panels. The materials were evaluated in accordance with ASTM, BS, and ECP standards to determine their physical and mechanical properties, and they were also visually inspected for cleanliness and overall quality.

2.1. Cement

Ordinary Portland cement (OPC), CEM I 42.5 N, was used in the experimental program, as shown in Fig. 1. The cement was supplied by El-Sewedy Cement Company. The chemical composition of the cement is presented in Table 1 according to the manufacturer's data. As shown in Table 2, the cement satisfied the physical and chemical requirements of the Egyptian standard specification ESS 4756-1/2022.

Fig. 1. Cement used in the mixes.

Table 1. Chemical composition of OPC CEM I / 42.5 N.

Constituents	Concentration in weight (%)	Constituents	Concentration in weight (%)
Silica as SiO_2	19.8	Lime saturation factor	100.4
Alumina as AL_2O_3	5.6	Lime combination factor	98.9
Iron as FeO_3	2.4	Silica ratio	2.48
Potassium as k_2O	0.58	Alumina ratio	2.33
Calcium as CaO	65.9	Tricalcium Cilicate (C_3S)	65.1
Sodium as Na_2O	0.29	Dicalcium Cilicate (C_2S)	7.6
Sulphur as SO_3	2.8	Tricalcium Aluminate (C_3A)	10.8
Loss in ignition	1.2	Insoluble residue	0.4

Table 2. Characteristics of cement used.

Test description		Test results	E.S.S. 4756-1/2022 Egyptian specification limits
Setting time (Vicat test) Initial Final		hour: min 1: 55 4: 10	 Not less than 60 min Not more than 10 h
The soundness of cement (Le Chatelier test)		4 mm	Not more than 10mm
The fineness of cement, percentage retained on the standard 0.09 mm sieve by weight		7%	Not more than 10%
Specific surface area		3140 cm^2/g	Not less than 2800 cm^2/g
Compressive strength of cement mortar (MPa)	2 days	14	≥10
	28 days	48	≥42.5

2.2. Fine aggregate

Natural siliceous sand was used as the fine aggregate. The sand was free from impurities and had a specific gravity of 2.6 and a fineness modulus of 2.91. These properties comply with ESS 1109/2008 and ICS 91.100.10 EN 12620/2002+A1. The properties of the sand are presented in Table 3, while its grading is shown in Table 4 and Fig. 2.

Table 3. Properties of fine aggregate used.

Property	Test results for sand
Specific gravity (S.S.D)	2.6
Unit weight	1.7 t/m^3
Fineness modulus	2.91
Clay, silt, and fine dust	2% (by weight)
Chloride	0.03% (by weight)

Table 4. Results of sieve analysis test for fine aggregate.

Sieve diameter (mm)	4.75	2.36	1.18	0.60	0.30	0.15
% Passing	100	92.8	82.6	37.7	9.50	0
% Passing (E.S.S. 1109/2008) (Medium Zone)	100	60–100	30–90	15–45	5–40	0

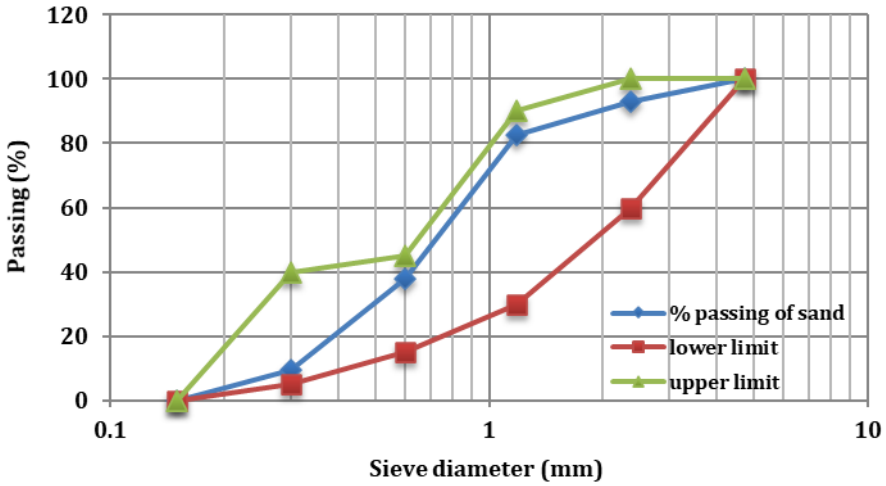

Fig. 2. Grading curve of sand used.

2.3. Water

Clean potable water, free from impurities, was used for mixing and curing the plates in accordance with ECP 203/2020.

2.4. Superplasticizer

The superplasticizer used in this study was a high-range water reducer (HRWR) designed to improve mix workability. As shown in Fig. 3, this additive was produced by Sika Group and marketed as Sika ViscoCrete 3425. It complies with ASTM C494, Types A and F. The product reduces mixing time by improving polymer dispersion, enhances water resistance, improves bonding between new and old concrete or plaster, increases strength properties, and helps minimize shrinkage and cracking. Its relative density is 1.02 ± 0.01 at 25 °C.

2.5. Polypropylene fibers

PP 300-e3 polypropylene fibers were used in the concrete mixtures, as shown in Fig. 4. These fibers are available in the Egyptian market and were added to improve the properties of the mortar. The recommended dosage was 900 g/m^3, as specified by the manufacturer.

2.6. Silica fume

Silica fume, or microsilica, is a non-crystalline form of silicon dioxide. As shown in Fig. 5, it is an ultrafine powder produced during the manufacture of silicon and ferrosilicon alloys. It contains spherical particles with an average size of approximately 150 nm. Its primary use is as a pozzolanic material in high-performance concrete. The silica fume used in this study had a specific gravity of 2.63, and the recommended dosage was 7-10% of the cement weight.

2.7. Reinforcement

2.7.1. Welded steel bars

A mesh panel made of welded steel bars, with dimensions of 500 mm × 1200 mm, openings of 100 mm × 100 mm, and a wire diameter of 5.5 mm, was used as shown in Fig. 6. This product was manufactured in accordance with standard specifications and supplied by Ezz Steel Company, ensuring adequate quality and strength.

Fig. 3. Superplasticizer.

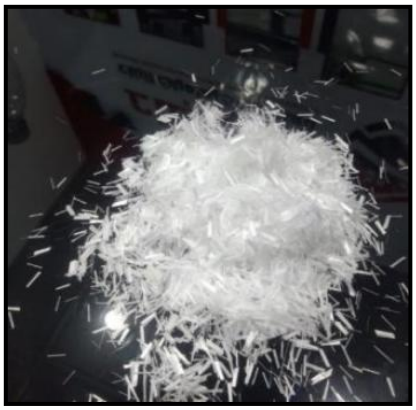

Fig. 4. Polypropylene fibers PP 300-e3.

Fig. 5. Silica fume.

Fig. 6. Welded steel bars used.

2.7.2. Welded metal mesh

Welded metal mesh was used as additional reinforcement together with the welded steel bars in the ferrocement plates. The welded wire mesh consisted of galvanized wires with a diameter of 0.7 mm and openings of 12.5 mm × 12.5 mm, as shown in Fig. 7. The technical specifications and mechanical properties provided by the manufacturer are given in Table 5.

Fig. 7. Welded mesh used.

Table 5. Technical specifications and mechanical properties of welded mesh.

Property	Dimensions	Weight	Modulus of elasticity	Proof stress	Ultimate strength	Ultimate strain	Proof strain
Value	12.5×12.5 mm	430 g/m^2	170 GPa	400 N/mm^2	600 N/mm^2	58.8×10^{-3}	1.17×10^{-3}

2.7.3. Gavazzi mesh

Gavazzi mesh is a fiberglass mesh produced by Gavazzi Company in Italy and is available in the Egyptian market, as shown in Fig. 8. According to the manufacturer, the mesh opening is 8.3 mm × 9.5 mm, the longitudinal cross-section is 1.66 mm × 0.66 mm, and the transverse cross-section is 1.0 mm × 0.5 mm. The mesh has a weight of 222 g/m^2 and a volume fraction of 0.535%. Its longitudinal tensile strength is 32.5 MPa, with an elongation of 5.5%, as presented in Table 6.

2.7.4. Tenax mesh

Tenax mesh is a non-metallic wire mesh known as uniaxial Geogrid TT060 and is made of high-density polyethylene. As shown in Fig. 9, it has an aperture size of 21 mm × 7 mm, a weight of 1.5 kg/m^2, and a volume fraction of 2.04%. The Tenax mesh has a tensile strength of 24.7 MPa at an elongation of 21%. Table 7 presents the technical and mechanical properties of uniaxial Geogrid TT060.

Fig. 8. Gavazzi mesh used.

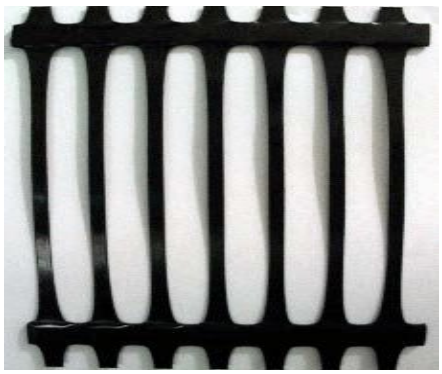

Fig. 9. Tenax mesh used.

Table 6. Technical and mechanical properties of Gavazzi mesh.

Product name	Gavazzi 0225-A
Mesh opening	8.3×9.5 mm
Weight	222 g/m² ± 5%
Modulus of elasticity	72 GPa
Composition	Fiberglass approx. 87% Alkali-resistant finish approx. 13
Tensile resistance	Breaking strength elongation Warp approx. 3200 N/5 cm 5% ± 1 Weft approx. 3200 N/5 cm 5% ± 1

Table 7. Technical and mechanical properties of uniaxial Geogrid TT060.

Technical characteristics	Units	MD values
Tensile strength at 5% strain	kN/m	35
Tensile strength at 5% strain	kN/m	100
Junction strength	kN/m	50
Modulus of elasticity	MPa	100
Flexural stiffness	mg·cm	730.000
Technical characteristics	Units	MD Values

2.7.5. Corrugated foam panels

Corrugated foam panels with a thickness of approximately 40 mm and strengthened with metal wire meshes were obtained from the Egyptian Italian Company for Modern Construction, Cairo, Egypt. As shown in Fig. 10, the panels were subjected to standard laboratory tests by the manufacturer in accordance with the applicable Egyptian standard specifications. The test results are presented in Table 8.

Fig. 10. Corrugated foam panels used.

Table 8. Physical properties extracted from European foam manufacturers.

Description	Value
Mold net dimension	1.20 × 0.80 × 4.0 m
Density	19–21 kg/m³
Compressive strength at 10% deformation (at 20°C)	1.60 kg/cm²
Compressive strength at 10% deformation (at 70°C)	1.20 kg/cm²
Compressive creep strength for 50 years at 2% deformation (20°C)	0.48 kg/cm²
Compressive creep strength for 50 years at 2% deformation (70°C)	0.36 kg/cm²
Tensile strength at 20°C	2.6 kg/cm²
Tensile strength at 70°C	1.8 kg/cm²

3. Experimental Program

Ten ferrocement plates were tested to evaluate their performance under flexural loading. The specimens were cast with dimensions of 1200 mm × 500 mm × 120 mm in accordance with the design, mixing, and curing requirements of the Egyptian Code of Practice (ECP 203/2020). Each specimen consisted of ferrocement plates reinforced at the top and bottom with 1200 mm × 500 mm steel mesh panels having 100 mm × 100 mm openings and a 5.5 mm wire diameter. Additional reinforcement was provided using welded galvanized steel mesh, Gavazzi mesh, and Tenax mesh.

- Group A included four specimens and was used to evaluate the effect of increasing the number of welded steel mesh layers from one to four.
- Group B included three specimens and was used to evaluate the effect of increasing the number of Tenax mesh layers from one to three.
- Group C included two specimens and was used to investigate the performance of Gavazzi mesh and a hybrid Gavazzi-Tenax reinforcement system. One specimen (PC) was kept as the control specimen without additional reinforcement. This specimen matrix enabled a comparative evaluation of ultimate load, ductility, energy absorption, serviceability response, and load-to-weight ratio while keeping the experimental scope consistent with similar recent studies.

The number of mesh layers was limited to four to ensure full mortar infiltration around the corrugated foam core within the 120 mm composite section. Exceeding this limit could create physical barriers, cause internal voids, and reduce bond integrity. Symmetric reinforcement was used on both faces to maintain structural integrity under positive and negative bending during handling and service and to control shrinkage-induced cracks on both sides.

A plain mortar mixture without additives was not included because the study aimed to develop a high-performance mortar capable of meeting the structural demands of 120 mm lightweight slabs. The additives used were already available in the local market. Silica fume acted as a micro-filler and pozzolanic material, increasing compressive strength and improving the interfacial transition zone between the mortar, mesh, and corrugated foam core. Polypropylene fibers were added to enhance tensile strength, control shrinkage cracking, and increase toughness. Together, these materials produced a dense and durable matrix with the flowability required for full infiltration around the foam corrugations, which standard mortar could not provide.

The primary variables were the reinforcement mesh type and the number of additional mesh layers placed at the top and bottom of the plates, as detailed in Table 9. All tests were performed in the construction materials laboratory at Menoufia University, Egypt. Fig. 11 shows the cross-sectional details of all tested plates.

Table 9. Details of the tested specimens.

Group number	Specimen name	Foam with steel wires	Additional mesh reinforcement		Steel mesh
1	PC	One foam layer with a thickness of 40 mm and steel wires (top + bottom) with 3.3 mm thickness	No mesh		steel mesh at top and bottom with 5.5 mm wire diameter
2	PW1		Welded mesh top and bottom	1 layer	
	PW2			2 layers	
	PW3			3 layers	
	PW4			4 layers	
3	PT1		Tenax mesh top and bottom	1 layer	
	PT2			2 layers	
	PT3			3 layers	
4	PG1		Gavazzi mesh top and bottom	1 layer	
	PG1+T1		Gavazzi mesh + Tenax mesh	1 layer + 1 layer	

3.1. Mortar mix design

Mortar quality is one of the most important factors affecting the behavior of ferrocement units. Therefore, the mix was designed to produce a highly flowable, high-strength, and well-compacted mortar suitable for casting the specimens. The mortar used for the plates was designed to achieve a compressive strength of 35 MPa after 28 days. A mechanical laboratory mixer was used to prepare the mixes. The materials were first dry mixed, after which water was added and the mixture was mixed again for each specimen. The proportions of the mortar mix per cubic meter are listed in Table 10. The compressive strength of the mix was experimentally evaluated in accordance with ISO 1920-3/2004. Three cube specimens measuring 150 mm × 150 mm × 150 mm were cast and tested in compression at curing ages of 7 and 28 days. The results are summarized in Table 11.

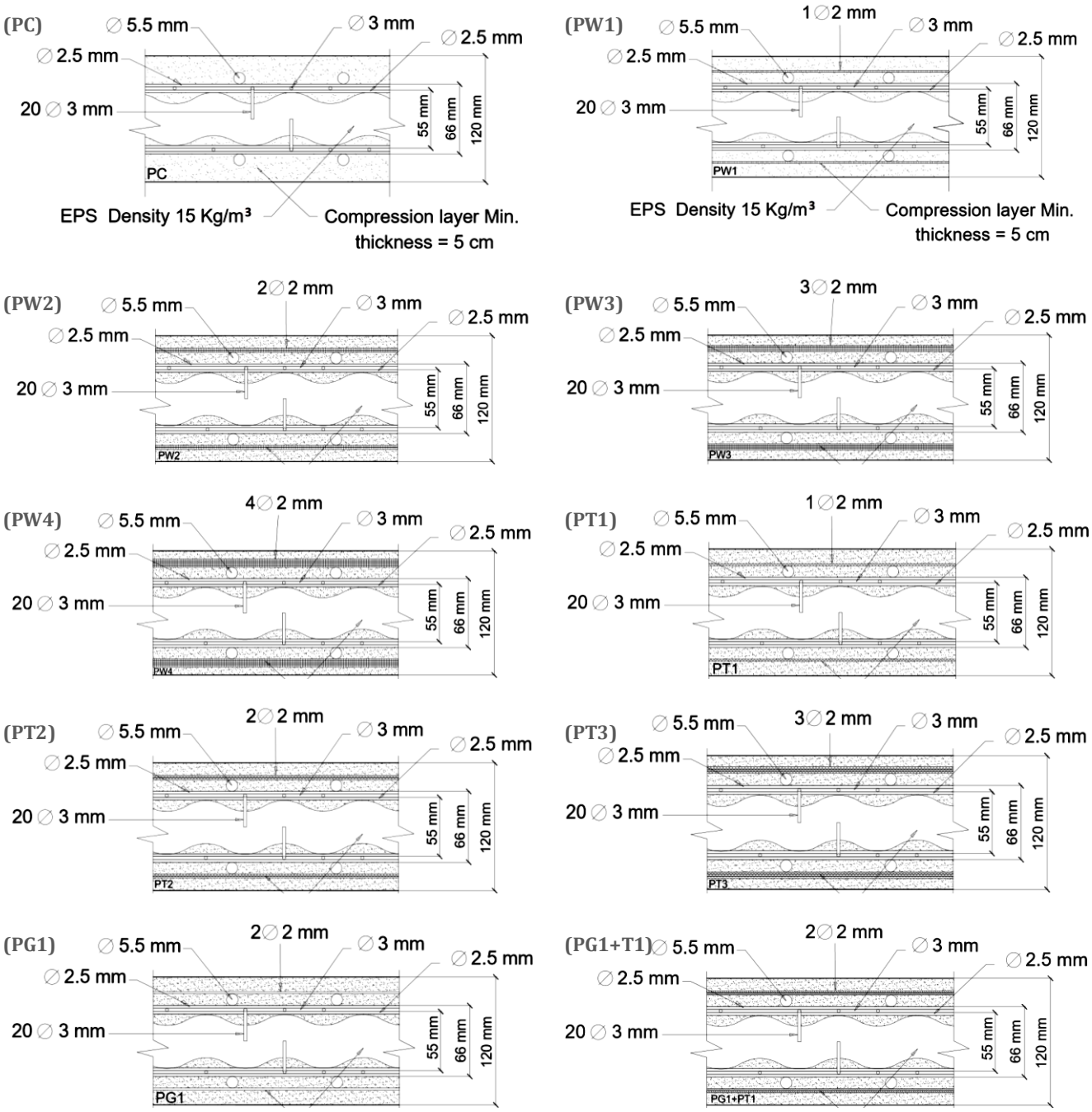

Fig. 11. Cross-sectional details of the tested plates.

Table 10. Mortar constituents for 1 m^3.

Constituent	Cement	Silica fume (kg)	Sand	Water	Superplasticizer (kg)	Fiber (e300) (kg)
Quantity (kg/m^3)	650	65	1250	240	14	1

Table 11. Compression test results.

Period (days)		7 days	28 days	Average compressive strength (MPa)
		Maximum compressive strength (MPa)		
Cubic specimen no.	1	21.2	37.3	35.1
	2	23.0	33.4	
	3	26.1	34.6	

3.2. Specimen fabrication and casting process

Wooden molds with the required dimensions were used to cast the specimens, as shown in Fig. 12. The welded steel bars, corrugated foam panels, and reinforcing meshes were assembled outside the molds according to the specified dimensions. The assembled reinforcement system was then placed inside the wooden mold before casting. After 24 hours, the specimens were demolded and cured with wet burlap for 7 consecutive days, as recommended by ECP 203/2020.

Fig. 12. Preparation, casting, and curing of the tested plates.

3.3. Test setup and instrumentation

After 28 days, the specimens were painted white to facilitate crack detection during testing. Rubber pads were placed between the plates and the testing device. The first cracking load, crack propagation, and failure mode of each specimen were recorded. Four demec points were positioned on one side of each specimen to measure strain during loading, as shown in Fig. 13. The experimental work was carried out in the Laboratory of Properties and Testing Materials, Faculty of Engineering, Menoufia University, Egypt.

Each specimen was placed in a universal testing machine with a maximum capacity of 200 kN. The tests were conducted using a four-line loading system, as illustrated in Fig. 13. The specimen was centered in the machine, and the distance between the two supports was maintained at 1100 mm. A dial gauge with an accuracy of 0.01 mm was positioned at mid-span under the specimen to measure deflection with increasing load, as shown in Fig. 14.

The load was applied in 5 kN increments using a load-control protocol. This increment was selected to provide a sufficient number of data points for accurately plotting the load-deflection curve, particularly in the pre-cracking and early post-cracking stages. It also enabled clear identification of the first cracking load while maintaining a manageable test duration. At each load increment, the horizontal distance between each pair of demec points was measured using a mechanical strain gauge reader, and the mid-span deflection was recorded using the dial gauge. Cracks were traced on the specimen sides and marked with a black marker. The load was gradually increased until complete failure occurred.

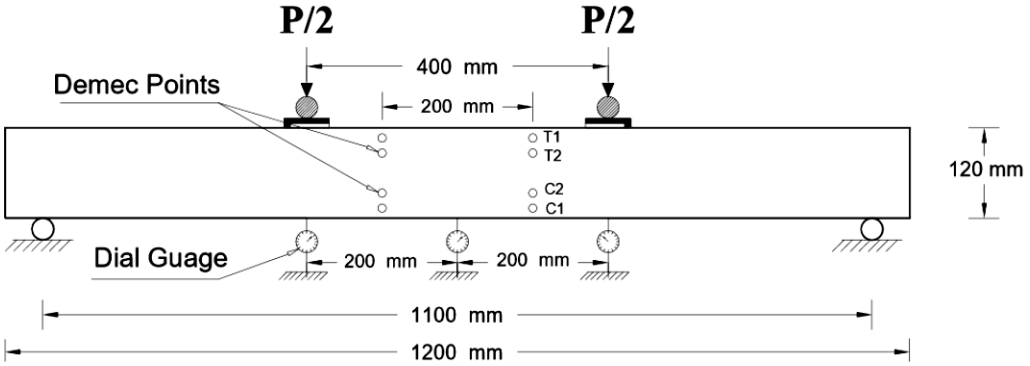

Fig. 13. Location of the demec points and dial gauges.

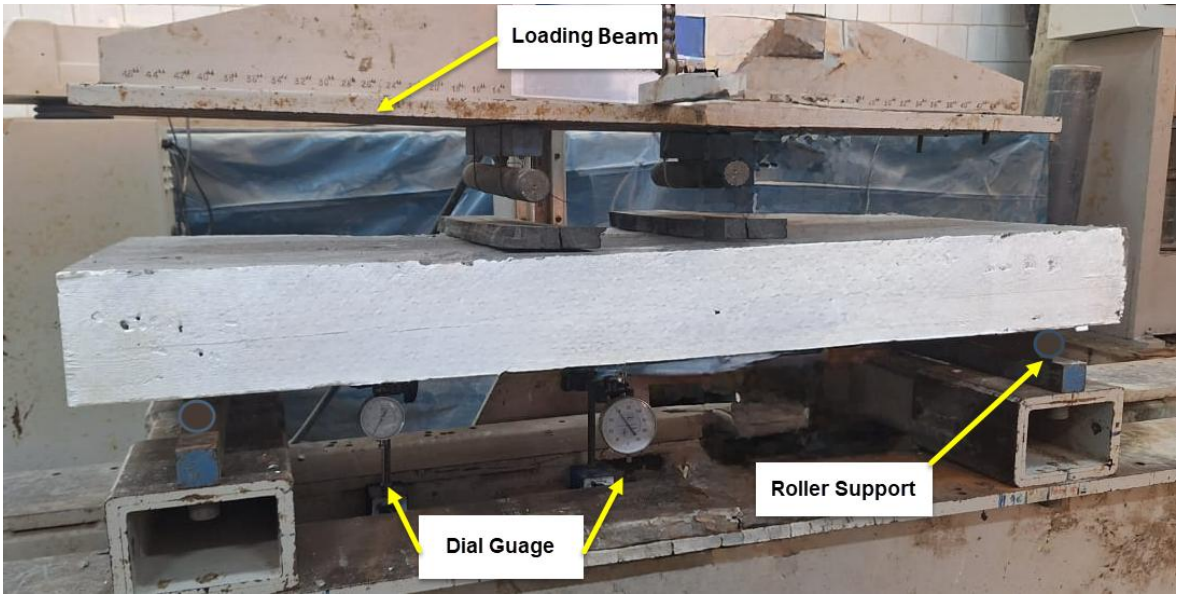

Fig. 14. Test setup.

4. Results and Discussion

4.1. Load-deflection relationship

Fig. 15 presents the load-deflection relationships for all tested plates, and Fig. 15(e) compares the responses of all groups. The control specimen (PC) had the lowest ultimate load (31.6 kN) and maximum deflection (11.22 mm). All reinforced plates exhibited higher strength and ductility than the control specimen. Group A (PW) showed a progressive increase in ultimate load from 35.2 to 52.3 kN as the number of welded mesh layers increased. Group B (PT) showed moderate improvement, with ultimate loads ranging from 40.7 to 46.2 kN. Group C (PG) achieved high performance, with specimen PG1+T1 reaching an ultimate load of 51.4 kN, confirming that the combined use of Tenax and Gavazzi meshes enhanced the ultimate strength.

The serviceability load was defined as the load corresponding to a mid-span deflection equal to the slab span divided by 250, as specified by ECP 203/2020. As summarized in Table 12, the control specimen (PC) exhibited a serviceability load of 11.3 kN. Specimens reinforced with welded and Tenax meshes showed significant increases in serviceability load, ranging from 13.63% to 97.10% for Group A and from 46.26% to 75.21% for Group B. The specimen reinforced only with Gavazzi mesh showed a slight increase of 3.41%, whereas the hybrid specimen (PG1+T1) exhibited a 66.64% increase.

The higher stiffness observed in specimens with welded wire mesh was directly associated with its high modulus of elasticity (E = 170 GPa) and proof strength (F_y = 400 MPa). This metallic reinforcement provides a rigid internal skeleton within the 120 mm plate, offering strong resistance to initial deformation in the linear elastic stage and maintaining the slope of the load-deflection curve before first cracking. Although welded mesh provided greater stiffness, Gavazzi mesh (E = 72 GPa, F_u = 325 MPa) was more flexible and had higher strain capacity.

4.2. Ductility ratio

The ductility ratio is defined as the ratio of the mid-span deflection at ultimate load (Δu) to the deflection at first cracking load (Δy). Therefore, the ductility ratio ($\Delta u/\Delta y$) represents the deformation capacity of the plate beyond first cracking. As shown in Table 12, the control plate (PC) exhibited the lowest ductility ratio (1.00). Plates reinforced with welded wire mesh (Group A) showed clear improvement, reaching a maximum value of 2.36 for specimen PW4. Tenax mesh plates (Group B) also showed improved ductility, with values ranging from 1.67 to 2.11. In contrast, the Gavazzi mesh plate (PG1) recorded the lowest ductility ratio (0.75), while the hybrid plate (PG1+T1) improved to 1.71. Overall, most reinforced plates exhibited higher ductility than the control specimen.

4.3. Energy absorption

Energy absorption (EA) was calculated as the area under the load-deflection curve for each plate. This area was obtained by integrating the applied load with respect to displacement from the beginning of loading to the displacement at failure. The trapezoidal numerical integration method was used to calculate the area according to Eq. (1).

$$EA = \sum_{i=1}^{n} \frac{F_i + F_{i+1}}{2} \Delta_{x_i} \quad (1)$$

As shown in Table 12, the control specimen (PC) absorbed 227.09 kN·mm, whereas all reinforced plates exhibited higher energy absorption. Specimens PG1 (398.98 kN·mm) and PG1+T1 (391.30 kN·mm) showed the highest values, indicating that non-metallic reinforcement meshes increased the energy absorption capacity of the plates compared with the control specimen. The use of Gavazzi and Tenax meshes improved energy absorption because their lower elastic modulus allowed greater deformation and, consequently, a larger area under the load-deflection curve. Overall, plates reinforced

with Tenax mesh (Group B) absorbed less energy than those reinforced with welded wire mesh (Group A), while Gavazzi and the hybrid mesh system provided the highest energy dissipation.

4.4. Concrete strain

Fig. 16 shows the load-strain curves for all tested plates. In general, increasing the number of reinforcement mesh layers increased the compressive strain because of the higher stiffness and load-carrying capacity of the plates. Specimen PW4 achieved the maximum compressive strain value (-0.00083). In contrast, the tensile strain on the concrete surface decreased as the number of reinforcement layers increased, indicating that the additional mesh layers helped reduce surface tensile deformation.

4.5. Cracking behavior

Fig. 17 shows the crack patterns for the different test groups. In all specimens, cracking began near the mid-span region. As the applied load increased, cracks propagated from the tension side toward the compression side and extended across the plate. The first cracking load varied according to mesh type, as shown in Table 12. With further loading, new cracks formed on both sides of the initial crack, while the first crack continued to propagate vertically. Additional cracks also developed as the load increased, although the earlier cracks mainly continued to grow vertically. The first cracking load was recorded during testing, and the flexural serviceability load was determined for each specimen, as listed in Table 12. Plates reinforced with welded mesh showed fewer but wider cracks, indicating a more localized and brittle failure once the steel yielded. In contrast, specimens reinforced with Gavazzi mesh (PG1) or with the Gavazzi-Tenax hybrid system (PG1+T1) exhibited a multi-cracking pattern with many fine and closely spaced cracks. This confirms that the Gavazzi mesh effectively arrested crack propagation and distributed energy across the plate span, thereby improving toughness and ductility. All specimens failed in flexure.

Table 12. Summary of results for all tested plates.

Specimen group	Specimen	First crack load (kN)	Ultimate load (kN)	Maximum deflection (mm)	Serviceability load (kN)	Ductility ratio Δ_u / Δ_y	Energy absorption (kN·mm)	Weight (kg)	Load / weight ratio (kN/kg)
Control	PC	8	31.6	11.22	11.3	1	227.09	135	0.23
A	PW1	10	35.2	11	12.8	1.16	259.15	136	0.26
	PW2	12	39.3	10.23	15.4	1.5	276.88	137	0.29
	PW3	13.5	42	9.98	16.8	1.69	294.1	138	0.30
	PW4	15	52.3	9.42	22.2	2.36	316.82	139	0.38
B	PT1	9	40.7	9.88	16.5	1.67	242.97	138	0.29
	PT2	11	44.4	9.43	18.8	2.00	240.52	139	0.32
	PT3	12.5	46.2	9.36	19.7	2.11	251.87	140	0.33
C	PG1	12	39.5	14.52	11.9	0.75	398.98	139	0.28
	PG1+T1	14	51.4	10.95	18.776	1.71	391.3	142	0.36

5. Conclusions

The following conclusions can be drawn from the experimental results and observations:

- Adding reinforcing mesh significantly improved ultimate load, service load, ductility, and energy absorption compared with the control plate (PC).
- Plates reinforced with welded mesh (Group A) increased the ultimate load by an average of 34% compared with PC.
- The plate reinforced with four layers of welded mesh (PW4) achieved the highest ultimate load (52.3 kN) and ductility ratio (2.36).
- The plate reinforced with one layer of Gavazzi mesh (PG1) achieved the highest energy absorption value (398.98 kN·mm), which was 75.9% higher than that of the control specimen.
- Service loads increased by 48.88% for PW4 and by 31.48% for PT3 compared with PC.
- The highest ductility ratios were obtained for PT3 and PW4, with improvements of 111% and 136%, respectively, compared with PC.
- The plate reinforced with four layers of welded mesh (PW4) achieved the highest load-to-weight ratio of 0.38 kN/kg, corresponding to an increase of more than 65% compared with the control plate. This indicates a higher load-carrying capacity for the same structural weight.

6. Recommendations

- Investigate the behavior of lightweight ferrocement plates reinforced with different meshes under impact and dynamic loading.
- Study the effect of high temperature and fire exposure on ultimate load, ductility, and energy absorption.
- Evaluate alternative mesh materials, such as polyethylene or geogrid systems, and their influence on strength and durability.
- Assess the acoustic performance of lightweight ferrocement plates used in building floors and walls.
- Conduct an economic study covering materials, fabrication, labor, and maintenance to evaluate cost-effectiveness.
- Investigate long-term durability under harsh environmental conditions, including moisture, chemicals, and temperature variations.

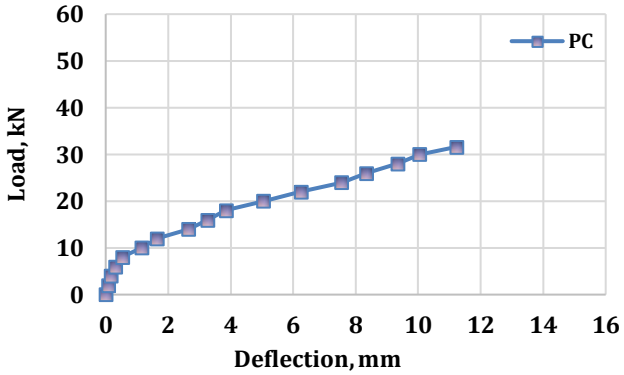

(a) Control plate

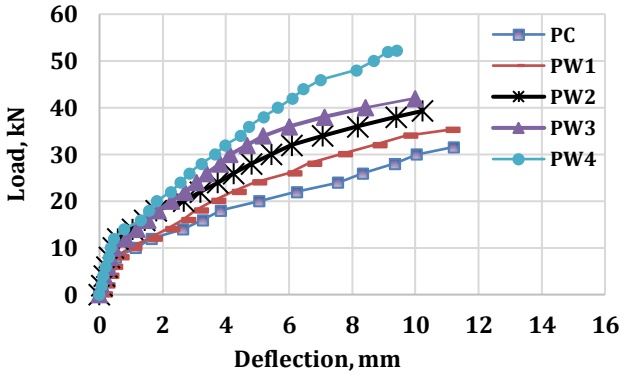

(b) Group A

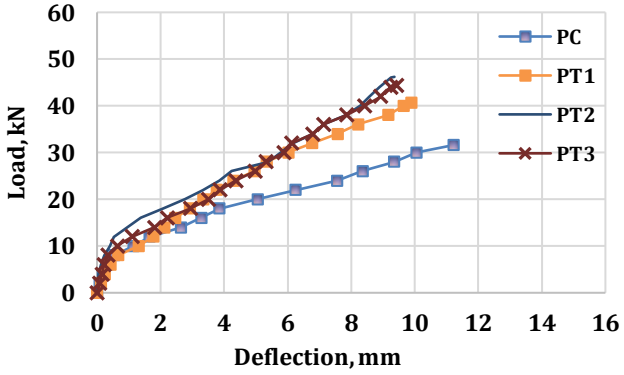

(c) Group B

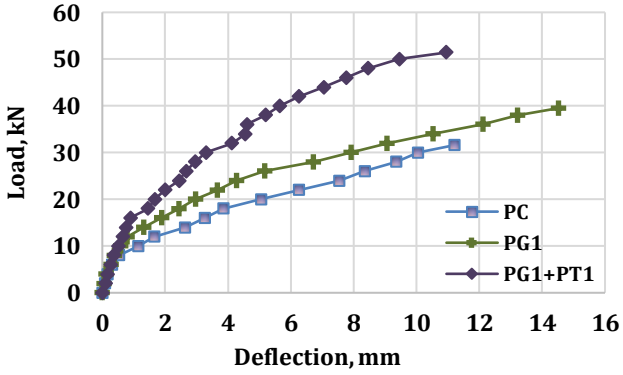

(d) Group C

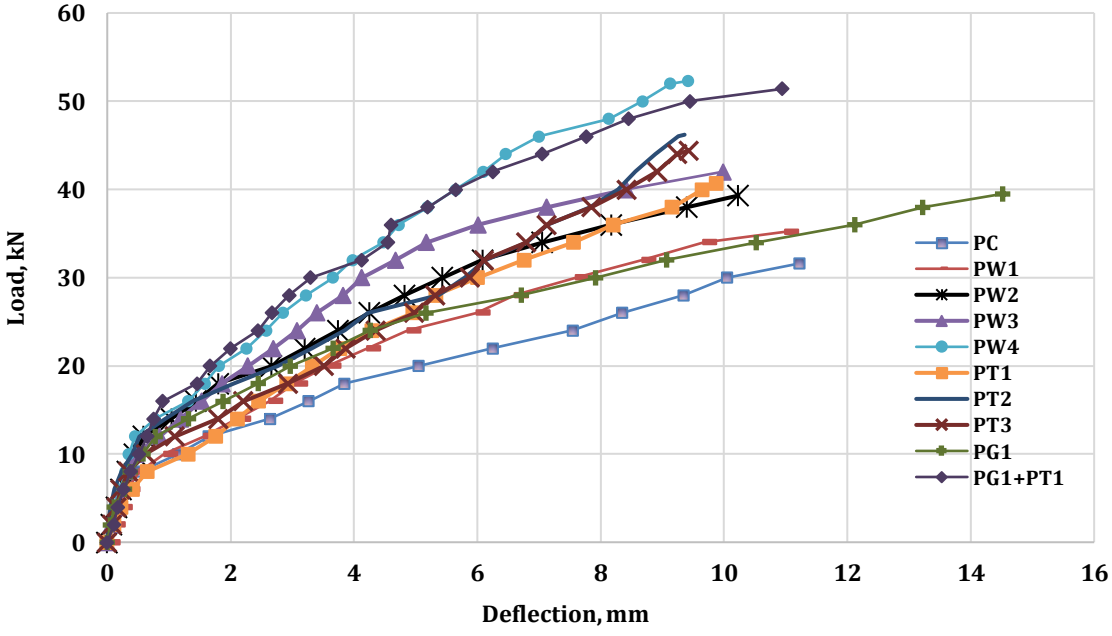

(e) All groups

Fig. 15. Load-deflection curves of different groups.

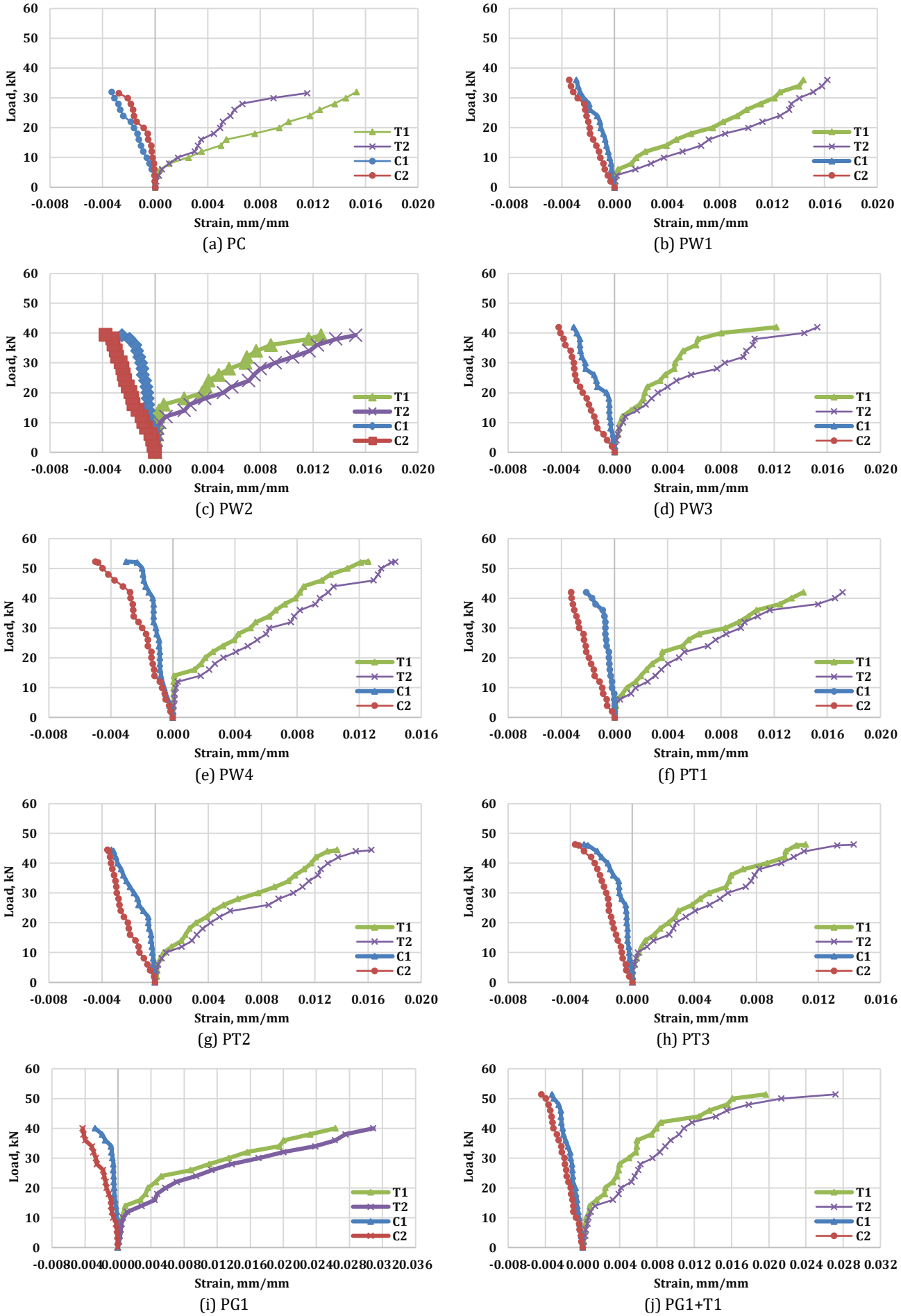

Fig. 16. Load-strain curves of different groups.

(a) PC

(b) PW1

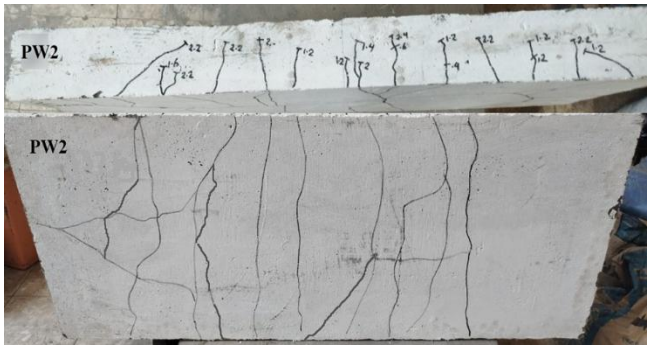

(c) PW2

(d) PW3

(e) PW4

(f) PT1

(g) PT2

(h) PT3

(i) PG1

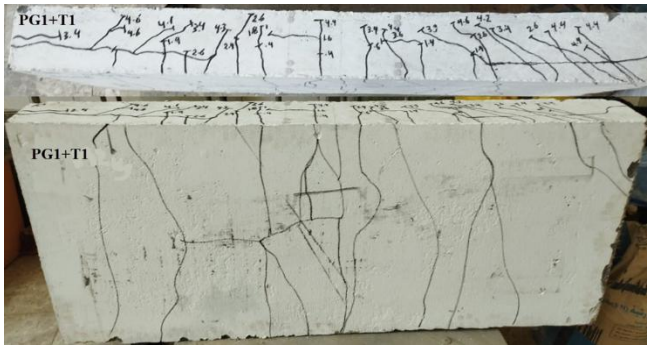

(j) PG1+T1

Fig. 17. Cracking patterns of different groups.

Acknowledgements

None declared.

Funding

The authors received no financial support for the research, authorship, and/or publication of this manuscript.

Conflict of Interest

The authors declare no potential conflicts of interest with respect to the research, authorship, and/or publication of this manuscript.

Data Availability

The datasets generated and/or analyzed during the current study are not publicly available but are available from the corresponding author upon reasonable request.

AI Assistance

No AI-based tools were used in the preparation of this manuscript.

Author Contributions

All authors made substantial contributions to the conception and design of the study, acquisition of data, analysis and interpretation of data; drafted or critically revised the manuscript for important intellectual content; and approved the final version to be published.

REFERENCES

Abdel Tawab A (2006). Development of Permanent Formwork for Beams Using Ferrocement Laminates. *Ph.D. thesis*, Menoufia University, Shebin El-Kom, Egypt.

Acma LMC, Dumpasan GC, Salva MI, Mansaguiton MP, Supremo RP, Daquiado NFP (2015). Flexural strength and ductility behavior of ferrocement I-beam. *Mindanao Journal of Science and Technology*, 13(1), 99-108.

Dawood ET, Shawkat AS, Abdullah MH (2021). Flexural performance of ferrocement based on sustainable high-performance mortar. *Case Studies in Construction Materials*, 15, e00566.

ECP 203/2020 (2020). Egyptian code of practice: Design and construction of reinforced concrete structures. Housing and Building National Research Center (HBRC), Cairo, Egypt.

El-Sayed TA, Deifalla AF, Shaheen YBI, Ahmed HH, Youssef AK (2023). Experimental and numerical studies on flexural behaviour of GGBS-based geopolymer ferrocement beams. *Civil Engineering Journal*, 9(3), 629-653.

Eltaly BA, Shaheen YBI, El-Boridy AT, Fayed S (2023). Ferrocement composite columns incorporating hollow core filled with lightweight concrete. *Engineering Structures*, 280, 115672.

EOS 1658-4 (2018). Testing hardened concrete. Part 4: Making and curing specimens for strength test. Egyptian Organization for Standardization and Quality (EOS), Cairo, Egypt.

ESS 1109 (2021). Aggregates for concrete. Egyptian Organization for Standardization and Quality (EOS), Cairo, Egypt.

ESS 4756-1 (2022). Cement. Part 1: Composition, specifications and conformity criteria for common cements. Egyptian Organization for Standardization and Quality (EOS), Cairo, Egypt.

ISO 1920-3 (2004). Testing of concrete. Part 3: Making and curing test specimens. International Organization for Standardization, Geneva, Switzerland.

Madadi A, Eskandari-Naddaf H, Shadnia R, Zhang L (2018). Digital image correlation to characterize the flexural behaviour of lightweight ferrocement slab panels. *Construction and Building Materials*, 189, 967-977.

Murali G, Amran M, Fediuk R, Vatin N, Raman SN, Maithreyi G, Sumathi A (2020). Structural behaviour of fibrous-ferrocement panel subjected to flexural and impact loads. *Materials*, 13(24), 5648.

Naveen GM, Suresh GS (2020). A study of fiber reinforced light weight ferrocement beams under monotonic and repeated loading. *International Research Journal of Engineering and Technology*, 7(12), 41-47.

Qureshi HJ, Khurram N, Akmal U, Arifuzzaman M, Habib Q, Al Fuhaid AF (2023). Flexure performance of ferrocement panels using SBR latex and polypropylene fibers with PVC and iron welded meshes. *Polymers*, 15(10), 2304.

Rajguru RS, Patkar M (2022). Torsion behaviour of strengthened RC beams by ferrocement. *Materials Today: Proceedings*, 61, 138-142.

Rao TC, Rao TG, Rao NR (2008). An experimental study on ferro cement channel units under flexural loading. *International Journal of Mechanics and Solids*, 3(2), 195-203.

Shaheen YBI, Soliman NM, Hafiz AM (2013). Structural behaviour of ferrocement channels beams. *Concrete Research Letters*, 4(3), 621-638.

Shaheen YBI, Nasser AA, El-Habashy WS (2016). Behaviour of ferrocement sandwich panels slabs under shear. *Concrete Research Letters*, 7(1), 11-23.

Shaheen YBI, Eltaly BA, Yousef SG, Fayed S (2023a). Structural performance of ferrocement beams incorporating longitudinal hole filled with lightweight concrete. *International Journal of Concrete Structures and Materials*, 17(1), 21.

Shaheen YBI, Etman ZA, Kandil DE (2023b). Performance of light weight ferrocement composite walls. *Challenge Journal of Concrete Research Letters*, 14(3), 110-125.

Shaheen YBI, Etman ZA, Mohamed AAF (2024). Structural behavior of ferrocement beams with circular openings. *Challenge Journal of Structural Mechanics*, 10(4), 116-137.

Challenge Journal of CONCRETE RESEARCH LETTERS

Research Article

The effect of Mount Sinabung volcanic ash and the addition of silica fume as a partial substitution of cement weight on the compressive strength of concrete

Fahrizal Zulkarnain [a,*], Zulkifli Siregar [a], Fadzil Mat Yahaya [b]

[a] *Department of Civil Engineering, Universitas Muhammadiyah Sumatera Utara, 20238 Medan, Sumatera Utara, Indonesia*
[b] *Faculty of Civil Engineering Technology, Universiti Malaysia Pahang Al-Sultan Abdullah, 26300 Kuantan, Pahang, Malaysia*

ABSTRACT

The use of concrete continues to grow due to its superior performance compared to alternative construction materials; however, rising cement costs significantly increase production expenses. This study investigates the use of Mount Sinabung volcanic ash and silica fume as partial cement replacements to improve cost efficiency, reduce cement consumption, and enhance sustainability and mechanical properties. This approach not only contributes to the development of eco-friendly concrete technology but also provides a potential solution for managing volcanic ash waste from volcanic eruptions in Indonesia. Previous studies have primarily evaluated volcanic ash and silica fume separately, whereas their combined effects in concrete mixtures remain insufficiently explored, particularly in terms of compressive strength and mixture performance. Therefore, this study aims to evaluate the influence of incorporating both materials simultaneously. A total of 18 cylindrical concrete specimens (150 mm in diameter and 300 mm in height) were prepared with a target compressive strength of 25 MPa, consisting of six mix variations with three specimens each. The results showed that normal concrete achieved an average compressive strength of 25.16 MPa, while mixtures containing volcanic ash alone exhibited lower strengths, although an increasing trend was observed with higher replacement levels. However, the combination of volcanic ash and silica fume demonstrated improved performance compared to volcanic ash-only mixtures. These findings indicate that silica fume enhances the pozzolanic reaction and improves the concrete microstructure, suggesting that the combined use of these materials offers a promising approach for producing sustainable and cost-effective concrete with acceptable mechanical performance in practical construction applications.

ARTICLE INFO

Article history:
Received – January 30, 2026
Revision requested – March 13, 2026
Revision received – April 3, 2026
Accepted – April 10, 2026

Keywords:
Volcanic ash
Silica fume
Compressive strength
Environmentally friendly construction
Concrete mixtures

Citation: Zulkarnain F, Siregar Z, Mat Yahaya F (2026). The effect of Mount Sinabung volcanic ash and the addition of silica fume as a partial substitution of cement weight on the compressive strength of concrete. *Challenge Journal of Concrete Research Letters*, 17(2), 192–206.

1. Introduction

Indonesia, as a developing country, continues to enhance its infrastructure to support public services. At the same time, government policies and regulations in the construction sector increasingly emphasize environmental considerations, leading to the adoption of sustainable and environmentally friendly building practices (Firmansyah et al. 2022).

Further research is required to support the advancement of construction technology, particularly in concrete innovation, by utilizing locally available materials through low-technology approaches such as recycled or natural resources. In this context, Indonesia's abun-

* *Corresponding author*. E-mail address: fahrizalzulkarnain@umsu.ac.id (F. Zulkarnain)
ISSN: 2548-0928 / DOI: https://doi.org/10.20528/cjcrl.2026.02.009

dance of active volcanoes presents significant potential for the utilization of volcanic materials as alternative constituents in concrete production (Adi et al. 2018; Mulyadhi and Zulkarnain 2021). Mount Sinabung, an active volcano located in Karo Regency, produces large quantities of volcanic ash that can be utilized as a sustainable construction material. Its application as a partial replacement for cement provides dual benefits, namely reducing environmental impact and promoting eco-friendly construction practices (Lamotokana et al. 2021).

In addition to volcanic ash, this study incorporates silica fume as a supplementary cementitious material to enhance concrete performance. Silica fume is a silica-rich industrial by-product that reacts with calcium hydroxide in the cement matrix to form additional calcium silicate hydrate (C–S–H), thereby improving the mechanical properties and overall quality of concrete (Posman and Zulkarnain 2022; Purba et al. 2021).

Previous studies have extensively investigated supplementary cementitious materials such as silica fume, fly ash, and natural pozzolans to improve the mechanical and durability properties of concrete (Zhang et al. 2022). Silica fume has been reported to enhance compressive strength and microstructure due to its high pozzolanic activity and ultrafine particle size, which contribute to the formation of additional C–S–H and the densification of the cement matrix (Han et al. 2024; Azizi and Samimi 2025). Meanwhile, volcanic ash has also been explored as a natural pozzolanic material in cement-based composites, particularly in regions with high volcanic activity (Hamada et al. 2023; Rashad 2021).

However, despite the abundance of volcanic ash resources in Indonesia, particularly from Mount Sinabung, its utilization as a sustainable construction material remains limited. Most previous studies have focused on the independent use of volcanic ash or other industrial by-products, while research investigating the combined effect of volcanic ash and silica fume is still scarce. Furthermore, the specific influence of Sinabung volcanic ash on compressive strength when combined with silica fume has not been widely reported (Abutaqa et al. 2024; Khan et al. 2024; Nadia 2011).

Therefore, this study aims to investigate the combined use of Mount Sinabung volcanic ash and silica fume as partial replacements for cement in concrete mixtures. Unlike previous studies that examined these materials separately, this research evaluates their combined effect on compressive strength, using a fixed silica fume content of 5% and volcanic ash contents of 4% and 8% by weight of cement. This study also examines whether these combinations can achieve compressive strength comparable to normal concrete while promoting more sustainable construction materials.

The novelty of this research lies in the integration of locally available Sinabung volcanic ash with silica fume in concrete mixtures. This approach provides a sustainable solution for utilizing volcanic by-products while maintaining acceptable mechanical performance. In addition, it contributes to the development of eco-friendly concrete technology and offers a potential solution for managing volcanic ash waste in Indonesia.

2. Materials and Methods

2.1. Research stages

This study was initiated after the final project proposal had been officially approved by the study program. Subsequently, the experimental work was carried out at the Civil Engineering Laboratory of Universitas Muhammadiyah Sumatera Utara, beginning with preliminary material characterization and basic testing procedures. This study employed an experimental method to investigate the mechanical properties of concrete mixtures containing volcanic ash and silica fume.

The material preparation stage involved setting up testing equipment and evaluating the fundamental properties of the constituent materials used in the concrete mixtures, including fine and coarse aggregates, Portland cement, water, and supplementary cementitious materials such as volcanic ash from Mount Sinabung and silica fume. All preparation and preliminary material testing were conducted in accordance with standard laboratory procedures (Sani 2021).

The concrete mixture was designed in compliance with the provisions of SNI 7656 (2012) with proportions selected to meet the required performance parameters. The mix design was developed based on the results of preliminary material characterization, including tests on cement, fine aggregate, coarse aggregate, water, Mount Sinabung volcanic ash, and silica fume. These tests provided essential parameters for determining the appropriate proportions of each material in the concrete mixture. All concrete specimens used in this study were prepared according to the final mix design (Alkhaly 2015).

This stage included a series of procedures, such as preparing the concrete mixture, evaluating workability through slump testing in accordance with SNI 1972:2008, casting fresh concrete into cylindrical molds, and demolding after the specimens had reached sufficient initial setting. Curing was carried out by immersing all concrete specimens in water until they reached the testing age of 28 days (Sebayang 2020).

After reaching the curing age of 28 days, the compressive strength of the specimens was tested using a compression testing machine. The results obtained from this test were used as the primary data for analysis and interpretation (Alfiandinata 2020).

At this stage, the experimental data were processed and analyzed systematically. The results were then interpreted and discussed in accordance with the research objectives. Finally, conclusions were drawn based on the findings of the study.

2.2. Data sources and data collection

The data collected in this study comprised laboratory test results, including aggregate gradation analysis in accordance with SNI ASTM C136 (2012), determination of specific gravity and water absorption of both coarse and fine aggregates following SNI 1969 (2016), and evaluation of aggregate unit weight based on SNI 1973 (2008). In addition, the moisture content of aggregates was measured in accordance with SNI 1971 (2011), while the

clay and silt content was assessed following SNI 03-4142 (1996). Concrete mixture proportioning was carried out in accordance with SNI 7656 (2012), and the preparation as well as curing of concrete specimens followed SNI 2493 (2011). The workability of fresh concrete was evaluated through slump testing in accordance with SNI 1972 (2008), while compressive strength testing was conducted based on SNI 1974 (2011).

In addition to primary laboratory data, secondary data were obtained from relevant textbooks and scientific publications related to concrete technology and engineering. References used in the preparation of concrete mixtures include the SNI (Indonesian National Standards) guidelines (Sihombing 2017).

The selected replacement levels of Mount Sinabung volcanic ash and silica fume were determined based on their pozzolanic characteristics and findings from previous studies, which indicate their potential to enhance concrete performance.

The physical and chemical properties of Mount Sinabung volcanic ash and silica fume utilised in this study were comprehensively characterised to establish a clear understanding of their roles within the concrete mixture. Key parameters, including particle size distribution, specific surface area, chemical composition-particularly SiO_2 content-and pozzolanic activity, were considered to elucidate their contributions to strength development and workability. Such detailed material characterisation enhances the reliability of the analysis and provides a robust scientific basis for interpreting the performance of the concrete mixtures (Scrivener et al., 2018; Mehta and Monteiro, 2014).

2.3. Materials

The cement used in this study was Type I Portland cement (Ordinary Portland Cement) under the brand name Semen Padang. This cement complies with the requirements of SNI 15-2049 (2004), ASTM C 150 (2007), BS 12 (1996), and JIS R5210 (1981). The cement was obtained from a local building materials supplier in Medan City.

Fine aggregate (sand) used in this study was sourced from Binjai. Coarse aggregate, in the form of crushed stone, was also obtained from Binjai, North Sumatra (Kamil and Zulkarnain 2021). The water used in this research was obtained from the Civil Engineering Laboratory and was used for both mixing and curing processes.

Mount Sinabung volcanic ash was obtained from an eruption site located in Karo Regency, specifically from Sukanalu Teran Village. The ash was used at replacement levels of 4% and 8% by weight of cement. The material was dried under sunlight until completely dry and then sieved using sieve No. 100.

Silica fume, supplied as a commercial product (SikaFume®), was used at 5% by weight of cement and was obtained from a local building materials supplier in Medan City (Lamotokana et al. 2021).

Details of the concrete mixtures are provided in Table 1.

2.4. Mount Sinabung volcanic ash

The volcanic ash used in this study was obtained from Mount Sinabung, located in Karo Regency. After collection, the ash was dried under sunlight until completely dry (Rochmah et al. 2023).

The preparation process included placing the volcanic ash in a container, drying it using a pan under sunlight, collecting the dried ash, and then crushing it to obtain finer particles. The ash was subsequently sieved using sieve No. 100 and retained on sieve No. 200 to ensure uniform particle size (Widianto et al. 2021).

2.5. Casting

A total of 18 cylindrical specimens, each with a diameter of 15 cm and a height of 30 cm, were prepared. A schematic illustration of the cylindrical mold is shown in Fig. 1.

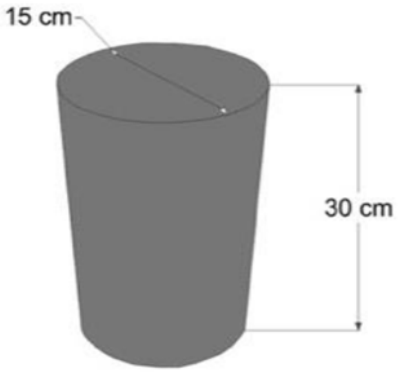

Fig. 1. Sketch of a cylindrical test object (Sultan et al. 2023).

Table 1. Test specimens and concrete mixtures.

Test object code	Cement	Coarse aggregate	Fine aggregate	Volcanic ash	Silica fume	Amount sample
BN	100%	100%	100%	0%	0%	3
BSF 5%	95%	100%	100%	0%	5%	3
BAV 4%	96%	100%	100%	4%	0%	3
BAV 8%	92%	100%	100%	8%	0%	3
BAV 4% + SF 5%	91%	100%	100%	4%	5%	3
BAV 8% + SF 5%	87%	100%	100%	8%	5%	3
					Amount	18

BN: Normal Concrete; BSF: Silica Fume Concrete; BAV + SF: Volcanic Ash Concrete + Silica Fume.

2.6. Slump testing

The slump value was determined for both the control concrete and the concrete mixtures containing supplementary materials. The slump test was performed on fresh concrete using an Abrams cone. The cone was filled in three layers, each approximately one-third of the total height. Each layer was compacted 25 times using a stainless-steel tamping rod (Mboru et al. 2022).

After filling, the surface was leveled using a trowel. The slump value was then measured by lifting the cone vertically and determining the difference in height between the cone and the slumped concrete (Karolina et al. 2018). The workability of concrete is closely related to its consistency and ease of flow. A higher slump value indicates better workability and ease of placement. Therefore, the slump test is commonly used to evaluate the workability of fresh concrete mixtures SNI 1972 (2008).

The procedure for slump testing was as follows: the Abrams cone and base plate (1 m × 1 m) were first moistened and placed on a flat surface. The cone was positioned at the centre of the plate, and the concrete mixture was poured into the cone in three layers. Each layer was compacted 25 times using a tamping rod and leveled. The mixture was allowed to rest briefly before the cone was lifted vertically. The spread of the concrete was then observed and measured. The diameter of the spread was recorded using a ruler in both vertical and horizontal directions. A larger spread diameter indicates lower viscosity and higher fluidity of the concrete mixture (Handayani 2019).

2.7. Curing

After casting, the concrete specimens were demoulded and cured by immersion in water under controlled laboratory conditions until the testing age of 28 days. After removal from the curing tank, the specimens were allowed to dry before weighing (Khalik Nasution et al. 2021).

2.8. Concrete strength in compression test

The compressive strength test was conducted in accordance with SNI 1974:2011 using a compression testing machine with an appropriate capacity. A total of 18 cylindrical concrete specimens, each with a diameter of 150 mm and a height of 300 mm, were prepared in this study. The specimens were divided into six mixture variations, with three specimens for each variation, as presented in Table 2. All specimens were tested for compressive strength at the age of 28 days. This experimental design ensures consistency and allows a reliable comparison of the effects of each variation on concrete performance.

A total of 18 test specimens was prepared in this study, comprising six mixture variations, each consisting of three samples, as shown in Table 2.

During testing, each specimen was placed in the testing machine, and load was applied gradually until failure occurred. The maximum load sustained by each specimen was recorded and used to calculate the compressive strength of the concrete.

Table 2. Number of variations in concrete test samples.

No	Concrete mix variations	Sample testing (28 days)
1	Normal concrete	3 pieces
2	Silica fume concrete 5%	3 pieces
3	Volcanic ash concrete 4%	3 pieces
4	Volcanic ash concrete 8%	3 pieces
5	4% Volcanic ash concrete using 5% silica fume	3 pieces
6	8% Volcanic ash concrete using 5% silica fume	3 pieces
	Total	18 pieces

3. Results and Discussion

3.1. Concrete failure mode

At the initial stage of the compressive strength test, each concrete specimen was positioned at the center of the testing machine to ensure uniform load distribution. The applied load increased gradually, and the concrete exhibited elastic behavior, characterized by reversible deformation without visible damage.

As the load increased, the material entered the elastic–plastic phase, where internal microcracks began to develop, particularly at the interface between the cement paste and aggregates. Although these cracks were not yet visible, they indicated the onset of internal structural deterioration. With continued loading, the microcracks propagated and became visible on the surface as fine cracks, generally aligned with the loading direction or appearing as inclined cracks due to combined stress effects.

Approaching the maximum load, crack propagation intensified and was accompanied by minor surface spalling, indicating a reduction in the integrity of the concrete matrix. Failure occurred when the load reached its peak value, marked by the formation of a dominant crack that split the specimen and caused a sudden drop in load. The failure patterns and cracking behaviour observed during testing are presented in Figs. 2 and 3.

Overall, the failure process occurred progressively, starting from microcrack initiation and ending in complete fracture. This behaviour confirms that concrete failure under compression is gradual and governed by progressive internal damage.

Fig. 2. Failure pattern of concrete cylinder specimen under compressive strength testing.

Fig. 3. Concrete cracking pattern in 28 days compressive strength test.

3.2. Fine aggregate inspection

The specific gravity test was conducted to determine the physical characteristics of the fine aggregate. The results show consistent values for bulk, saturated surface dry, and apparent specific gravity, indicating that the aggregate has suitable density and quality for concrete production (Tables 3 and 4).

Table 3. Fine aggregate specific gravity test.

Testing	Notation	I	II	Units
The weight of the test object in surface dry saturated conditions	S	500	500	grams
Oven dry test object weight	A	487	482	grams
The mass of a pycnometer with water in it	B	662	661	grams
When the test object and water are added, the pycnometer's weight is up to reading limit	C	964	975	grams

Table 4. Calculation of fine aggregate.

Calculation	Equality	I	II	Average
Bulk specific gravity (S_d)	A/(B+S-C)	2.46	2.59	2.53
Surface dry saturated particular gravity (S_s)	S/(B+S-C)	2.53	2.69	2.61
Specific gravity apparent (S_a)	A/(B+A-C)	2.63	2.87	2.75
Absorption of water (S_w)	((S-A)/A)×100%	2.67	3.73	3.20

The gradation analysis (Table 5) indicates that the particle size distribution of the fine aggregate is well graded. This condition is important for achieving good packing density, reducing voids, and improving the workability of the concrete mixture.

The sludge content test (Tables 6–9) shows the presence of fine particles passing through sieve No. 200. The average value obtained is 4.39%, which is still within an acceptable range. However, excessive fines may affect the bond between the cement paste and aggregates.

Table 5. Fine aggregate gradation analysis.

Filter	Mass stuck	Amount stuck	Cumulative percentage (%)	
mm (inch)	Grams (a)	Grams (b)	Stuck (c)	Get away (d)
No. 3/8	3	3	0.6	100
No. 4	2	5	1.0	99.0
No. 8	4	9	1.8	98.2
No. 16	411	420	84.0	16.0
No. 30	58	478	95.6	4.4
No. 50	18	496	99.2	0.8
No.100	2	498	99.6	0.4
No. 200	1	499	99.8	0.2
Pan	1	500	100.0	0.0

Table 6. Testing of fine aggregate sludge content.

Fine aggregate passes sieve no.4	Notation	I	II	Units
Weight of container + contents	W1	1,618	1,802	grams
Container weight	W2	504	510	grams
Dry sample weight + container	W4	1,565	1,750	grams

Table 7. Results of fine aggregate sludge content test.

Calculation	Equality	I	II	Average
Dry weight of initial sample (W3)	W1-W2	1,114	1,292	1,203
Dry weight of the sample after washing (W5)	W4-W2	1,061	1,240	1,150.5
The weight of aggregate dirt passing through the filter No. 200 (W6)	W3-W5	53	52	52.5
Percentage of aggregate impurities passing sieve No.200	(W6/W3)×100	4.76	4.02	4.39

Based on the test results, the mud content value in sample 1 was 4.76% and in sample 2 it was 4.02%. So, the average mud content value in the two samples is 4.39%.

The water content test (Table 10) shows an average value of 5.39%. This value must be considered when calculating the total water content in the concrete mixture to maintain the desired workability and strength.

Table 8. Testing of fine aggregate content weight 200.

Coarse aggregate	Notation	Free	Tapping	Shake	Units
Weight of container + contents	1	16,982	17,890	17,908	grams
Container weight	2	5,300	5,300	5,300	grams
Container volume	3	10,851.84	10,851.84	10,851.84	cm^3

Table 9. Fine aggregate sludge content passing sieve no. 200

Calculation	Equality	I	II	III	Units
Sample weight (4)	(1-2)	11,682	12,590	12,608	grams
Content weight	(3/4)	1.076	1.160	1.162	$grams/cm^3$
Average		1.133			$grams/cm^3$
		1,132.83			kg/m^3

Table 10. Fine aggregate water content testing.

Calculation	1st test object	2nd test object
Mass of container + test object	2,509	2,498
Mass of container	488	511
Mass of test object (W1)	2,021	1,987
Mass of container + test object	2,405	2,397
Mass of container	488	511
Mass of oven-dry specimen (W2)	1,917	1,886
Total water content (P)	5.43	5.36
((W1-W2)/W2)×100%		
Average total water content (P)	5.39	

3.3. Coarse aggregate inspection results

The specific gravity and water absorption tests were conducted to evaluate the physical properties of the coarse aggregate (Tables 11 and 12). The results indicate that the aggregate has good density and relatively low porosity, which are important characteristics for producing durable concrete SNI 1969 (2016).

Based on the specific gravity test results, the average SSD (saturated surface dry) specific gravity was 2.59 and the water absorption from the test results was 1.93%. The gradation analysis (Table 13) shows that the coarse aggregate has an appropriate particle size distribution, with a fineness modulus of 7.34. A well-graded aggregate contributes to better interlocking between particles and improves the overall strength and stability of the concrete.

The sludge content test (Tables 14–17) indicates the presence of fine impurities in the aggregate. The average value obtained is 1.95%, which is within acceptable limits and suggests that the aggregate is sufficiently clean for use in concrete production.

Table 11. Tests for coarse aggregate absorption and specific gravity.

Testing	Notation	I	II	Units
Oven dry test object weight	A	1,964	1,972	grams
Surface dry saturated test object weight	B	2,002	2,010	grams
In the air	C	1,245	1,250	grams

Table 12. Results of coarse aggregate absorption and specific gravity test.

Calculation	Equality	I	II	Average
Bulk specific gravity (S_d)	A/(B-C)	2.59	2.59	2.59
Surface dry saturated particular gravity (S_s)	B/(B-C)	2.64	2.64	2.64
Specific gravity apparent (S_a)	A/(A-C)	2.73	2.73	2.73
Absorption of water (S_w)	((B-A)/A)×100%	1.93	1.93	1.93

Table 13. Coarse aggregate gradation analysis.

Filter	Detained mass	Retained amount	Cumulative percentage (%)	
mm (inch)	Grams (a)	Grams (b)	Stuck (c)	Get away (d)
No. 3/4	1,141	1,141	22.82	77.18
No. 1/2	1,431	2,572	51.44	48.56
No. 3/8	845	3,417	68.34	31.66
No. 4	1,176	4,593	91.86	8.14
No. 8			100	0
No. 16			100	0
No. 30			100	0
No. 50			100	0
No. 100			100	0
No. 200			100	0
Pan	407	5,000	100	0
Fineness modulus			734.46	7.34

Table 14. Coarse aggregate sludge content testing.

Coarse aggregate passes sieve no.4	Notation	I	II	Units
Weight of container + contents	W1	1,505	1,519	grams
Container weight	W2	505	519	grams
Weight Dry sample weight + container	W4	1,484	1,501	grams

Table 15. Results of coarse aggregate sludge content test.

Calculation	Equality	I	II	Average
Dry weight of initial sample (W3)	W1-W2	1,000	1,000	1,000
Dry weight of the sample after washing (W5)	W4-W2	979	982	980.5
The weight of aggregate dirt passing through the filter	W3-W5	21	18	19.5
The weight of aggregate dirt passing through the filter	(W6/W3)×100	2.1	1.8	1.95

The unit weight test results show that the coarse aggregate has an average unit weight of 1.67 g/cm^3. This value falls within the standard range for normal concrete, indicating that the aggregate meets the required specifications and is suitable for mix design calculations.

The water content (Table 18) of the coarse aggregate was measured to determine the amount of moisture present in the material. The average value obtained is 1.70%, which is an important parameter for adjusting the total water content in the concrete mixture to maintain consistency and achieve the desired performance.

Table 16. Coarse aggregate content weight test.

Coarse aggregate	Notation	Free	Tapping	Shake	Units
Weight of container + contents	1	22,974	24,023	23,272	grams
Container weight	2	5,300	5,300	5,300	grams
Container volume	3	10,851.84	10,851.84	10,851.84	cm^3

Table 17. Calculation of coarse aggregate content weight.

Calculation	Equality	I	II	III	Units
Sample weight (4)	(1-2)	17,674	18,723	17,972	grams
Content weight	(3/4)	1.628	1.725	1.656	grams/cm^3
Average			1.670		grams/cm^3
			1,670.039		kg/m^3

Table 18. Coarse aggregate water content testing.

Calculation	1st test object	2nd test object
Mass of container + test object	2,027	2,044
Mass of container	505	486
Mass of test object (W1)	1,522	1,558
Mass of container + test object	1,992	2,028
Mass of container	505	486
Mass of oven-dry specimen (W2)	1,487	1,542
Total water content (P)		
((W1-W2)/W2)×100%	2.35	1.04
Average total water content (P)	1.70	

3.4. Mix design

The parameters used in the concrete mix design were derived from preliminary material characterisation tests. The mix design was carried out in accordance with SNI 7656 (2012) to achieve a target compressive strength of 25 MPa. The selected mix design parameters are summarised in Table 19.

The concrete mixture was designed to achieve a target compressive strength of 25 MPa, with a specified slump range of 75–100 mm to ensure adequate workability for casting and compaction. A maximum aggregate size of 19 mm was selected to maintain proper grading and compatibility with the specimen dimensions.

The coarse aggregate content in oven-dry condition was determined as 1514.5 kg/m^3, while the specific

gravity of cement was taken as 3.15. The fine aggregate exhibited a fineness modulus of 3.8, indicating relatively coarse grading, with a specific gravity (SSD) of 2.61. Similarly, the coarse aggregate had a specific gravity (SSD) of 2.64, reflecting its density characteristics. Water absorption values were recorded as 3.20% for fine aggregate and 1.93% for coarse aggregate, and these parameters were considered in the adjustment of the mixing water to ensure accurate control of the effective water content in the concrete mixture.

Overall, these material properties and mix design parameters provided a consistent basis for proportioning the concrete mixtures and evaluating the influence of volcanic ash and silica fume on the performance of the hardened concrete.

Table 19. Mix design data table.

No	Data	Units	Value
1	Concrete quality	MPa	25
2	Slump	mm	75–100
3	Maximum aggregate size	mm	19
4	Oven dry weight of coarse aggregate	kg/m^3	1,514.5
5	The cement's specific gravity without air added	–	3.15
6	High-quality aggregate fineness modulus	–	3.8
7	Specific gravity (SSD) of fine aggregate	–	2.61
8	Specific gravity (SSD) of coarse aggregate	–	2.64
9	Water for fine aggregate absorption	%	3.20
10	Water aggregate that is coarse absorption	%	1.93

3.5. Material requirements

The test specimens consisted of 18 cylindrical concrete samples, each with a diameter of 15 cm and a height of 30 cm, resulting in a volume of 0.0053 m^3 per specimen. The total volume required for one variation was calculated as 0.0159 m^3.

Based on the mix design proportions, the quantities of cement, fine aggregate, coarse aggregate, water, volcanic ash, and silica fume were determined for each variation. These calculations ensure that each mixture maintains the required composition and allows consistent comparison between variations. The detailed material requirements for each mixture variation are presented in Table 20.

Table 20. Material requirements for each mixture variation.

No	Test object code	Volume (m^3)	Material composition						
			Cement (kg)	Silica fume (kg)	Fine aggregate (kg)	Coarse aggregate (kg)	Volcanic ash (kg)	Water (kg)	W/C ratio
1	BN	0.0053	5.34	–	13.47	16.16	–	2.94	0.55
2	BSF 5%	0.0053	5.07	0.26	13.47	16.16	–	2.94	0.58
3	BAV 4%	0.0053	5.12	–	13.47	16.16	0.21	2.94	0.57
4	BAV 8%	0.0053	4.91	–	13.47	16.16	0.42	2.94	0.60
5	BAV 4% + SF 5%	0.0053	4.86	0.26	13.47	16.16	0.21	2.94	0.60
6	BAV 8% + SF 5%	0.0053	4.64	0.26	13.47	16.16	0.42	2.94	0.63
	Total	0.0371	29.97	0.80	80.87	96.97	1.28	17.6	–

BN: Normal Concrete;

BSF 5%: Cylindrical concrete with a mixture of 5% silica fume substituted for part of the weight of the cement;

BAV 4%: Cylindrical concrete with a mixture of 4% volcanic ash can be used in place of cement in partial weight applications;

BAV 8%: Cylindrical concrete with a mixture of 8% volcanic ash can be used in place of cement in partial weight applications;

BAV 4% + SF 5%: Cylindrical concrete with a mixture of 4% volcanic ash and 5% silica fume substituted for part of the weight of cement;

BAV 8% + SF 5%: Cylindrical concrete mixed with a combination of 8% volcanic ash and 5% silica fume substituted for part of the mass of cement.

The water-to-cement (W/C) ratio in this study ranges from 0.55 to 0.63, which is within the acceptable range for conventional concrete mixtures. The increase in W/C ratio in mixtures containing volcanic ash and silica fume is attributed to the reduction in cement content due to partial replacement, while the water content remains

constant. In addition, the high specific surface area of silica fume and the irregular particle characteristics of volcanic ash contribute to increased water demand to maintain adequate workability. Although higher W/C ratios generally increase porosity and reduce compressive strength, the incorporation of silica fume helps mitigate this effect through its pozzolanic reactivity and microstructural densification.

The physical and chemical properties of volcanic ash and silica fume used in this study are presented in Table 21. The characterisation includes particle size distribution, specific surface area, specific gravity, chemical composition, and pozzolanic activity. The results indicate that volcanic ash consists of relatively coarser and irregular particles with moderate pozzolanic activity, whereas silica fume contains ultrafine spherical particles with significantly higher specific surface area and pozzolanic reactivity. These differences influence both workability and strength development of the concrete mixtures. Silica fume contributes to microstructural densification and enhanced mechanical performance, while volcanic ash requires appropriate proportioning due to its comparatively lower reactivity.

Table 21. Physical and chemical properties of volcanic ash and silica fume.

Parameter	Volcanic ash (Mount Sinabung)	Silica fume
Particle size distribution (μm)	1 – 100 μm (irregular distribution)	0.1 – 1 μm (ultrafine, uniform)
Specific surface area (m^2/kg)	350 – 750	15,000 – 30,000
Specific gravity	2.30 – 2.60	2.10 – 2.25
SiO_2 (%)	50 – 65%	85 – 98%
Al_2O_3 (%)	15 – 25%	0.5 – 1.5%
Fe_2O_3 (%)	5 – 10%	0.5 – 1.0%
CaO (%)	5 – 10%	< 1%
Chemical composition	Predominantly silicate minerals	Predominantly amorphous SiO_2
Pozzolanic activity index (%)	70 – 85%	> 100%
Particle shape	Angular / irregular	Spherical
Water demand	Moderate	High
Effect on workability	Slight reduction	Significant reduction
Effect on compressive strength	May reduce (if used alone)	Significantly enhances

The material composition presented above ensures that each concrete mixture variation is prepared with consistent proportions, allowing a clear comparison of the effects of volcanic ash and silica fume on concrete performance. These variations are then evaluated in terms of workability and compressive strength in the subsequent tests.

The inclusion of supplementary materials such as silica fume and volcanic ash may influence the workability of the concrete mixture due to their fine particle size and high surface area. Silica fume, in particular, tends to increase water demand, which may reduce workability if the water content is not properly adjusted. Therefore, maintaining adequate workability was important to ensure that the fresh concrete mixture could be properly compacted and that the resulting hardened concrete specimens would exhibit consistent mechanical properties during testing.

During the preparation and curing stages, the concrete specimens were maintained under controlled laboratory conditions to minimize variations that could affect the test results. The specimens were stored in a laboratory environment with an approximate temperature range of 25 ± 2°C, which is generally considered suitable for normal cement hydration processes. Maintaining stable temperature conditions helps ensure that the hydration reactions occur uniformly, allowing the concrete to develop its strength in a consistent manner.

To improve reproducibility, the mix design, experimental conditions, and testing procedures have been clarified and presented more systematically. The mix proportions are now explicitly detailed, including the percentage replacement levels of Mount Sinabung volcanic ash and silica fume. In addition, key experimental conditions such as curing method, testing age, and environmental parameters have been specified. The testing procedures, including slump and compressive strength tests, are described in accordance with relevant standards to ensure clarity and consistency. These revisions enhance the transparency and reliability of the study.

The cement content of 5.34 kg was determined by converting the mix design proportion per cubic meter to the total volume of concrete specimens in one variation, considering the number of specimens, individual specimen volume, and an adjustment factor for material loss during mixing and casting.

3.6. Slump test

The workability of fresh concrete mixtures was assessed using the standard slump test in accordance with ASTM C143/C143M (Table 22 and Fig. 4). The test was conducted using a standard Abrams cone placed on a rigid, non-absorbent surface. The cone was filled with fresh concrete in three equal layers, each compacted with 25 strokes using a tamping rod. After filling, the top

surface was levelled, and the mould was carefully lifted vertically to allow the concrete to subside. The slump value was determined as the vertical difference between the height of the mould and the highest point of the displaced concrete. This procedure provides a quantitative measure of the consistency and workability of the concrete mixtures. No measurement of horizontal spread or diameter was performed, as the procedure strictly follows the standard slump test rather than slump-flow testing.

Concrete mixtures containing volcanic ash without silica fume (BAV 4% and BAV 8%) showed slump values of 75 mm and 80 mm, respectively (Fig. 5), indicating slightly lower workability compared to normal concrete. However, when volcanic ash was combined with silica fume, the slump values increased. The mixture BAV 4% + SF 5% reached 85 mm, while BAV 8% + SF 5% achieved 100 mm, which is comparable to normal concrete.

This behaviour can be attributed to the fine particle sizes of silica fume and volcanic ash, which improve particle packing and reduce internal friction within the mixture. As a result, the concrete becomes more cohesive and easier to work with.

Table 22. Slump values of concrete specimens.

Concrete type	Slump value (mm)
BN	100
BSF 5%	80
BAV 4% + SF 5%	85
BAV 8% + SF 5%	100
BAV 4%	75
BAV 8%	80

Fig. 4. Slump testing.

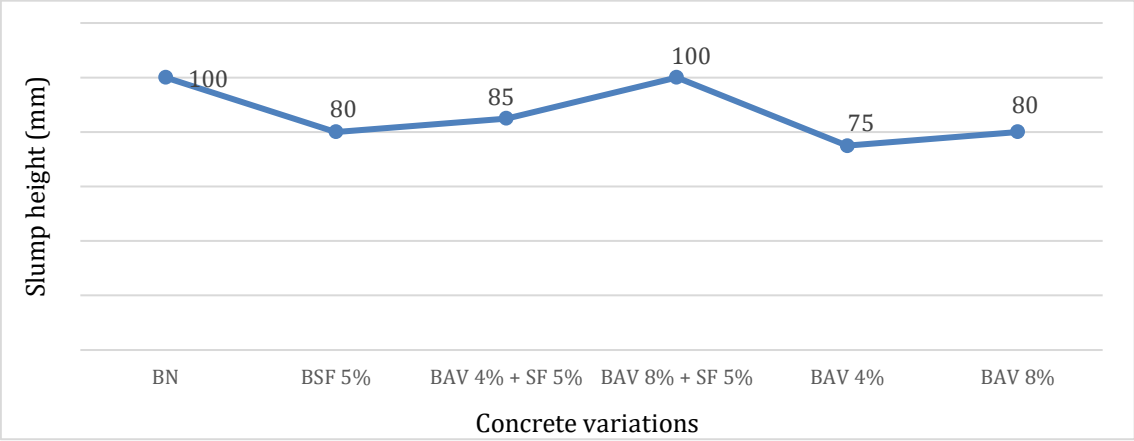

Fig. 5. Slump values of concrete specimens.

Based on Fig. 5, the slump test results indicate that the workability of concrete is influenced by the incorporation of volcanic ash and silica fume. The BAV 8% + SF 5% mixture achieved a slump value of 100 mm, which is comparable to that of normal concrete (BN) and higher than several other variations such as BAV 4% (75 mm), BAV 8% (80 mm), and BSF 5% (80 mm).

The improvement in slump value can be attributed to the presence of silica fume, which acts as a very fine filler material that enhances particle packing and reduces internal friction within the mixture. As a result, the concrete becomes more cohesive and exhibits better workability. In contrast, mixtures containing volcanic ash without silica fume tend to show lower slump values due to less efficient particle packing (Hamada et al. 2023).

Volcanic ash at an 8% replacement level also acts as a natural pozzolanic material with relatively fine particles. These fine particles contribute to improving the particle size distribution within the concrete mixture. When the gradation of particles becomes more optimal, internal friction among particles decreases. This reduction in friction allows the concrete mixture to flow more easily, leading to an increase in slump value (Abutaqa et al. 2024; Mehta and Monteiro 2014).

3.7. Testing the compressive strength of concrete

The compressive strength test was conducted at the age of 28 days using cylindrical specimens. The results (Figs. 6 and 7) are presented in graphical form to illustrate the variation in compressive strength for each concrete mixture SNI 1974 (2011).

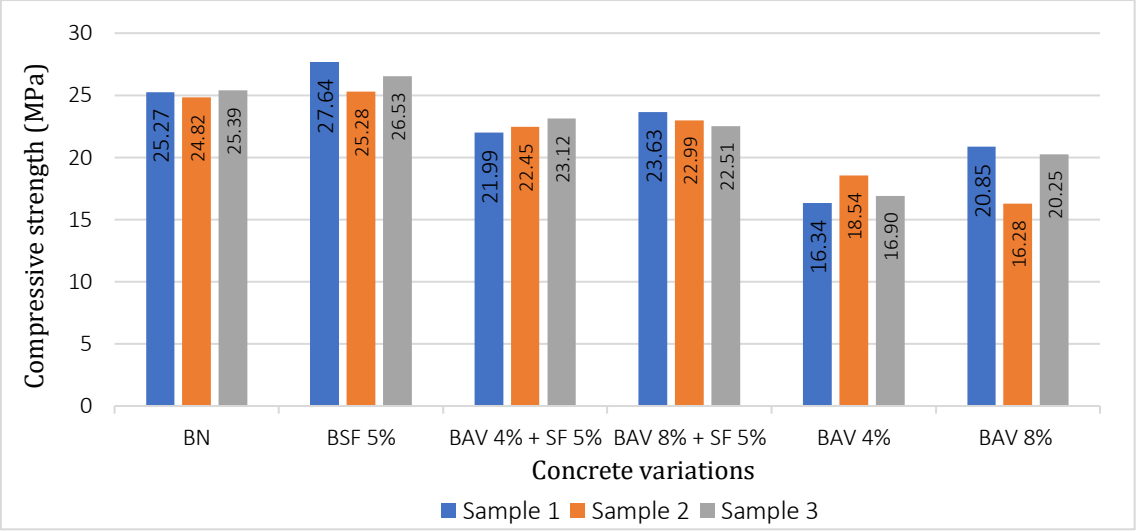

Fig. 6. Individual compressive strength values of concrete specimens.

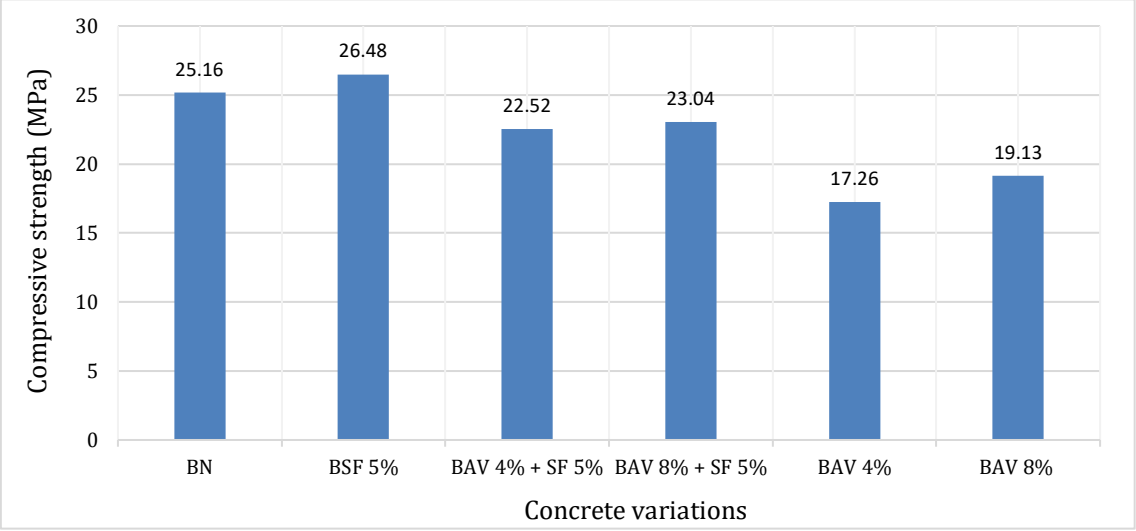

Fig. 7. Average compressive strength values of concrete specimens.

The normal concrete (BN) achieved compressive strength values of 25.27 MPa, 24.82 MPa, and 25.39 MPa, resulting in an average value of 25.16 MPa (Table 23). This indicates that the control mixture successfully met the targeted compressive strength.

The mixture containing 5% silica fume (BSF 5%) showed an increase in compressive strength, with an average value of 26.48 MPa. This result demonstrates the effectiveness of silica fume in enhancing the mechanical properties of concrete.

Table 23. Average results of the concrete compressive strength test.

Concrete variations	Cross-sectional area (mm²)	Concrete age	Compressive strength (MPa)
BN	17671.46	28 days	25.16
BSF 5%	17671.46	28 days	26.48
BAV 4% + SF 5%	17671.46	28 days	22.52
BAV 8% + SF 5%	17671.46	28 days	23.04
BAV 4%	17671.46	28 days	17.26
BAV 8%	17671.46	28 days	19.13

In contrast, the use of volcanic ash as a partial cement replacement resulted in a reduction in compressive strength. The BAV 4% mixture achieved an average strength of 17.26 MPa, while BAV 8% reached 19.13 MPa. Although the strength increased with higher volcanic ash content, it remained lower than that of normal concrete.

When volcanic ash was combined with silica fume, the compressive strength improved compared to mixtures containing volcanic ash alone. The BAV 4% + SF 5% mixture achieved an average strength of 22.52 MPa, while BAV 8% + SF 5% reached 23.04 MPa. However, these values were still lower than those of the control mixture and the silica fume-only mixture.

These results indicate that silica fume plays a significant role in improving compressive strength due to its high pozzolanic reactivity and fine particle size. In contrast, volcanic ash alone tends to reduce strength, likely due to its lower reactivity. However, when combined, silica fume partially compensates for the strength reduction caused by volcanic ash, resulting in improved performance compared to volcanic ash-only mixtures.

Overall, the results demonstrate that the addition of silica fume significantly enhances the compressive strength of concrete, whereas the use of volcanic ash as a partial cement replacement tends to reduce the compressive strength when used alone. This reduction may be associated with the lower pozzolanic reactivity and heterogeneous mineral composition of volcanic ash, which limits its contribution to the formation of additional calcium silicate hydrate (C–S–H) during cement hydration. Consequently, the concrete matrix becomes less dense and more porous compared to mixtures containing highly reactive pozzolanic materials such as silica fume. Therefore, the findings of this study highlight that silica fume plays a crucial role in improving the mechanical performance of concrete, while volcanic ash requires careful proportioning or combination with other supplementary cementitious materials to avoid significant reductions in compressive strength.

The increase in compressive strength observed in mixtures containing silica fume can be primarily attributed to its high pozzolanic reactivity and ultrafine particle size, which significantly influence the microstructure of cementitious materials. Silica fume consists predominantly of amorphous silicon dioxide (SiO_2) with a very high specific surface area. During cement hydration, calcium hydroxide ($Ca(OH)_2$) is produced as a by-product, which reacts with the amorphous silica through a secondary pozzolanic reaction to form additional C–S–H gel, the primary phase responsible for strength and durability. Previous studies have confirmed that the incorporation of silica fume enhances hydration products and improves the internal microstructure of concrete, leading to increased compressive strength (Zhao et al. 2024).

Furthermore, the pozzolanic reaction of silica fume not only contributes to strength development but also improves durability and microstructural properties, particularly at optimal replacement levels. This enhancement is associated with reduced porosity and microstructural densification due to both chemical reactions and particle packing effects (Bouzoubaa et al. 2025). In contrast, volcanic ash alone may not provide sufficient reactivity to compensate for reduced cement content, highlighting the importance of considering both chemical reactivity and microstructural development when evaluating supplementary cementitious materials (Shaheen et al. 2025).

Although previous studies have shown that supplementary cementitious materials may exhibit slower early-age strength development but improved long-term strength due to continued pozzolanic reactions, this study focuses on 28-day compressive strength to evaluate the initial mechanical performance and feasibility of using Mount Sinabung volcanic ash and silica fume. The results indicate that volcanic ash reduces compressive strength when used alone, while its combination with silica fume improves performance, although it does not exceed that of normal concrete. These findings are consistent with previous studies (Abutaqa et al. 2024; Zhang et al. 2022; Hamada et al. 2023), confirming that silica fume enhances concrete performance through pozzolanic reactions and matrix densification. Therefore, the combined use of volcanic ash and silica fume demonstrates considerable potential as a sustainable alternative material, provided that the mix proportions are carefully optimized.

4. Conclusions

The results of this study indicate that the normal concrete (BN) achieved an average compressive strength of 25.16 MPa, meeting the targeted design strength. The addition of silica fume at 5% (BSF 5%) increased the compressive strength to 26.48 MPa, demonstrating its effectiveness in enhancing the mechanical properties of concrete.

In contrast, the use of Mount Sinabung volcanic ash as a partial cement replacement resulted in a reduction in compressive strength. The mixture with 4% volcanic ash (BAV 4%) produced the lowest average strength of 17.26 MPa, while the 8% variation (BAV 8%) showed a slight improvement to 19.13 MPa, although still below the strength of normal concrete.

The combination of volcanic ash and silica fume showed improved performance compared to mixtures containing volcanic ash alone. The BAV 4% + SF 5% and BAV 8% + SF 5% mixtures achieved average compressive strengths of 22.52 MPa and 23.04 MPa, respectively. Although these values did not exceed that of normal concrete, the results indicate that silica fume can partially compensate for the lower reactivity of volcanic ash.

Overall, the findings suggest that silica fume plays a significant role in enhancing compressive strength, while volcanic ash requires proper proportioning or combination with other materials to achieve acceptable performance. Therefore, the combined use of volcanic ash and silica fume has potential as a more sustainable alternative material in concrete production, provided that further optimization of mix proportions is carried out.

The findings of this study demonstrate that the use of Mount Sinabung volcanic ash as a partial cement replacement tends to reduce compressive strength when applied independently; however, its combination with silica fume enhances performance, indicating a benefi-

cial interaction between the materials. Although the resulting strength does not fully exceed that of normal concrete, the improved behavior of the blended mixtures suggests that appropriate proportioning can achieve acceptable mechanical properties. From an economic perspective, the utilization of locally available volcanic ash offers potential cost savings through reduced cement consumption, despite additional processing requirements. Therefore, the combined use of volcanic ash and silica fume presents a promising approach for developing sustainable and cost-effective concrete materials with balanced mechanical performance, while also contributing to the advancement of eco-friendly concrete technology and offering a potential solution for managing volcanic ash waste in Indonesia.

Future research should focus on optimising mix design by evaluating a wider range of replacement levels (0–20%) and incorporating superplasticisers to improve workability without increasing the water–cement ratio. Long-term mechanical properties, including compressive strength at 56 and 90 days, should also be investigated to assess the continued pozzolanic reaction.

Further studies are recommended to conduct detailed material characterisation, including particle size distribution, specific surface area, chemical composition, and pozzolanic activity using advanced techniques such as X-ray fluorescence (XRF), scanning electron microscopy (SEM), and particle size distribution (PSD) analysis. Durability performance, including resistance to sulphate attack, chloride penetration, and permeability, should also be evaluated.

In addition, environmental and economic assessments, such as life cycle analysis (LCA) and cost–benefit analysis, are required to evaluate sustainability. Field-scale applications should also be considered to validate laboratory findings under practical conditions.

Acknowledgements

The authors would like to thank the Universitas Muhammadiyah Sumatera Utara for the ongoing support, valuable guidance, and assistance throughout this research process. The encouragement and resources provided by the university played a significant role in the successful completion of this research.

Funding

The authors received no financial support for the research, authorship, and/or publication of this manuscript.

Conflict of Interest

The authors declare no potential conflicts of interest with respect to the research, authorship, and/or publication of this manuscript.

Data Availability

The datasets generated and/or analyzed during the current study are not publicly available but are available from the corresponding author upon reasonable request.

AI Assistance

No AI-based tools were used in the preparation of this manuscript.

Author Contributions

All authors made substantial contributions to the conception and design of the study, acquisition of data, analysis and interpretation of data; drafted or critically revised the manuscript for important intellectual content; and approved the final version to be published.

REFERENCES

Abutaqa A, Mohsen MO, Aburumman MO, Senouci A, Taha R, Maherzi W, Qtiashat D (2024). Eco-sustainable cement: Natural volcanic tuffs' impact on concrete strength and durability. *Buildings*, 14(9), 2902.

Adi MM, Sofyan SS, Hajar YY (2018). Pengaruh kuat lentur beton terhadap penambahan serat tandan kosong kelapa sawit. *Teras Jurnal*, 8(2), 426-433.

Alfiandinata (2020). Pengaruh Penggunaan Fly Ash Sebagai Pengganti Sebagian Semen Terhadap Sifat Mekanik Beton. *B.Sc. thesis*, Universitas Muhammadiyah Mataram, Mataram, Nusa Tenggara Barat, Indonesia.

Alkhaly YR, Panondang CN, Zulfahmi Z (2015). Kuat tekan beton polimer berbahan abu vulkanik Gunung Sinabung dan resin epoksi. *Teras Jurnal*, 5(2), 125-132.

ASTM C143/C143M (2015). Standard test method for slump of hydraulic-cement concrete. ASTM International, West Conshohocken, PA, USA.

ASTM C150-07 (2007). Standard specification for Portland cement. ASTM International, West Conshohocken, PA, USA.

Azizi M, Samimi K (2025). Effect of silica fume on self-compacting earth concrete: Compressive strength, durability and microstructural studies. *Construction and Building Materials*, 472, 140815.

Bouzoubaa N, Amziane S, Benzerzour M, Abriak NE (2025). Effect of silica fume on self-compacting earth concrete: Compressive strength, durability and microstructural studies. *Construction and Building Materials*, 472, 140815.

BS 12 (1996). Specification for Portland cement. British Standards Institution, London, UK.

Firmansyah A, Halim A, Aditya C (2022). Pengaruh penambahan abu vulkanik Gunung Semeru sebagai bahan additive terhadap kuat tekan dan modulus elastisitas beton. *Proceedings of the 5th Conference on Innovation and Application of Science and Technology (CIASTECH)*, Malang, Indonesia, 429-438.

Hamada HM, Abed F, Katman HYB, Humada AM, Al Jawahery MS, Majdi A, Yousif ST, Thomas BS (2023). Effect of silica fume on the properties of sustainable cement concrete. *Journal of Materials Research and Technology*, 24, 8887-8908.

Han C, Pang J, Hu S, Yang C (2024). Study on static and dynamic mechanical properties and microstructure of silica fume-polypropylene fiber modified rubber concrete. *Scientific Reports*, 14, 12573.

Handayani T (2019). Memprediksi kuat lentur berdasarkan kuat tekan beton normal. *Jurnal Ilmiah Desain & Konstruksi*, 18(2), 197-211.

JIS R 5210 (1981). Portland cement. Japanese Standards Association, Tokyo, Japan.

Kamil B, Zulkarnain F (2021). Perbandingan kuat tekan beton menggunakan pasir Sungai Wampu sebagai agregat halus dengan variasi bahan tambah Sica Fume pada perendaman air laut. *Proceedings of Seminar Nasional Penelitian LPPM UMJ*, Jakarta, Indonesia, 1-10.

Karolina R, Muhammad W, Saragih MDSM, Mustaqa T (2018). The effectiveness of stone ash and volcanic ash of Mount Sinabung as a filler on the initial strength of self-compacting concrete. *IOP Conference Series: Materials Science and Engineering*, 308(1), 012045.

Khalik Nasution A, Tarigan J, Perwira Mulia A (2021). Kuat tekan dan tarik beton mutu tinggi dengan menggunakan PP Fibre dan abu vulkanik Gunung Sinabung. *Jurnal Syntax Admiration*, 2(10), 1797-1807.

Khan K, Johari MAM, Amin MN, Nasir M (2024). Development and evaluation of basaltic volcanic ash-based high-performance concrete incorporating metakaolin, micro and nano-silica. *Developments in the Built Environment*, 17, 100330.

Lamotokana MS, Latuconsina SI, Adek DS (2021). Studi eksperimental abu vulkanik sebagai bahan substitusi parsial semen terhadap kuat tekan beton normal. *Jurnal Dintek*, 13(1), 63-71.

Mboru DM, Halim A, Aditya C, Suraji A (2022). Pengaruh Sika dan abu vulkanik Gunung Semeru sebagai pengganti sebagian semen terhadap kuat tekan beton. *Proceedings of the 5th Conference on Innovation and Application of Science and Technology (CIASTECH)*, Malang, Indonesia, 401-410.

Mehta PK, Monteiro PJM (2014). Concrete: Microstructure, Properties, and Materials. 4th ed. The McGraw-Hill Companies, Inc., New York, USA.

Mulyadhi M, Zulkarnain F (2021). Pemanfaatan abu batok kelapa sebagai substitusi pasir pada campuran beton dengan bahan tambah Sikament NN ditinjau dari kuat tekan beton. *B.Sc. thesis*, Universitas Muhammadiyah Sumatera Utara, Medan, Sumatera Utara, Indonesia.

Nadia AF (2011). Pengaruh kadar silika pada agregat halus campuran beton. *Jurnal Konstruksia*, 3(1), 1-9.

Posman AS, Zulkarnain F (2022). Pengaruh penambahan abu vulkanik Gunung Sinabung dan abu sekam padi sebagai filler terhadap kuat tekan beton. *B.Sc. thesis*, Universitas Muhammadiyah Sumatera Utara, Medan, Sumatera Utara, Indonesia.

Purba VE, Sianturi NM, Saragih DS, Damanik DRS (2021). Kombinasi abu dasar batu bara dan abu vulkanik sebagai material beton. *Jurnal Pemukiman*, 16(1), 10-20.

Rashad AM (2021). A comprehensive overview about the influence of supplementary cementitious materials on concrete properties. *Construction and Building Materials*, 307, 124948.

Rochmah N, Ariansyah AL, Pertiwi D (2023). Perbandingan beton normal dengan beton menggunakan abu vulkanik Gunung Semeru ditinjau dari kuat tekan dan setting time. *Jurnal Teknik Sipil*, 4(1), 519-526.

Sani II (2021). Perbandingan pemakaian air kapur serta pengaruh penambahan Sika Fume terhadap ketahanan beton mutu tinggi. *Jurnal Ilmiah Mahasiswa Teknik*, 1(2), 1-9.

Scrivener KL, John VM, Gartner EM (2018). Eco-efficient cements: Potential economically viable solutions for a low-CO2 cement-based materials industry. *Cement and Concrete Research*, 114, 2-26.

Sebayang MD (2020). Analyze the proportion of volcanic ash of Sinabung volcano at the most optimum to get the compressive strength and tensile strength of concrete. *IOP Conference Series: Materials Science and Engineering*, 725(1), 012044.

Shaheen A, Ahmad S, Farooq F, Khan MI (2025). Design of reactive powder concrete mortar mixes through high strength and durability. *Challenge Journal of Concrete Research Letters*, 16(3), 142-154.

Sihombing L (2017). Pengaruh penambahan Sika Fume® terhadap kuat tekan beton porous. *B.Sc. thesis*, Universitas Medan Area, Medan, Indonesia.

SNI 03-4142 (1996). Metode pengujian jumlah bahan dalam agregat yang lolos saringan No.200. Badan Standardisasi Nasional, Jakarta, Indonesia.

SNI 15-2049 (2004). Semen Portland. Badan Standardisasi Indonesia, Jakarta, Indonesia.

SNI 1969 (2016). Cara uji berat jenis dan penyerapan air agregat kasar. Badan Standardisasi Nasional, Jakarta, Indonesia.

SNI 1971 (2011). Cara uji kadar air total agregat dengan pengeringan. Badan Standardisasi Nasional, Jakarta, Indonesia.

SNI 1972 (2008). Cara uji slump beton. Badan Standardisasi Nasional, Jakarta, Indonesia.

SNI 1973 (2008). Cara uji berat isi, volume produksi campuran dan kadar udara beton. Badan Standardisasi Nasional, Jakarta, Indonesia.

SNI 1974 (2011). Cara uji kuat tekan beton dengan benda uji silinder. Badan Standardisasi Nasional, Jakarta, Indonesia.

SNI 2493 (2011). Tata cara pembuatan dan perawatan benda uji beton di laboratorium. Badan Standardisasi Nasional, Jakarta, Indonesia.

SNI 7656 (2012). Tata cara pemilihan campuran untuk beton normal, beton berat dan beton massa. Badan Standardisasi Nasional, Jakarta, Indonesia.

SNI ASTM C136 (2012). Metode uji untuk analisis saringan agregat halus dan agregat kasar. Badan Standardisasi Nasional, Jakarta, Indonesia.

Sultan TAFA, Ali IW, Gaus A, Sultan MA (2023). Efek penambahan serat polypropylene terhadap kuat tekan beton pada perkerasan kaku. *Jurnal Teknik Sipil Rancang Bangun*, 9(1), 49-55.

Widianto SM (2021). Pengaruh penggunaan abu vulkanik Gunung Sinabung sebagai bahan subtitusi parsial semen terhadap kuat tekan dan daya serap air mortar. *Jurnal Teknik Sipil*, 13(2), 50-55.

Zhang P, Wang J, Li Q, Wang K (2022). Influence of silica fume on workability, mechanical properties, and durability of concrete: A review. *Construction and Building Materials*, 344, 128142.

Zhao C, Li B, Li K, Li Z (2024). Research on mechanical properties of silica fume cementitious materials excited by wet grinding methods. *Buildings*, 14(12), 3757.

Challenge Journal of CONCRETE RESEARCH LETTERS

Research Article

Behavior of GGBFS-modified DSM columns in clay soil: Strength–permeability characteristics and predictive laboratory modeling

Murat Olgun [a], Gülsüm Yalçınyiğit [b], Alican Şenkaya [a], Ekrem Burak Toka [a,*], Mustafa Abdalwahid Noori Noori [c], İbrahim Hakkı Erkan [a]

[a] *Department of Civil Engineering, Konya Technical University, 42250 Konya, Türkiye*
[b] *Investments Department of Konya Provincial Health Directorate, 42100 Konya, Türkiye*
[c] *Independent Researcher, 42000 Konya, Türkiye*

ABSTRACT

This study investigated the influence of partially substituting cement with ground granulated blast furnace slag (GGBFS) on the unconfined compressive strength (UCS), splitting tensile strength (STS), and permeability coefficient (k_{DSM}) of deep soil mixing (DSM) columns formed in clay soil. The water/binder ratio was kept constant at 1.0. Cast specimens were prepared using two binder contents, a_w = 15% and 20% by dry soil mass, and five GGBFS substitution ratios of 0%, 10%, 20%, 35%, and 50%. Strength specimens were tested after 7, 28, and 56 days of curing, whereas permeability specimens were tested after 28 and 56 days. Four laboratory-scale DSM columns with a diameter of 300 mm and a length of 600 mm were formed for selected mixtures with a_w = 20% and GGBFS ratios of 0%, 20%, 35%, and 50%; core samples were extracted after 28 days. UCS values ranged from 859 to 4939 kPa, STS from 182 to 830 kPa, and k_{DSM} from 0.16×10^{-10} to 9.17×10^{-10} cm/s for cast specimens. GGBFS reduced early-age strength at 7 days, but improved strength and reduced permeability at later curing ages. The UCS and STS values of core samples were 45.26–69.79% and 63.00–77.58% of the corresponding cast specimen values, respectively, while permeability values of core samples were higher. SEM and XRD observations supported the formation of hydration and pozzolanic products.

ARTICLE INFO

Article history:
Received – April 9, 2026
Revision requested – May 7, 2026
Revision received – May 20, 2026
Accepted – May 26, 2026

Keywords:
Deep soil mixing
Ground granulated blast furnace slag
Permeability
Splitting tensile strength
Unconfined compressive strength

Citation: Olgun M, Yalçınyiğit G, Şenkaya A, Toka EB, Noori MAN, Erkan İH (2026). Behavior of GGBFS-modified DSM columns in clay soil: Strength–permeability characteristics and predictive laboratory modeling. *Challenge Journal of Concrete Research Letters*, 17(2), 207–221.

1. Introduction

Deep soil mixing (DSM) is a ground improvement method that has been widely used in recent years. In this method, in-situ DSM columns are formed by mixing cement and soil. The resulting cement-soil mixture improves the strength and settlement characteristics of soils (Abbey et al. 2015; Chen et al. 2016). The DSM application prevents large shear deformation and excessive settlements, and increases bearing capacity of soils (Shakri et al. 2014). In addition, the water impermeability of the soil is improved.

The production of cement, a building material used in almost all construction processes, results in high amounts of CO_2 emissions, which cause environmental pollution. Roughly one ton of CO_2 is released during the production of one ton of cement (Ganjian et al. 2008; Paniagua et al. 2023). Approximately 8% of the CO_2 released into the atmosphere is related to the cement production process (Ganjian et al. 2015). The use of cement

* *Corresponding author*. E-mail address: ebtoka@ktun.edu.tr (E. B. Toka)
ISSN: 2548-0928 / DOI: https://doi.org/10.20528/cjcrl.2026.02.010

is nevertheless attractive in soil stabilization because it substantially improves soil strength (Holm 2003; Consoli et al. 2015). To reduce cement consumption and its associated environmental impacts, amorphous materials rich in silicates and/or aluminates, such as GGBFS, fly ash (FA), and silica fume (SF), can be incorporated as partial cement substitutes. These industrial by-products can support waste recycling and more sustainable construction practices. Studies on waste-derived binders further show that their contribution is governed by chemical and mineralogical composition, processing conditions, particle characteristics, replacement level, and curing conditions. Consequently, their suitability should be assessed through their combined effects on fresh behavior, mechanical performance, microstructure, and transport properties rather than environmental benefits alone (Mahmud et al. 2025; Mohamad et al. 2025; Ünal and Canbaz 2026; Urbánek and Antoš 2026). Moderate replacement levels may improve particle packing and matrix compactness, whereas excessive substitution may reduce the effective binder content, increase porosity, and adversely affect mechanical or durability-related properties (Turan et al. 2025). Therefore, the partial replacement of cement with suitable industrial by-products represents a potential approach for reducing the environmental impact of soil improvement applications (Lindh and Lemenkova 2022).

GGBFS, a by-product of the steel manufacturing industry, is generally used as a partial cement substitute. This material is mainly composed of calcium oxide (CaO), amorphous silicon dioxide (SiO_2), and aluminum oxide (Al_2O_3). In addition to its pozzolanic properties, GGBFS may exhibit partial hydraulic binding behavior because of the CaO in its chemical composition. Therefore, it can contribute to the development of cementitious bonds when used together with cement. The performance of GGBFS-containing and other fine reactive binder systems is strongly influenced by binder composition, particle fineness, substitution level, water demand, and curing regime, which together govern workability and strength development (Abutaha and Çelik 2025; Shaheen et al. 2025). Considering that slag constitutes approximately 16–20% of steel production by mass (Subathra Devi and Gnanavel 2014) and that less than 50% of the world's waste steel slag is reused (Chaudhary and Pal 2002), the use of GGBFS in DSM column formation offers an important opportunity to reduce cement consumption and promote waste valorization.

Several researchers have investigated the utilization of various industrial waste materials as alternatives to cement for forming DSM columns and soil stabilization (Åhnberg 2006; Abbey et al. 2017; He et al. 2019; Ye et al. 2021; Paniagua et al. 2023; Ramírez and Korkiala-Tanttu 2023; Suksiripattanapong et al. 2023). Some researchers have evaluated in-situ application of DSM (Xue et al. 2024; Forsman et al. 2025; Savila et al. 2025; Swamynaidu and Tyagi 2025). Paniagua et al. (2023) improved a clay soil using bio-ash and slag in combination with cement. Considering the strength and stiffness criteria, they stated that bio-ash and slag can be used as an alternative to cement and lime in soil improvement. Åhnberg (2006) investigated the effect of cell pressure on the strength of a DSM column for specimens prepared using cement, FA and slag; and successfully modeled the DSM column strength for drained and undrained conditions using mathematical equations based on the concept of pre-consolidation pressure and determined the parameters affecting the strength. Suksiripattanapong et al. (2023) investigated the improvement of soft clay soils by DSM with bottom ash and cement. They stated that bottom ash can be used together with cement for both cost reduction and an environmentally friendly DSM column formation process. Ye et al. (2021) investigated the use of binder material containing gypsum and slag as a cement replacement for the improvement of soft soils. The improvement with this binder material resulted in a more rigid structure than cement improvement and a significant increase in strength compared to the unimproved soil. Ramírez and Korkiala-Tanttu (2023) used 6 different low CO_2 emitting binders as an alternative to cement for the improvement of soft clay soils and found that alternative binders for ground improvement not only provide an environmentally friendly solution but also show satisfactory performance in terms of binding properties. He et al. (2019) investigated the effect of the combination of soda residue and GGBFS in soft soils. When these two materials were used together, the strength of the improved soil after 28 days of curing was close to the strength when soda residue and cement were used as binder. Abbey et al. (2017) used pulverized fuel ash and GGBFS with cement for soil stabilization and observed a better improvement in low plasticity soils. They stated that the amount of cement in the binder can be reduced by using GGBFS and pulverized fuel ash. Xue et al. (2024) investigated the application of DSM in soft soils using UCS tests. They observed that UCS values were lower in silty and peat soils than in clay soils and suggested that FA-based cement was suitable for DSM in acidic soils containing organic matter. Savila et al. (2025) evaluated the field applicability of DSM columns. They reported that the strength of field DSM columns met the target values anticipated at the design stage and even increased to more than seven times the target strength after 3.5 years. Swamynaidu and Tyagi (2025) examined the suitability of DSM, which is formed using a certain amount of GGBFS, for in situ use in terms of permeability. They found that permeability decreased significantly with an increase in GGBFS up to 50%, and they developed a correlation between permeability, UCS, and water/binder ratios. Forsman et al. (2025) investigated the usability of 11 different binder types, including GGBFS, in DSM columns, considering lime-cement mixture as a reference. They conducted experiments at six different test sites, focusing on the effects of variables including soil and binder properties on strength changes.

There are limited and insufficient studies simultaneously examining the effects of GGBFS substitution on UCS, STS and k_{DSM} of DSM columns, together with a direct comparison between cast specimens and core samples obtained from laboratory-scale DSM columns. Additionally, there is a lack of research on laboratory-scale model DSM columns that represent in-situ formed DSM columns. The relation between DSM samples prepared as cast specimens in small molds and core samples obtained from laboratory DSM columns is also unclear. In this study, UCS, STS and permeability tests were carried

out on cast specimens to comprehensively investigate the effect of GGBFS on the strength and permeability properties of the DSM columns. Based on the test results on DSM specimens prepared as casting; model DSM columns with a diameter of 300 mm and a length of 600 mm were formed in the laboratory for 4 different designs. The UCS, STS, and k_{DSM} values of core samples extracted from the laboratory DSM columns were compared with those of the cast specimens.

2. Materials and Methods

2.1. Materials and design

The soil used in the study was classified as low plasticity clay (CL) according to the Unified Soil Classification System (USCS) (ASTM D2487 2017). The soil used in this study had a particle size distribution consisting of 8% sand, 34% silt, and 58% clay fraction. The liquid limit of the soil is 33%, the plastic limit is 22%, and the particle density of the soil solids is 2.64 g/cm^3. CEM I 42.5R was used as cement. GGBFS was obtained from Adana Cement Iskenderun Plant and its mineralogical properties are given in Table 1.

The water content of the clay was selected as 27%, which lies between the liquid limit and plastic limit of the soil, to ensure a workable and representative clay consistency. Based on previous studies, binder ratio (a_w; the ratio of the amount of binder to the dry weight of the soil) in DSM applications is generally reported to vary between 10% and 30% (Broms 2003; Bruce et al. 2013; Han 2015; Yu et al. 2021). Within this commonly adopted range, a_w values of 15% and 20% were selected in order to represent moderate and relatively high binder contents that are frequently used in practice, while maintaining workability and avoiding excessive binder consumption. This selection allowed the influence of GGBFS substitution on mechanical and hydraulic properties to be evaluated without introducing extreme binder ratios. Accordingly, GGBFS was used by substituting cement in certain proportions. Previous studies (Åhnberg 2006; Abbey et al. 2017; Paniagua et al. 2023) support the replacement of up to 50% of cement by mass with GGBFS as a reasonable approach. Taking this limit value into account, the ratio of the mass of GGBFS to the total mass of cement+GGBFS was selected as 0, 10, 20, 35 and 50%. These variables and levels were used to establish the design given in Table 2. B, S and D denote a_w, GGBFS and curing period, respectively. The numbers next to the letters represent the percentage for B and S and the number of days for D. For instance, B15S0D7 indicates a mixture with 15% a_w, 0% GGBFS and 7 days curing period. Based on test results, laboratory DSM columns were formed for designs numbered 21, 23, 24 and 25 from Table 2.

Table 1. Chemical composition of the GGBFS.

Chemical composition	SiO_2	Al_2O_3	Fe_2O_3	CaO	MgO	SO_3	K_2O	LOI	Other
Percentage (%)	37.65	13.58	0.92	34.73	8.57	0.95	0.88	0.25	2.47

Table 2. Established design and mixtures.

Design no	Design	a_w (%)	GGBFS (%)	Day	Design no	Design	a_w (%)	GGBFS (%)	Day
1	B15S0D7	15	0	7	16	B20S0D7	20	0	7
2	B15S10D7	15	10	7	17	B20S10D7	20	10	7
3	B15S20D7	15	20	7	18	B20S20D7	20	20	7
4	B15S35D7	15	35	7	19	B20S35D7	20	35	7
5	B15S50D7	15	50	7	20	B20S50D7	20	50	7
6	B15S0D28	15	0	28	21	B20S0D28	20	0	28
7	B15S10D28	15	10	28	22	B20S10D28	20	10	28
8	B15S20D28	15	20	28	23	B20S20D28	20	20	28
9	B15S35D28	15	35	28	24	B20S35D28	20	35	28
10	B15S50D28	15	50	28	25	B20S50D28	20	50	28
11	B15S0D56	15	0	56	26	B20S0D56	20	0	56
12	B15S10D56	15	10	56	27	B20S10D56	20	10	56
13	B15S20D56	15	20	56	28	B20S20D56	20	20	56
14	B15S35D56	15	35	56	29	B20S35D56	20	35	56
15	B15S50D56	15	50	56	30	B20S50D56	20	50	56

2.2. Determining the water/binder ratio

In previous studies (Shen et al. 2012; Takano et al. 2015; Yu et al. 2021), it was suggested that a water/binder ratio of 1.0 was appropriate for the formation of DSM columns. Therefore, a water/binder ratio of 1.0 was selected for both the cast specimens and the laboratory-scale DSM columns. The rheological properties of the grouts were determined using Marsh funnel (ASTM C939 2016) and sedimentation (ASTM C940 2016) tests. The Marsh funnel test (Fig. 1(a)) and sedimentation test (Fig. 1(b)) were used to evaluate the flow times (Fig. 1(c)) and bleeding ratios (Fig. 1(d)) of grouts containing up to 50% GGBFS within the binder. According to the test results, increasing the GGBFS substitution ratio produced a more viscous consistency but did not substantially impair workability or injectability. This rheological response is consistent with observations from blended cementitious systems, in which fine supplementary materials influence flowability by altering specific surface area and water demand, with the magnitude of the effect depending on material reactivity, dosage, and overall mixture composition (Mohamad et al. 2025; Shaheen et al. 2025). S30 and S40, representing 30% and 40% GGBFS substitution, respectively, were used only in the preliminary workability assessment to characterize the continuity of the rheological trends over a wider range of substitution levels and were not included in the main experimental design presented in Table 2.

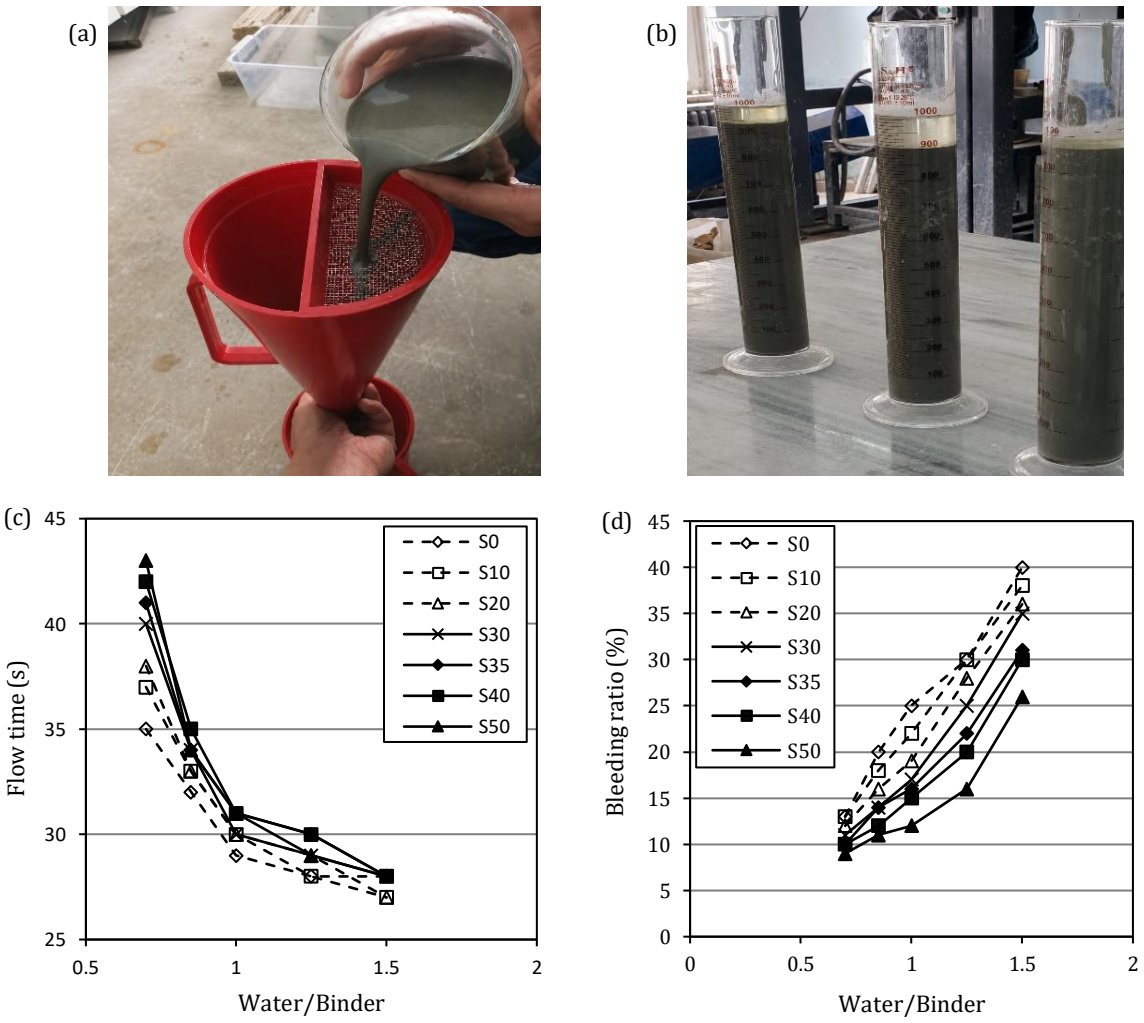

Fig. 1. Preliminary workability studies for mixtures:
(a) Marsh funnel test; (b) Sedimentation test; (c) Flow time; (d) Bleeding ratio.

2.3. Preparation of cast specimens and tests

The clay was dried, ground, and sieved through a 2 mm diameter sieve to prepare cast specimens. The clay, cement, and GGBFS were dry-mixed, and then water was added to achieve both a 27% water content for the clay and a water/binder ratio of 1.0 for the grout. The mixture was mixed for 5 minutes using a laboratory type mixer after adding water to the mixture. Subsequently, the mixture was poured into PVC molds with an inner surface previously coated with grease, having a diameter of 50 mm and a height of 100 mm. Molds with a diameter of 50 mm and a height of 30 mm were used for permeability tests. The mixtures were placed in the molds in three layers. Each layer was properly skewered (Kitazume et al. 2015) to prevent the formation of air pockets within the mixture specimens. To ensure consistency in specimen density, a constant mold volume was used, and the mass of fresh mixture placed into each mold was controlled for each mixture. After demolding,

the specimen dimensions and mass were measured to verify density consistency. In this manner, three samples were prepared for each design, for UCS test (ASTM D4832 2016), STS test (ASTM C496 2017), and permeability test (ASTM D5084 2016). The UCS and STS tests were conducted under displacement control at a rate of 0.5 mm/min. The specimens were cured in air-tight bags at 97±2% relative humidity and 23±2°C for 7, 28, and 56 days. The permeability test specimens were cured for 28 and 56 days. Since curing temperature was kept constant throughout the experimental program, temperature was controlled and was not treated as an independent variable in this study. Permeability tests were performed following ASTM D5084. Each cylindrical specimen was placed within a latex membrane inside the test cell. Saturation was achieved by applying back pressure in incremental steps ensuring full saturation. The cell pressure was maintained at 500 kPa, while back pressure was 450 kPa. A back pressure of 450 kPa was maintained throughout the test and used as the driving hydraulic pressure for water flow through the specimen. The outflow volume measured from a volume change unit connected to the perforated plate beneath the specimen was measured separately, and the k_{DSM} was then calculated using Darcy's law.

2.4. Formation of DSM columns, core sampling and tests

The clay was initially dried, ground, and sieved through a 2 mm diameter sieve to form laboratory DSM columns. Water was added to the clay until 27% water content was achieved and the water and soil were mixed until a homogeneous form was obtained. The mixed soil was placed in a container with a diameter of 600 mm and a height of 900 mm in two stages. The chosen soil water content of 27% is very close to the in-situ water content. The in-situ bulk density (natural/wet density) was previously determined as 1.87 g/cm^3 at 27% water content. Accordingly, the soil was placed in the test container to achieve a density of 1.87 g/cm^3. Since the container volume was known, the container was filled by calculating the mass of soil that could fill this volume. The test container was used only as a laboratory-scale preparation container for forming DSM columns under controlled conditions. No visible or measurable permanent deformation was observed on the HDPE container wall before or after column formation. Nevertheless, the possible influence of container rigidity and scale effects should be considered when interpreting the laboratory-scale DSM column results, and the findings should not be directly generalized to field-scale DSM applications without site-specific trial columns and field verification. The prepared soil was allowed to stabilize for two days. After the waiting period, DSM columns were formed. First, CEM I 42.5R, GGBFS, and water were mixed in a separate container to form the injection grout. While the prepared grout was injected into the soil at a constant pressure of 10 bar, a DSM column with a diameter of 300 mm and a length of 600 mm was formed by mechanically mixing the soil using a mixing blade. The injection pressure of 10 bar was selected as it represents typical laboratory-scale DSM mixing pressures and ensures sufficient grout penetration and homogenization in fine-grained soils (Broms 2003; Takano et al. 2015). During the column formation process, the mixing blade was reciprocated vertically five times within the soil to promote uniform mixing and consistent column formation (Fig. 2(a)). This method ensured the reliable formation of DSM columns. The top of the formed columns was covered with plastic bags, and the columns were left to cure for 28 days. Using this method, a total of four DSM columns were formed with an a_w value of 20% and GGBFS substitution ratios of 0%, 20%, 35%, and 50%. The a_w value of 20% was selected based on the cast specimen results, which indicated that this binder ratio provided higher and more stable mechanical performance. Therefore, this value was considered representative for laboratory-scale DSM columns intended to simulate in-situ applications. After the curing period, core sampling of different parts of the columns was done to evaluate strength and permeability properties (Figs. 2(b-c)). The coring machine operated at 1000 rpm during the core sampling. The core sampling process was performed at least four different locations for each DSM column. The core samples were cut to a diameter of 50 mm and a height of 100 mm for UCS and STS tests and were cut to a diameter of 50 mm and a height of 30 mm for permeability tests. The UCS, STS, and permeability tests of core samples were performed using the same methods as for cast specimens. Separate duplicate DSM columns for each mixture were not formed, but the number of core samples extracted was arranged to ensure that at least three samples could be obtained for UCS, STS and permeability test.

2.5. Statistical analysis using ANOVA

Statistical analysis was performed using analysis of variance (ANOVA) to evaluate the significance of the effects of a_w, GGBFS content, and curing period on UCS, STS, and k_{DSM}. ANOVA was selected as it allows the assessment of both individual factors and their interaction effects on the measured responses. The significance level was set at $p < 0.05$, corresponding to a 95% confidence level, which is commonly adopted in geotechnical and materials engineering studies. Model adequacy was evaluated using the coefficient of determination (R^2).

3. Results and Discussion

3.1. UCS of cast specimens

UCS test results were given in Fig. 3 and stress-strain curves of some selected designs were presented in Fig. 4. For cast specimens, the highest UCS was obtained for B20S50D56 with 4939 kPa and the lowest UCS was obtained for B15S50D7 with 859 kPa (Fig. 3). As the curing period increased, the strength increased as expected. The increase in the GGBFS ratio caused an initial decrease in strength at 7 days curing but significant increase in strength at the end of 28 and 56 days of curing. A similar behavior was observed in a study by Estabragh et al. (2016). Compared with the non-GGBFS reference specimens, the UCS values of the GGBFS-containing specimens corresponded to 73–98% of the reference at 7

days, 105–179% at 28 days, and 110–171% at 56 days as the GGBFS substitution ratio increased from 10% to 50%. The fundamental reason for the increase in strength with the use of GGBFS is due to the pozzolanic properties (Lindh and Lemenkova 2022) of GGBFS reacting with the calcium hydroxide (CH – $Ca(OH)_2$) formed as a result of hydration, thereby creating calcium-silicate-hydrates (C-S-H). Owing to its chemical composition, GGBFS can partially react with clay minerals in a way similar to cement–clay interactions (Richardson et al. 1994; Nidzam and Kinuthia 2010). However, since the hydration reaction capability of GGBFS alone is weak, the use of GGBFS without an additional activating agent like cement would not be appropriate (Yi et al. 2014). Thus, it was observed that cement and GGBFS work effectively together.

Fig. 2. DSM column formation and core sampling:
(a) DSM column formation in preparation container; (b) Core sampling; (c) Core samples.

The reason for the decrease in strength with an increase in the GGBFS ratio when the curing period is 7 days is that a 7-day curing period is not sufficient for the occurrence of pozzolanic reactions; because pozzolanic reactions develop and continue over a longer period (Davidson et al. 1965; Sargent 2015). When examining the model equation given in the ANOVA results (Table 3), the negative coefficient of GGBFS for the 7-day curing period is an indicator of this phenomenon. Accordingly, the positive effect of GGBFS on strength became evident as the curing period increased. The increase in strength was significant when the curing period was extended from 7 to 28 days, whereas the strength gain was comparatively smaller between 28 and 56 days. Therefore, the pozzolanic reactions of GGBFS continued in a time-dependent manner (Nidzam and Kinuthia 2010) and these reactions were more effective from 7 to 28 days in this study. In the ANOVA results (Table 3), the F-value of the interaction term of GGBFS and curing period being 45.20 and the F-value of the GGBFS term being 81.58, indicates that GGBFS was effective on the strength with the length of curing period. An R^2 of 97.84% and a p-value smaller than 0.05 indicate that this model is significant. It can be said that the model equation will be consistent in predicting the strength of the cast specimen, provided that the variables used in this study remain within the lowest and highest-level limits (in the model equations, the unit of a_w and GGBFS are "%" and the unit of UCS is "kPa"). Some terms in the UCS model had p>0.05 and are therefore statistically insignificant at the 95% confidence level; however, they were retained in the fitted equation for model interpretability and should not be interpreted as significant individual effects.

3.2. STS of cast specimens

Although natural clayey soils typically exhibit negligible tensile strength, cement and cement-GGBFS-stabilized DSM columns behave as semi-rigid structural elements that may be subjected to tensile and bending stresses under various loading scenarios. Specifically, tensile strength is critical in the following situations: (i) edge columns within group configurations under eccentric vertical loading, where bending moments induce tensile stresses on the column tension face (Kitazume and Maruyama 2007); (ii) seismic loading conditions, where lateral inertia forces produce bending and tensile failures, particularly in the upper portion of the columns (Boufarh et al. 2025); (iii) lateral spreading and liquefaction-induced kinematic forces in earthquake-prone regions; (iv) excavation-induced asymmetric earth pressures on retaining DSM walls; and (v) embankment loading, where columns near the slope toe experience significant bending moments. Recent comparative analyses

have shown that DSM columns can fail predominantly in tilting and bending modes (Fulambarkar et al. 2025), indicating that shear strength alone is insufficient to characterize their failure behavior. Accordingly, characterizing both UCS and STS provides a more complete description of the mechanical response of GGBFS-modified DSM columns and supports rational design under multidirectional loading scenarios.

For the cast specimens, the highest STS was 830 kPa for the B20S50D56, while the lowest STS was 182 kPa for the B15S50D7 (Fig. 5). The prolongation of the curing period increased STS. Increase in the GGBFS ratio led to an initial decrease in strength at 7 days curing but increase in strength at the end of 28 and 56 days of curing. The reasons behind these results are similar to the increase observed in UCS. For the 7-day curing period, there was a decrease in the STS with the increase in the ratio of GGBFS, while the STS increased with increasing GGBFS ratio at 28 and 56 days of curing. In other words, insufficient curing period combined with the presence of GGBFS in the binder negatively affected the strength. Conversely, as the curing period increased, continued hydration and pozzolanic reactions contributed to an increase in STS. Furthermore, in the established statistical model, the interaction term of GGBFS and curing period had an F-value of 17.2 and the GGBFS term had an F-value of 52.26 (Table 4), indicating that GGBFS significantly influenced strength in conjunction with curing time. Compared with the non-GGBFS reference specimens, the STS values of the GGBFS-containing specimens ranged from 92% to 98% of the reference at 7 days, from 104% to 151% at 28 days, and from 103% to 165% at 56 days as the GGBFS substitution ratio increased from 10% to 50%. The ANOVA results demonstrated that this model is a significant model with an R^2 of 95.97% and a p-value of <0.05, and that the STS for cast specimens can be predicted with high accuracy with this model (in the model equation, the units of a_w and GGBFS are "%" and the unit of STS is "kPa").

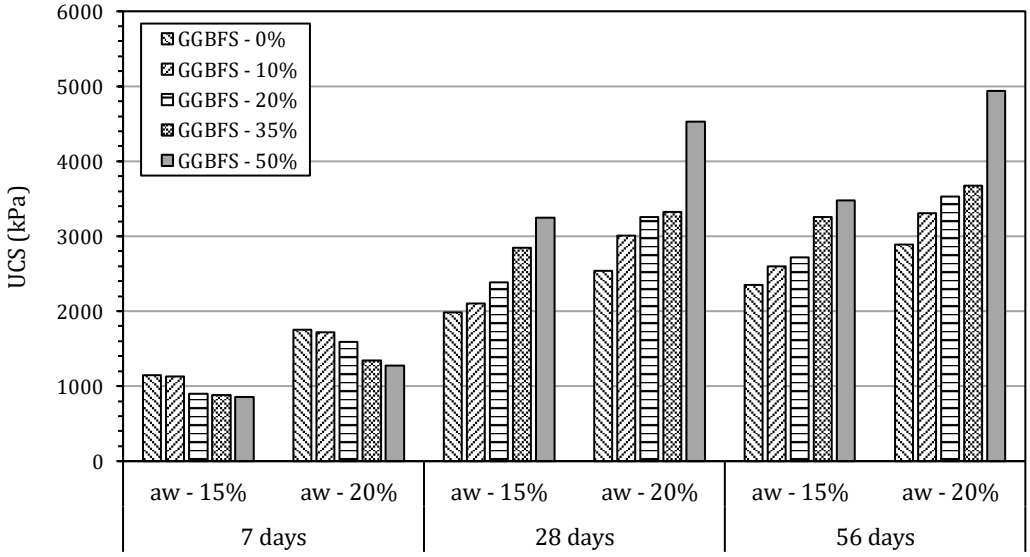

Fig. 3. UCS with respect to curing period, a_w and GGBFS ratio for cast specimens.

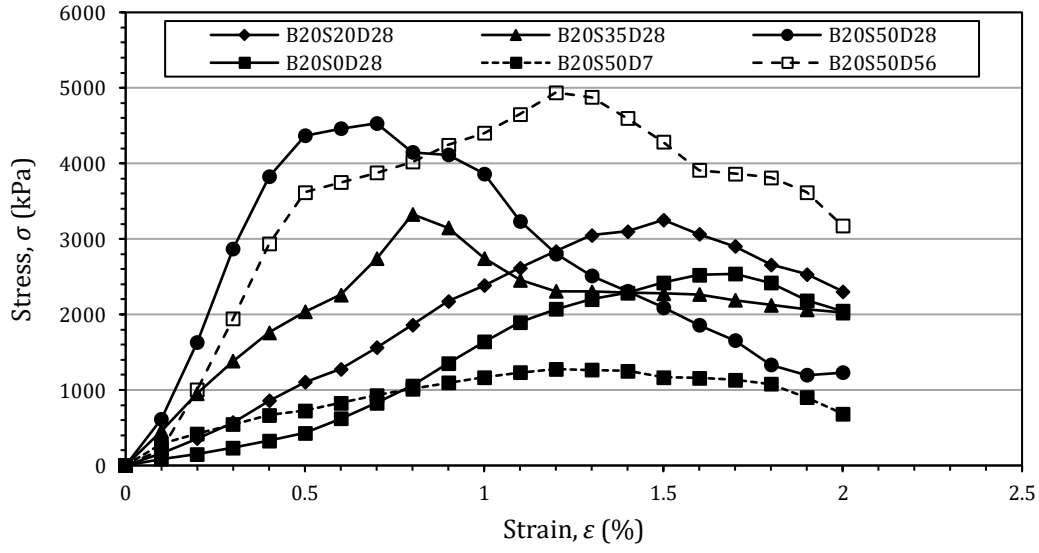

Fig. 4. Stress-strain curves of the selected designs.

Table 3. ANOVA results for UCS.

Source	Degrees of freedom	Sum of squares	Mean square	F-value	P-value
Model	8	33209393	4151174	118.67	<0.001
a_w (%)	1	3880084	3880084	110.92	<0.001
GGBFS (%)	1	2853762	2853762	81.58	<0.001
Day	2	23132028	11566014	330.64	<0.001
GGBFS^2	1	102727	102727	2.94	0.101
a_w (%) × GGBFS (%)	1	78260	78260	2.24	0.150
GGBFS (%) × Day	2	3162529	1581265	45.20	<0.001
Error	21	734586	34980	–	–
Total	29	–	–	–	–
Model equation	for 7 days: UCS = -529+117.4×a_w -40.1×GGBFS+0.228×GGBFS^2+1.149×a_w×GGBFS				
	for 28 days: UCS = 235+117.4×a_w -0.95×GGBFS+0.228×GGBFS^2+1.149×a_w×GGBFS				
	for 56 days: UCS = 602+117.4×a_w -1.7×GGBFS+0.228×GGBFS^2+1.149×a_w ×GGBFS				

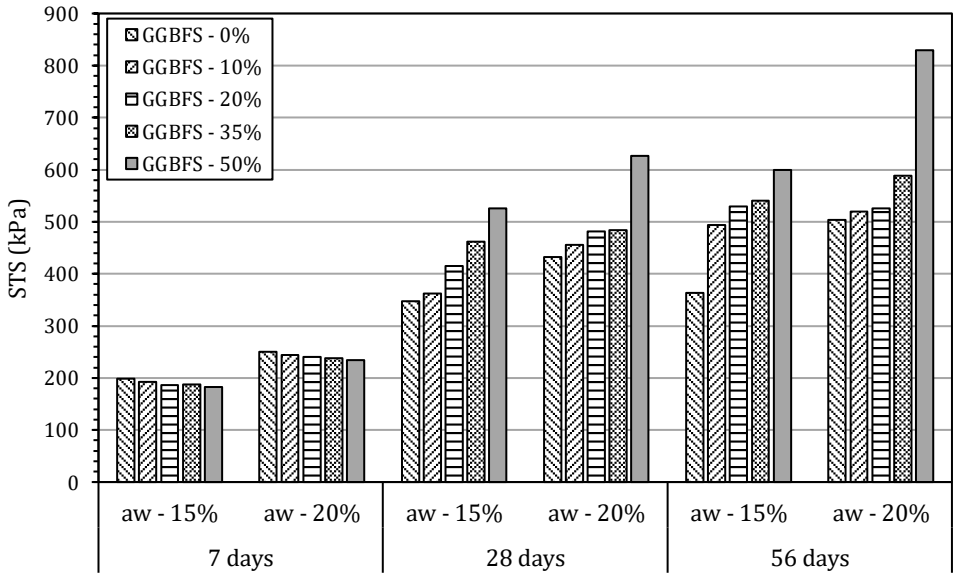

Fig. 5. STS with respect to curing period, a_w and GGBFS ratio for cast specimens.

Table 4. ANOVA results for STS.

Source	Degrees of freedom	Sum of squares	Mean square	F-value	P-value
Model	6	756046	126008	91.22	<0.001
a_w (%)	1	38092	38092	27.58	<0.001
GGBFS (%)	1	72191	72191	52.26	<0.001
Day	2	598200	299100	216.55	<0.001
GGBFS (%) × Day	2	47517	23758	17.20	<0.001
Error	23	31770	1381	–	–
Total	29	–	–	–	–
Model equation	for 7 days: STS = -27.6+14.25×a_w -0.289×GGBFS				
	for 28 days: STS = 128.2+14.25×a_w +3.544×GGBFS				
	for 56 days: STS = 184.6+14.25×a_w +5.024×GGBFS				

3.3. Permeability of cast specimens

The permeability test results indicated that the highest k_{DSM} value of 9.17×10^{-10} cm/s was obtained for B15S0D28, while the lowest k_{DSM} value of 0.16×10^{-10} cm/s was observed for B15S50D56 (Fig. 6). In parallel with the change in UCS and STS, the permeability decreased with the extension of the curing period. In addition, the increase in GGBFS ratio also decreased permeability. The presence of GGBFS, which led to better filling of pores in the specimens (Cheah et al. 2016; Lindh and Lemenkova 2022), was a significant factor in reducing permeability. Therefore, changes in k_{DSM} were influenced not only by UCS and STS but also by hydration and time-dependent pozzolanic reactions. Minor deviations in permeability trends can be attributed to differences in microstructural homogeneity and pore distribution, rather than binder ratio alone, as also supported by the SEM observations presented in Section 3.6. Compared to specimens without GGBFS in the binder, even 10% GGBFS content significantly reduced permeability. Compared with the non-GGBFS reference specimens, the k_{DSM} values of the GGBFS-containing specimens ranged from 18% to 55% of the references at 28 days and from 4% to 38% at 56 days. According to the ANOVA results (Table 5), an R^2 of 92.54% and a p-value of <0.05 indicate that the established model is statistically significant (in the model equations; the unit of GGBFS is "%" and the unit of k_{DSM} is "cm/s", ANOVA was performed for $k_{DSM}\times10^{10}$ cm/s). The ANOVA results showed that k_{DSM} for the cast specimens prepared in the laboratory can be predicted accurately using the model equations (Table 5).

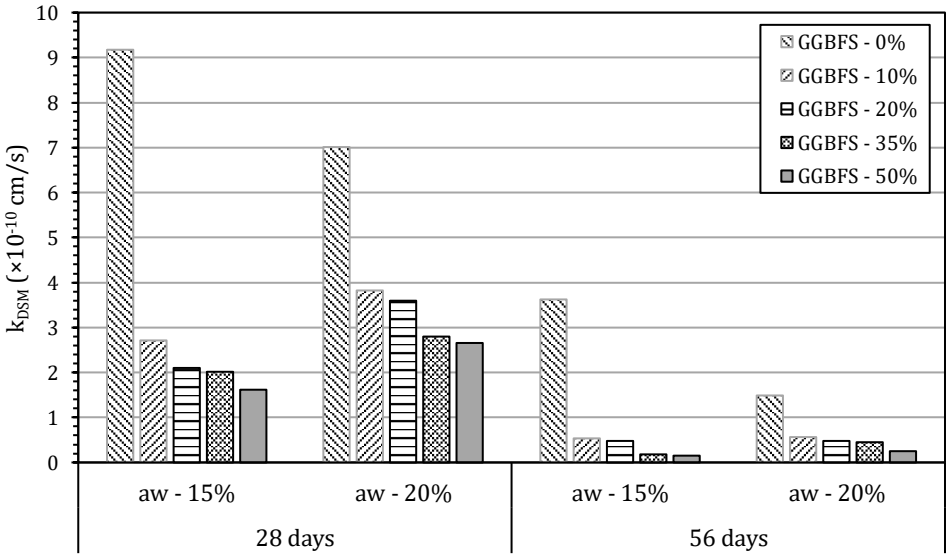

Fig. 6. k_{DSM} values with respect to curing period, a_w and GGBFS ratio for cast specimens.

Table 5. ANOVA results for k_{DSM} values.

Source	Degrees of freedom	Sum of squares	Mean square	F-Value	P-Value
Model	4	25.62	6.40	46.50	<0.001
GGBFS (%)	1	7.04	7.04	51.09	<0.001
Day	1	17.48	17.48	126.87	<0.001
GGBFS²	1	1.16	1.16	8.40	0.011
GGBFS (%) × Day	1	0.650	0.650	4.72	0.046
Error	15	2.07	0.138	–	–
Total	19	–	–	–	–
Model equation	for 28 days: $\ln(k_{DSM}\times10^{10}) = 1.991-0.07\times GGBFS+9.36\times10^{-4}\times GGBFS^2$				
	for 56 days: $\ln(k_{DSM}\times10^{10}) = 0.617-0.09\times GGBFS+9.36\times10^{-4}\times GGBFS^2$				

3.4. Correlation of UCS with STS and k_{DSM}

The relationship between UCS and STS was examined, as shown in Fig. 7(a). The coefficient of determination was R^2 = 94.67%, indicating a strong relationship between UCS and STS. The STS/UCS ratios ranged from 14% to 21%, and the regression equation presented in Fig. 7(a) can be used to estimate STS from UCS within the investigated experimental range. A relationship among UCS, STS, cohesion, and internal friction angle has also been reported for lime-improved soils (Consoli et al. 2014).

The relationship between UCS and k_{DSM} was also examined, as shown in Fig. 7(b). The coefficient of determination was only R^2 = 37.69%, indicating that UCS alone could not reliably predict k_{DSM}. Although mixtures with higher strength generally tended to exhibit lower k_{DSM} values, permeability was also governed by pore connectivity, microstructural homogeneity, and the distribution of hydration and pozzolanic products, as demonstrated by studies on stabilized fine-grained soils and cementitious composites (Lindh and Lemenkova 2022; Cheah et al. 2016). Related research on waste-modified concrete has similarly shown that replacement dosage can simultaneously alter compressive strength and water permeability, with the most favorable balance between these properties occurring at an intermediate replacement level (Mahmud et al. 2025). In the present study, increasing the curing period and GGBFS ratio generally increased UCS and STS while decreasing k_{DSM}. However, the rate of reduction in k_{DSM} did not correspond directly to the rate of increase in UCS. Therefore, a reliable predictive relationship between UCS and k_{DSM} could not be established.

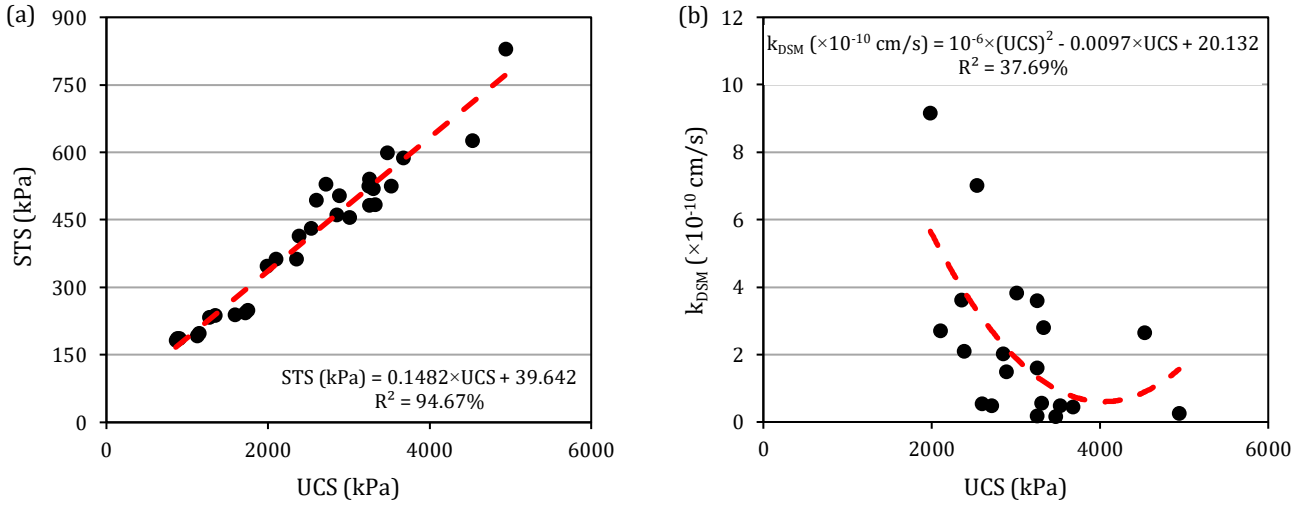

Fig. 7. Correlation between different properties: (a) UCS–STS relationship; (b) UCS–k_{DSM} relationship.

3.5. Comparison of the properties of cast specimens and core samples

The relation between the UCS of the cast specimens and core samples of 4 designs, for which DSM columns were formed, was analysed (Fig. 8(a)). The core sample UCS values were between 45.26% and 69.79% of the cast specimen UCS values. According to the specifications, the core sample strengths of in-situ DSM columns can be 20-50% (EuroSoilStab 2002) and 20-100% (CDIT 2002) or at a minimum 50% (Bruce et al. 2013) of the cast specimen strengths. In this study, since the DSM columns were formed in the laboratory in a similar manner as in-situ application, the ratios of core sample strengths to cast specimen strengths fell within the recommended ranges of specifications. The lower strength of cores from in-situ DSM columns stems from the difficulty of attaining the homogeneity achievable in cast specimens. Therefore, higher strengths are expected for cast specimens. Indeed, in this study, since the core samples extracted from the DSM columns were formed in a manner similar to in-situ applications, their strengths were lower than those of the cast specimens.

A similar result was observed in the comparison between core samples and cast specimens for STS tests (Fig. 8(b)). Accordingly, core sample STS values were 63.00% - 77.58% of the cast specimen STS values. In addition, the comparison of the permeability test results for core samples and cast specimens showed that the core samples were more permeable (Fig. 8(c)). The core sample k_{DSM} values were 118.54% - 193.21% of the cast specimen k_{DSM} values. This relationship reflects the greater microstructural heterogeneity of mixed columns compared with homogeneous cast specimens.

Three mechanisms may contribute to this difference: (i) rotary mixing can produce binder-rich and binder-poor zones within the column matrix, consistent with the cement content variability reported by Zuo et al. (2023) and the in-situ shear strength variability observed by Forsman et al. (2025); (ii) entrapped air voids and partially saturated micro pockets formed during clay–slurry mixing may create preferential flow paths; and (iii) the lower unit weight of model/field DSM columns relative to cast specimens (Saride and Mypati 2024), together with FHWA observations that field-mixed material may attain only 20–50% of laboratory strength, suggests a more open pore structure. Minor coring-induced disturbance cannot be excluded but is considered secondary. From an engineering perspective, this is important for DSM applications where permeability is important such as cut-off walls and containment barriers. In this study, the k_{DSM} of core samples was 1.19–1.93 times higher than that of cast specimens; however, extrapolation to field conditions requires field scale verification. The observed core-to-cast UCS ratios of 45.26% and 69.79% suggest that mechanical performance may be predicted more reliably than hydraulic performance. The results indicated that the strength and permeability of core samples extracted from laboratory DSM columns can be useful in providing a preliminary prediction of the mechanical and hydraulic performance of in-situ DSM columns.

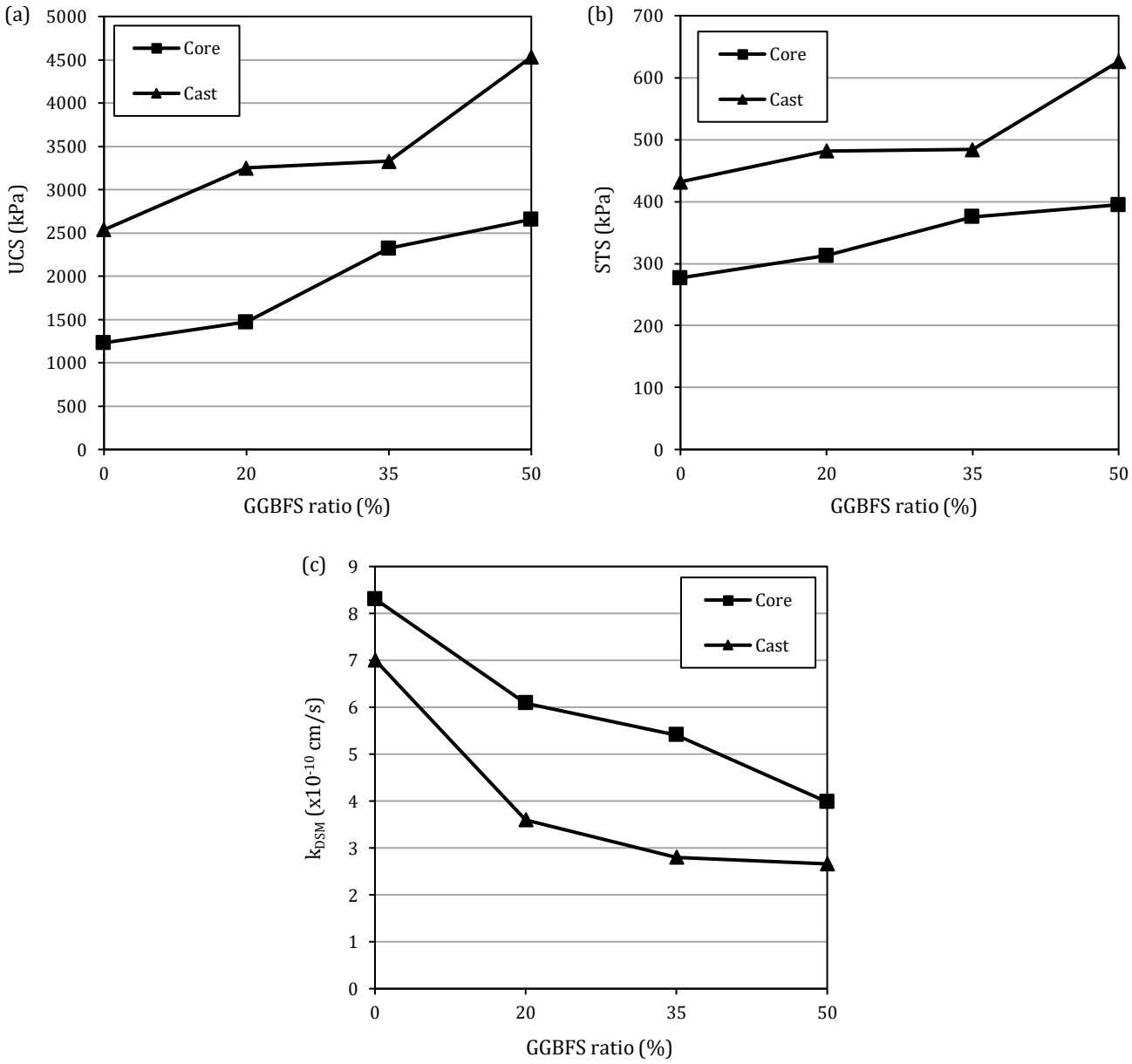

Fig. 8. Comparison of mechanical and hydraulic performance of core samples and cast specimens: (a) UCS values; (b) STS values; (c) k_{DSM} values.

3.6. SEM and XRD analysis results

In the DSM columns, in addition to ettringite, hydration products such as calcium-aluminum-silicate hydrates (C-A-S-H), C-S-H, and CH were identified from SEM images (Fig. 9). As the GGBFS ratio increased, the sample structure became less porous, the amount of C-S-H increased, and C-A-S-H formed. Moreover, the mixture containing 35% GGBFS had a less porous structure than the other samples. As observed from the SEM images, as the GGBFS ratio increased, the amount of C-S-H increased, pores decreased and C-A-S-H formed at 35% GGBFS ratio, which is consistent with the strength and permeability test results of the samples. The increase in UCS and STS and the decrease in permeability as the GGBFS ratio increases are an important indicator of the changing chemical content and amount of pores with the change in the GGBFS ratio on mechanical and hydraulic behavior. Therefore, the strength gain of the samples is primarily attributed to the hydration products formed, namely C-S-H and C-A-S-H, contributing directly to the increase in UCS and STS. The size and amount of pores in the sample structures may also be related to permeability. SEM images also supported the fact that mixtures containing 20% and 35% GGBFS, which had a less porous structure, had lower permeability than the mixture without GGBFS. It was observed that the XRD analysis results (Fig. 10) were consistent with the SEM images. Accordingly, in the presence of cement and GGBFS, peaks were formed in the diffractograms where C-S-H, C-A-S-H, CH and ettringite occurred at the relevant 2θ values. Thus, as determined in the SEM images, it was revealed by the XRD analysis that both hydration and pozzolanic reaction products were formed by mixing the clay soil with cement and GGBFS.

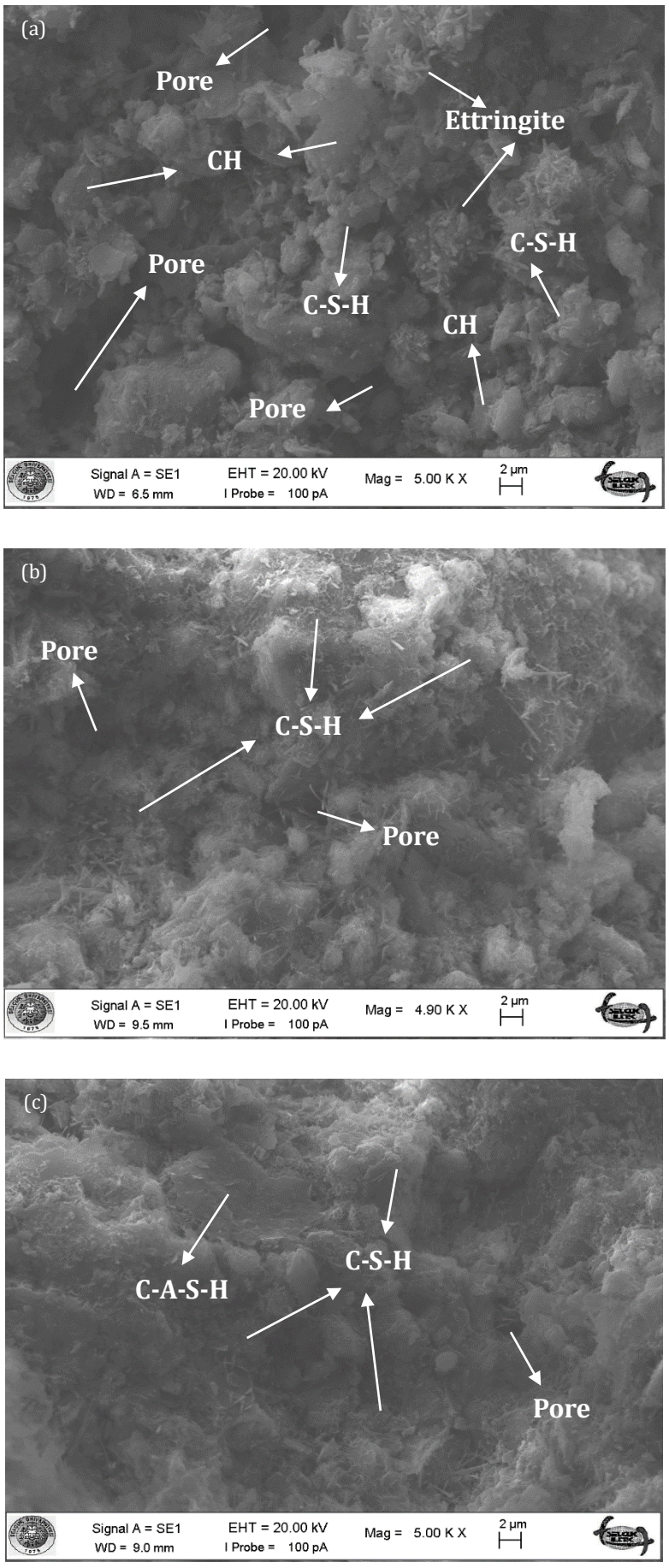

Fig. 9. SEM images for DSM columns: (a) 0% GGBFS; (b) 20% GGBFS; (c) 35% GGBFS.

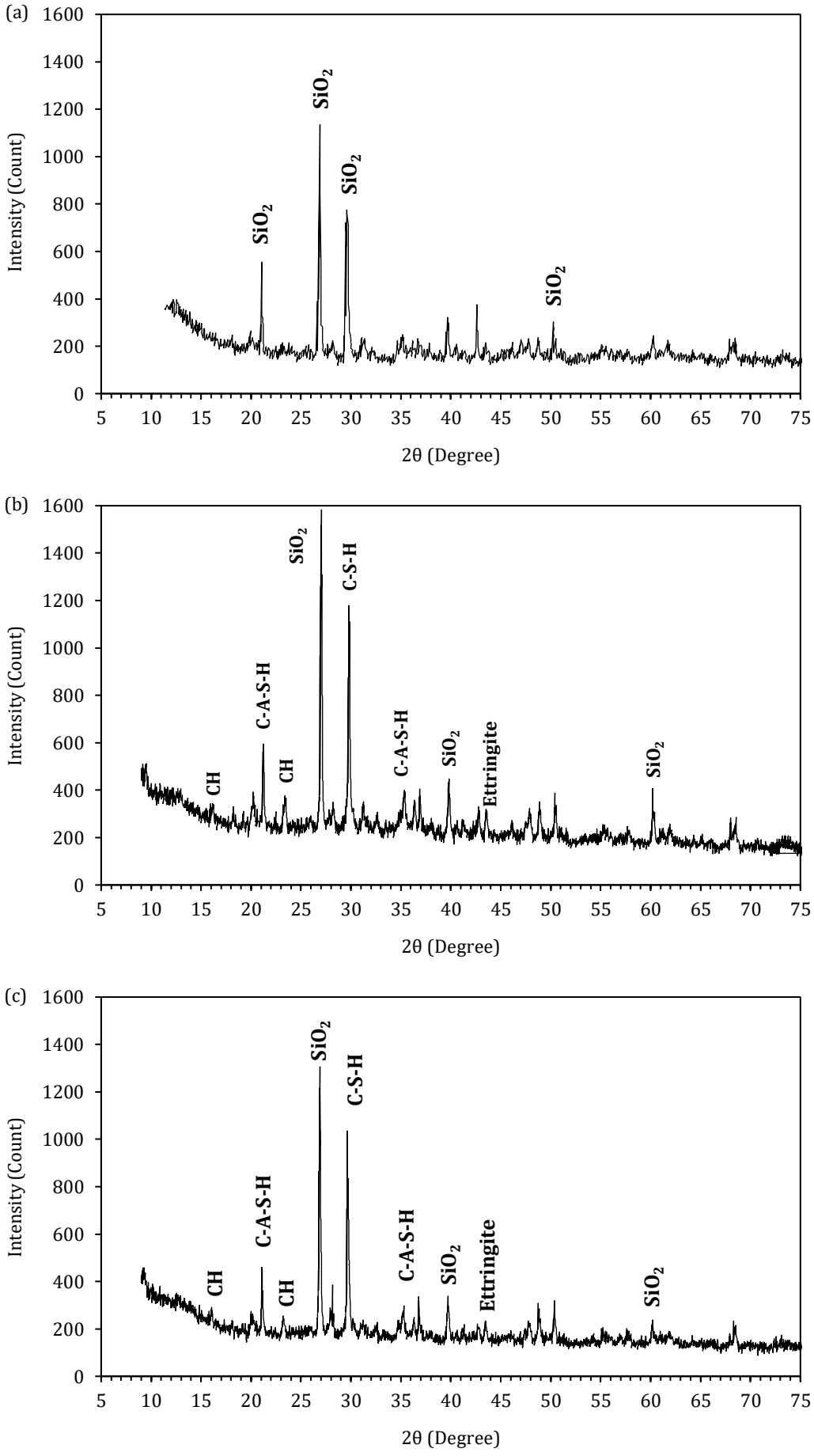

Fig. 10. XRD diffractograms for DSM columns and clay: (a) Clay; (b) 20% GGBFS; (c) 35% GGBFS.

4. Conclusions

In this study, the effect of GGBFS, which is used by substituting cement at certain ratios, on the mechanical and permeability properties of DSM columns was investigated by performing UCS, STS and permeability tests using cast specimens and core samples, and the following results were observed:

- Relative to the corresponding non-GGBFS reference specimens, GGBFS-containing specimens showed lower UCS and STS at 7 days, but higher values at 28 and 56 days, confirming the time-dependent contribution of GGBFS-related hydration and pozzolanic reactions. At 28 and 56 days, UCS reached 105–179% and 110–171% of the reference values, while STS reached 104–151% and 103–165%, respectively.
- The k_{DSM} values of cast specimens decreased with increasing GGBFS substitution. The k_{DSM} values of GGBFS-containing specimens were 18–55% at 28 days and 4–38% at 56 days of the non-GGBFS reference specimens, owing to the pore-filling and additional C-S-H/C-A-S-H formation associated with GGBFS hydration.
- A statistically significant correlation was identified between UCS and STS (R^2 = 94.67%, with STS/UCS = 14–21%), supporting the use of UCS as a reliable predictor of STS within the experimental range. In contrast, the UCS–k_{DSM} relationship yielded R^2 = 37.69%, indicating that permeability is governed by additional microstructural factors that cannot be captured by UCS alone.
- The UCS values of core samples of laboratory-scale DSM columns were 45.26–69.79% of the cast specimen UCS values; STS values were 63.0–77.6%; and k_{DSM} values were 118.5–193.2%. These relationships indicate that laboratory-scale DSM columns may be used as a preliminary tool that laboratory-scale DSM columns can be used as a preliminary tool for evaluating DSM behavior in situ. Laboratory DSM columns exhibited adequate strength and permeability characteristics, demonstrating that effective interactions between soil, cement, and GGBFS can be achieved under controlled laboratory conditions.

Overall, the results suggest that laboratory DSM columns can be effectively used as a preliminary experimental tool to investigate soil–cement–GGBFS interactions and to support the design stage of in-situ DSM applications but not as a direct substitute for field trial columns or site-specific quality control.

Acknowledgements

This publication is based on the master's thesis entitled "Experimental Investigation of Deep Mixing Column Behavior with Blast Furnace Slag Additive".

Funding

This research was supported by Konya Technical University Scientific Research Projects Coordinatorship under grant number 191004004.

Conflict of Interest

The authors declare no potential conflicts of interest with respect to the research, authorship, and/or publication of this manuscript.

Data Availability

The datasets generated and/or analyzed during the current study are not publicly available but are available from the corresponding author upon reasonable request.

AI Assistance

No AI-based tools were used in the preparation of this manuscript.

Author Contributions

All authors made substantial contributions to the conception and design of the study, acquisition of data, analysis and interpretation of data; drafted or critically revised the manuscript for important intellectual content; and approved the final version to be published.

References

Abbey SJ, Ngambi S, Ngekpe BE (2015). Understanding the performance of deep mixed column improved soils: A review. *International Journal of Civil Engineering and Technology*, 6(3), 97-117.

Abbey SJ, Ngambi S, Ganjian E (2017). Development of strength models for prediction of unconfined compressive strength of cement/by-product material improved soils. *Geotechnical Testing Journal*, 40(6), 928-935.

Abutaha F, Çelik Aİ (2025). The engineering properties of silica fume and GGBS-based geopolymer mortars cured in elevated temperature. *Challenge Journal of Concrete Research Letters*, 16(2), 69-84.

Åhnberg H (2006). Consolidation stress effects on the strength of stabilised Swedish soils. *Proceedings of the Institution of Civil Engineers - Ground Improvement*, 10(1), 1-13.

ASTM C496 (2017). Standard test method for splitting tensile strength of cylindrical concrete specimens. ASTM International, West Conshohocken, PA, USA.

ASTM C939 (2016). Standard test method for flow of grout for preplaced-aggregate concrete (flow cone method). ASTM International, West Conshohocken, PA, USA.

ASTM C940 (2016). Standard test method for expansion and bleeding of freshly mixed grouts for preplaced-aggregate concrete in the laboratory. ASTM International, West Conshohocken, PA, USA.

ASTM D2487 (2017). Standard practice for classification of soils for engineering purposes (unified soil classification system). ASTM International, West Conshohocken, PA, USA.

ASTM D4832 (2016). Standard test method for preparation and testing of controlled low strength material (CLSM) test cylinders. ASTM International, West Conshohocken, PA, USA.

ASTM D5084 (2016). Standard test methods for measurement of hydraulic conductivity of saturated porous materials using a flexible wall permeameter. ASTM International, West Conshohocken, PA, USA.

Boufarh R, Aissaoui A, Djellali A, Goudjil K, Boukhatem G, Kırgız MS, Nagaprasad N, Krishnaraj R (2025). Comparative seismic analysis of T-shaped and conventional deep cement mixing columns in highway embankments on soft soil. *Scientific Reports*, 15, 45367.

Broms B (2003). Deep Soil Stabilization: Design and Construction of Lime and Lime/Cement Columns. Royal Institute of Technology, Stockholm, Sweden.

Bruce MEC, Berg RR, Filz GM, Terashi M, Yang DS, Collin JG (2013). Federal Highway Administration Design Manual: Deep Mixing for Embankment and Foundation Support. Technical Report FHWA-HRT-13-046. Federal Highway Administration, Washington, DC, USA.

CDIT (2002). The Deep Mixing Method: Principle, Design and Construction. Coastal Development Institute of Technology, A.A. Balkema Publishers, Lisse, Netherlands.

Chaudhary PN, Pal J (2002). An overview of treatment of steel-making slag for recovery of lime and phosphorus values. *Proceedings of the Seminar on Resurgence of Metallic Materials the Current Scenario (ROMM-2002)*, Jamshedpur, India, 186-190.

Cheah CB, Chung KY, Ramli M, Lim GK (2016). The engineering properties and microstructure development of cement mortar containing

high volume of inter-grinded GGBS and PFA cured at ambient temperature. *Construction and Building Materials*, 122, 683-693.

Chen EJ, Liu Y, Lee FH (2016). A statistical model for the unconfined compressive strength of deep-mixed columns. *Géotechnique*, 66(5), 351-365.

Consoli NC, da Silva Lopes L Jr, Consoli BS, Festugato L (2014). Mohr-Coulomb failure envelopes of lime-treated soils. *Géotechnique*, 64(2), 165-170.

Consoli NC, Winter D, Rilho AS, Festugato L, Teixeira BS (2015). A testing procedure for predicting strength in artificially cemented soft soils. *Engineering Geology*, 195, 327-334.

Davidson LK, Demirel T, Handy RL (1965). Soil pulverization and lime migration in soil-lime stabilization. *Highway Research Record*, 92, 103-126.

Estabragh AR, Khatibi M, Javadi AA (2016). Effect of cement on treatment of a clay soil contaminated with glycerol. *Journal of Materials in Civil Engineering*, 28(4), 04015157.

EuroSoilStab (2002). Development of Design and Construction Methods to Stabilize Soft Organic Soils: Design Guide Soft Soil Stabilization. European Commission, Industrial and Materials Technologies Programme (Brite-EuRam III), Brussels, Belgium.

Forsman J, Löfman M, Ikävalko J, Korkiala-Tanttu L (2025). Low-carbon binders in six test deep mixing cases: Variation of in-situ strength. *Transportation Geotechnics*, 53, 101597.

Fulambarkar S, Manna B, Shahu JT (2025). Effect of deep mixed column pattern on the performance of basal reinforced embankment resting on soft soil. *Soils and Foundations*, 65(2), 101578.

Ganjian E, Sadeghi-Pouya H, Claisse P, Waddell M, Hemmings S, Johansson S (2008). Plasterboard and gypsum waste in a novel cementitious binder for road construction. *Concrete*, 42(6), 20-22.

Ganjian E, Jalull G, Sadeghi-Pouya H (2015). Using waste materials and by-products to produce concrete paving blocks. *Construction and Building Materials*, 77, 270-275.

Han J (2015). Principles and Practice of Ground Improvement. John Wiley & Sons, Hoboken, NJ, USA.

He J, Wang X, Su Y, Li Z, Shi X (2019). Shear strength of stabilized clay treated with soda residue and ground granulated blast furnace slag. *Journal of Materials in Civil Engineering*, 31(3), 06018029.

Holm G (2003). State of practice in dry deep mixing methods. *Proceedings of the 3rd International Conference on Grouting and Ground Treatment*, New Orleans, LA, USA, 145-163.

Kitazume M, Maruyama K (2007). Internal stability of group column type deep mixing improved ground under embankment loading. *Soils and Foundations*, 47(3), 437-455.

Kitazume M, Grisolia M, Leder E, Marzano IP, Correia AAS, Oliveira PJV, Åhnberg H, Andersson M (2015). Applicability of molding procedures in laboratory mix tests for quality control and assurance of the deep mixing method. *Soils and Foundations*, 55(4), 761-777.

Lindh P, Lemenkova P (2022). Permeability, compressive strength and Proctor parameters of silts stabilised by Portland cement and ground granulated blast furnace slag (GGBFS). *Archive of Mechanical Engineering*, 69(4), 667-692.

Mahmud H, Ahmed T, Islam MS (2025). Combined effect of rice husk ash and animal bone powder on strength and permeability of concrete. *Challenge Journal of Structural Mechanics*, 11(1), 1-13.

Mohamad N, Embong R, Othman NH, Muthusamy K, Jaafar MFM (2025). Flowability and compressive strength of ternary blended cement mortar of coal bottom ash and ground cockle shell ash. *Challenge Journal of Concrete Research Letters*, 16(1), 25-32.

Nidzam RM, Kinuthia JM (2010). Sustainable soil stabilisation with blast furnace slag: A review. *Proceedings of the Institution of Civil Engineers - Construction Materials*, 163(3), 157-165.

Paniagua P, Ritter S, Moseid M, Okkenhaug G (2023). Bioashes and steel slag as alternative binders in ground improvement of quick clays. *Proceedings of Geo-Congress 2023: Soil Improvement, Geoenvironmental, and Sustainability*, Los Angeles, CA, USA, 25-34.

Ramírez AL, Korkiala-Tanttu L (2023). Stabilisation of Malmi soft clay with traditional and low-CO2 binders. *Transportation Geotechnics*, 38, 100920.

Richardson IG, Brough AR, Groves GW, Dobson CM (1994). The characterization of hardened alkali-activated blast-furnace slag pastes and the nature of the calcium silicate hydrate (C-S-H) phase. *Cement and Concrete Research*, 24(5), 813-829.

Sargent P (2015). The development of alkali-activated mixtures for soil stabilisation. In: Pacheco-Torgal F, Labrincha JA, Leonelli C, Palomo A, Chindaprasirt P, editors. *Handbook of Alkali-Activated Cements, Mortars and Concretes*. Woodhead Publishing, Sawston, Cambridge, UK, 555-604.

Saride S, Mypati VNK (2024). Effect of area improvement ratio of geopolymer-based deep mixing columns on swell-shrink behavior of expansive soils. *Construction and Building Materials*, 417, 135163.

Savila I-M, Korkiala-Tanttu L, Forsman J, Löfman M (2025). Mechanical properties of stabilized soil: Study on recovered field samples from deep stabilization sites. *Transportation Geotechnics*, 51, 101540.

Shaheen YBI, Etman ZA, Sabiha HL (2025). Design of reactive powder concrete mortar mixes through high strength and durability. *Challenge Journal of Concrete Research Letters*, 16(3), 142-154.

Shakri MS, Hafez MA, Adnan MA, Nazaruddin AT (2014). Effects of use of PFA on strength of stone column and sand column. *Electronic Journal of Geotechnical Engineering*, 19, 3745-3755.

Shen S-L, Xu Y-S, Han J, Zhang J-M (2012). A ten-year review on the development of soil mixing technologies in China. *Proceedings of the 4th International Conference on Grouting and Deep Mixing*, New Orleans, LA, USA, 343-356.

Subathra Devi V, Gnanavel BK (2014). Properties of concrete manufactured using steel slag. *Procedia Engineering*, 97, 95-104.

Suksiripattanapong C, Tesanasin T, Tiyasangthong S, Tabyang W, Sukontasukkul P, Chindaprasirt P (2023). Use of cement and bottom ash in deep mixing application for stabilization of soft Bangkok clay. *Arabian Journal for Science and Engineering*, 48(4), 4583-4593.

Swamynaidu M, Tyagi A (2025). Hydraulic conductivity characteristics of slag-cement clay mixes applicable to in-situ soil mixing techniques. *International Journal of Geosynthetics and Ground Engineering*, 11, 40.

Takano M, Suzuki K, Shinkawa N (2015). Cement deep mixing in Lach Huyen port infrastructure construction project in northern Vietnam. *Proceedings of the Deep Mixing 2015 Conference*, San Francisco, CA, USA.

Turan E, Alameri IA, Oltulu M (2025). Long-term durability of red mud-modified cement mortars: Effects of high temperature and freeze-thaw cycles. *Challenge Journal of Structural Mechanics*, 11(3), 116-127.

Urbánek J, Antoš P (2026). Utilization of fly dust generated during fired shale production for the preparation of aggregates and geopolymers. *Challenge Journal of Concrete Research Letters*, 17(1), 71-81.

Ünal S, Canbaz M (2026). Development of a sustainable geopolymer structural element with waste glass powder: Mechanical characteristics. *Challenge Journal of Structural Mechanics*, 12(1), 22-29.

Xue Z, Zhang W, Zhao X, Meng F, Qin F, Xiao G, Nie Z, Chen J (2024). Utilization of cement deep mixing pile for soft soil foundation: A Malaysian case study. *Frontiers in Materials*, 11, 1484228.

Ye G, Shu H, Zhang Z, Kang S, Zhang S, Wang Q (2021). Solidification and field assessment of soft soil stabilized by a waste-based binder using deep mixing method. *Bulletin of Engineering Geology and the Environment*, 80(6), 5061-5074.

Yi Y, Liska M, Al-Tabbaa A (2014). Properties and microstructure of GGBS-magnesia pastes. *Advances in Cement Research*, 26(2), 114-122.

Yu H, Yi Y, Yao K, Romagnoli A, Tan WL, Chang ABP (2021). Effect of water/cement ratio on properties of cement-stabilized Singapore soft marine clay for wet deep mixing application. *International Journal of Geotechnical Engineering*, 15(9), 1198-1205.

Zuo J, Wang B, Li W, Han S, Wang J, Zhang F (2023). Quality assessment and quality control of deep soil mixing columns based on a cement-content controlled method. *Scientific Reports*, 13, 4813.